博士論文

Polarization and microstructure characteristics of solid oxide fuel cell composite cathodes

(固体酸化物形燃料電池コンポジット空気極の分極特性および電極微細構造に関する研究)

金　容兌

Contents

Abstract

Fuel cells attract great attention as one of the promising power systems for next generation due to its various merits. Fuel cells can achieve high system efficiency since they directly convert chemical energy to electrical energy. Fuel cells are also environmental-friendly since pollutants do not emit during operation. Especially, solid oxide fuel cells (SOFCs) which operate at high temperature, e.g. 700 ~1000°C, show high efficiency and fuel flexibility compared to other types of fuel cells. The system efficiency can be further improved by combining with waste heat recovery systems.

In SOFC, oxygen is ionized in the cathode, and oxide ion diffuses through the electrolyte and reacts with the fuel in the anode. However, high operation temperature also brings some serious issues. System durability is deteriorated by high thermal stresses in the systems. Furthermore, system cost is increased due to the usage of expensive materials which have durability at high temperatures. If operation temperature of SOFC can be decreased, reliability and system cost are also reduced drastically. However, the efficiency of SOFC will be deteriorated especially for the cathode side. In order to overcome this issue, recent SOFCs employ mixed ionic-electronic conductors (MIECs) for cathode materials. Conventional SOFC cathodes consist of three phases, i.e. pore, electronic and ionic conductors. Electrochemical reaction takes place at triple phase boundary (TPB) where three phases meet at a same position. On the other hand, electrochemical reactions can take place not only at the TPB, but also at the surface for the MIECs. Thus, cathode performance is improved due to the increase of reaction area. Representative MIEC materials are $La_{1-x}Sr_xCo_{1-y}Fe_yO_{3-\delta}$ or $La_{1-x}Sr_xCoO_{3-\delta}$ (x, y = from 0.1 to 0.9). However, ionic conductivity of MIEC materials decreases drastically at low operation temperatures. Therefore, composites of MIEC with high ionic conductors have been investigated in order to improve the cathode performance at low operation temperatures. In fact, performance enhancements of MIEC-ionic conductor composites have been experimentally reported by several researchers. However, MIEC surface area is decreased due to the increase of ionic conducting phase of the composite. Therefore, it is considered that performance is enhanced by not only by the improvement of ionic conduction kinetics, but also by the TPB reactions in the composite. In order to develop efficient MIEC-ionic conductor composite cathodes, it is necessary to investigate concrete electrochemical reaction mechanisms of composite cathodes.

In the present study, electrochemical reaction mechanisms of MIEC-ionic conductor are investigated by both experiments and numerical simulations. $La_{0.6}Sr_{0.4}Co_{0.2}Fe_{0.8}O_{3-\delta}$ (LSCF) and $La_{0.6}Sr_{0.4}CoO_{3-\delta}$ (LSC) were used as the MIEC materials, and $Gd_{0.1}Ce_{0.9}O_{2-\delta}$ (GDC) was used as the ionic conductor. An electrolyte-supported cell was prepared for the experiments. Ni-GDC was used as the anode material and GDC was used as the solid electrolyte material. LSCF-GDC and LSC-GDC

composite cathodes with different volume ratios were fabricated onto the GDC electrolyte by screen printing method. Cathode-reference measurements were conducted, and I-V characteristics and electrochemical impedance spectroscopy were measured at 700°C with 100 % of pure oxygen. Activation overpotentials were quantified by extracting ohmic losses. Polarization resistances were obtained from the electrochemical impedance spectroscopy results.

Cathode microstructures were reconstructed by dual beam focused ion beam-scanning electron microscopy (FIB-SEM). Epoxy resin was infiltrated into the post-tested cells in order to distinguish pore phases in the cathodes. Then, the specimens were polished by a cross-section polisher. An energy selective backscattered (EsB) detector was used for the FIB-SEM measurement. Microstructure parameters were calculated, and the results were correlated with cathode polarization characteristics.

Electrochemical reaction mechanisms were investigated by Lattice Boltzmann Method (LBM). In the numerical simulation, both surface reaction and TPB reaction were considered. Exchange current densities for the surface reaction were fitted by the experimental results of pure LSCF and LSC cathodes. Those for the TPB reaction were fitted by the experimental results of composites. Current and oxygen chemical potential distributions were quantified. Electrochemical reaction and ionic conduction kinetics were discussed.

For the LSCF-GDC composite cathodes, the best performance is achieved at a volume ratio of LSCF:GDC = 30:70 %. Neither LSCF surface reaction nor TPB reaction can individually explain the performance of LSCF-GDC composites by a single reaction mechanism. As the volume fractions of GDC in the composites increase, reactive thicknesses are elongated. Slight discrepancies between experimental and simulation overpotential results are observed for the volume ratios of LSCF:GDC = 50:50 and 70:30 %. It is considered that improvement of effective ionic conductivity by GDC addition contributes to the performance enhancement of LSCF-GDC composite cathode. Dependence on ionic conductivity of LSCF is investigated by the numerical simulations. The effective thickness of LSCF:GDC = 30:70 % is achieved at around 40 μm by experiments.

For the LSC-GDC composite cathodes, again a volume ratio of LSC:GDC = 30:70 % shows the best performance. It is considered that reaction mechanisms of LSC-GDC are the same with those of the LSCF-GDC composite. Reactive thicknesses are elongated for all volume ratios of the composite cathodes. Experimental and simulation results of LSC-GDC are compared to those of LSCF-GDC. Performances of LSC-GDC composite cathodes are better for all volume ratios than the LSCF-GDC. It is shown that LSC shows high sinterability which leads to small surface area but higher active TPB density at low GDC volume fractions. It is considered that not only the increase of reaction area due to the sintering of LSC, but also the improvement of effective ionic conductivity of the LSC contribute to the performance enhancement of LSC-GDC composite cathodes.

In order to investigate more deeply the contribution of surface and TPB reactions of the LSC-

GDC composite, different sizes of original powder are prepared. LSC of 0.5 μm and GDC of 3 μm (GDC3), LSC of 3 μm and GDC of 0.5 μm (LSC3) are mixed with a volume ratio of 50:50 %. It is assumed that TPB length do not change significantly because the volume ratio is fixed. The GDC3 cathode showed better performance compared to the LSC3 cathode. For the GDC3 cathode, LSC surface area and active TPB density are increased due to higher sinterability of LSC compared to GDC. Tortuosity factor of GDC didn't change with different original particle sizes. However, for LSC, the tortuosity factor is decreased significantly when started from small powder size. It is considered that the increase of reaction area and improvement of ionic conductivity inside the LSC due to the sintering of LSC contributes to the performance enhancement of GDC3 cathode.

LSC-GDC composite cathodes with the volume ratios of 30:70, 50:50 and 70:30 % are discharged with current density of 0.2 A/cm^2 for 100 hrs. As the volume fraction of GDC increases, cathode performance is degraded more significantly. Microstructure parameters before and after operation are investigated. It is shown that performance degradation cannot be explained by microstructural variations. After operation, inhomogeneous microstructures of LSC are observed. It is considered that the LSC-GDC performance is degraded by the morphological change of LSC. Best performance at initial condition and lower performance degradation rate are achieved for a volume ratio of LSC:GDC = 30:70 %. Therefore, it is expected that a 30:70 % is the most promising volume ratio of LSC-GDC composite for the SOFC cathode material.

Nomenclature

Roman symbols

A	surface area [m^2]
C_{O_2}	oxygen concentration [mol/m^3]
$\vec{c}$	particle velocity
D	diffusion coefficient [m^2/s]
$D_{\text{effective}}$	effective diffusion coefficient [m^2/s]
F	Faraday constant [C/mol]
f_i	velocity distribution function
f_i^{eq}	equilibrium distribution of Maxwell
G	Gibbs free energy [J]
i	current density [A/m^2]
i_0	exchange current density [A/m^2]
i_{reac}	reaction current [A/m^3]
k	Boltzmann constant [J/K]
L_{TPB}	active TPB length [m]
M	molecular weight
N_i	molar flux [$mol/m^2 \cdot s$]
P	pressure [atm]
Q	activation energy [J/mol]
R	gas constant [$J/K \cdot mol$]
r	mean pore radius [m]
T	absolute temperature [K]
Δt	time per one step
t^*	relaxation time
u	mole velocity
V	volume fraction
w	production term
$\vec{x}$	position vector
y	mole fraction

Greek symbols

γ	pressure constant
δ	oxygen nonstoichiometry
ε	geometric intermolecular force constant
ζ	arithmetic intermolecular force constant [Å]
η	overpotential [V]
θ	parameter for reaction coverage
$\tilde{\mu}$	electrochemical potential [J/mol]
σ	conductivity [S/m]
Ω_D	collision integral
χ	electrostatic surface potential

Subscripts

e^-	electron
O_2	oxygen
O^{2-}	oxygen ion
H_2O	water
H_2	hydrogen

Chapter 1
Introduction

1.1 Background

After the Industrial Revolution with the development of steam engine from the 18th century in England, fossil fuels such as coal or oil are used as the primary energy sources. As the society has developed extensively, the fuel usage increased drastically. However, it is considered that the fossil fuel usage is semi-permanent as their reserves are limited. Figure 1-1 shows the world energy consumption from 1990 to 2040 [1]. Organization for Economic Co-operation and Development (OECD) members maintain certain energy consumption, while energy consumption of Non-OECD members increases continuously. It is considered that the increase of energy demand is remarkable especially in developing countries. According to International Energy Outlook 2016, it is assumed that total world energy consumption will increase by about 48 % from 2012 to 2040. Figure 1-2 shows the variations of oil demand and supply until 3rd quarter of 2016. As shown in Fig.1-2, both oil demand and supply are increasing steadily. As mentioned above, fossil fuel reserves are finite and the development of alternative energy sources has become an urgent issue.

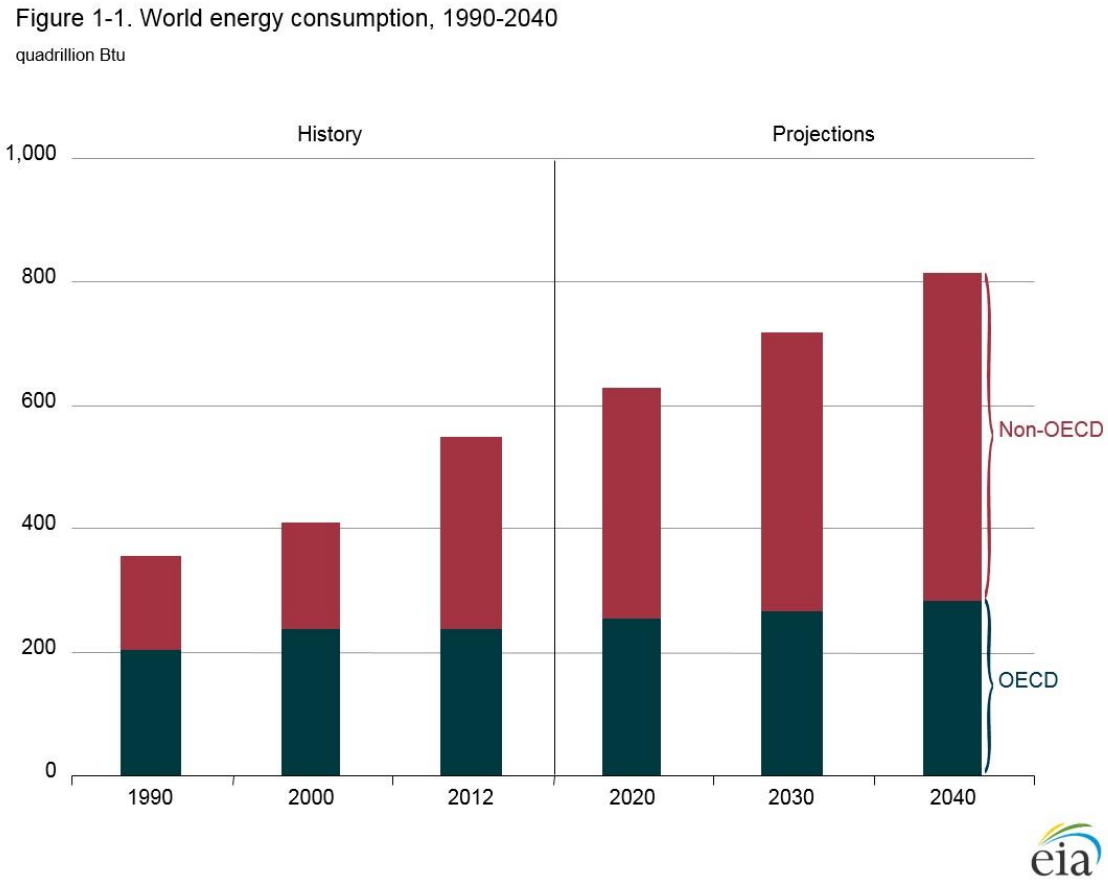

Fig. 1-1 World Energy Consumption [1].

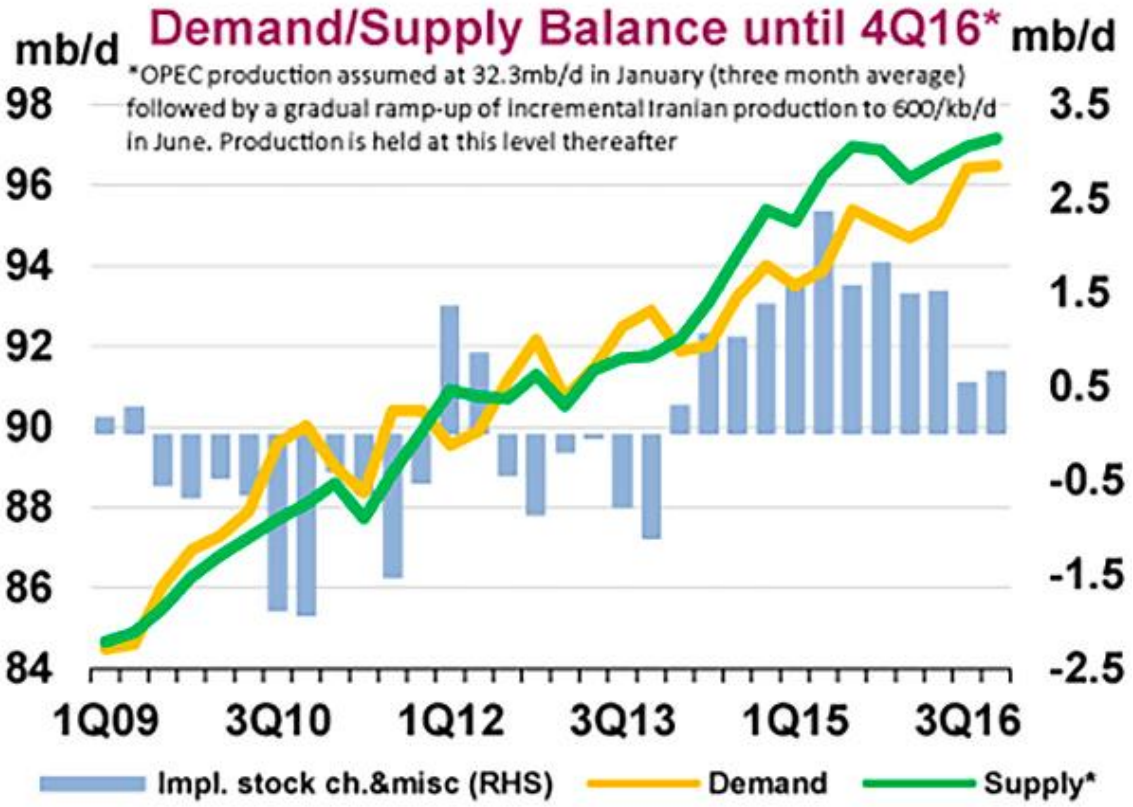

Fig. 1-2 World oil demand and supply until 3rd quarter of 2016 [2].

Global warming is another issue of fossil fuel usage. As widely known, global warming arises from greenhouse gas such as carbon dioxide which is emitted from combustion of fossil fuels. Figure 1-3 shows the global carbon dioxide emission from 1751 to 2010. Carbon dioxide emission increased drastically from the 18th century and it coincides with the Industrial Revolution when fossil fuel has come into use for the energy source. Thus, alternation of energy source becomes a main issue to prevent many problems caused by fossil fuel usage from the viewpoints of finite reserves and environment protection.

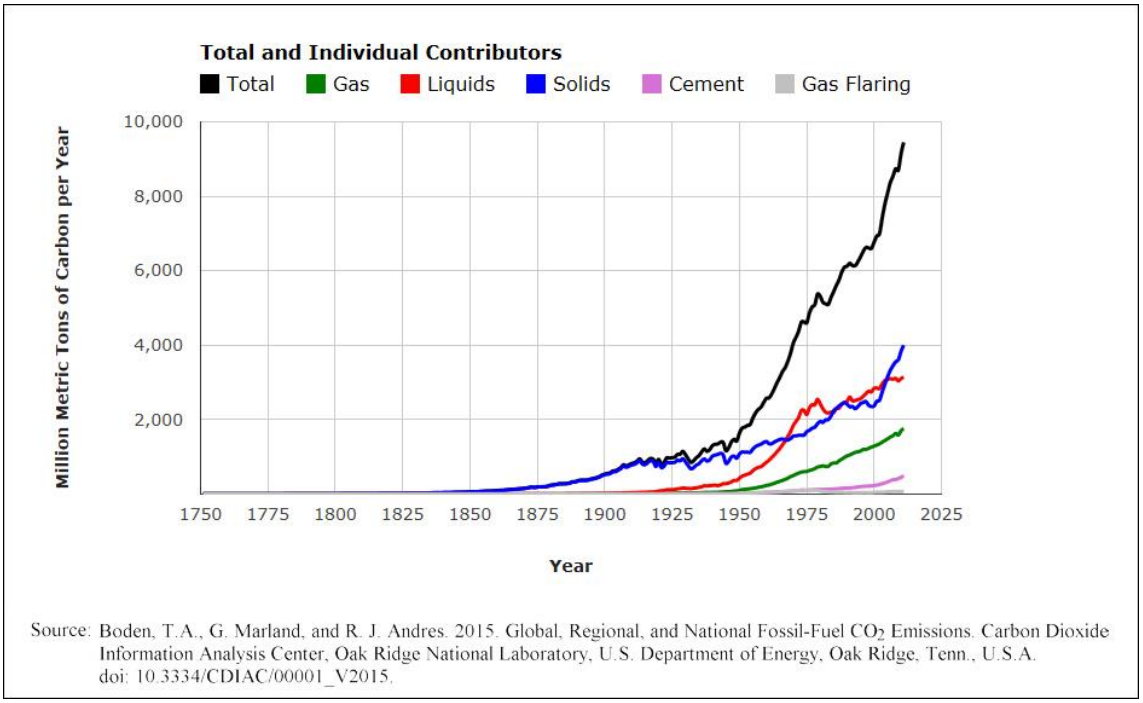

Fig. 1-3 Global carbon dioxide emission [3].

1.2 Alternative Energy

1.2.1 Renewable Energy

As mentioned in Chap. 1.1, alternation of energy sources have been considered to solve many problems caused by fossil fuel usage. Solar, wind and so on are spotlighted as one of the alternative energy sources because of zero emission of greenhouse gas. Figure 1-4 shows the electricity production of OECD members in 2015 and 2016 [4]. In Fig. 1-4, renewable energy increased from 18.4 % to 18.7 % from 2015 to 2016.

One of the renewable energy sources is solar energy. According to Ref. [5], the top country of the solar electricity generation is Germany. Germany has about 38,000 MW solar power plants in 2015. Japan has about 23,000 MW and ranked 3rd. However, solar energy has some serious shortcomings. Solar energy is very sensitive to climate because its energy source is sunlight. Solar energy cannot be effectively obtained in rainy or cloudy days. Besides solar energy, the other energy sources from nature such as wind has similar problem of climate dependency.

Biomass energy is also one of the renewable energies. However, it has been concerned whether the raw materials for biomass energy generation are sustainable source or not. In addition, it has a risk to disturb nature ecosystem because artificial big farms should be constructed to cultivate the crops.

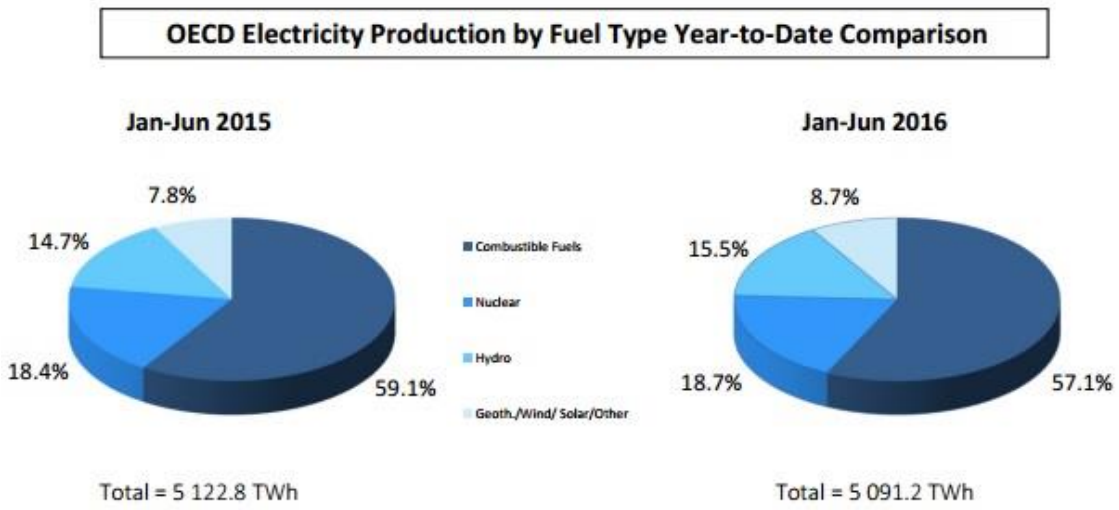

Fig. 1-4 OECD members electricity production [4].

In Fig. 1-4, hydro energy also shows the tendency of increase from 14.7 % to 15.5 %. Hydro energy is also an environment-friendly energy source because it just generates electricity directly by gravity.

1.2.2 Fuel Cells

Fuel cells show high efficiency because it directly generates electricity from chemical energy without converting chemical energy into heat compared to conventional heat engines. Various kinds of fuel cells are listed in Table 1-1.

Table 1-1 Various kinds of fuel cells.

	Proton Exchange Membrane Fuel Cells (PEMFCs)	Morten Carbonate Fuel Cells (MCFCs)	Phosphoric Acid Fuel Cells (PAFCs)	Solid Oxide Fuel Cells (SOFCs)
Electrolyte	Proton Exchange Membrane	Alkali Metal Carbonates	Phosphoric Acid	Oxide Ionic Conducting Ceramic
Operation temperature	Room ~ 80℃	600 ~700℃	160 ~ 220℃	800 ~ 1000℃
Electrical efficiency	40 ~ 60 %	45 ~ 60 %	50 ~ 60 %	60 ~65 %
Fuel oxidant	H_2, O_2, air	Natural gas, Bio gas, Coal gas, H_2, O_2, air	Natural gas, Bio gas, H_2, O_2, air	Natural gas, Bio gas, Coal gas, H_2, O_2, air
Energy output	1 ~ 10 KW	Above MW	100 ~ 200 KW	Above MW

Proton Exchange Membrane Fuel Cells (PEMFCs) are suited for transportation application such as vehicles. However, PEMFCs show the limitation of fuel flexibility, since it requires high purity hydrogen as a fuel. Therefore, PEMFCs should be considered as a potential electricity generation devices for systems based on pure hydrogen. Phosphoric Acid Fuel Cells (PAFCs) are used for both the stationary power generators and mobile power generators for vehicles. Molten Carbonated Fuel Cells (MCFCs) have fuel flexibility with high efficiency and they have been developed for power plants. However, the primary disadvantage of MCFCs is the high degradation rate due to the high operation temperature. Solid Oxide Fuel Cells (SOFCs) are the most promising power generation devices because of its high efficiency and fuel flexibility. With the high operation temperature of SOFCs, system efficiency can be further enhanced by combining it with heat engines using exhausted heat. However, SOFCs show low durability due to high operation temperature. Furthermore, high costs of materials and production processes should be improved. Therefore, intermediate temperature-SOFCs (IT-SOFCs) have been investigated by many researchers in order to overcome this problem. The primary goal is to improve the durability by decreasing the operation temperature for long time

operation.

1.3 Solid Oxide Fuel Cells

1.3.1 Principle

SOFCs are one of the promising power generation devices due to high efficiency and high fuel flexibility as mentioned in Chap. 1.2. SOFC is composed of anode, cathode and solid electrolyte. Figure 1-5 shows a typical cross-sectional image of a SOFC porous electrode on an electrolyte. Representative materials of SOFC components are yttria stabilized zirconia (YSZ) for the electrolyte, Ni-YSZ composite for the anode, and $La_{0.8}Sr_{0.2}MnO_3$ (LSM)-YSZ composite for the cathode. Ni and LSM are electronic conductors and YSZ is the ionic conductor. Gas is diffused through pores in the composite electrode. Electrochemical reaction takes place at triple phase boundary (TPB) where ion, electron and gas can exist.

Anode : $H_2 + O^{2-} \rightarrow H_2O + 2e^-$ (1.1)

Cathode : $\frac{1}{2}O_2 + 2e^- \rightarrow O^{2-}$ (1.2)

A schematic image of SOFC reaction mechanisms is shown in Fig. 1-6. Oxygen is reduced in the cathode and oxide ion conducts to the anode through dense electrolyte. Water and electron are generated after electrochemical reaction between oxide ion and hydrogen at TPB. Electron is conducted from anode to cathode through the external circuit and generates electric power. Theoretical SOFCs electromotive force (EMF) can be defined by Gibbs free energy and the pressures of gas components as follows:

EMF : $E = \frac{-\nabla G^o_{H_2O}}{2F} + \frac{RT}{2F}\ln\left[\frac{P_{H_2}P_{O_2}^{1/2}}{P_{H_2O}}\right]$ (1.3)

This equation is called ‘Nernst Equation’. Under polarization, there are voltage losses called overpotentials due to the internal resistances of the cell which are composed of activation, concentration and ohmic overpotentials as shown in Fig. 1-7.

Activation overpotential is a voltage loss caused by dissociation, adsorption, diffusion and charge transfer processes of reactants and products involved in the electrochemical reaction. Concentration overpotential is a voltage loss caused by the concentration distribution required for gas diffusion. Ohmic overpotential is the loss due to ionic and electronic diffusions in the component materials and at the interfaces or boundaries between electrode and electrolyte.

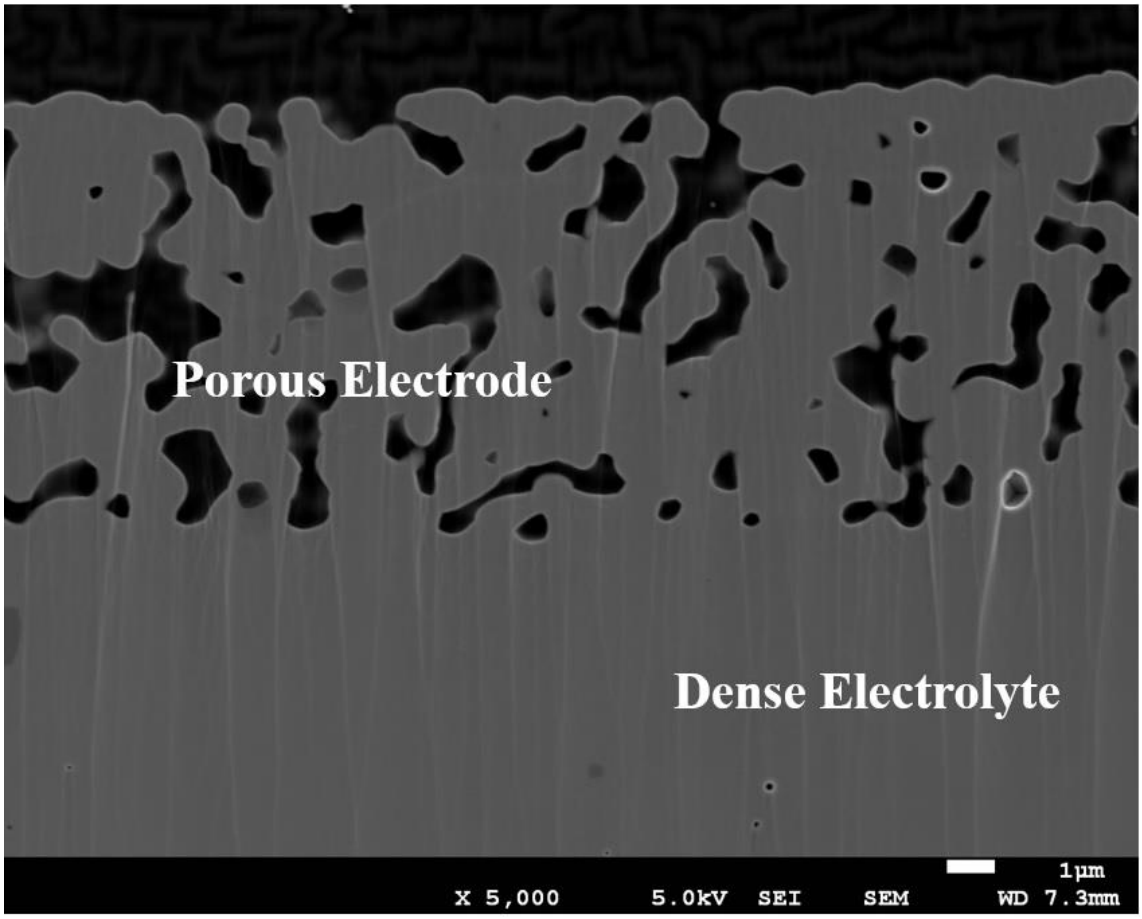

Fig. 1-5 An example Scanning Electron Microscopy (SEM) image of SOFC cell (black: pore).

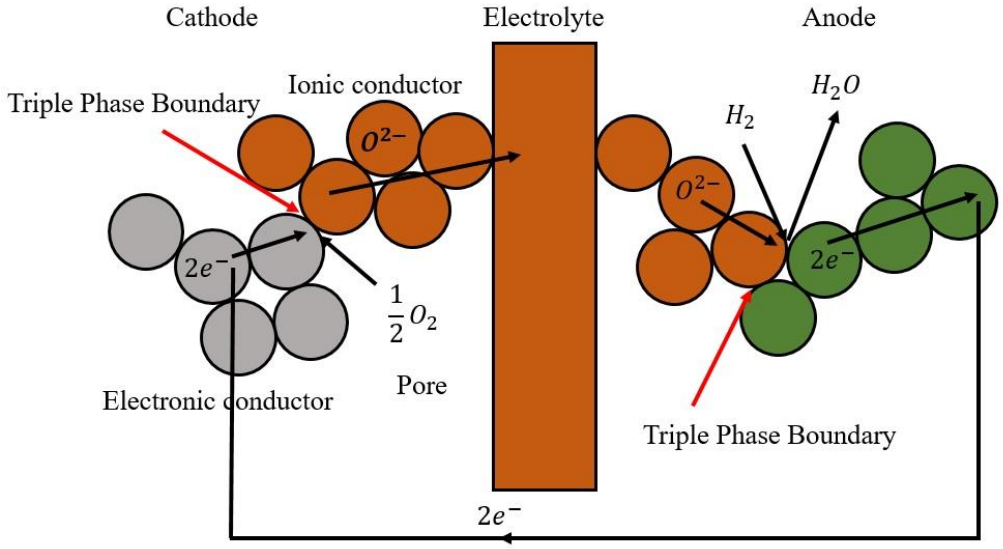

Fig. 1-6 A schematic image of the reaction mechanism.

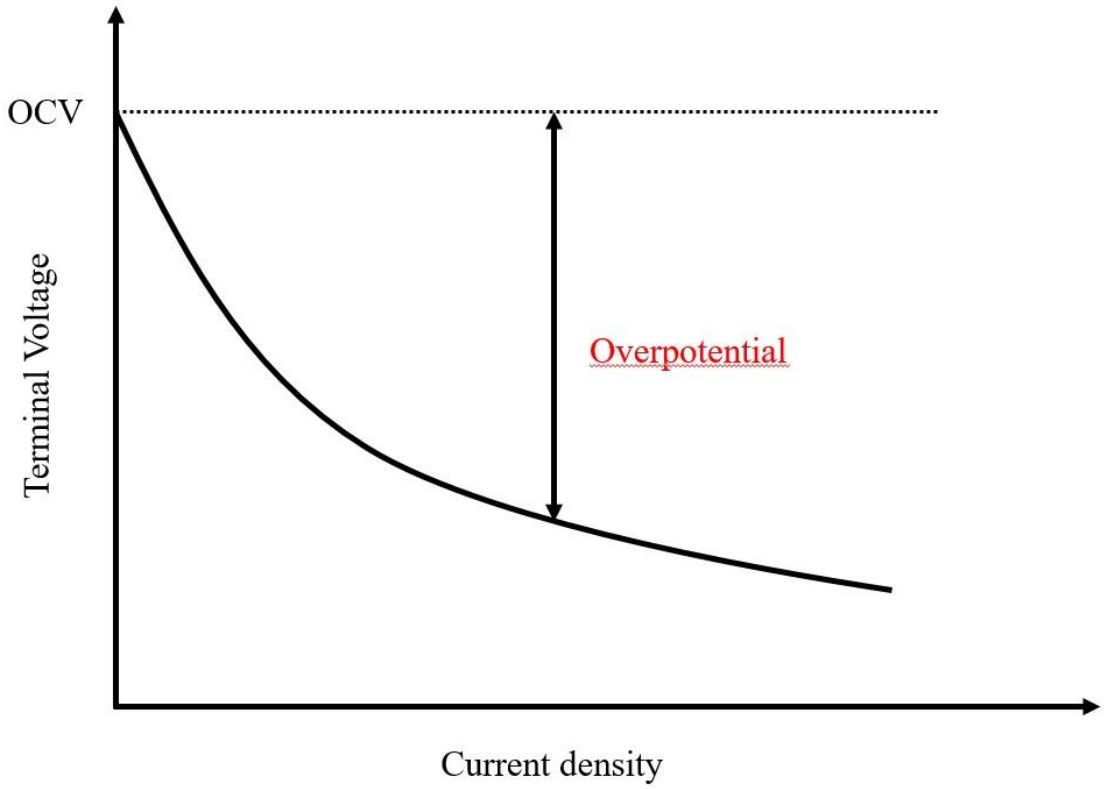

Fig. 1-7 Overpotential against current density.

Performance of SOFCs is deteriorated due to the increase of overpotentials during operation. To suppress degradation is one of the major issues for SOFC research.

1.3.2 Mixed Ionic-Electronic Conductor (MIEC)

High operation temperature becomes one of the disadvantages for the SOFCs' operation. However, if operation temperature is reduced, cell performance is degraded due to the degradation of electrochemical characteristics, especially for the cathode side. Performance of LSM-YSZ, which is the conventional cathode material, drastically decreases at low temperature due to the decrease in conductivities and reaction activities. To compensate this problem, alternative cathode materials such as $La_{0.6}Sr_{0.4}Co_{0.2}Fe_{0.8}O_3$ (LSCF) have been investigated [6–54]. LSCF is one of the MIEC material which has higher conductivity compared to LSM. In the LSCF, not only TPB, but also LSCF surface contributes for the electrochemical reaction. Therefore, cathode performance is enhanced by the expansion of the reaction sites. A principle of performance enhancement is shown in Fig. 1-8.

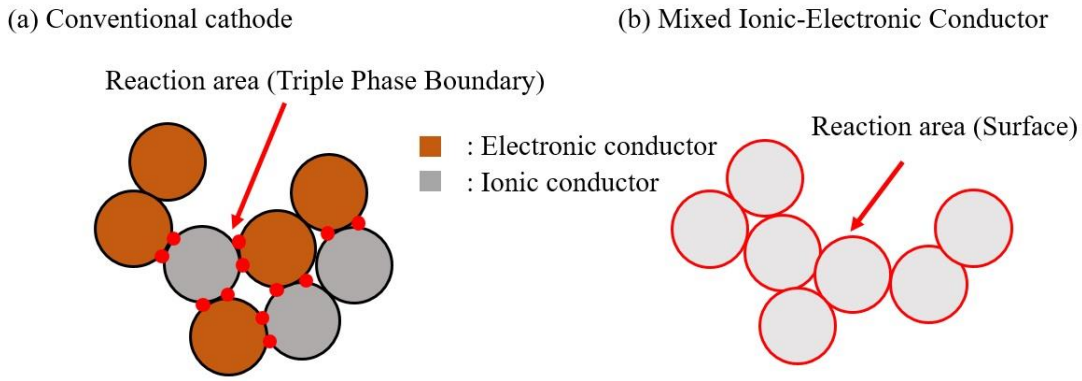

Fig. 1-8 A schematic image of expanded reaction area by MIEC.

It is known that LSCF reacts with YSZ at high temperature and forms non-conductive secondary phase such as $SrZrO_3$. In order to prevent the formation of $SrZrO_3$ phase, ceria-based ionic conducting materials such as $Gd_{0.1}Ce_{0.9}O_{1.95}$ (GDC) or $Sm_{0.1}Ce_{0.9}O_{1.95}$ (SDC) are used for the barrier interlayer between LSCF and YSZ [12]. Khan et al. [11] reported that LSCF cathode with GDC interlayer showed low degradation of 10 % after 1000 hrs operation due to reduced $SrZrO_3$ formation and the microstructural change. Wang et al. [12] reported that Zr was diffused into GDC interlayer along the GDC grain boundary and formed $SrZrO_3$ on the GDC/YSZ interface.

Interfacial cation diffusion between LSCF and GDC is also one of the main issues [29,32]. Izuki et al. [32] reported that La cation in LSCF diffuses into GDC and forms probable LDC fluorite secondary phases in the vicinity of the interface. In this case, La substitutes Ce or Gd in GDC. A secondary ion mass spectrometry (SIMS) result is shown in Fig. 1-9 [32].

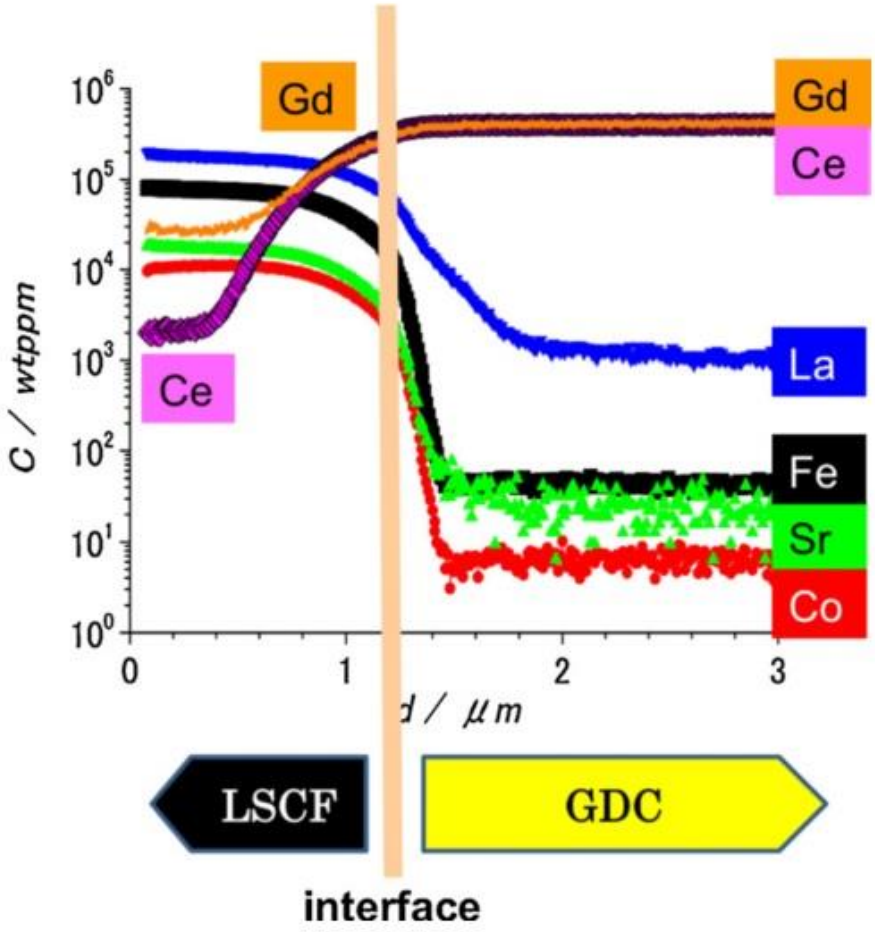

Fig. 1-9 SIMS depth profile of LSCF/GDC diffusion couple (M. Izuki et al., [32]).

LSCF has also similar tendency with LSM, which shows the decrease of both electronic and ionic conductivities at low operation temperature [24,54]. The decrease of ionic conductivity at low operation temperature are more serious than decrease of electronic conductivity because ionic conductivity of LSCF is comparatively lower than electronic conductivity. Therefore, it can be considered that compensation of ionic conductivity under low operation temperature is more important. One way to solve this problem is mixing the ionic conductor with high conductivity such as GDC with LSCF. Leng et al. [10] reported that the best performance is achieved at a mixing rate of LSCF:GDC = 40:60 wt. %. Hwang et al. [22] reported that performance is enhanced due to the compensation of sufficient reaction area for the LSCF-GDC composite cathode in the temperature range of 500ºC to 700ºC, because GDC suppresses the grain growth of LSCF. Comparisons of performance and microstructures between pure LSCF and LSCF-GDC composite cathodes are shown in Fig. 1-10, 11 and 12.

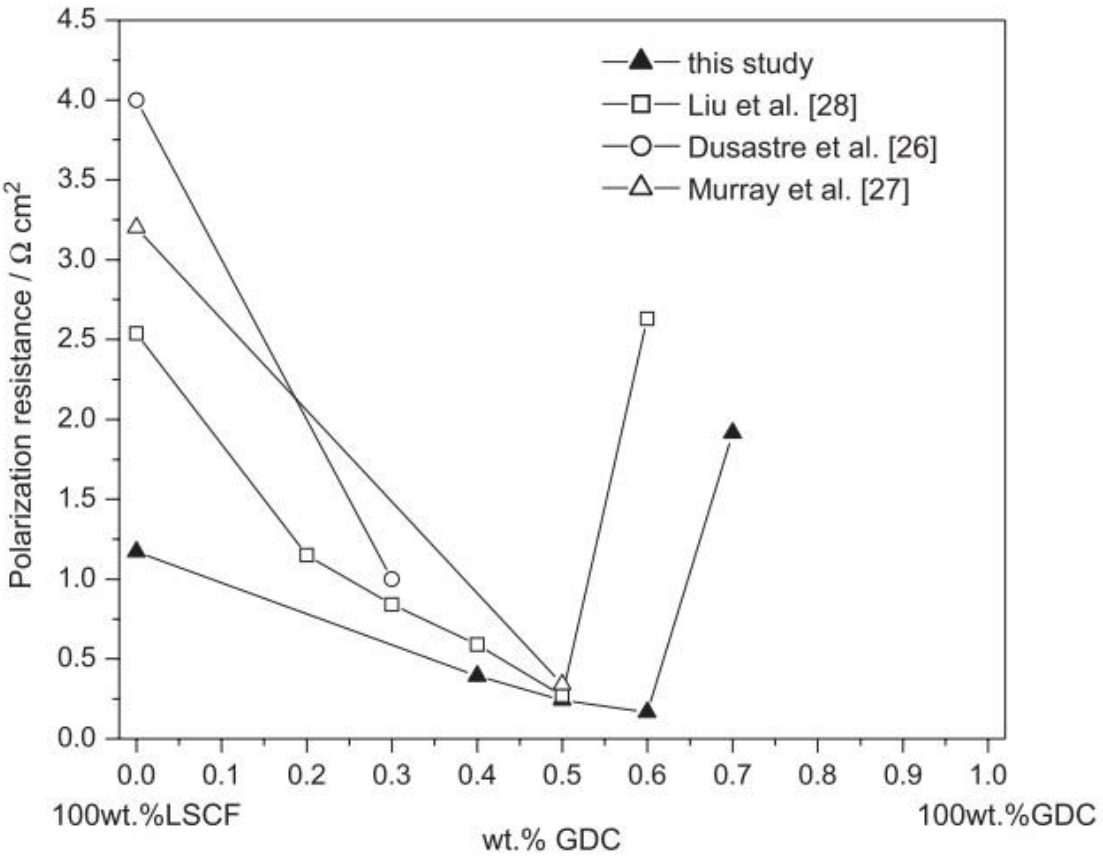

Fig. 1-10 Performance enhancement with LSCF-GDC composite cathodes (Leng et al., [10]).

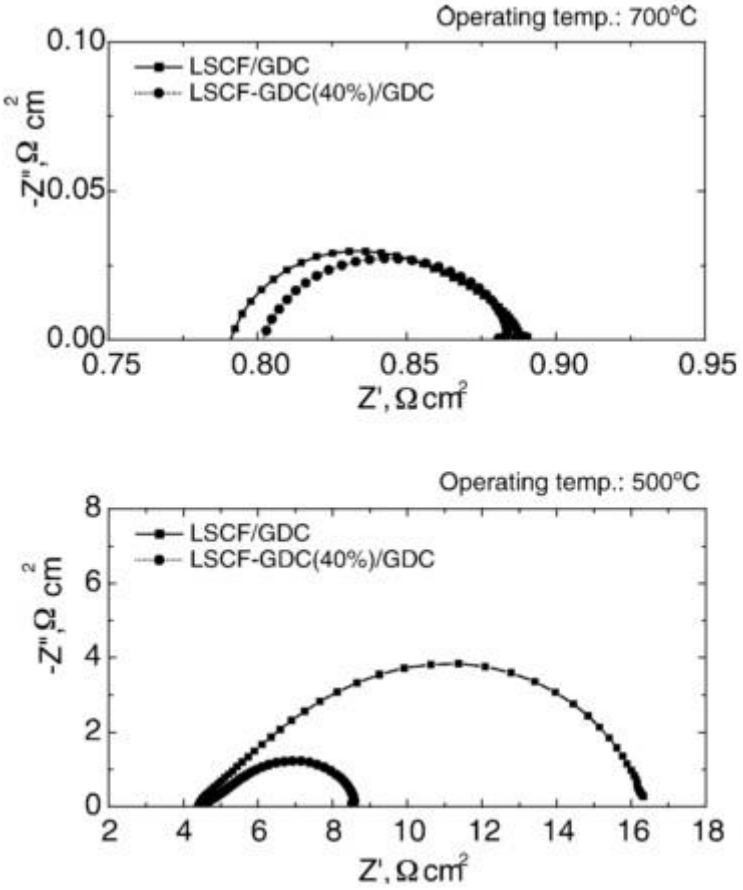

Fig. 1-11 Comparison of impedance spectra between pure LSCF and LSCF-GDC composite (Hwang et al., [22]).

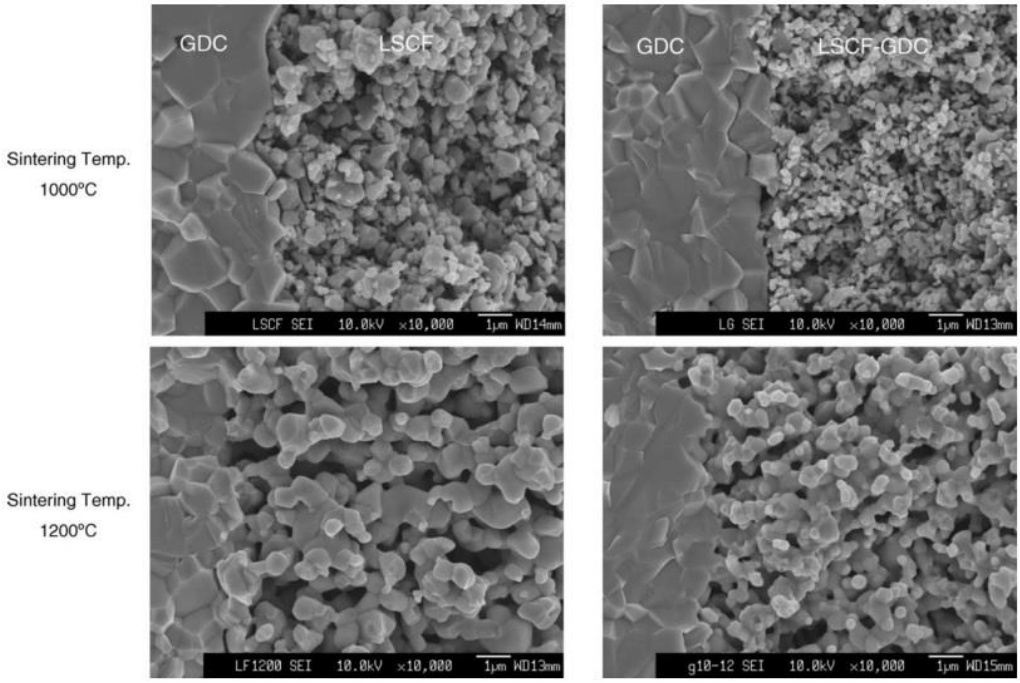

Fig. 1-12 SEM images of LSCF and LSCF-GDC composite cathodes (Hwang et al., [22]).

$La_{0.6}Sr_{0.4}CoO_3$ (LSC) is also one of the promising MIEC cathode materials [55–85]. LSC shows higher conductivity compared to LSCF [60]. Hayd et al. [75] achieved area specific resistance (ASR) of $0.023\Omega cm^2$ at 600ºC by nano-scaled thin LSC cathode as shown in Fig. 1-13. However, LSC has several serious intrinsic problems. Petric et al. [24] investigated that thermal expansion coefficient (TEC) of LSC is 20.5 ($K^{-1}/10^{-6}$) which is higher than 17.5 ($K^{-1}/10^{-6}$) for LSCF. In addition, reduction of Co^{4+} to Co^{3+} in LSC causes unit cell volume expansion at fixed pO_2 [68]. LSC-GDC composite cathodes also have been suggested to solve many problems of pure LSC cathode [55,57,69,73,76,84]. Performance enhancement is shown for the LSC-GDC composite cathode compared to pure LSC cathode.

As shown in Fig 1-14, three possible reaction mechanisms can be considered for MIEC-high ionic conductor composite cathodes.

i) Electrochemical reaction at entire MIEC surface.

ii) Surface reaction activated at the vicinity of TPB.

iii) Absorbed oxygen on MIEC surface is diffused on the MIEC surface and electrochemical reaction takes place at TPB.

Hu et al. [15] quantified the contribution ratio of TPB by using effective surface exchange coefficient at TPB with different mole fraction of Sm in LSCF- $Sm_xCe_{1-x}O_{2-\delta}$ (SDC) composites. They reported that contribution ratio of TPB is the highest at x = 0.2. However, their sample was sintered at 1500°C to obtain dense sample, which is much higher than the usual sintering temperature of SOFC

cathode. Moreover, it is known that time delay in switching the gas in the conductivity relaxation method sometimes greatly affects the measurement results. Fujimaki et al. [86] suggested a new design of LSC pattern electrode for the cases with and without TPB in order to investigate the contribution of TPB reaction, as shown in Fig. 1-16.

For the case of MIEC-GDC composite cathode, TPB length of MIEC and GDC composite increases, while MIEC surface is decreased. It is considered that performance will be decreased if surface reaction is the dominant mechanism. However, performance is enhanced as shown in many literatures. Therefore, it can be considered that reactions which can be scaled by TPB contribute to the performance enhancement of MIEC-GDC composite cathodes. However, concrete quantified contribution from each electrochemical reaction is not fully understood. In order to further improve MIEC-GDC composite performance, it is important to quantitatively investigate the mechanisms of performance enhancement.

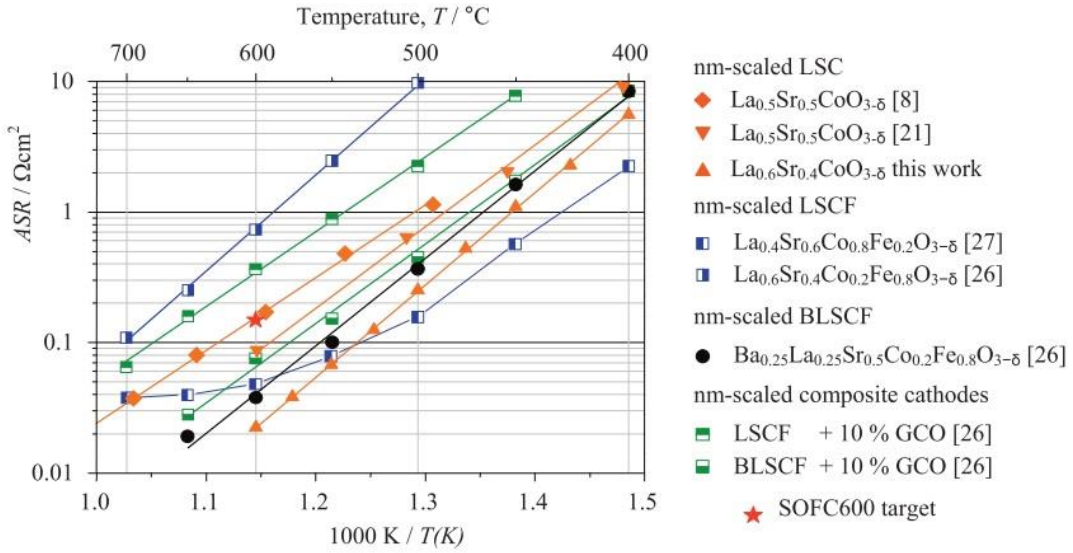

Fig. 1-13 Performance comparison of the best nano-scaled LSC thin film cathode with other literature data (Hayd et al., [75]).

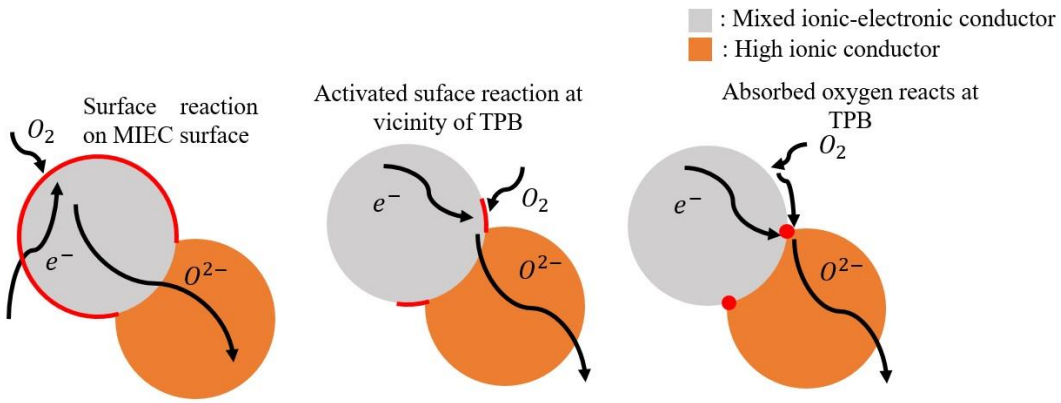

Fig. 1-14 Three possible electrochemical reaction mechanisms.

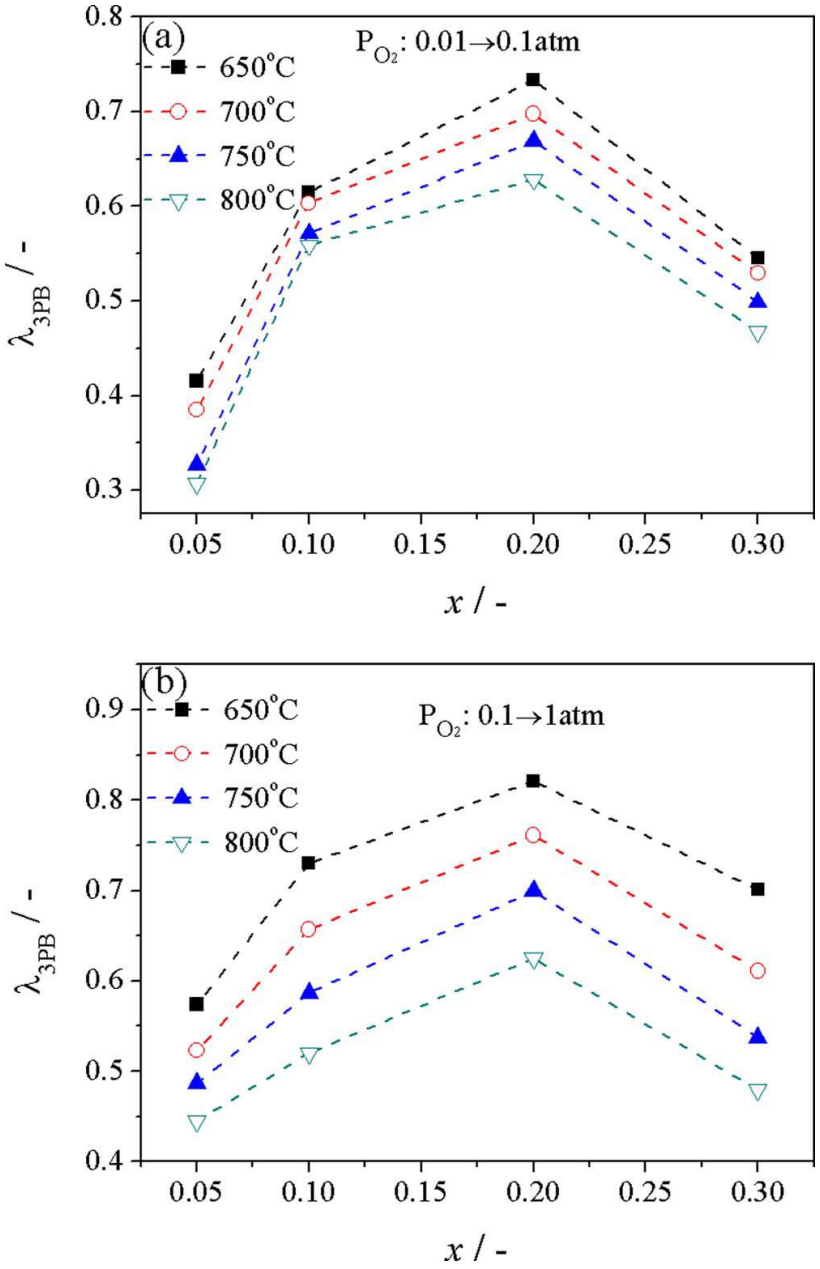

Fig. 1-15 Contribution ratio of TPB reaction (Hu et al., [15]).

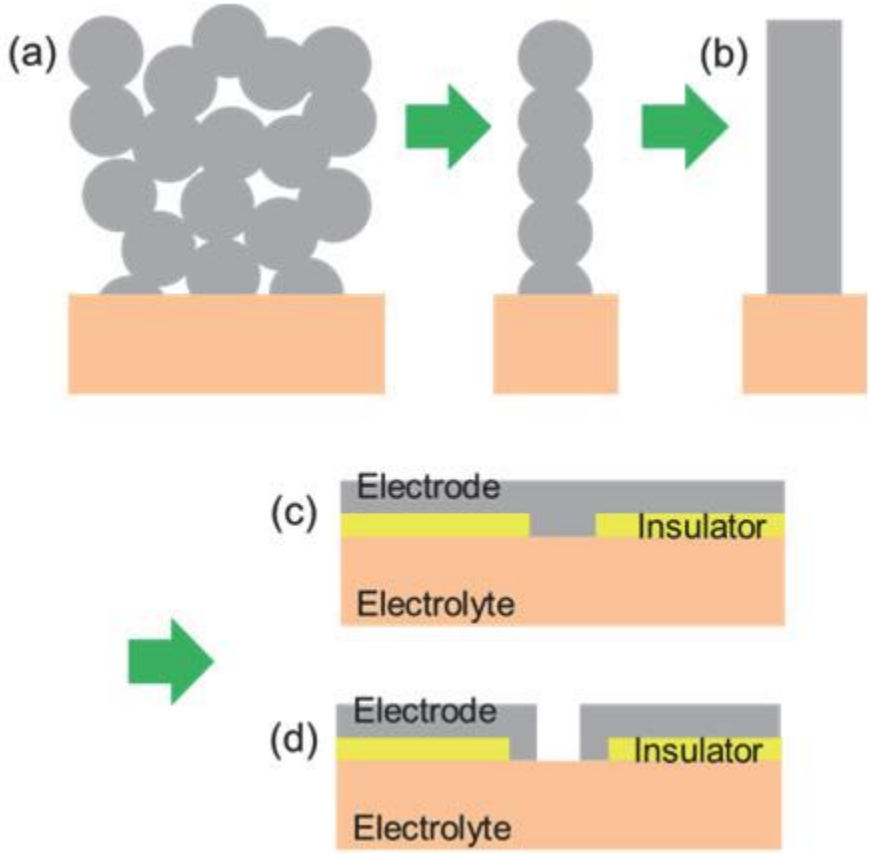

Fig. 1-16 Pattern electrodes with and without TPB (Fujimaki et al., [86]).

1.3.3 Microstructure

For the porous SOFC electrodes, microstructure parameters such as TPB, specific surface area and tortuosity factor have strong influence on the performance of the electrode. To reconstruct three-dimensional (3D) microstructure of the electrode, focused ion beam (FIB)-scanning electron microscopy (SEM) is widely used [87–99]. FIB and SEM have a coincident angle. The target is sliced by FIB with constant slice pitch and cross-sectional images are captured by SEM, continuously. Figure 1-17 shows the principle of FIB-SEM technique.

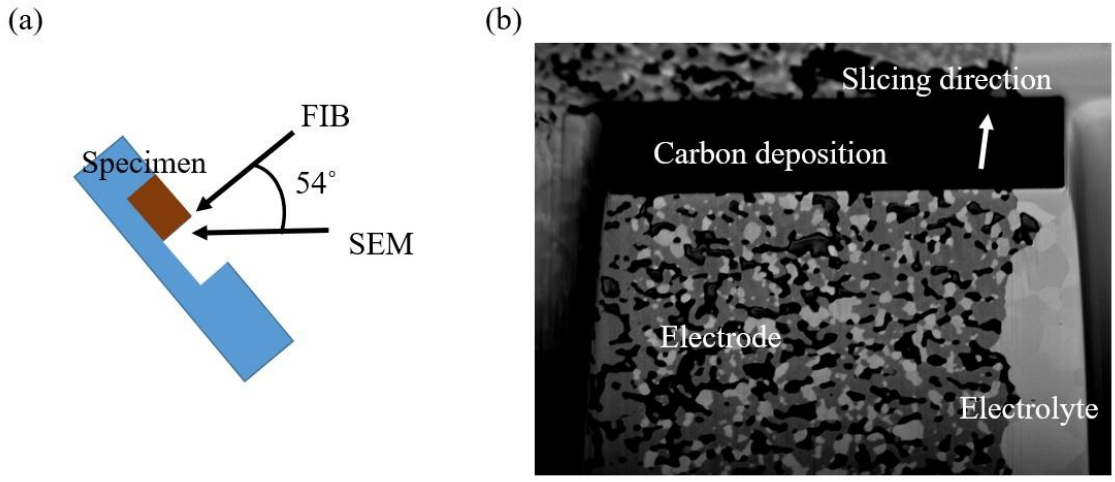

Fig. 1-17 Principle of FIB-SEM technique. (a) A schematic image of FIB-SEM and (b) an example image of the slicing process.

Iwai et al. [92] investigated the microstructure parameters of Ni-YSZ such as TPB, tortuosity factor using FIB-SEM technique. Chen et al. [87] reported the correlation between threshold values which are used during image analysis and microstructure parameters variation. Cronin et al. [88] reported that polarization resistance of LSM-YSZ increases when the cathode sintering temperature is reduced. The lowest sintering temperature of LSM-YSZ causes the reduction of active TPB density due to the decrease of LSM phase percolation [88]. Microstructural change of LSM-YSZ with different sintering temperatures is shown in Fig. 1-18 and 19.

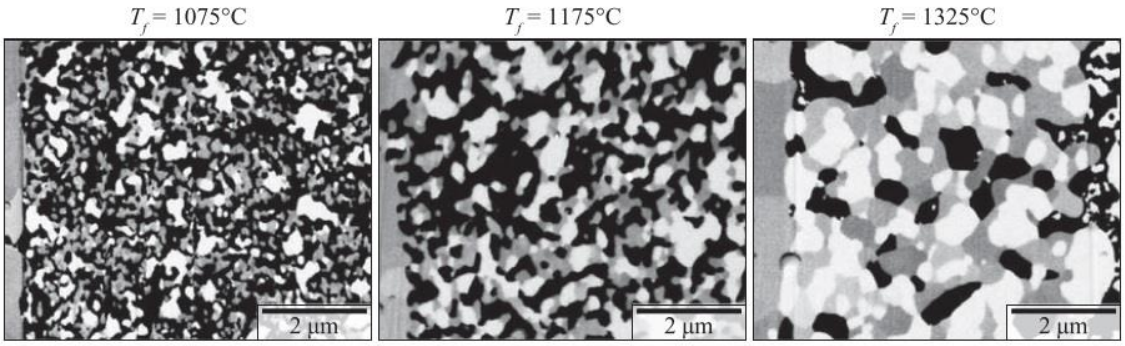

Fig. 1-18 Cross sectional images of LSM-YSZ with different sintering temperatures. Bright, dark and black phases represent LSM, YSZ and pore, respectively (Cronin et al., [88]).

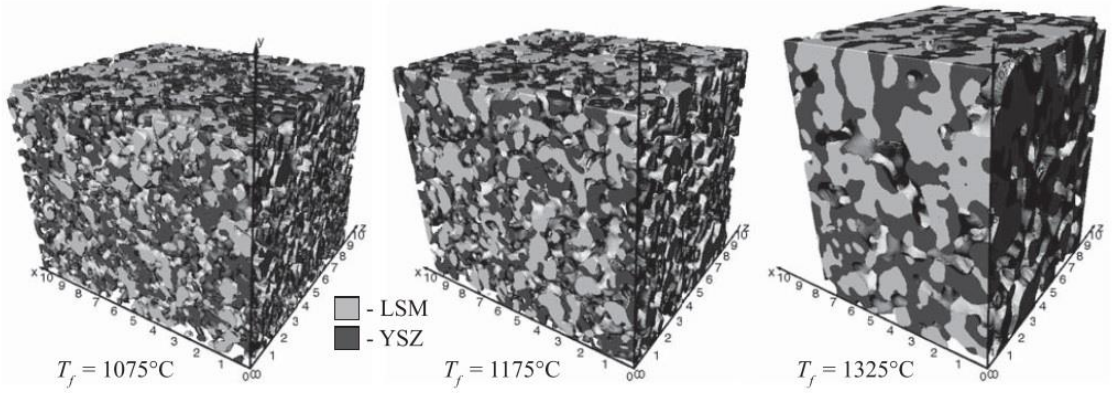

Fig. 1-19 3D reconstructed microstructures of LSM-YSZ (Cronin et al., [88]).

3D reconstructed microstructure data are valuable in order to investigate not only the microstructure parameters, but also the electrochemical reaction mechanism inside the electrode. Electrochemical characteristics such as current and potential distributions can be quantified by numerical simulation methods using 3D reconstructed microstructures [92, 95, 99–101]. Shikazono et al. [100] reported that oxide ion potential and current distributions inside Ni-YSZ anode is inhomogeneous due to the scattered active TPBs and poor percolation of solid phases. The model which can provide information of electrochemical characteristics such as oxygen flux and gradient inside the LSCF cathode is proposed by Carrao et al. [101]. Figures 1-20 and 21 show examples of the quantification of electrochemical characteristics.

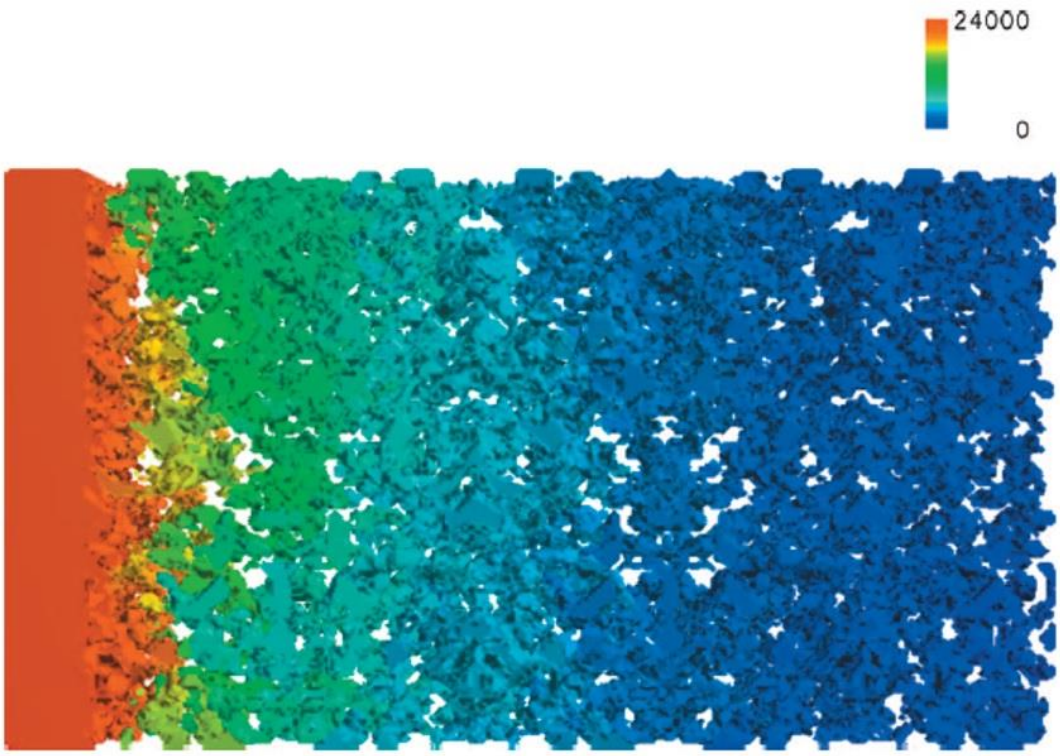

Fig. 1-20 Oxide ion potential distribution in YSZ phases (Shikazono et al., [100]).

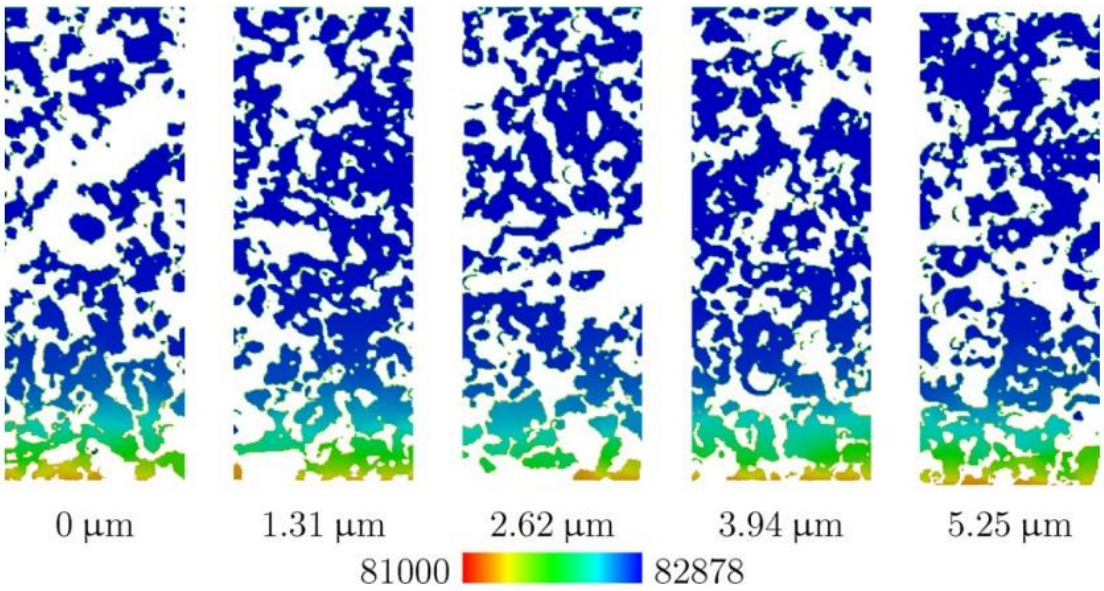

Fig. 1-21 Oxide ion concentrations in MIEC (Carraro et al., [101]).

1.4 Objectives of the Present Study

MIEC-GDC composite is one of the most promising cathode materials for low to intermediate temperature operation of SOFCs due to the significant enhancement of cathode performance. In order to further improve MIEC-GDC composite performance, several parameters such as volume ratio, particle size, and sintering conditions must be optimized. It is thus important to quantitatively investigate the mechanisms of performance enhancement. However, factors which mostly contribute to performance enhancement are not fully understood. Therefore, it is necessary to clarify the dominating factors of performance enhancement in order to design optimal SOFC cathode.

Different from conventional cathodes, two electrochemical reaction mechanisms should be considered, i.e. electrochemical reactions on MIEC surface and at TPBs. In the present study, contribution of electrochemical reaction of MIEC-GDC composite cathodes will be investigated based on the button cell measurement and microstructure reconstruction. Both LSCF and LSC are used as primary MIEC materials in the present study. Main contents of this study are as follows:

- Fabrication of LSCF-GDC and LSC-GDC composite cathodes.
- Performance measurements under intermediate operation temperature.
- 3D microstructure reconstructions by FIB-SEM.
- Investigation of microstructure parameters.
- Quantification of electrochemical characteristics by numerical simulation method.

In the present study, performance with different volume ratios of LSCF-GDC and LSC-GDC are evaluated with identical cathode fabrication method and experimental conditions. Experimental conditions are introduced in Chap. 2.

The 3D microstructures are reconstructed by FIB-SEM. Microstructure parameters are calculated by several methods and correlated with cathode performance. It is seen that MIEC surface and TPB density are correlated to electrochemical reaction, while tortuosity factor and porosity are correlated to ion, electron and gas diffusions, respectively. LBM is applied in the present study for the numerical simulation. It is considered that performance variation can be explained not only by microstructure parameters, but also by the electrochemical potential and current distributions inside the cathode. Overpotentials are calculated by solving electrochemical reaction equations, and exchange current densities are fitted based on the experimental results. The details of the numerical simulation methods are also introduced in Chap. 2.

It is considered that performance is influenced by the volumetric effect of GDC phases. In Chap. 3, correlations between cathode performance and microstructure characteristics with different volume ratios of LSCF-GDC composite are investigated. The dependence of MIEC ionic conductivity in the

numerical simulation and the effective thickness of LSCF-GDC composite cathode are investigated in Chap. 4. In Chap. 5, LSC-GDC composite cathodes with an identical volume ratio are fabricated and measured. Then, the results are compared with LSCF-GDC. Numerical simulation results based on 3D reconstructed microstructures of LSC-GDC composite are also introduced in Chap. 5. In Chap. 6, performance and microstructure parameters variations with different original powders are investigated using the volume ratio of LSC:GDC = 50:50 % in order to evaluate the sinterability of LSC. In Chap. 7, cathodes are discharged to investigate the effect of GDC phases in composite cathodes using LSC:GDC = 30:70, 50:50, 70:30 vol. %. Conclusions will be given in Chap. 8.

Chapter 2
Experimental and Numerical Simulation Method

2.1 Experimental

2.1.1 Electrolyte-supported Cells

In the present study, electrolyte-supported button cells were used for the cathode performance measurements. $Ce_{0.9}Gd_{0.1}O_{1.95-x}$ (GDC, Shin-etsu Chemical Co., Ltd., Japan) was used as the electrolyte material. 5 g of GDC powders were pressed at 60 MPa by hand pressing for 30 mins. Then, the pellet was further pressed at high pressure of 200 MPa for 30 mins by cold isostatic pressing (CIP, Figure 2-1) in order to obtain highly densified pellet. The pellet was sintered at 1550°C in air for 5 hrs. After sintering, both top and bottom sides of the pellet were grinded in order to obtain flat electrolyte surface. For the anode material, 60:40 wt. % of NiO (Seimi Chemical Co., Ltd., Japan)-GDC composite was used in the present study. NiO and GDC powders were ball-milled with ethanol for 24 hrs. Then, NiO-GDC composite solution was dried in air. Anode slurry was fabricated by mixing terpineol with 3 wt. % of ethyl cellulose as a binder. The anode slurry was screen printed onto the GDC pellet and sintered at 1450°C in air for 3 hrs. Different composite cathodes were also fabricated by the same method as the anode. All cathodes were sintered at 1150°C in air for 1 hr. During the sintering process, slurries were kept at 400°C for 1 hr to volatilize the organic binders in the slurries. Temperature ramp rate was kept at 10°C/min. Thin layers of NiO and LSCF were used for current collection for the anode and the cathode sides, respectively. For the anode, NiO was reduced before the measurements and pure Ni was used for the electronic conductor. Cell fabrication procedures are summarized in Fig. 2-2. After fabrication, cathodes have a diameter of 10 mm, a thickness of 25 μm and a current collecting layer thickness of 10 μm. Figures 2-3 and 2-4 show a schematic of the experimental button cell and a typical SEM image of porous composite cathode, respectively.

Fig. 2-1 CIP used in the present study.

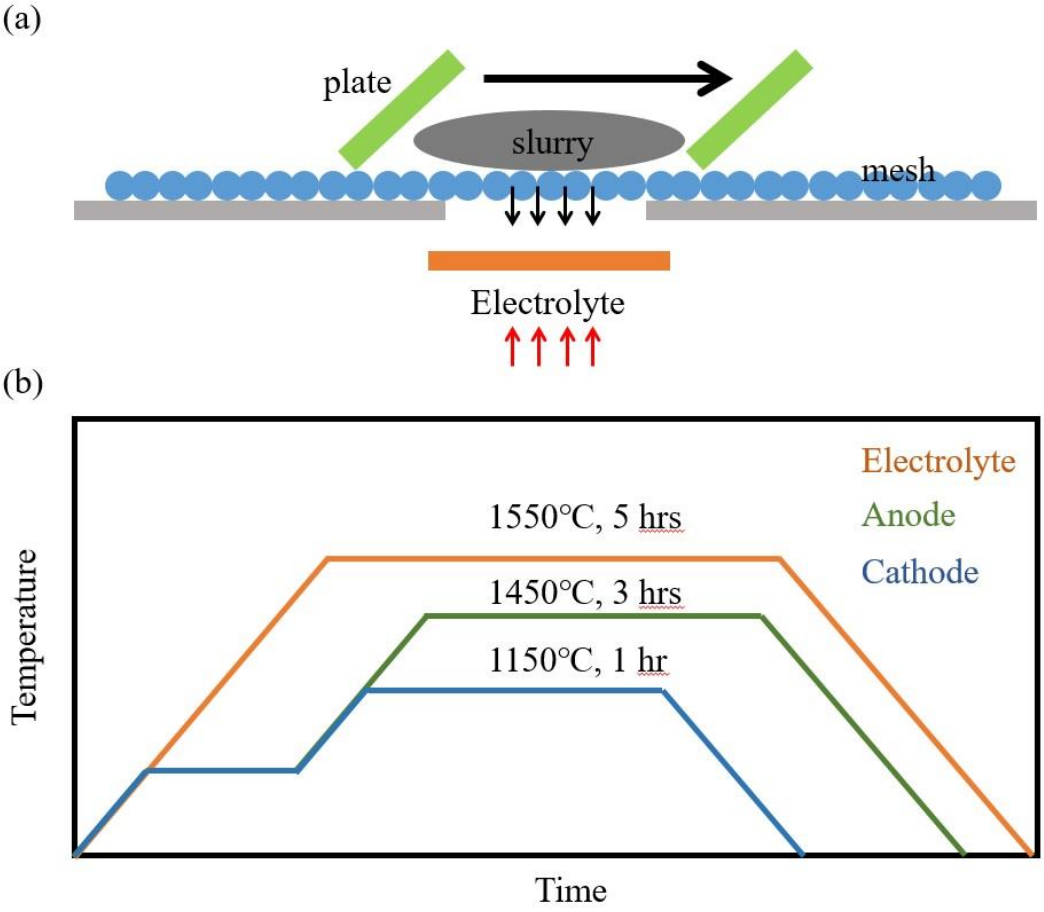

Fig. 2-2 Fabrication method of an experimental button cell.
(a) Screen printing method, (b) sintering temperature conditions.

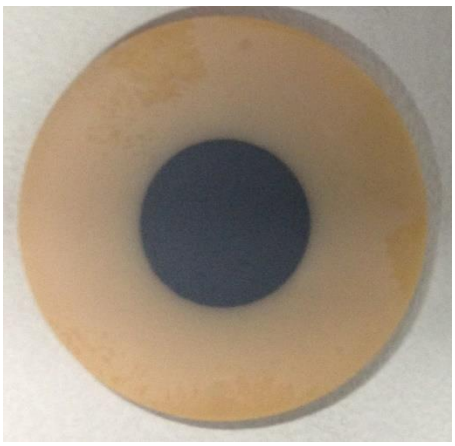

Fig. 2-3 A button cell (cathode side).

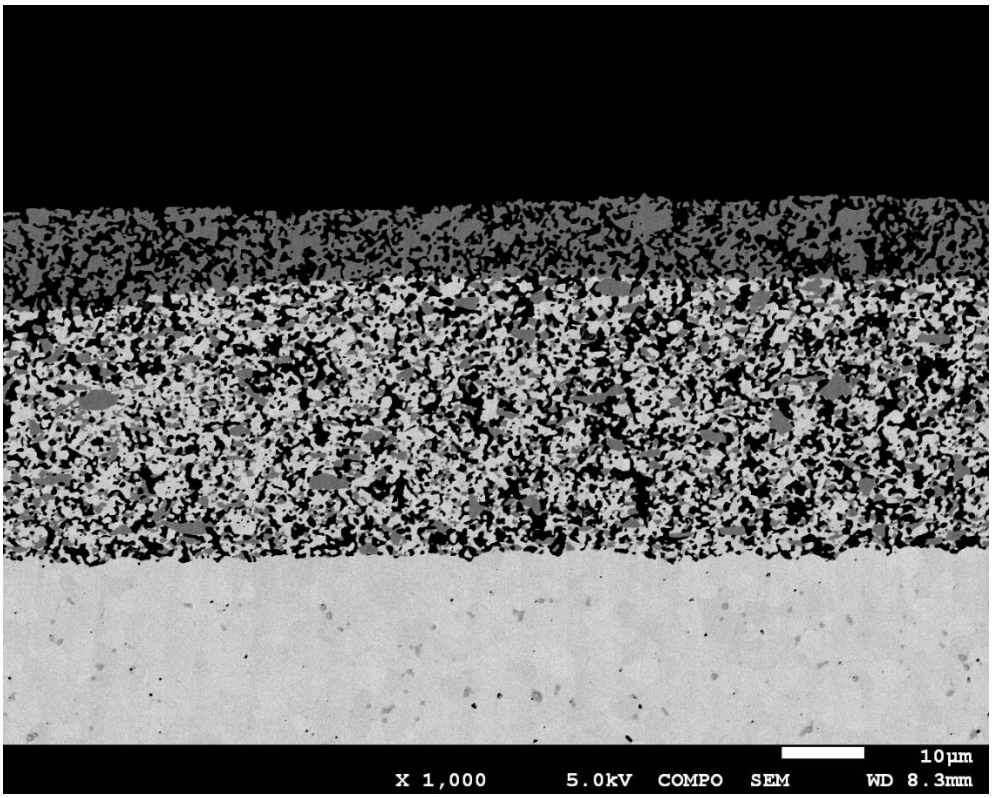

Fig. 2-4 Cross sectional SEM image of LSCF-GDC composite cathode.
(Light gray: GDC, Dark gray: LSCF).

2.1.2 Experimental Procedures

In the present study, SOFC measurement setup (MicrotracBEL Co., Ltd, Japan) was used for evaluating the cathode performance. A button cell was sandwiched with two alumina tubes and sealed by Pyrex glass rings to prevent gas leak. A Pt ring was used as a reference electrode which is wound around the electrolyte rim. Au mesh and Ni mesh (The Nilaco Co., Ltd, Japan) were used as current collectors for the cathode and the anode sides, respectively. Figures 2-5 and 2-6 show the schematic images of the experimental setup and the measurement device chamber, respectively. Pure oxygen gas was supplied to the cathode as an oxidant with the flow rate of 50 sccm, and 3 % humidified hydrogen was supplied to the anode as a fuel. Operation temperature was set at 700°C.

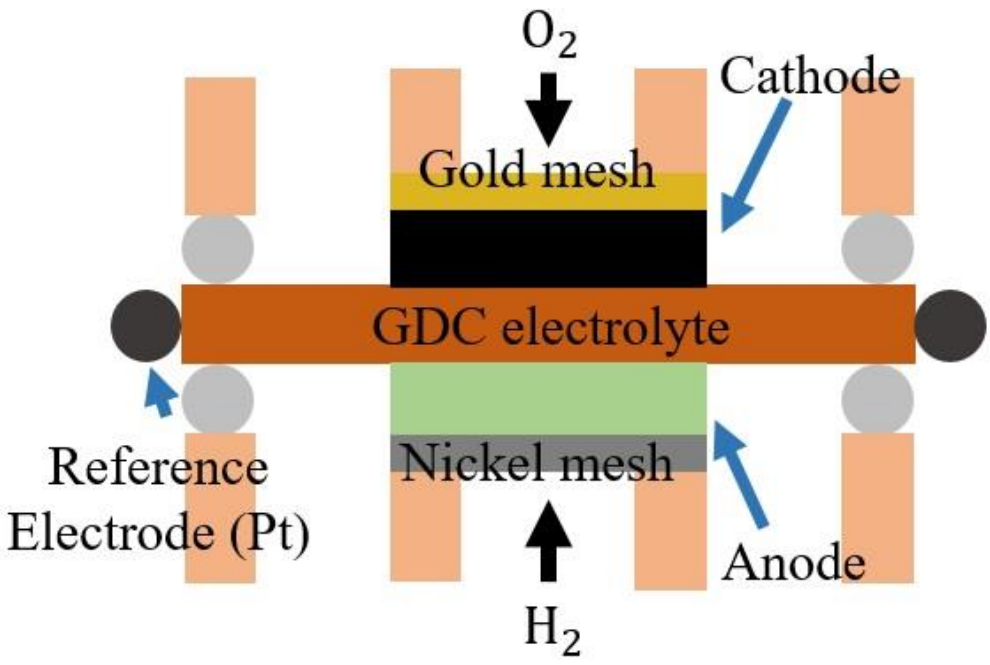

Fig. 2-5 A schematic image of the experimental setup.

Fig. 2-6 Thermal chamber of the measurement setup.

2.1.3 Performance Evaluations

In the present study, cathode performance was investigated by I-V curves and electrochemical impedance spectroscopy (EIS). Voltage losses were measured in the current density range from 0 to 0.6 A/cm^2. Then activation overpotential η was quantitatively investigated by subtracting voltage losses caused by ohmic overpotential in the I-V curves as shown in Fig. 2-7 and Eq. (2.1).

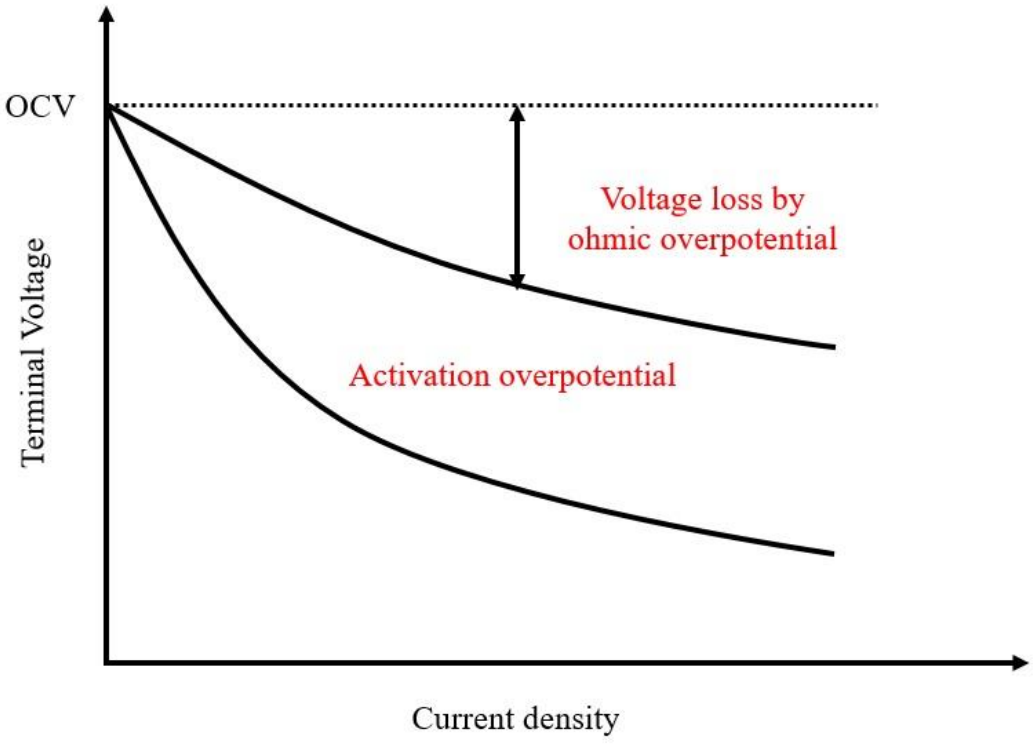

Fig. 2-7 Activation overpotential.

$$\eta(V) = OCV - V_{\mathrm{t}} - (R_{\mathrm{ohm}} \times A \times I) \tag{2.1}$$

EIS is the effective technique for SOFC electrode performance evaluation. Definition of impedance is shown as follows:

$$Z = \frac{\Delta V}{\Delta I} \tag{2.2}$$

AC voltage of sinusoidal wave current is introduced with set frequencies. In the present study, cathode-reference measurement was conducted by 4 terminal AC impedance method. Current is introduced between the working electrode and the counter electrode by Pt lines. Then, voltage difference between working electrode and reference electrode is measured. Figure 2-8 shows the principle of 4 terminal AC impedance method for the case of cathode-reference measurement.

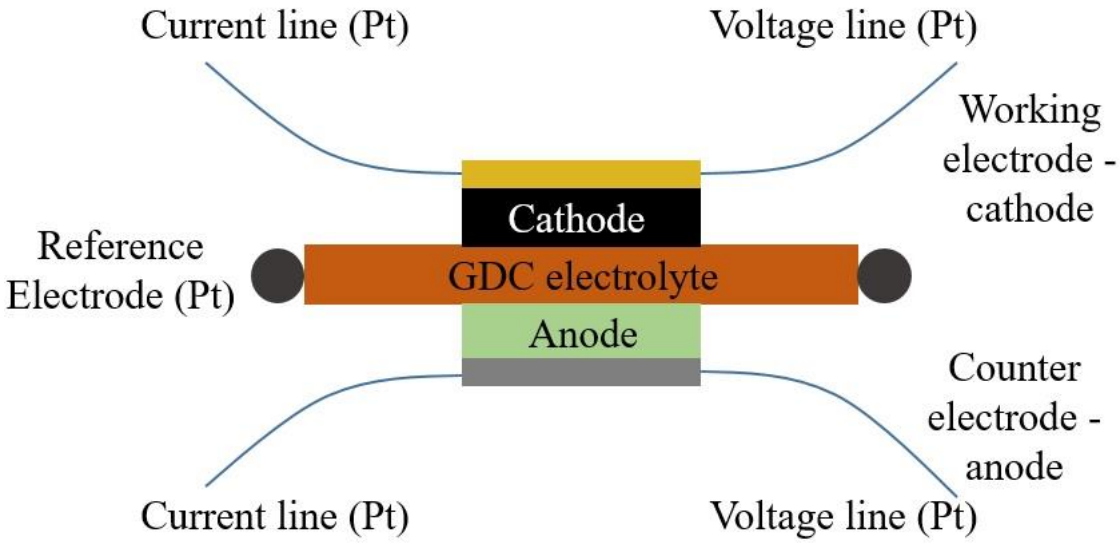

Fig. 2-8 Four terminal AC impedance measurement (C-R).

Impedance is plotted by a Nyquist diagram as shown in Fig. 2-9. Ohmic resistance (R_Ω) is obtained at the real number of high frequency intercept. Polarization resistance (R_p) is obtained by the distance between high and low frequency intercepts. However, it is difficult to directly quantify polarization resistance from the Nyquist diagram. In order to investigate the electrode resistances, an equivalent circuit is modeled. Figure 2-10 shows the correlation between the electrochemical reaction and the equivalent circuit.

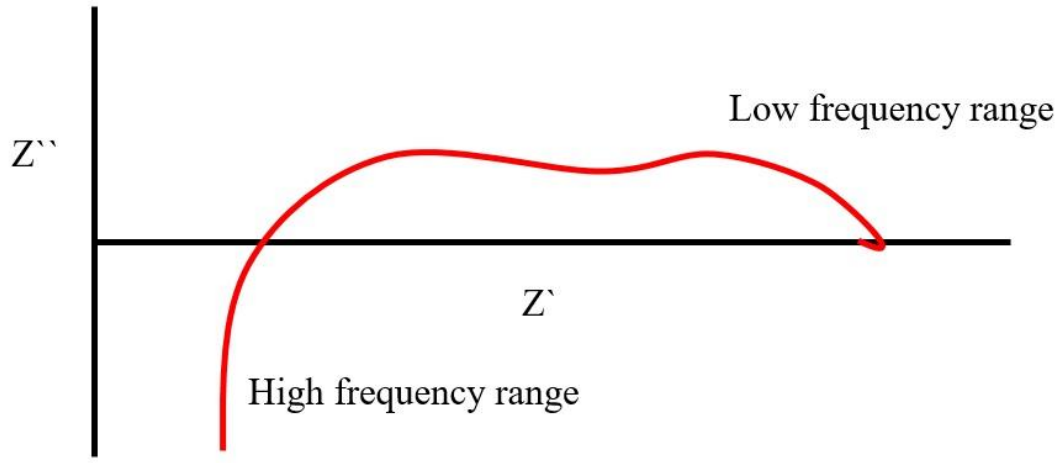

Fig. 2-9 A Nyquist diagram.

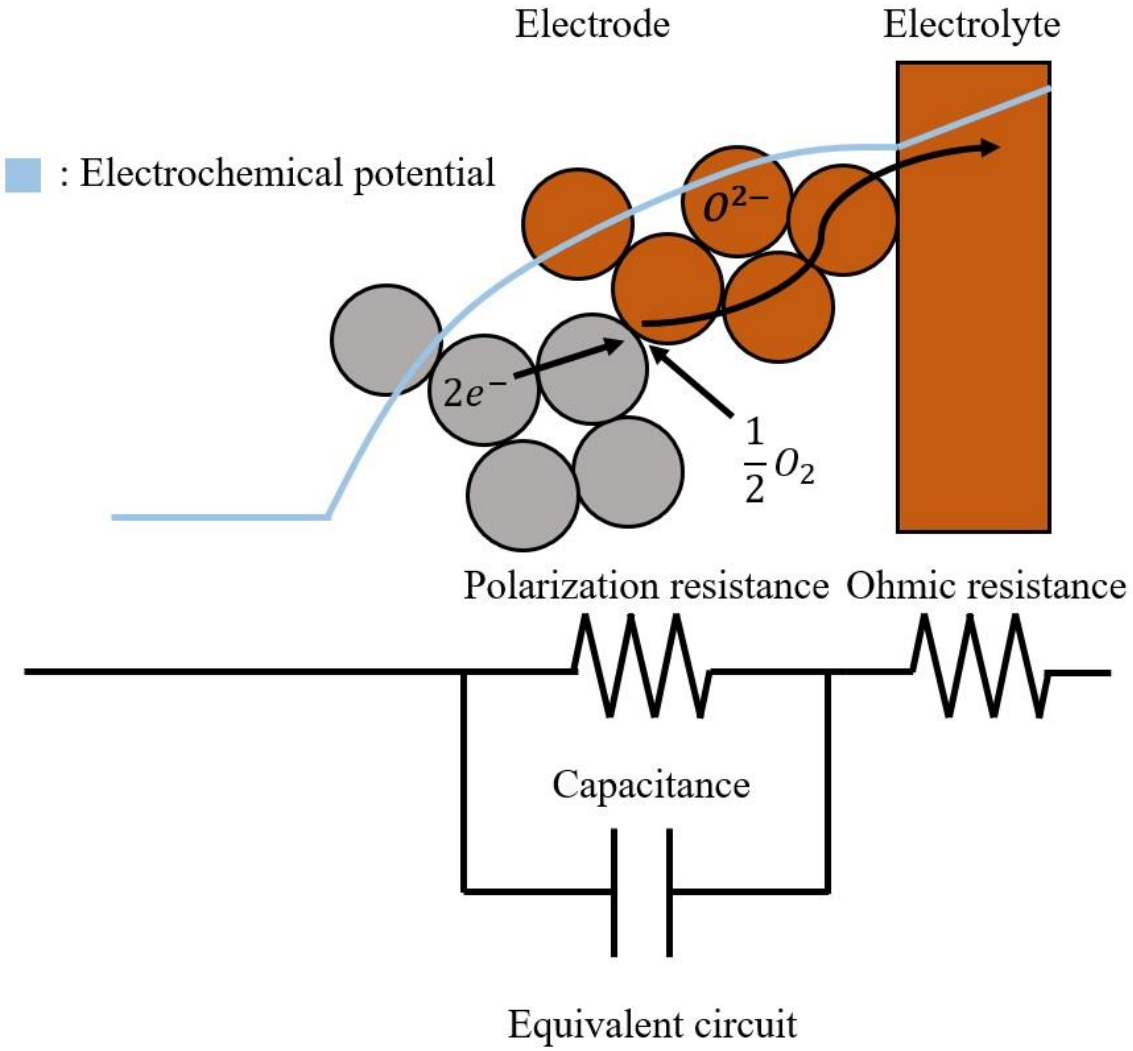

Fig. 2-10 Equivalent circuit corresponding to electrochemical reaction in the cathode.

In the present study, impedance results were fitted using AC circuit consisting of one resistor, inductor and two resistance-CPE (RC) units as shown in Fig. 2-11. Constant phase elements (CPEs) were used for the impedance fitting instead of capacitance. Definitions of circuit components are shown in Eqs. (2.3), (2.4) and (2.5). Two RC units indicate the polarization resistances corresponding to high and low frequency ranges, respectively. Polarization resistance at high frequency range is assigned to charge transfer resistance associated with oxide ion incorporation and transport. Low frequency range polarization corresponds to gas diffusion resistance associated with oxygen adsorption and dissociation. T and p correspond to the CPE constant and the CPE exponent, respectively. If p equals to unity, Z_{CPE} and T correspond to Z_{C} and C, respectively.

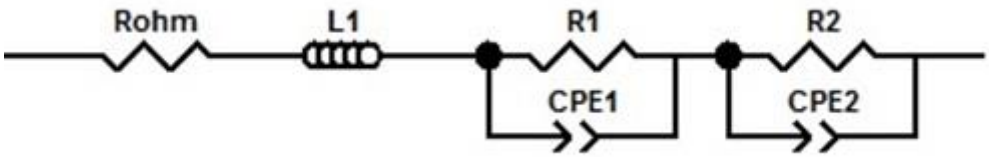

Fig. 2-11 Equivalent circuit used in the present study.

$$Z_{\mathrm{R}}(\omega) = R \tag{2.3}$$

$$Z_{\mathrm{C}} = \frac{1}{j\omega C} \tag{2.4}$$

$$Z_{\mathrm{CPE}} = \frac{1}{(j\omega)^{p}T} \tag{2.5}$$

Solartron 1255B and 1287 (Solartron, UK) were used as a frequency analyzer and a galva-potentiostat for the LSCF-GDC composite cathode measurements. Solartron 1400A and 1470E (Solartron, UK) were used as a frequency analyzer and multi-channel galva-potentiostats for the LSC-GDC composite cathode measurements. ElS was conducted with the frequency range of 0.1 Hz ~ 10 MHz. Current was applied from i = 0 to 0.2 A/cm^2 with the interval of 0.05 A/cm^2.

In the present study, SEM (TM-1000, Hitachi, Japan) and SEM-energy disperse x-ray (EDX) (JSM-7001F, JEOL, Japan) were used to observe the cathode microstructural characteristics after the measurements.

2.2 Microstructure Parameters

2.2.1 Three Dimensional Reconstruction

In the present study, FIB-SEM was used for the reconstruction of 3D cathode microstructures. The specimen was fabricated by preparing the post-tested cell fragment. Epoxy resin was infiltrated into the specimen to fill the pores in a vacuum (Struers Co., Ltd, UK). Pore phases can be distinguished by difference in contrast of SEM observation. Then the specimen was attached to a metal block and polished by a cross section polisher (CP, IB-09010CP, JEOL, Japan). Thin carbon layer was deposited onto the specimen to prevent charging during FIB-SEM observation. Figure 2-12 shows the prepared specimen and Figs. 2-13 and 2-14 show the SEM micrographs after cross section polishing with low and high magnifications. The cathode microstructures were reconstructed as introduced in section 1.3.3. Two FIB-SEM devices were used, NVison 40 (Carl Zeiss Co., Ltd, Germany) for LSCF-GDC cathode, and JIB-4600F (JEOL, Japan) for LSC-GDC cathode, respectively. Figure 2-15 and 2-16 show the pictures of two FIB-SEM devices.

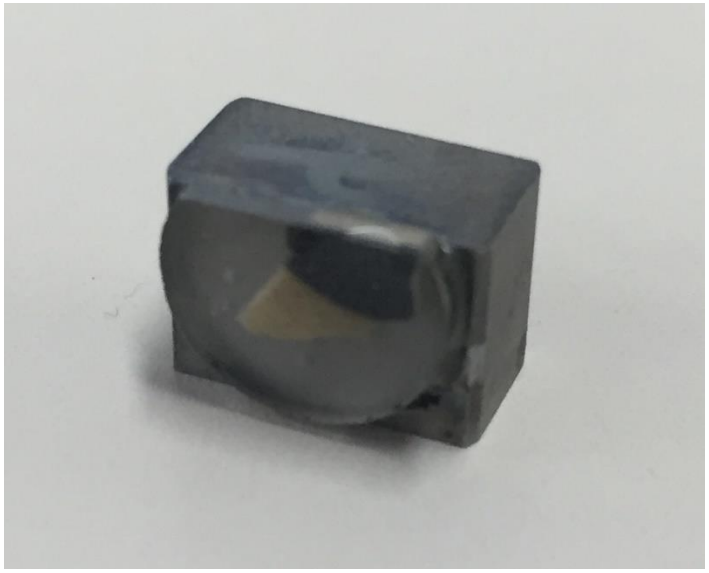

Fig. 2-12 A fully prepared specimen for FIB-SEM observation.

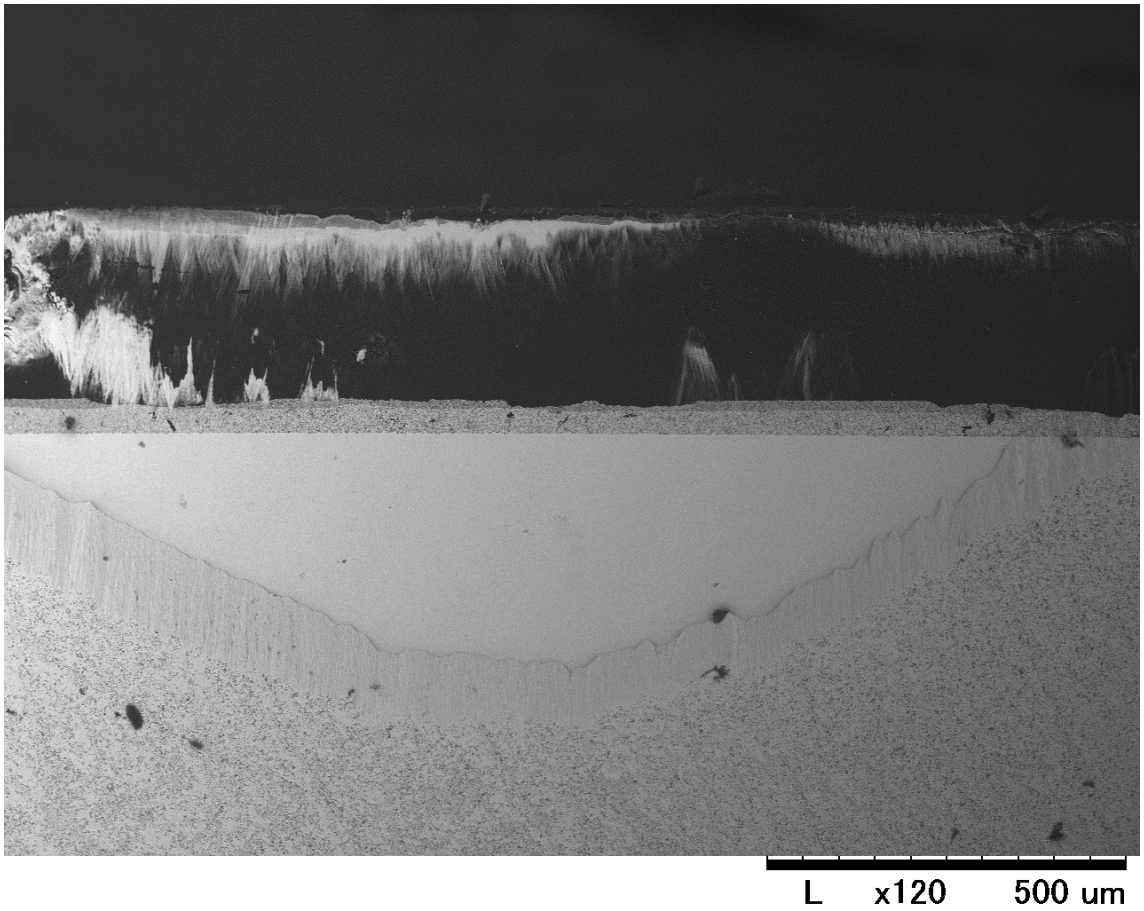

Fig. 2-13 A SEM image of specimen after CP with low magnification.

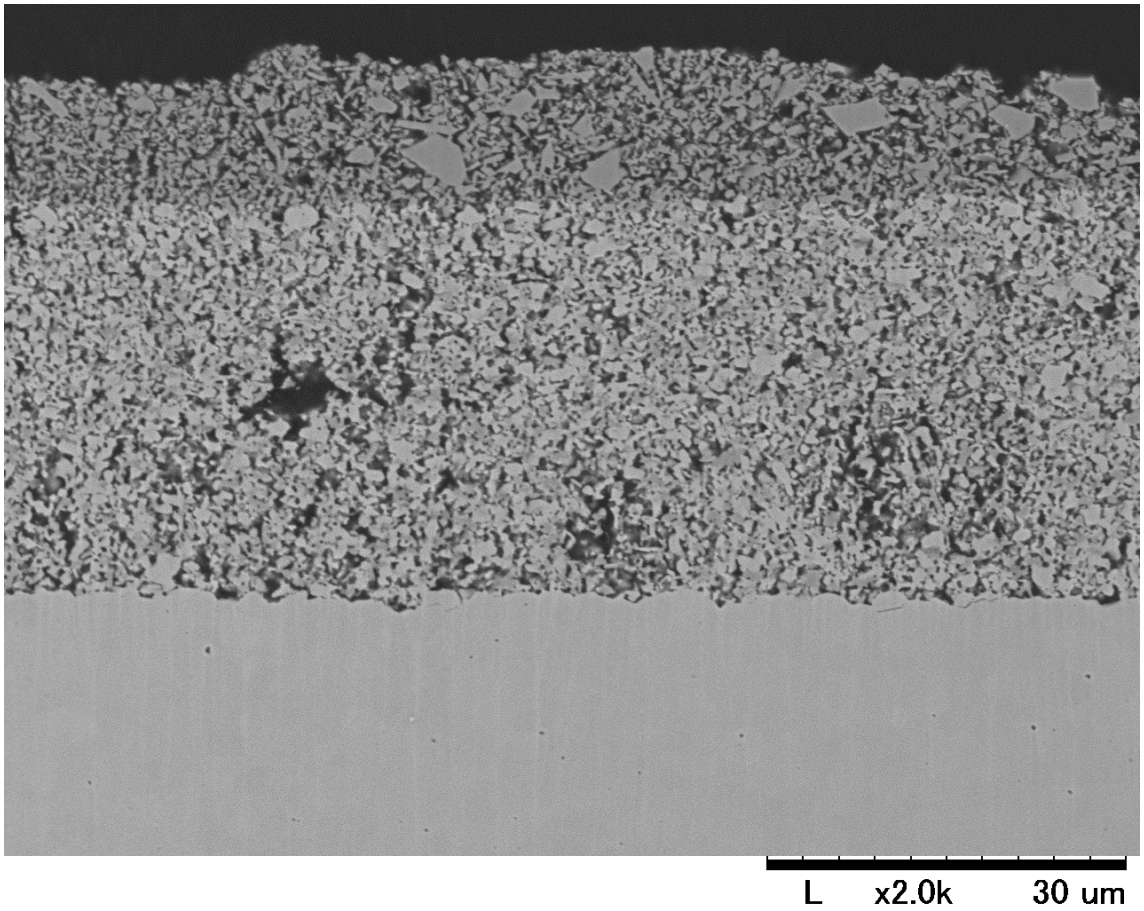

Fig. 2-14 A SEM image of specimen after CP with high magnification.

Fig. 2-15 NVison 40 FIB-SEM.

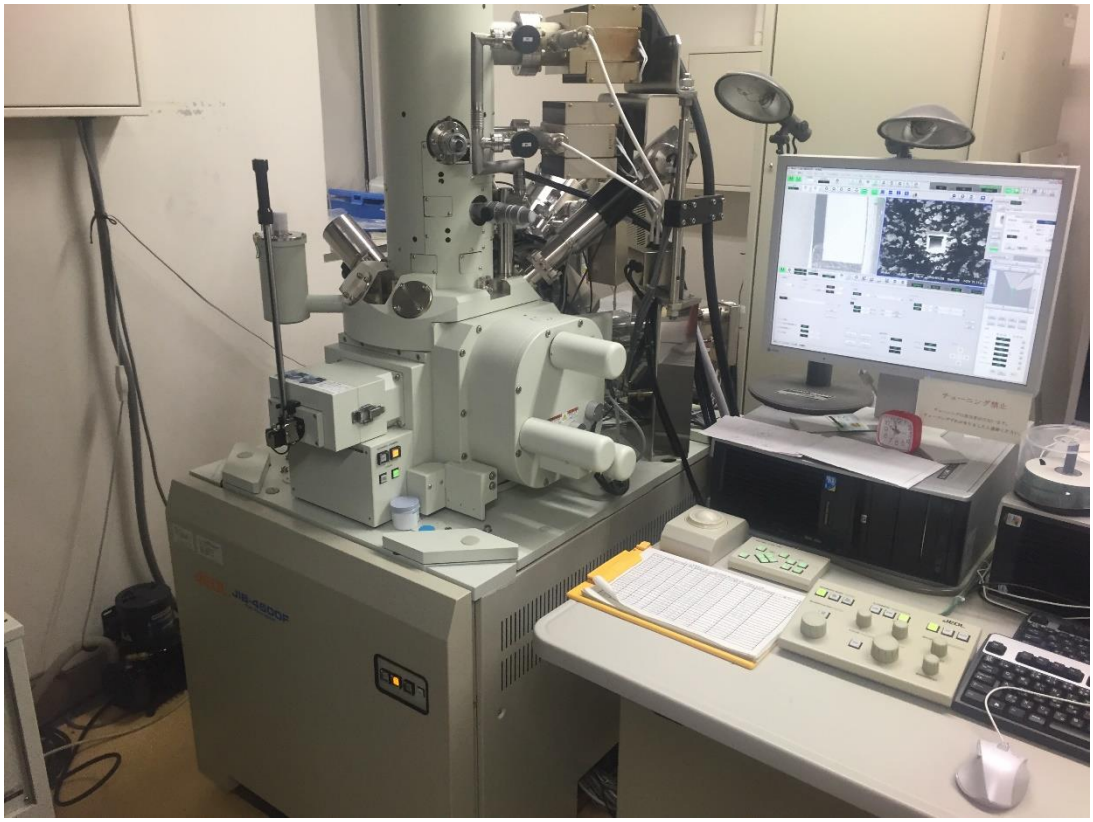

Fig. 2-16 JIB-4600F FIB-SEM.

2.2.2 Image Analysis

The image analysis processes are summarized in Fig. 2-17. All series of images were aligned to compensate position drifting of the target area caused by long time operation of FIB slicing. Then, despeckle process was conducted to minimize the noises in all images. Brightness and contrast were controlled for the optimal differentiation of MIEC, GDC and pore as shown in Fig. 2-17 (b). The interface edges were detected as shown in Fig. 2-17 (c). Image J was used for the above processes. The images were merged by controlling the brightness and contrast as shown in Fig. 2-17 (d). Average threshold values of each area covered by closed edges were investigated. Three phases in the microstructures were distinguished by the threshold values using the average value of each area. However, certain additional hand-work was also conducted to modify the errors during the processing of image ternarization as shown in Fig. 2-17 (e). The threshold values were determined as 127 for MIEC, 255 for GDC and 0 for pore.

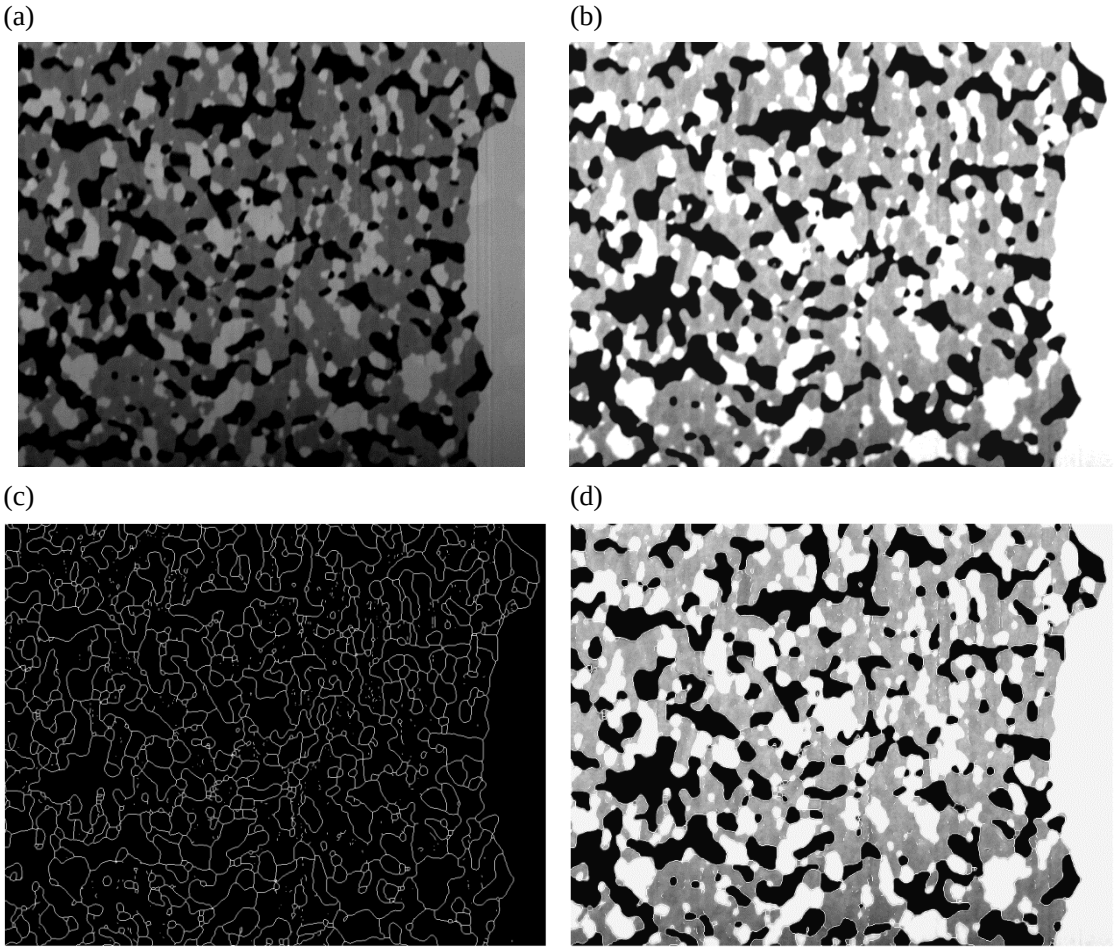

(e) (f)

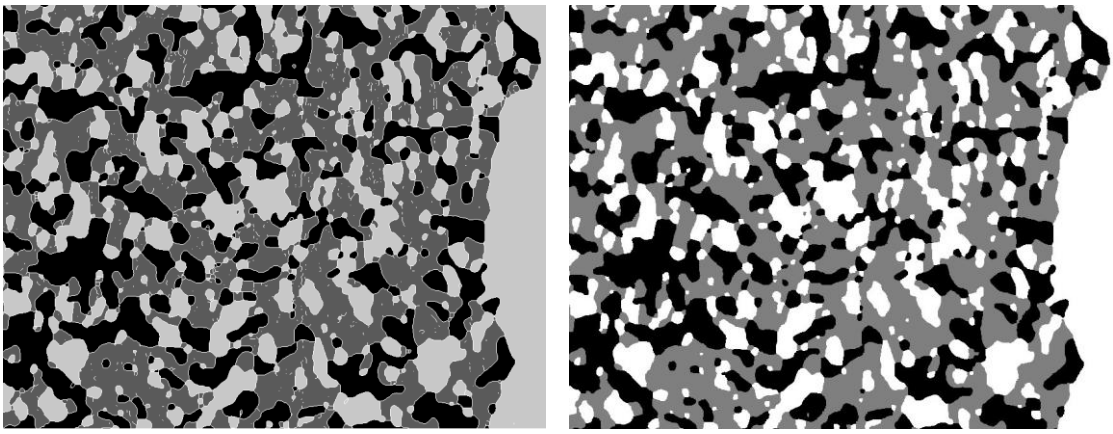

Fig. 2-17 Image analyzing process. (a) A raw-image, (b) bright and contrast compensation, (c) edges formation, (d) merge process, (e) hand treatment and (f) final image.

2.2.3 Parameter Calculations

In the present study, microstructure parameters were calculated by several methods which are introduced below.

Specific surface density

Marching cube method was used for the calculation of the specific surface density [102]. In marching cube method, a cube of adjacent eight voxels are considered. Triangle patches are defined in a cube based on the pattern of each voxel. Surface area is calculated by the sum of considered triangle areas as introduced in Fig. 2-18. Specific surface area of solid phase is calculated and the specific surface areas of interfaces are calculated as follows:

$$S_{\text{phase}} = \frac{A_{\text{phase}}\ (\text{Surface area})}{V_{\text{phase}}\ (\text{Total volume})} \tag{2.6}$$

$$S_{\text{MIEC-pore}} + S_{\text{MIEC-GDC}} = S_{\text{MIEC}} \tag{2.7}$$

$$S_{\text{MIEC-GDC}} + S_{\text{GDC-pore}} = S_{\text{GDC}} \tag{2.8}$$

$$S_{\text{MIEC-pore}} + S_{\text{GDC-pore}} = S_{\text{pore}} \tag{2.9}$$

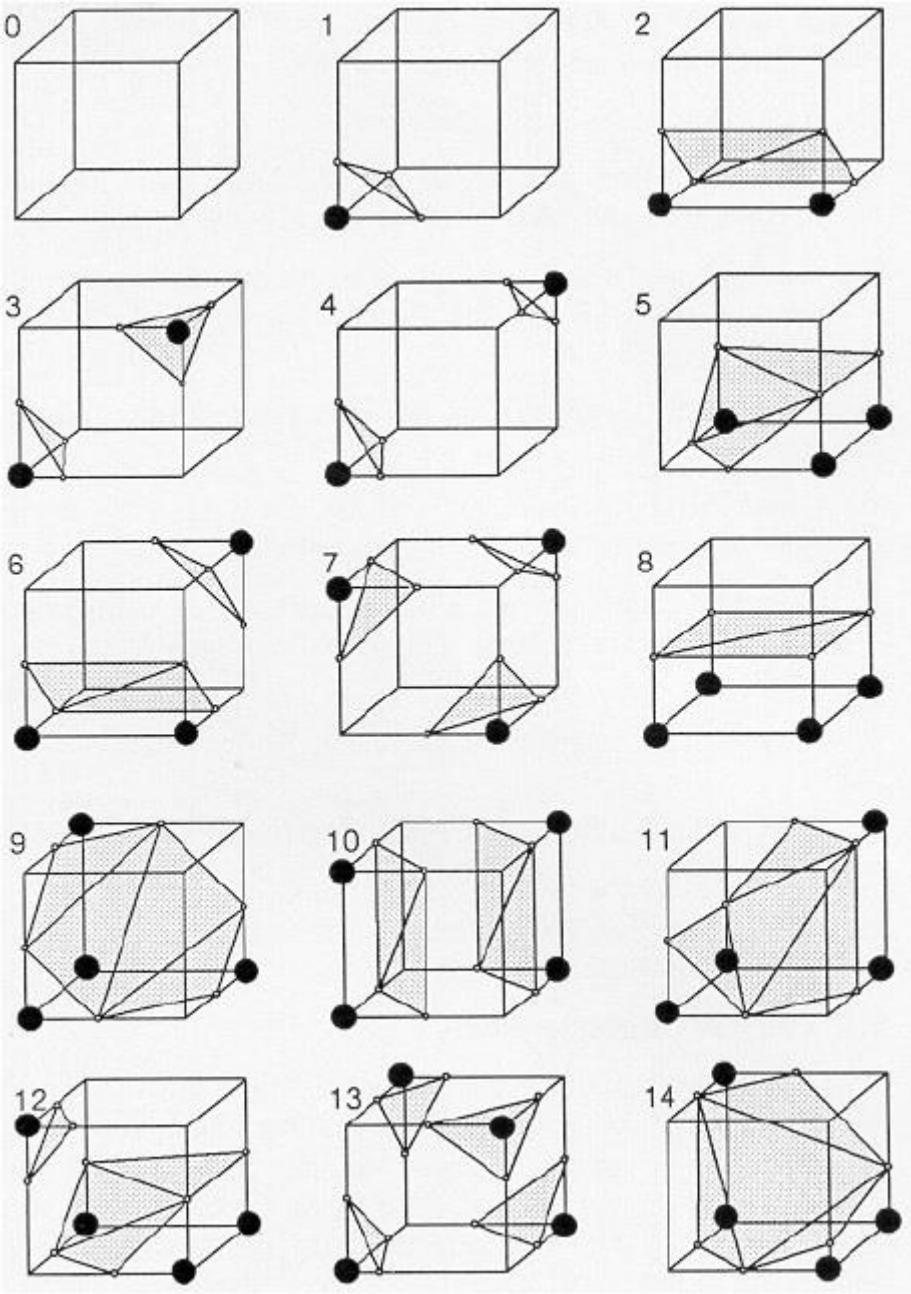

Fig. 2-18 Marching cube method (Lorensen et al., [102]).

Triple phase Boundary

In the present study, centroid method was used for the calculation of TPB length [100]. Figure 2-19 shows the principle of the centroid method. For each edge of voxel corresponding to TPB, triangle area formed by three adjacent center points of edges was considered. Then, total TPB length was calculated as the total length of the lines connecting the centroids of the triangles. Active TPB length was calculated by excluding non-conducting phases such as isolated phases in the microstructures.

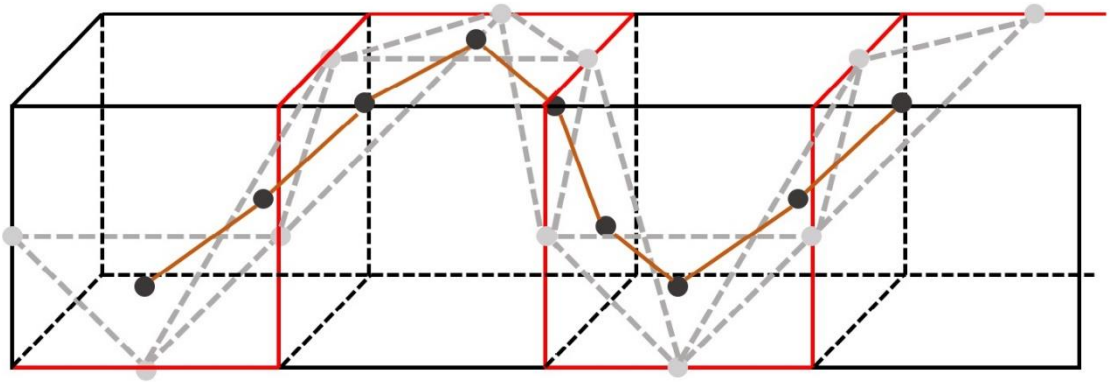

Fig. 2-19 Centroid method (Shikazono et al., [100])

Tortuosity factor

Tortuosity factor is a microstructure parameter which is correlated to the material conduction characteristics. In the present study, random walk method was applied to calculate the tortuosity factor [92]. Walkers are randomly distributed into each voxel and move to one of the neighboring voxel with free direction after 1 step. If the neighboring voxel is the same phase as the former position, walkers move to the next voxel. On the other hand, if the neighboring voxel is a different phase, walkers stay at the current voxel and wait for the next step. By repeating this procedure, the mean square displacement of walkers, r, is calculated. Then, the diffusion coefficient D is calculated using correlation with the mean square displacement as follows:

$$D = \frac{1}{6}\frac{\mathrm{d}(r^2(t))}{\mathrm{d}t} \tag{2.10}$$

Then, tortuosity factor, τ is calculated as,

$$D_{\mathrm{effective}} = \frac{V}{\tau}D \tag{2.11}$$

where $D_{\mathrm{effective}}$ is the effective diffusion coefficient, and V is the volume fraction of the specific phase.

2.3 Numerical Simulation

In the numerical simulation, diffusion characteristics for gas, electron and ion were simulated by solving the diffusion equations as shown below.

$$\nabla D \nabla C_{\mathrm{O_2}} = \frac{-i_{\mathrm{reac}}}{4F} \tag{2.12}$$

$$\nabla \frac{\sigma_{\mathrm{e^-}}}{F} \nabla \tilde{\mu}_{\mathrm{e^-}} = -i_{\mathrm{reac}} \tag{2.13}$$

$$\nabla \frac{\sigma_{\mathrm{O^{2-}}}}{2F} \nabla \tilde{\mu}_{\mathrm{O^{2-}}} = i_{\mathrm{reac}} \tag{2.14}$$

where D (m^2/s) is the oxygen gas diffusion coefficient, $C_{\mathrm{O_2}}$ (mol/m^3) is the oxygen concentration, i_{reac} (A/m^3) is the reaction current, F (C/mol) is the Faraday constant and $\sigma_{\mathrm{e^-}}$ and $\sigma_{\mathrm{O^{2-}}}$ are the electronic conductivity and the ionic conductivity, respectively.

2.3.1 Diffusion Coefficients

Gas

DGM (Dusty Gas Model) is used to simulate diffusion process in the gaseous phase [103]. Definition of DGM is explained below.

$$\frac{N_{\mathrm{i}}}{D_{\mathrm{i,k}}} + \sum_{\mathrm{i}\neq\mathrm{j}} \frac{y_{\mathrm{j}} N_{\mathrm{i}} - y_{\mathrm{i}} N_{\mathrm{j}}}{D_{\mathrm{i,j}}} = -\nabla C_{\mathrm{i}} \tag{2.15}$$

where *i* and *j* represent gas components such as oxygen and nitrogen, N_{i} is the molar flux, y_{j} is the mole fraction, C_{i} is the concentration of *i*-component and $D_{\mathrm{i,j}}$ and $D_{\mathrm{i,k}}$ are the binary diffusion coefficient and the Knudsen diffusion coefficient. Graham's rule was considered simultaneously as follows:

$$\sum_{\mathrm{i}} N_{\mathrm{i}} \sqrt{M_{\mathrm{i}}} = 0 \tag{2.16}$$

Diffusion coefficient of oxygen in gaseous phases can be expressed as:

$$D = \left(\frac{1-\alpha y_{O_2}}{D_{O_2,N_2}} + \frac{1}{D_{O_2,k}}\right)^{-1} \tag{2.17}$$

and,

$$\alpha = 1 - \sqrt{\frac{M_{O_2}}{M_{N_2}}} \tag{2.18}$$

where M_i is the molecular weight of the *i*-th component. Binary and Knudsen diffusion coefficients were calculated as follows [104]:

$$D_{O_2,N_2} = 0.018833\sqrt{\left(\frac{1}{M_{O_2}} + \frac{1}{M_{N_2}}\right) \times 10^{-3}}\frac{T^{\frac{3}{2}}}{P_{total}\Omega_D\zeta_{i,j}^2} \tag{2.19}$$

$$D_{O_2,k} = \frac{2}{3}r\sqrt{\left(\frac{8RT}{\pi M_i}\right)} \tag{2.20}$$

where Ω_D is the collision integral given as:

$$\Omega_D = 1.1336\left(\frac{k}{\varepsilon}T\right)^{-0.1814} \tag{2.21}$$

where P_{total} is the total pressure, T is the absolute temperature, R is the gas constant, k is the Boltzmann constant, r is the mean pore radius, ε and ζ are the intermolecular force constant corresponding to geometric and arithmetic means, respectively. The mean pore radius is calculated by maximum sphere inscription (MSI) method [105]. The gas parameters are shown in Table 2-1.

Table 2-1 Gas Parameters.

substance	M (g/mol)	ζ (Å)	ε/k (K)
O_2	31.9988×10^{-3}	3.54	88.0
N_2	28.0314×10^{-3}	3.68	91.5

Mixed ionic electronic conductor

In the present simulation, ionic conductivities of LSCF and LSC were calculated based on several experimental data. Kuhn et al. [106] reported the correlation between oxygen pressure and

oxygen nonstoichiometry (δ) of LSCF as shown in Fig. 2-20.

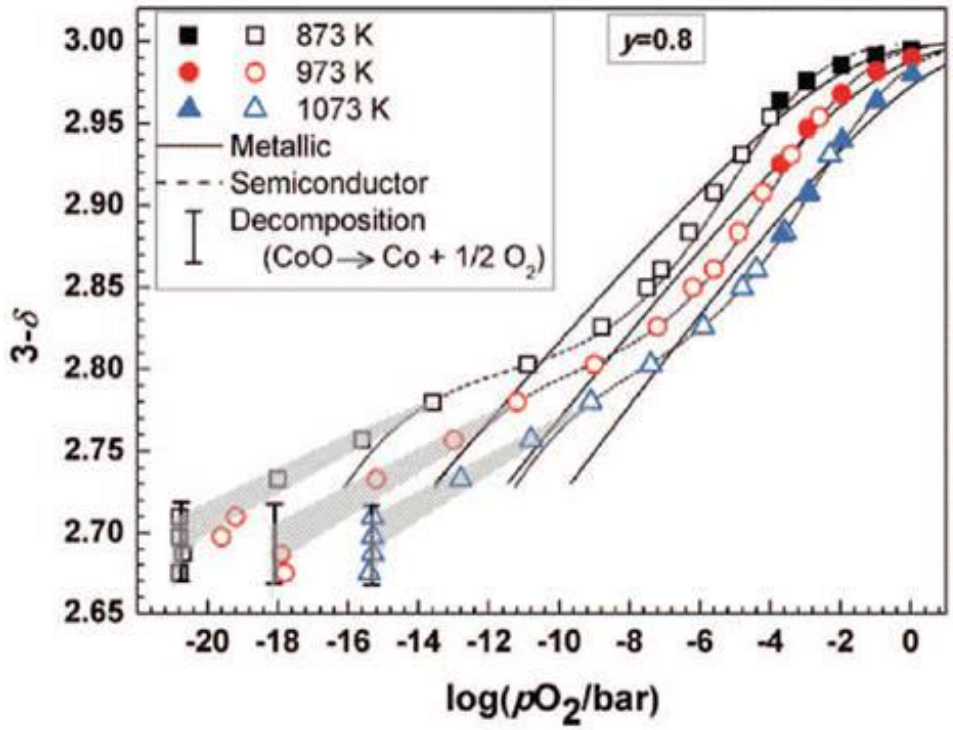

Fig. 2-20 Oxygen nonstoichiometry of LSCF (Kuhn et al., [106]).

Sigmoid function was used to fit the correlation between oxygen pressure and oxygen nonstoichiometry. Equation 2.22 and Table 2-2 represent the sigmoid function and the fitting parameters, respectively. Figure 2-21 shows the fitting results.

$$3-\delta = \mathrm{A} + \mathrm{B}\{1+\exp\left(-\frac{\log_{10}P_{O_2}+C}{D}\right)\}^{-1} \tag{2.22}$$

Table 2-2 Fitting parameters for LSCF

Temperature (K)	A	B	C	D
873	2.8303	0.1725	5.0549	1.2556
973	2.8297	0.1732	3.7100	1.2559
1073	2.8286	0.1742	2.6185	1.2563

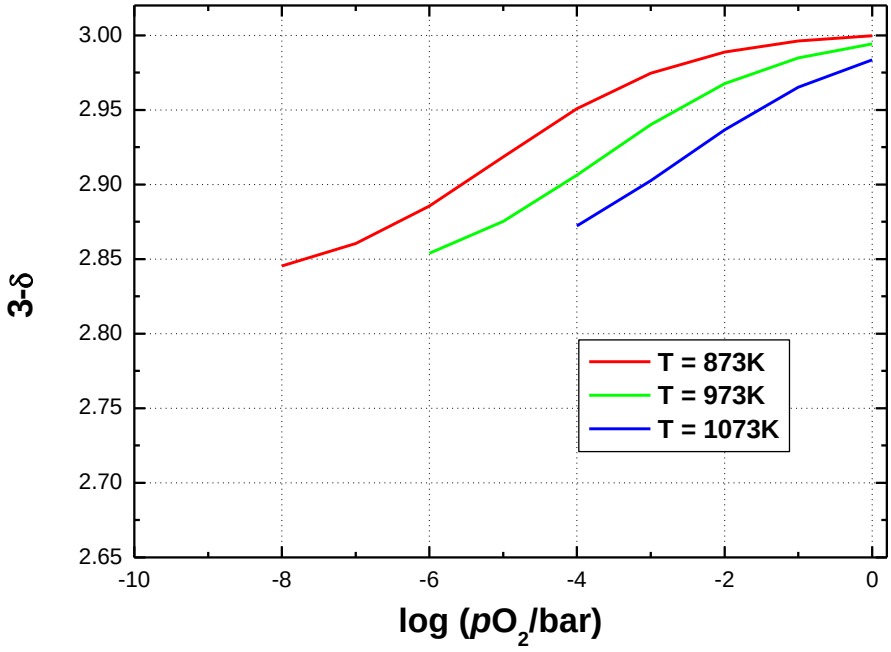

Fig. 2-21 Fitting results of LSCF oxygen nonstoichiometry.

For the case of LSC, oxygen nonstoichiometry reported by Kuhn et al. [77] was considered as shown in Fig. 2-22.

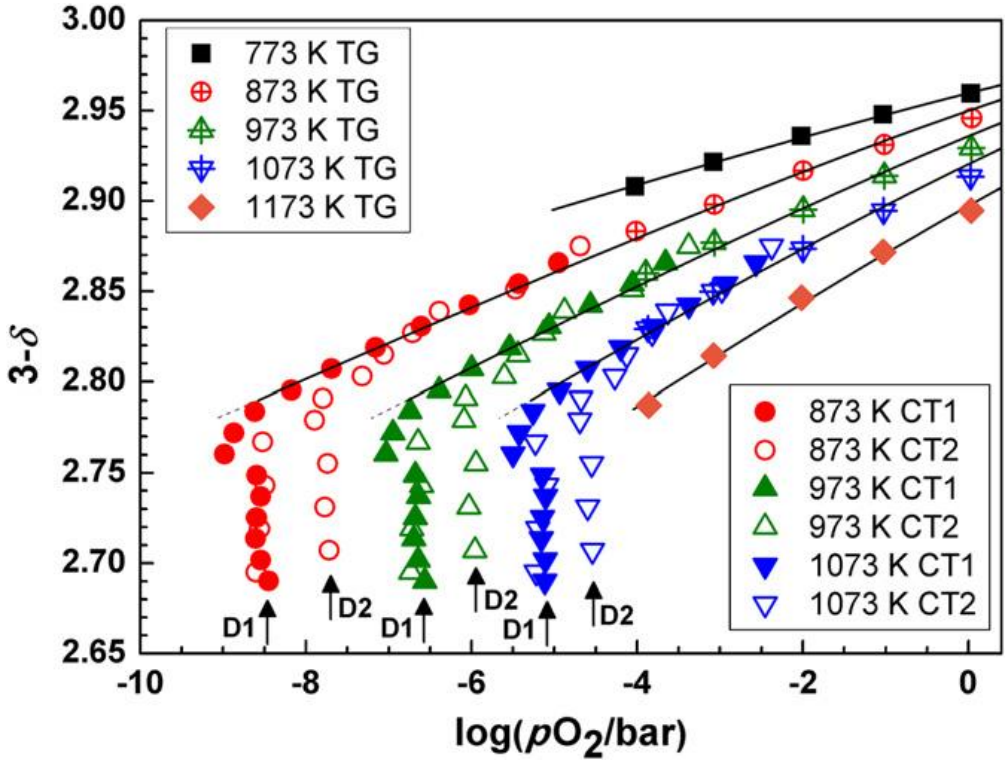

Fig. 2-22 Oxygen nonstoichiometry of LSC (Kuhn et al., [77]).

Only $\log_{10}P_{O_2}$ range from 0 to -5 were fitted with a quadratic equation. Equation 2.23 and Table 2-3 show the correlation and fitting parameters. Figure 2-23 shows the fitting results.

$$3-\delta = A\log_{10}P_{O_2}{}^2 + B\log_{10}P_{O_2} + C \tag{2.23}$$

Table 2-3 Fitting parameters for LSC

Temperature (K)	A	B	C
873	-6.17098×10^{-4}	0.01320	2.94546
973	-9.03789×10^{-4}	0.01481	2.92846
1073	-1.73×10^{-3}	0.01516	2.91292

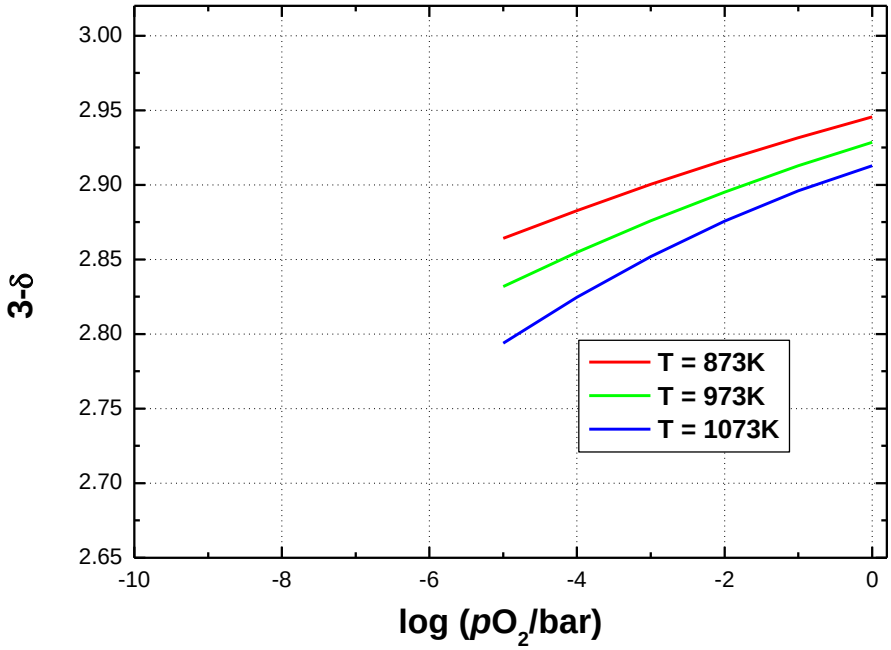

Fig. 2-23 Fitting results of LSC oxygen nonstoichiometry.

Ionic conductivity of LSCF was calculated by using the correlation between vacancy diffusion coefficient and oxygen chemical diffusion coefficient as follows [107]:

$$D_{\text{chem}} = D_{\text{v}}\left(-\frac{1\partial \ln P_{O_2}}{2\ln\delta}\right) \tag{2.24}$$

Vacancy diffusion coefficient, D_{v} was calculated using oxygen tracer diffusion coefficient, D^* and correlation factor f $(= 0.69)$ as introduced by Kudo et al. [108] for LSCF.

$$D_{\mathrm{v}} = \frac{3-\delta}{\delta}\frac{D^*}{f} \tag{2.25}$$

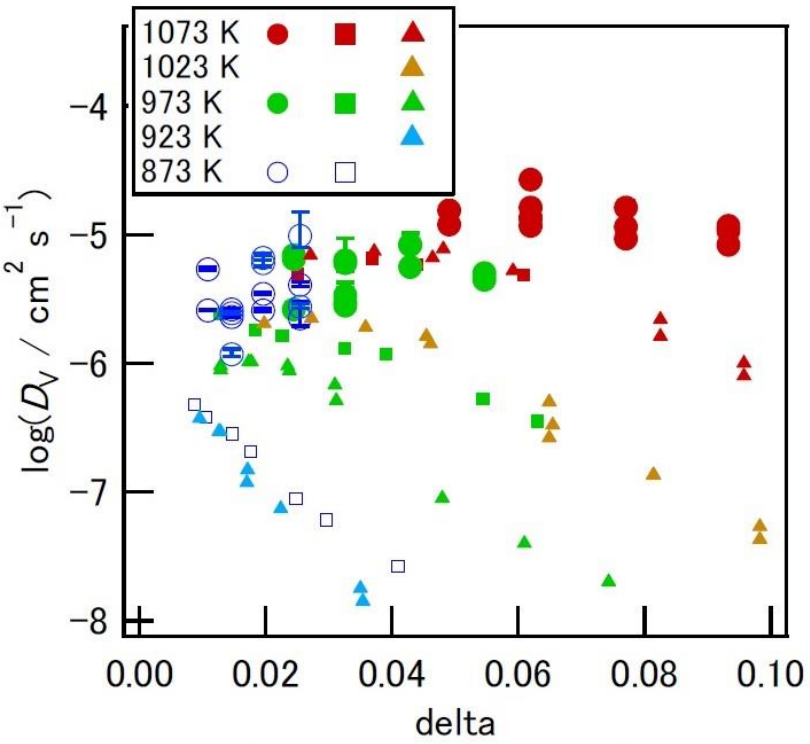

Fig. 2-24 Oxygen vacancy diffusion coefficient of LSCF, D_{v} (Kudo et al., [108]).

For LSC, chemical diffusion coefficient which was introduced by Søgaard et al. was used as shown in Fig. 2-25 [109].

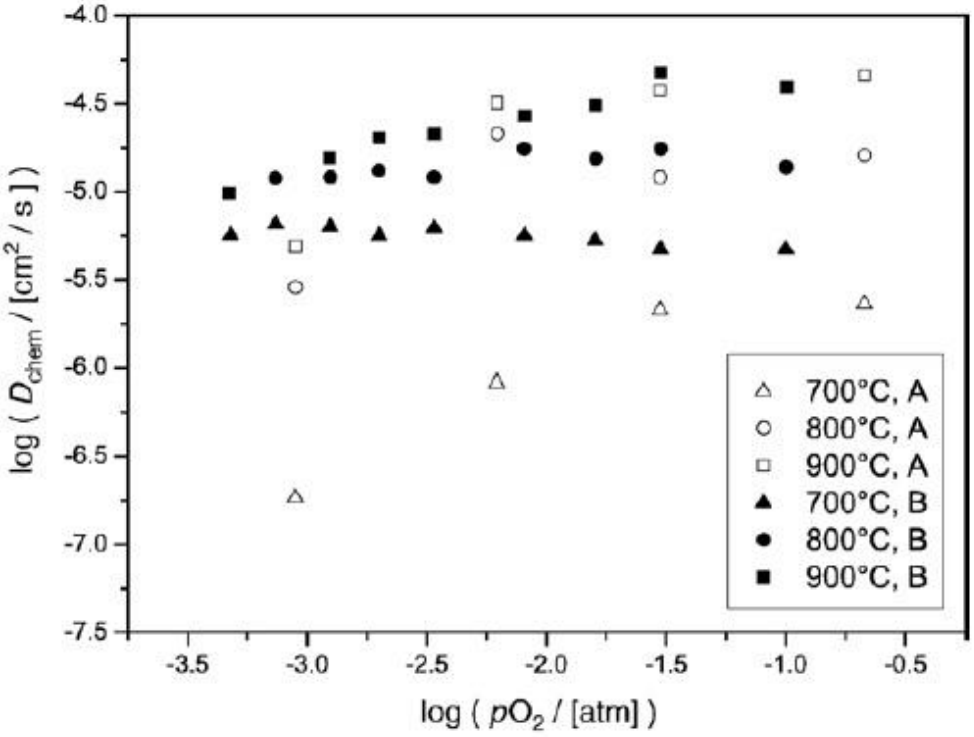

Fig. 2-25 Chemical diffusion coefficient of LSC with different oxygen partial pressures (Søgaard et al., [109]).

Chemical diffusion coefficient is quantified using oxygen vacancy diffusion coefficient as follows [44]:

$$D_{\text{chem}} = -\frac{RTV_{\text{mol}}}{8F^2}\sigma_{O^{2-}}\frac{\partial lnP_{O_2}}{\partial \delta} \tag{2.26}$$

where F is the Faraday constant (F = 9.6485×10^4 C/mol), V_{mol} is the molar volume (V_{mol} = 35.17×10^{-6} m^3/mol) [110].

Fitted function for the LSCF electronic conductivity proposed by Matsukazi et al. [99] was used:

$$\log_{10}\sigma_{e^-} = -0.0237\left(\log_{10}P_{O_2}\right)^2 + 0.0034\log_{10}P_{O_2} + 4.8126 \quad (\text{T} = 1073\,\text{K}) \tag{2.27}$$

$$\log_{10}\sigma_{e^-} = -0.0095\left(\log_{10}P_{O_2}\right)^2 + 0.0011\log_{10}P_{O_2} + 4.8152 \quad (\text{T} = 973\,\text{K}) \tag{2.28}$$

Electronic conductivity of LSC is calculated by fitting the experimental result reported by Matsuda et al. [67] as follows:

$$\log_{10}\sigma_{e^-} = -0.98716\left(\frac{1000}{T(K)}\right)^2 + 2.59208\left(\frac{1000}{T(K)}\right) + 1.55773 \quad (2.29)$$

In the present study, local equilibrium in the MIEC was assumed as shown in Eq. (2.30), and ionic and electronic conductivities were calculated with the oxygen chemical potential as defined in Eq. (2.31).

$$\mu_O = \tilde{\mu}_{O^{2-}} - 2\tilde{\mu}_{e^-} \quad (2.30)$$

$$\mu_O = \mu_O^0 + \frac{1}{2}RT\ln P_{O_2} \quad (2.31)$$

Ionic conductor (GDC)

In the present study, ionic conductivity of GDC by Steele is used [111].

$$\sigma_{O^{2-}} = 1.09 \times 10^5 \exp\left(-\frac{0.64eV}{kT}\right) \quad (2.32)$$

2.3.2 Electrochemical Reaction

Ionic conductions in both MIEC and GDC phases were calculated with individual conductivities. In the present simulation, electrochemical potential of electron $\tilde{\mu}_{e^-}$ was assumed to be constant due to the high electronic conductivity of LSCF and LSC [101], i.e. Eq. (2.13) was not solved. In addition, oxygen gas pressure was assumed to be constant inside the pores, because it was reported that the variation of oxygen partial pressure is significantly small under present current density range [99].

For the MIEC surface reaction model, oxygen adsorption and charge transfer model suggested by J. Fleig [112] was used.

$$\begin{aligned} &O_2 \rightarrow 2O_{ad} \\ &O_{ad} + e^- \rightarrow O^-_{ad} \\ &O^-_{ad} \rightarrow O^-_{MIEC} \\ &O^-_{MIEC} + e^- \rightarrow 2\,O^-_{MIEC} \end{aligned} \quad (2.33)$$

Oxygen molecules are absorbed on the MIEC surface and dissociates into oxygen atom O_{ad} as shown in Eq. (2.33). O^-_{ad} is led by charge transfer on the MIEC surface and incorporated into the oxygen vacancy. Then, oxygen is ionized by electrochemical reaction with the electrons. During this procedure, electron transfer to generate O^-_{ad} and ion transfer of O^-_{MIEC} are considered as rate determining steps, because the last ionization and transport steps of oxide ion in MIEC can be considered to be fast. Therefore, net current can be defined by using the gap of electrostatic surface potential step $\Delta\chi$ from the equilibrium value χ^{eq} as follows:

$$\Delta\chi = \chi - \chi^{eq} \tag{2.34}$$

$$\begin{aligned} j &= \overleftarrow{k}^{eq}\theta_{O^-_{ad}} \exp\left(\frac{\alpha F\Delta\chi}{RT}\right) - \vec{k}^{eq}\theta_{O_{ad}} \exp\left(-\frac{(1-\alpha)F\Delta\chi}{RT}\right) \\ &= \overleftarrow{k}^{eq}\theta^{eq}_{O^-_{ad}}\{\frac{\theta_{O^-_{ad}}}{\theta^{eq}_{O^-_{ad}}} \exp\left(\frac{\alpha F\Delta\chi}{RT}\right) - \vec{k}^{eq}\theta_{O_{ad}} \exp\left(-\frac{(1-\alpha)F\Delta\chi}{RT}\right)\} \end{aligned} \tag{2.35}$$

where j is the net current, $\overleftarrow{k}^{eq}$ is the overpotential-independent constant for the equilibrium, $\theta_{O^-_{ad}}$ is the surface coverage of absorbed oxygen ion, O^-_{ad}. If the adsorption on the surface is sufficient enough such as MIEC, it can be assumed that adsorption rate of oxygen ion is identical with equilibrium, i.e. adsorption rate of oxygen ion = 0. And for this case, the relationship between the gap of electrostatic surface potential step and the local activation overpotential can be written ed as follows:

$$\Delta\chi = 2\eta_{act} \tag{2.36}$$

By introducing this correlation into Eq. (2.35), reaction current at MIEC can be quantified by generalized Butler-Volmer equation as shown in Eq. (2.37).

$$i_{reac,surface} = i_{0,surface}A_{MIEC-pore}\{\exp\left(\frac{\theta_a F}{RT}\eta_{act}\right) - \exp\left(-\frac{\theta_c F}{RT}\eta_{act}\right)\}, \tag{2.37}$$

where $i_{reac,surface}$ is the reaction current caused by MIEC surface reaction, F is the Faraday constant. θ_a and θ_c are the transfer coefficients and $A_{MIEC-pore}$ is the MIEC surface area where oxygen reduction reaction takes place. The values for θ_a and θ_c were obtained from the experimental data measured by pulsed laser deposition method [113].

For the TPB reaction, the similar Butler-Volmer equation was considered as follows.

$$i_{reac,TPB} = i_{0,TPB}L_{TPB}\{\exp\left(\frac{\theta_{TPB}F}{RT}\eta_{act}\right) - \exp\left(-\frac{\theta_{TPB}F}{RT}\eta_{act}\right)\} \tag{2.38}$$

where L_{TPB} is the active TPB length, θ_{TPB} is the transfer coefficient corresponding to TPB reaction. The value for θ_{TPB} is reported elsewhere [114,115].

Exchange current density was calculated by a correlation as a function of oxygen partial pressure and activation energy as follows:

$$i_0 = i_0^* P_{O_2}^{\gamma} \exp(-\frac{Q}{RT}) \tag{2.39}$$

where i_0 is the exchange current density, γ is the pressure constant and Q is the activation energy.

The pressure constant and the activation energy were calculated by fitting the experimental data as follows [116]:

$$\log i_0 = \gamma \log P_{O_2} + \text{ constant} \qquad (T \text{ is constant}) \tag{2.40}$$

$$\log i_0 = -\frac{Q}{R}\frac{1}{T} + \text{constant} \qquad (P_{O_2} \text{ is constant}) \tag{2.41}$$

In the present simulation, γ = 0.2, $\frac{Q}{R}$ = 10327 were used. The exchange current density coefficients for the MIEC surface reaction, i_0^* were fitted using the experimental data of pure MIEC cathodes. Then the exchange current densities for the TPB reaction, $i_{0,\mathrm{TPB}}$ were fitted by using the experimental data of composite cathodes.

Local overpotential is defined by the oxygen chemical potential difference between the gas and the solid phases as follows:

$$\begin{aligned}\eta_{\mathrm{act}} &= -\frac{1}{2F}\left(\tilde{\mu}_{\mathrm{O}^{2-}} - 2\tilde{\mu}_{\mathrm{e}^-} - \mu_{\mathrm{O}}^0 - \frac{1}{2}RT\ln P_{\mathrm{O}_2}\right) \\ &= \frac{1}{2F}\left(\mu_{\mathrm{O}}^{\mathrm{gas}} - \mu_{\mathrm{O}}^{\mathrm{solid}}\right)\end{aligned} \tag{2.42}$$

In the present simulation, oxygen chemical potential inside the solid phase $\mu_{\mathrm{O}}^{\mathrm{solid}}$ is the variable that should be solved correctly for the overpotential calculation. It is obtained by calculating the difference between $\tilde{\mu}_{\mathrm{O}^{2-}}$ and $2\tilde{\mu}_{\mathrm{e}^-}$. Since only the difference between these two electrochemical potentials is of importance, absolute value of $\tilde{\mu}_{\mathrm{O}^{2-}}$ will be shifted according to the absolute value of $\tilde{\mu}_{\mathrm{e}^-}$. In the present simulation, a constant value of $\tilde{\mu}_{\mathrm{e}^-}$ = 100 J/mol is simply applied.

Total overpotential η of the cathode was calculated as Eq. (2.43) [99]. All numerical simulation conditions are summarized in Table 2-4.

$$\eta = -\frac{1}{2F}\left(\tilde{\mu}_{\mathrm{O}^{2-}\mathrm{Cathode/Electrolyte}} - 2\tilde{\mu}_{\mathrm{e}^-\mathrm{Cathode/\,C.C}} - \mu_{\mathrm{O}}^0 - \frac{1}{2}RT\ln P_{\mathrm{O}_2}\right) \tag{2.43}$$

Table 2-4 Numerical Conditions.

Properties	Value
Current density (A/cm^2)	0.05
Operation temperature (K)	973
Gas pressure (atm)	1.0
Gas composition (mol. %)	O_2 100 %
θ_{a}	1.2
θ_{c}	1.0
θ_{TPB}	2.0
Q (J/mol)	1242.06
Ionic conductivity of LSCF [106,108]	$\sigma_{O^{2-},\mathrm{LSCF}}$ = 0.474 Sm^{-1} at 700 ℃.
Ionic conductivity of LSC [77,109]	$\sigma_{O^{2-},\mathrm{LSC}}$ = 0.56 Sm^{-1} at 700 ℃.
Ionic conductivity of GDC [111]	$\sigma_{O^{2-},\mathrm{GDC}}$ = 5.43 Sm^{-1} at 700 ℃

2.3.3 Lattice Boltzmann method

In the present study, LBM (Lattice Boltzmann Method) was used to solve the governing equations [117,118]. LBM is a powerful method to simulate diffusion and convection dynamics especially in complicated porous structures such as SOFC electrodes. In the LBM, collision and translation mechanisms of each particles which have velocity vector are sequentially simulated by using velocity distribution function, f_{i}. In this simulation, gas, ion and electron were considered as particles and D3Q6 (3 direction and 6 velocity) model was used. LBM with approximation of collision term by LBGK [119] is shown as follows:

$$f_{\mathrm{i}}(\vec{x}+\vec{c}_{\mathrm{i}}\Delta t, t+\Delta t) = f_{\mathrm{i}}(\vec{x},t) - \frac{1}{t^*}\left[f_{\mathrm{i}}(\vec{x},t) - f_{\mathrm{i}}^{\mathrm{eq}}(\vec{x},t)\right] + w_{\mathrm{i}}\Delta t \tag{2.44}$$

where *i* indicates the directions of *x*, *y* and *z*. $\vec{x}$ is the position vector, $\vec{c}$ is the particle velocity, t is the time, and $w_i\Delta t$ corresponds to production term caused by electrochemical reaction. $f_{\mathrm{i}}^{eq}(\vec{x},t)$ corresponds to the equilibrium distribution. Average value of velocity distribution function of each direction were used for the equilibrium distribution.

$$f_{\mathrm{i}}^{eq}(\vec{x},t) = \frac{1}{6}\sum_{i=1,6} f_{\mathrm{i}}(\vec{x},t) \tag{2.45}$$

Production w_{i} can be given by dividing reaction current for each direction. Relaxation time t^* for each voxel was considered for efficient interpret of gas diffusion coefficient, electronic and ionic conductivity spatial distributions.

$$t^* = 0.5 + \frac{3D\Delta t}{\Delta x^2} \tag{2.46}$$

For the calculation of relaxation time, time step Δt is given by considering t^* to be 0.99 and diffusion coefficient of gas in the maximum porous radius $D = D_{\mathrm{r=r_{MAX}}}$. Ratio of ionic diffusion to electron diffusion is introduced into the diffusion equation by using $D_{\mathrm{r=r_{MAX}}}$ due to the variations of diffusion velocity in each phase as follows.

$$D_{\mathrm{electron,ion}} = \frac{D_{\mathrm{r=r_{MAX}}}}{\sigma_{\mathrm{theoretical}}} \tag{2.47}$$

In the LBM simulation, electrochemical potential, molar velocity and current density were quantified by using velocity function f_{i} as:

$$\rho = \sum_{\mathrm{i}=1}^{N} f_{\mathrm{i}} \tag{2.48}$$

$$u = \frac{1}{\rho}\sum_{\mathrm{i}=1}^{N} f_{\mathrm{i}} c_{\mathrm{i}} \tag{2.49}$$

$$N = \frac{t^* - 0.5}{t^*}\,\frac{1}{\rho}\sum_{\mathrm{i}=1}^{N} f_{\mathrm{i}} c_{\mathrm{i}} \tag{2.50}$$

where ρ corresponds to the electrochemical potential, u corresponds to the mole velocity, and N is the current density. For the case of gas phase, ρ corresponds to the gas concentration. For the boundary conditions inside the cathode, halfway bounce-back condition was applied. In the halfway bounce-back, if collision occurs at the wall for 1 time-step Δt, a particle which is collided to wall moves to reverse direction after 1 time step. At the boundary between the electrolyte and the cathode, current density of oxygen ion was considered to be constant. Gas concentration was considered to be constant at the boundary between the cathode and the current collector.

Chapter 3
LSCF-GDC Composite Cathode with Different Volume Ratios

3.1 Correlation between Performance and Microstructure

LSCF-GDC composite cathodes with volume ratios of 20:80, 30:70, 50:50, 70:30, and 100:0 % were fabricated by a screen printing method. An electrolyte-supported cell was prepared for the measurements. Cathode microstructures were reconstructed by FIB-SEM and microstructure parameters were correlated with polarization characteristics.

3.1.1 Overpotential and Polarization Resistance

In the present study, electrochemical performance measurements were conducted four times using four samples for each volume ratio, and error bars in the graphs indicate the standard deviations. Cathode overpotentials were obtained from the current-voltage measurements by subtracting voltage drop caused by ohmic loss. Figure 3-1 shows the overpotential results. The lowest overpotential was achieved at a volume ratio of LSCF:GDC = 30:70 %, and the overpotential increases in the order of 50:50, 70:30, 100:0 and 20:80 vol. %.

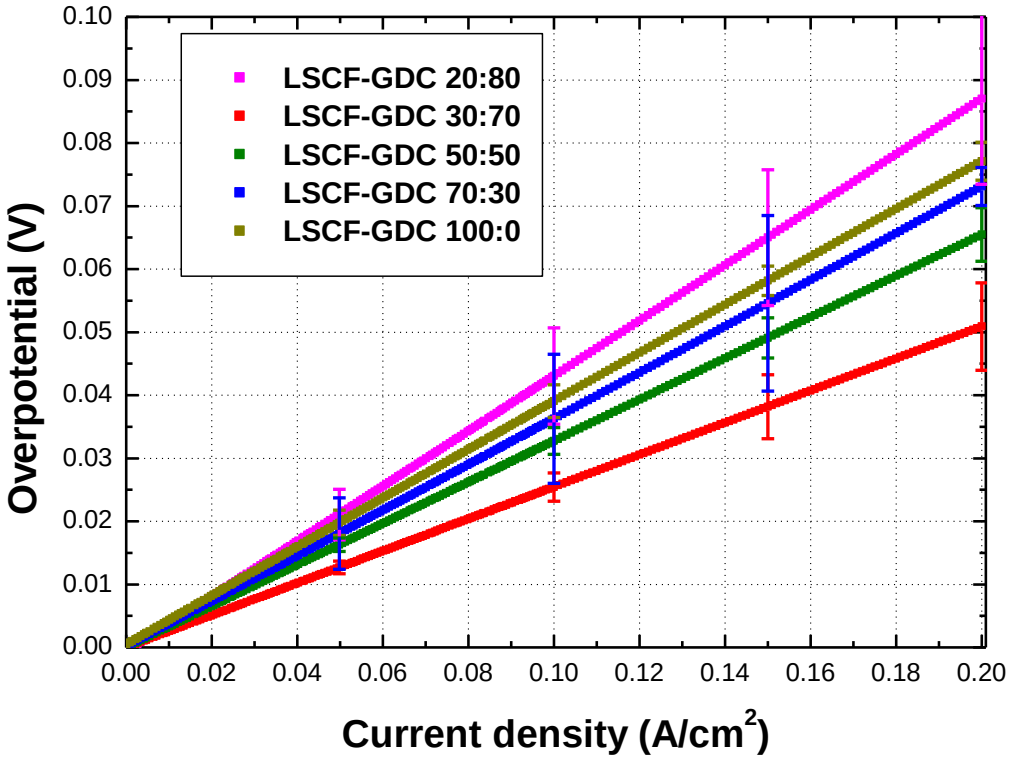

Fig. 3-1 Overpotentials of LSCF-GDC composite cathodes.

Polarization resistances at open circuit voltage (OCV) are shown in Fig. 3-2. The results show

the similar tendency with the overpotential results as shown in Fig. 3-1. A volume ratio of LSCF:GDC = 30:70 % shows the lowest polarization resistance and it increases in the order of 50:50, 70:30, 20:80 and 100:0 vol. %. In Ref. [10], it was reported that the best performance of LSCF-GDC composite cathode was achieved at a weight ratio of 40:60 % (volume ratio = 43.24:56.76 %). The results show the similar tendency with the results of the present study. The different tendency of 20:80 and 100:0 vol. % between Figs. 3-1 and 3-2 is considered to be due to the operating conditions, i.e. under OCV or polarized conditions. For a volume ratio of LSCF:GDC = 20:80 %, it is considered that deterioration of electron path due to the insufficient volume of electronic conductor, LSCF, results in the increase of overpotential and polarization resistance.

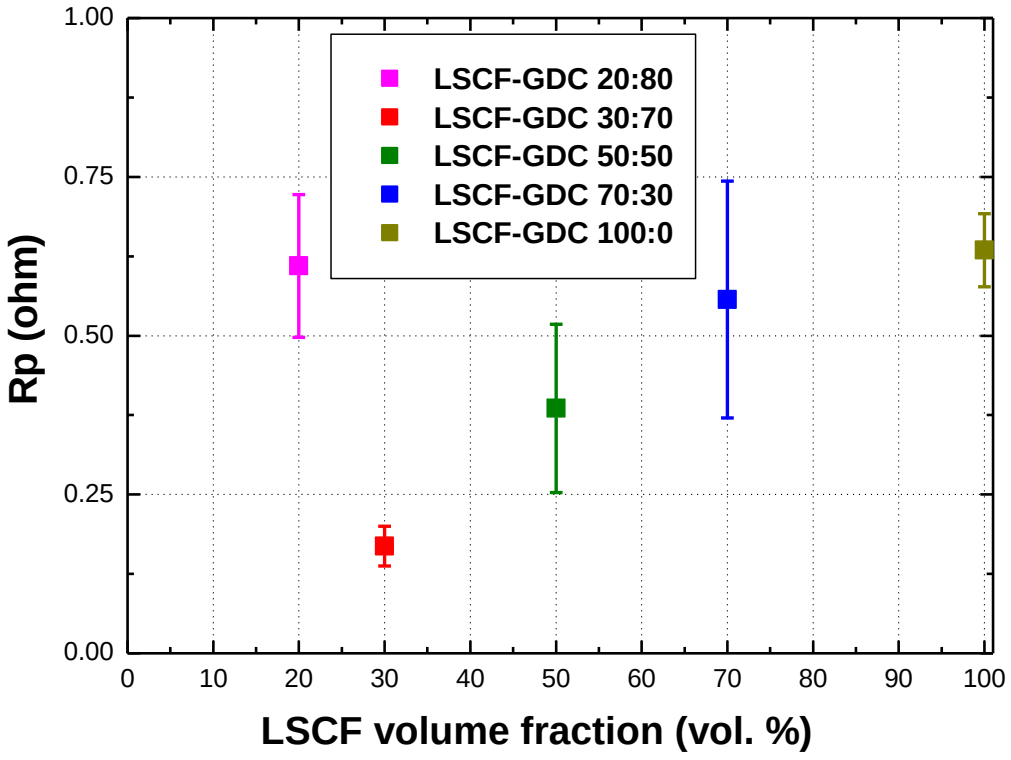

Fig. 3-2 Polarization resistances of LSCF-GDC composite cathodes at OCV.

3.1.2 Microstructure parameters

Microstructure parameters were calculated based on 3D cathode microstructures. Microstructures of LSCF-GDC composite cathodes were reconstructed by FIB-SEM. For SEM observation, energy selective backscatter (EsB) detector with an acceleration voltage of 1.5 keV was used. Figure 3-3 shows the FIB-SEM images.

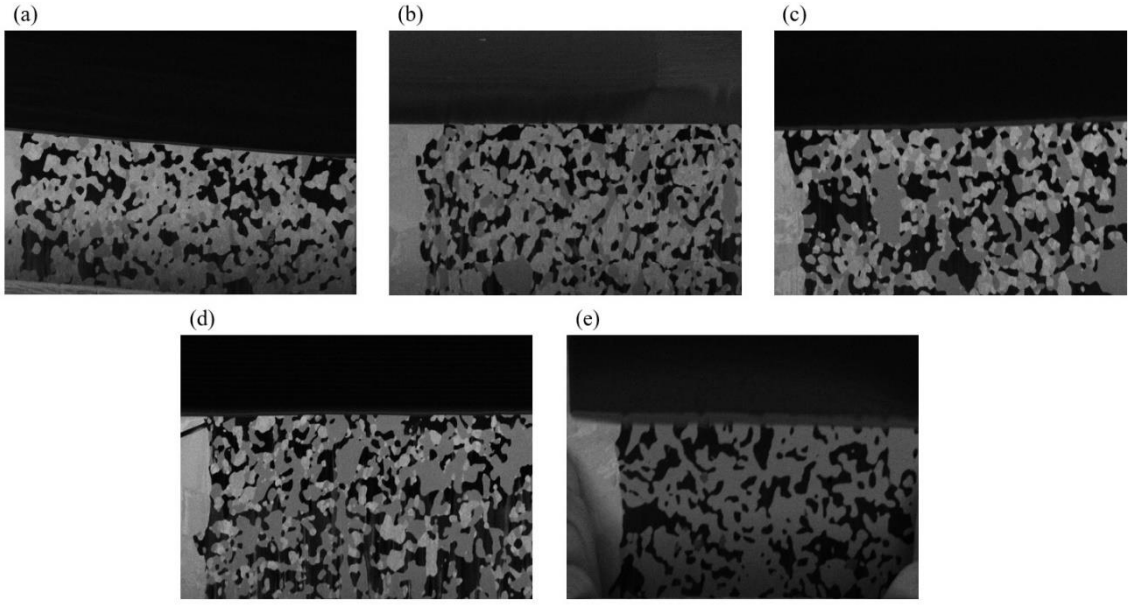

Fig. 3-3 Images from FIB-SEM.
The volume ratio of LSCF:GDC = (a) 20:80, (b) 30:70, (c)50:50, (d)70:30 and (e) 100:0 %.
(Black: pore, dark gray: LSCF, light gray: GDC).

Sequential images with a slice pitch of 49.6 nm and a pixel size of 25.9 nm were captured for all LSCF-GDC composite cathodes. Table 3-1 and Fig. 3-4 show the condition of the reconstruction and the images of 3D reconstructed microstructures, respectively.

Table 3-1 Condition of reconstruction.

LSCF:GDC	Number of pixels ($x \times y$)	Number of slices in z direction	Sample volume size
20:80 vol. %	900×336	305 slices	3075.08 μm^3
30:70 vol. %	840×336	297 slices	2791.16 μm^3
50:50 vol. %	900×340	301 slices	3066.62 μm^3
70:30 vol. %	900×336	300 slices	3021.65 μm^3
100:0 vol. %	672×376	300 slices	2525.60 μm^3

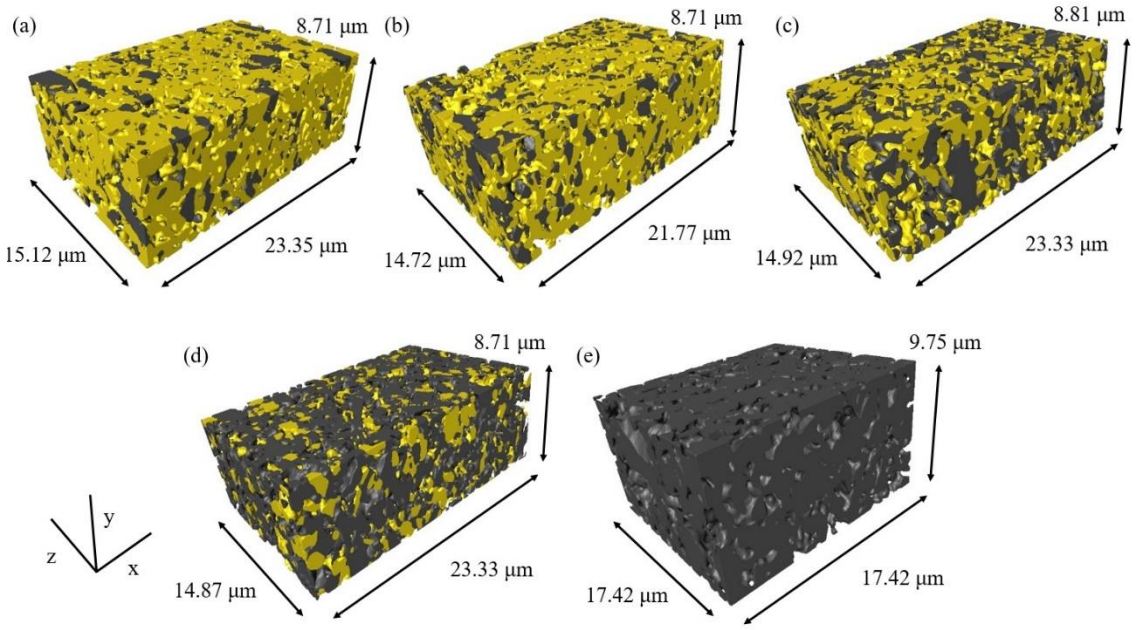

Fig. 3-4 3D reconstructed microstructures of LSCF-GDC composite cathodes.
The volume ratio of LSCF:GDC = (a) 20:80, (b) 30:70, (c) 50:50, (d) 70:30, and (e) 100:0 %.
(Yellow: GDC, dark gray: LSCF).

For the parameters calculation, 25.9 nm of pixel size and 49.6 nm of slice pitch were increased to 50 nm of voxel size in order to fix the resolution for all the samples. Figure 3-5 represents the method how the voxel size is increased when the voxel size is doubled. For example, if the number of "A" phase inside the original four voxels is the largest, "A" component is selected as the representative phase of the expanded 1 voxel.

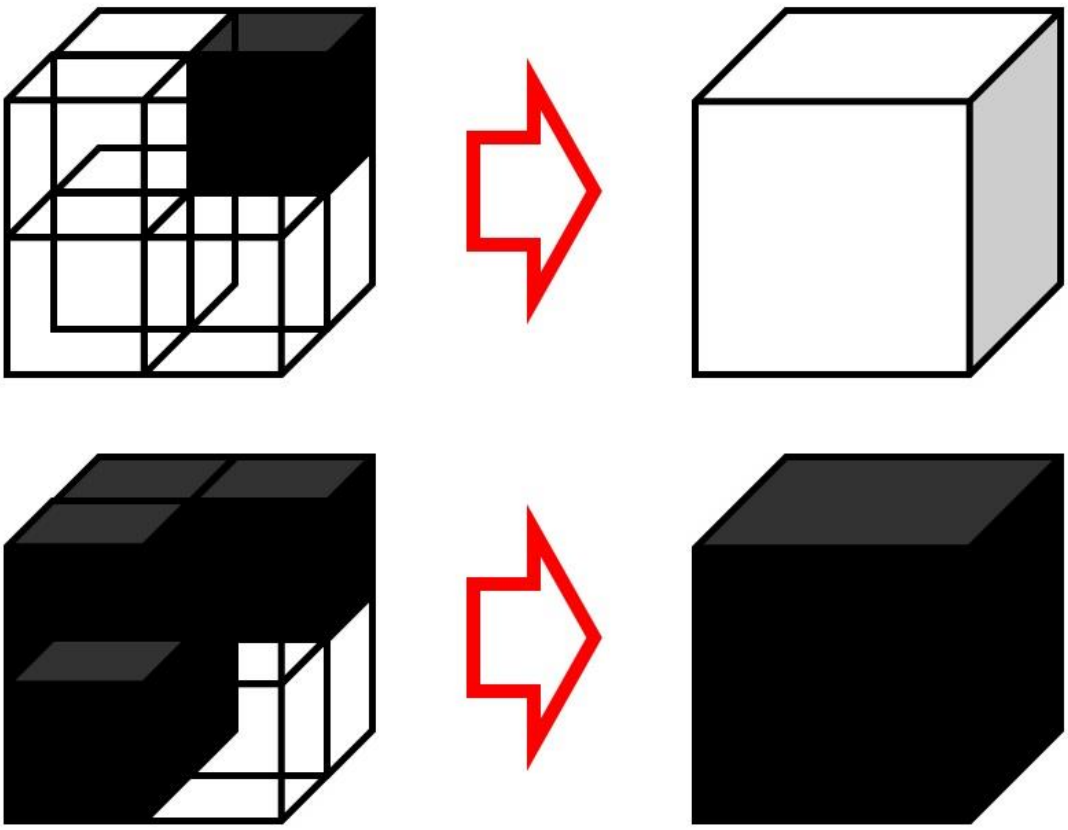

Fig. 3-5 Phase selection in the voxel expansion process.

For the LSCF-GDC composite cathode, two reaction mechanisms are considered for the electrochemical reaction, i.e. LSCF surface reaction and TPB reaction. Figure 3-6 represents both LSCF surface area densities and active TPB densities together with polarization resistances at OCV. Closed symbols represent polarization resistances and open symbols correspond to the LSCF surface area densities and active TPB densities. As can be seen in Fig. 3-6 (a), the LSCF surface area density shows monotonous decrease with the decrease of LSCF volume fraction. However, the fact that minimum polarization resistance is obtained at a volume ratio of LSCF:GDC = 30:70 % reveals that cathode performance is drastically enhanced regardless of the reduction of LSCF surface area. This implies that LSCF surface reaction alone cannot explain the reaction of LSCF-GDC composite cathodes as a single reaction mechanism. On the other hand, a volume ratio of LSCF:GDC = 50:50 % shows the highest active TPB density as shown in Fig. 3-6 (b), even LSCF:GDC = 30:70 vol. % shows the minimum polarization resistance. Thus, TPB reaction alone also cannot explain the cathode performance as a single reaction mechanism.

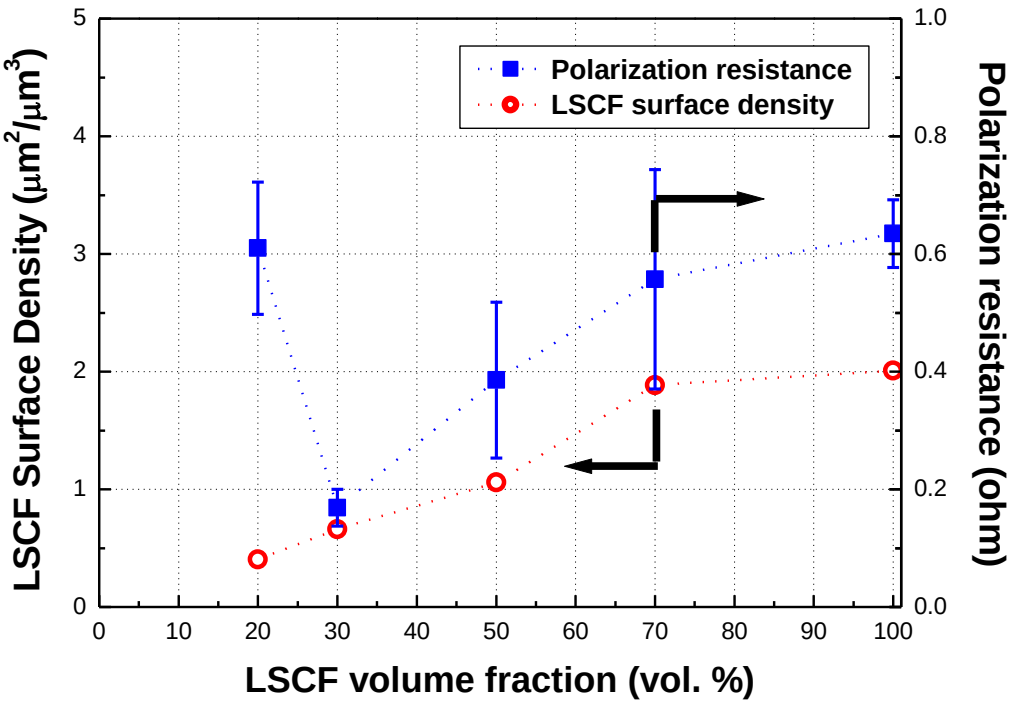

(a) LSCF surface area densities with polarization resistances.

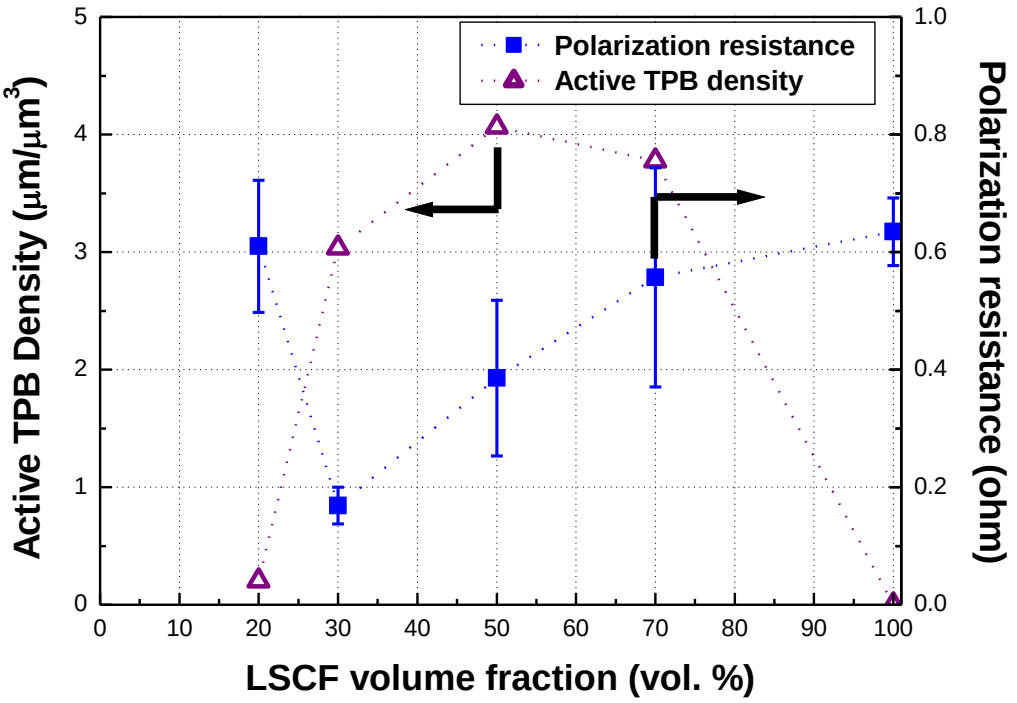

(b) Active TPB densities with polarization resistances.

Fig. 3-6 Comparison between reaction areas and polarization resistances of LSCF-GDC composite cathodes.

The other microstructure parameters are shown in Table 3-2. It is observed that the phase connectivity shows large variation against volume fraction. The phase connectivity deteriorates when the volume fraction becomes smaller than 30 % for each phase. The porosity increases with the decrease of GDC, and a volume ratio of LSCF:GDC = 100:0 % shows the lowest porosity. It is considered that grain growth of LSCF is suppressed by GDC in the composite.

Table 3-2 Microstructure parameters from FIB-SEM reconstruction.

LSCF:GDC =	20:80 vol.%	30:70 vol.%	50:50 vol.%	70:30 vol.%	100:0 vol.%
Porosity	32.03 %	33.88 %	38.76 %	42.47 %	31.16 %
GDC phase volume fraction	54.16 %	47.89 %	31.04 %	13.60 %	-
LSCF phase volume fraction	13.81 %	18.73 %	30.2 %	43.93 %	68.84 %
GDC connectivity	99.94 %	99.70 %	97.36 %	6.670 %	-
LSCF connectivity	10.91 %	58.34 %	98.19 %	99.64 %	99.99 %

Not only the surface area density and TPB density, but also effective ionic conductivity is one of the important parameters which affects the cathode performance. Tortuosity factor τ is defined as:

$$\sigma_{\text{effective}} = \frac{\varepsilon}{\tau}\sigma \tag{3.1}$$

where σ is the conductivity of the material, ε is the volume fraction. The effective ionic conductivity will increase with the decrease of tortuosity factor. It is considered that GDC which has higher ionic conductivity than LSCF contributes to the performance enhancement of LSCF-GDC composite cathode. Figure 3-7 represents the tortuosity factors of GDC and LSCF with the polarization resistances. The tortuosity factors which are out of range as the decrease of corresponding phases volume fractions were excluded in the graphs. As shown in Fig. 3-7, the volume fraction of each phase strongly affects the tortuosity factor. Cathode performance is enhanced with the decrease of GDC tortuosity factor. It is thus considered that improvement of effective ionic conductivity by GDC addition contributes to the performance enhancement. However, for the LSCF:GDC = 20:80 vol. %, disconnection of the electron path due to the decrease of LSCF phase connectivity caused the performance degradation as shown in Fig. 3-7.

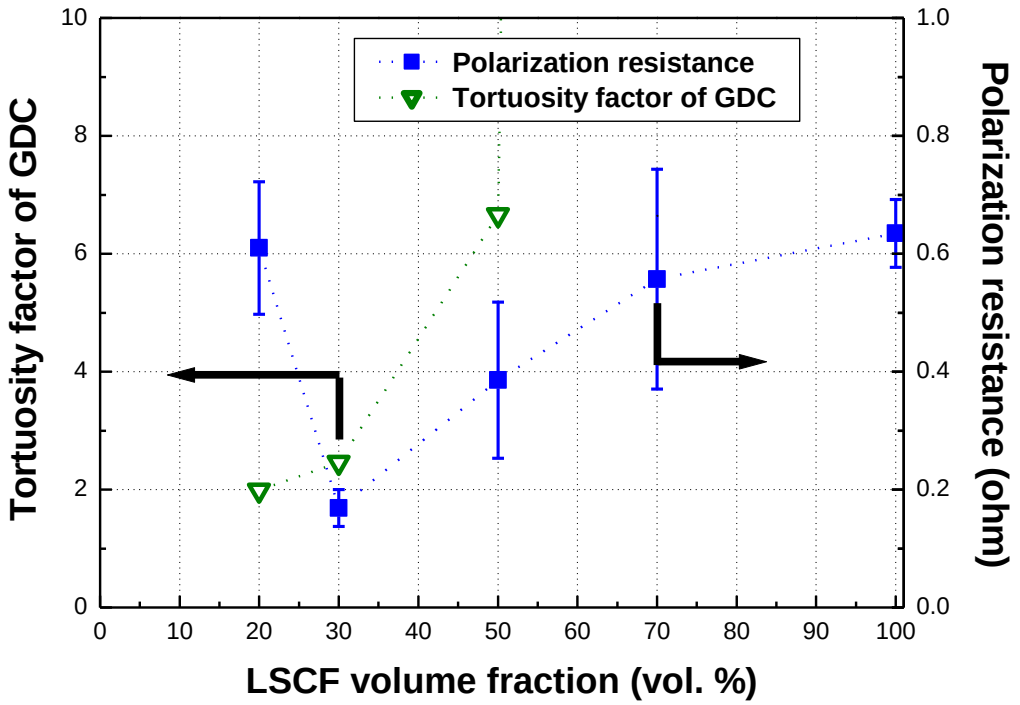

(a) GDC tortuosity factors with polarization resistances.

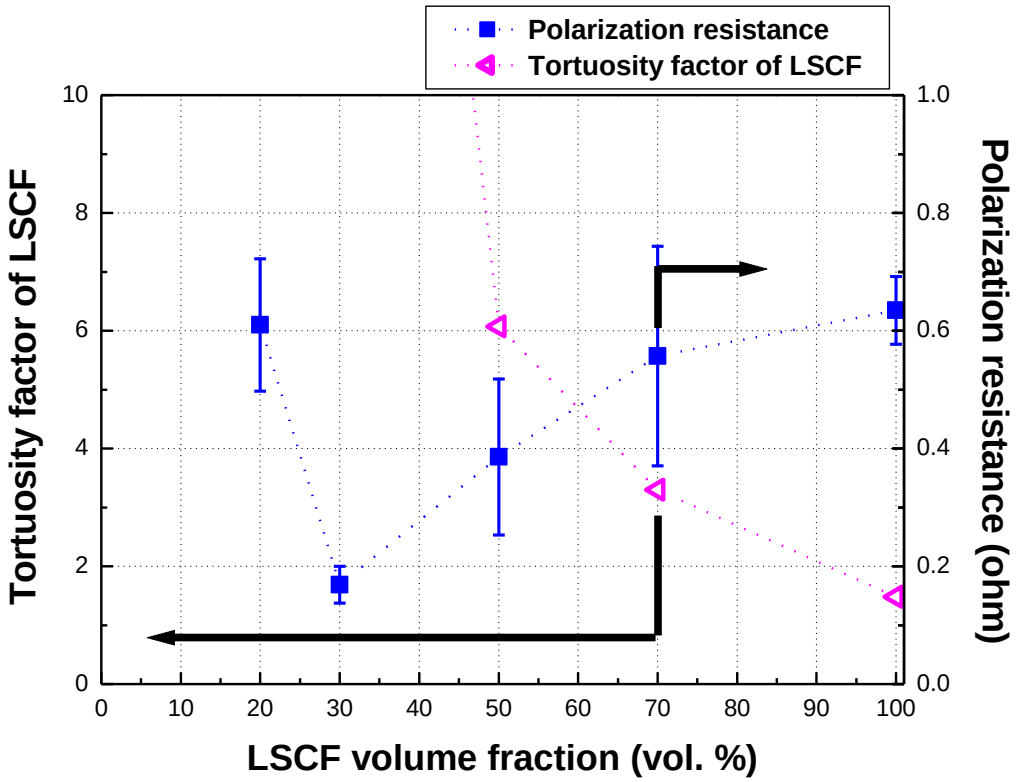

(b) LSCF tortuosity factors with polarization resistances.

Fig. 3-7 Comparison between tortuosity factors and polarization resistances of LSCF-GDC composite cathodes.

The volume size of the present samples are verified to check whether the present samples can considered as representative volume elements (RVEs). Microstructures were divided into three and four in *x*-direction, two in *y* and *z*-directions as introduced in Fig. 3-8. Microstructures which were divided into four in *x*-direction are not shown here. LSCF surface area densities and total TPB densities of each small volume were calculated in order to verify whether the volumes are sufficiently large or not to calculate microstructure parameters. Figure 3-9 shows the results.

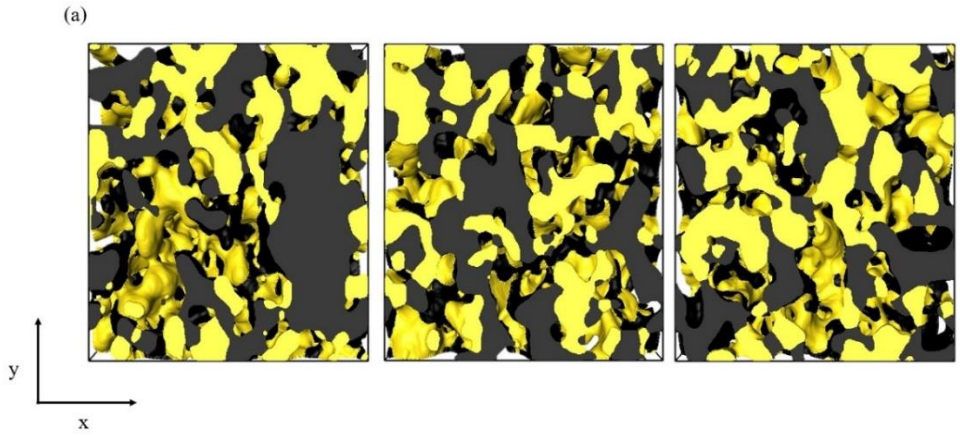

(a) Dividing in *x*-direction.

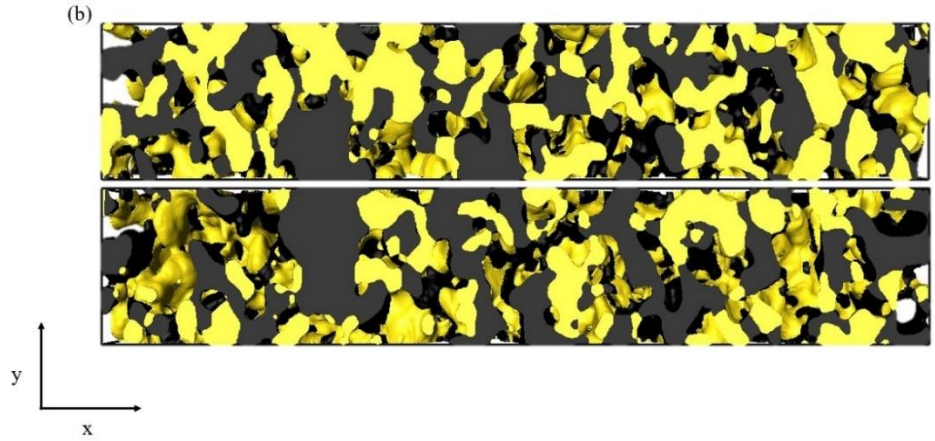

(b) Dividing in *y*-direction.

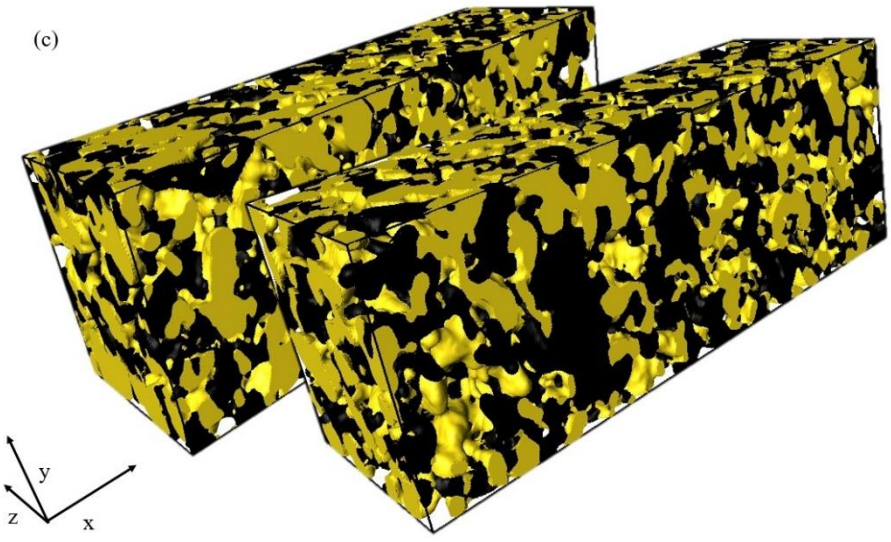

(c) Dividing in *z*-direction.

Fig. 3-8 Divided microstructures to verify representative volume elements for LSCF:GDC

= 50:50 vol. %.

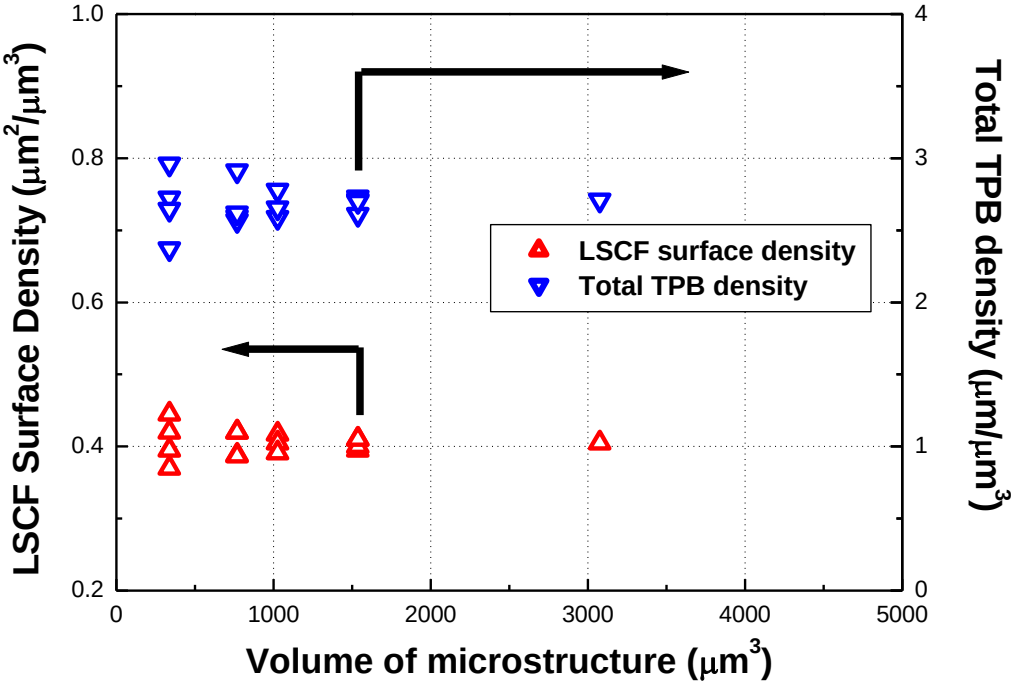

(a) LSCF:GDC = 20:80 vol. %.

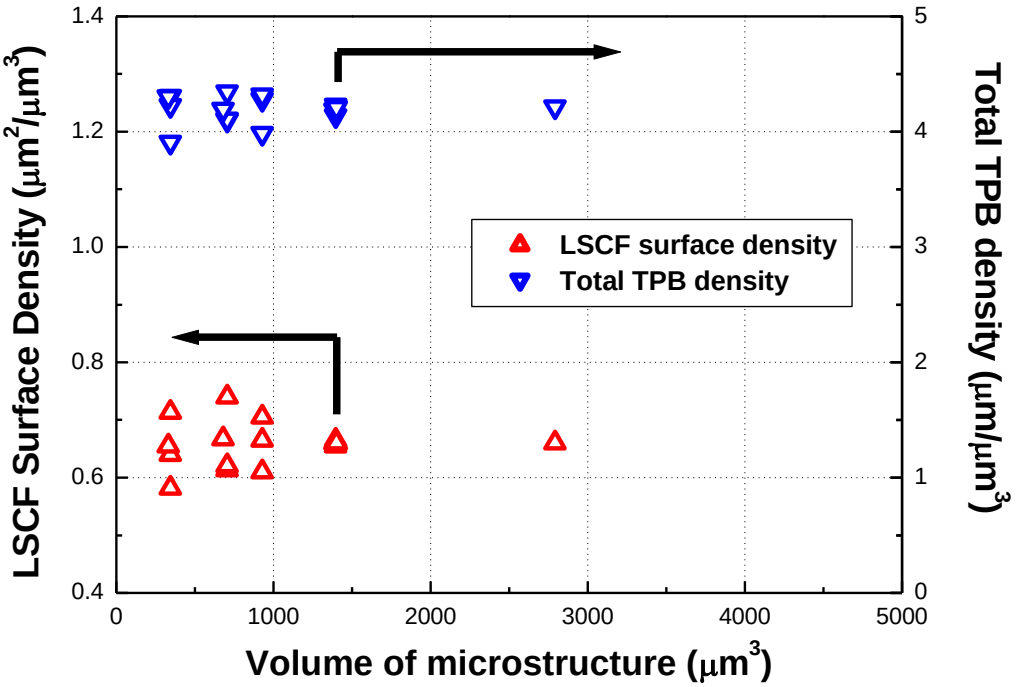

(b) LSCF:GDC = 30:70 vol. %.

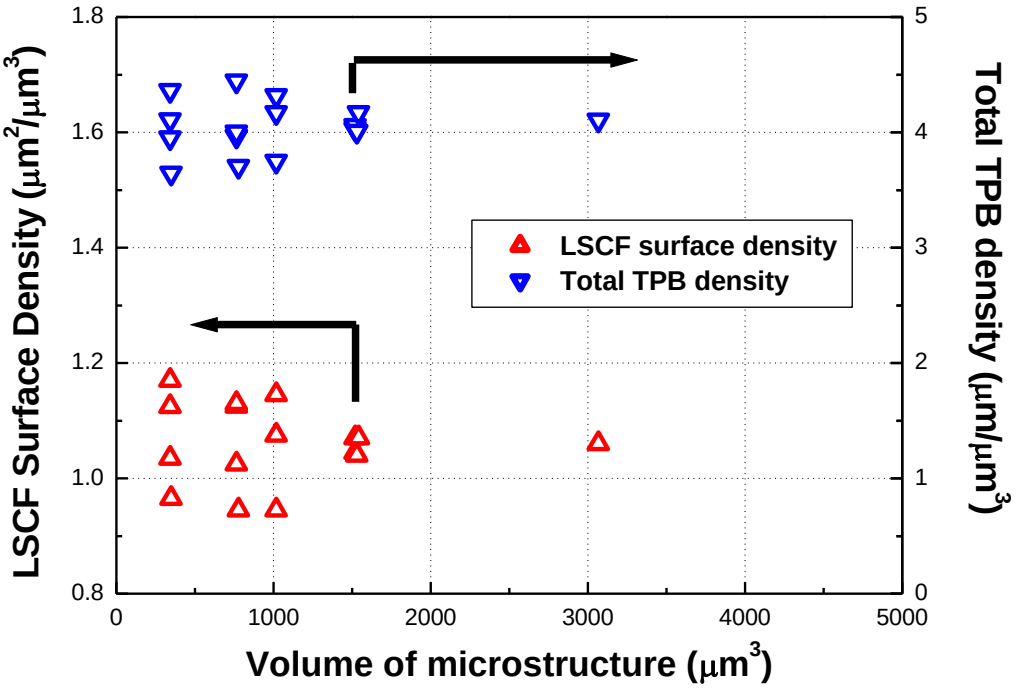

(c) LSCF:GDC = 50:50 vol. %.

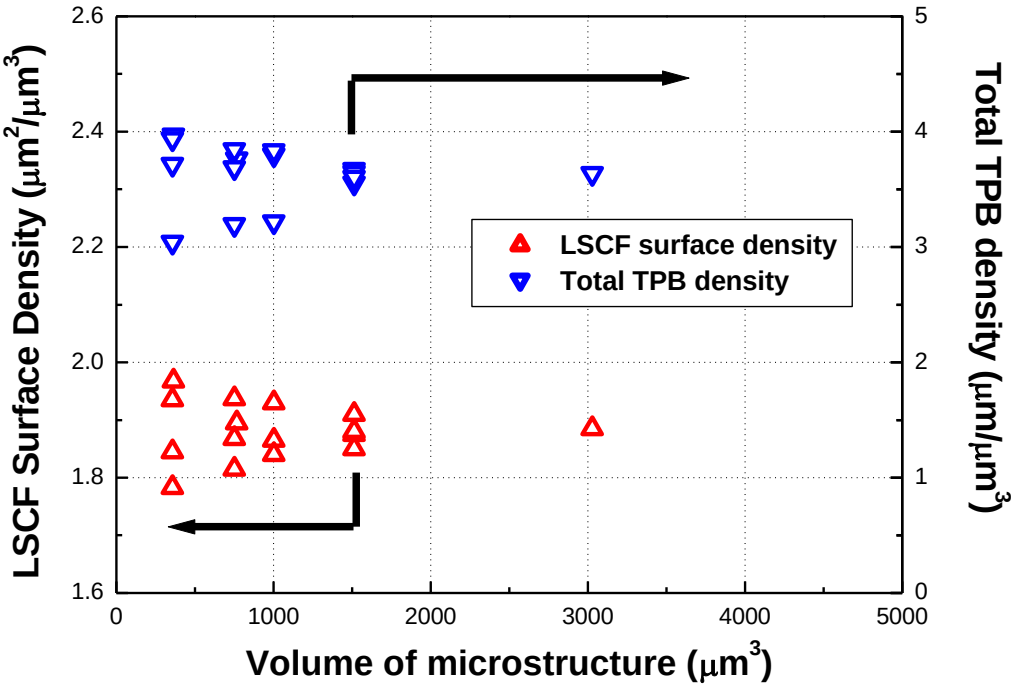

(d) LSCF:GDC = 70:30 vol. %.

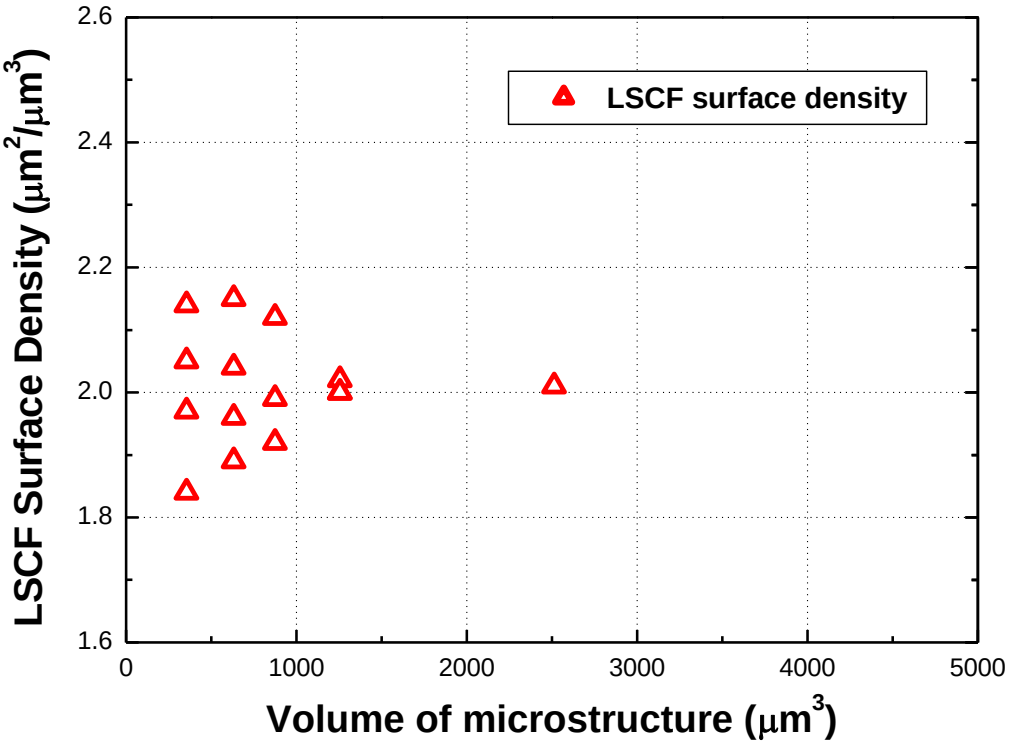

(e) LSCF:GDC = 100:0 vol. %.

Fig. 3-9 LSCF surface area density and total TPB density for LSCF:GDC = (a) 20:80, (b) 30:70, (c) 50:50, (d) 70:30, and (e) 100:0 vol. %.

Symbols which are located in the most right indicate the results of the microstructure parameters calculated by largest volume samples. As can be seen in Fig. 3-9, the values of LSCF surface densities and total TPB densities are converged on the right position for all cases. Therefore, it is considered that the original reconstructed microstructure can be considered as representative microstructure volume element to calculate the microstructure parameters.

3.2 Numerical Simulation

In this section, electrochemical reaction of LSCF-GDC composite cathodes with 30:70, 50:50, 70:30 and 100:0 vol. % were simulated by a Lattice Boltzmann Method (LBM). The case of LSCF:GDC = 20:80 vol. % was excluded because it did not converge due to the deterioration of electron path from the current collector to the electrolyte caused by the lowest LSCF phase connectivity.

3.2.1 Computational Domain

As introduced in Chap. 2, governing equations were solved by LBM. Due to the limitation of computational resources, resolution of 100 nm was used for the LBM simulation. Computational domains were elongated to 25 μm in the electrode thickness direction by mirroring the original microstructures. Then, porous LSCF current collection layer of 10 μm was additionally attached at the end of the domain in order to obtain identical condition with the experiment. Dense electrolyte of 0.5 μm and dense current collection layer were added to the LSCF porous current collector. Computational domains are shown in Fig. 3-10.

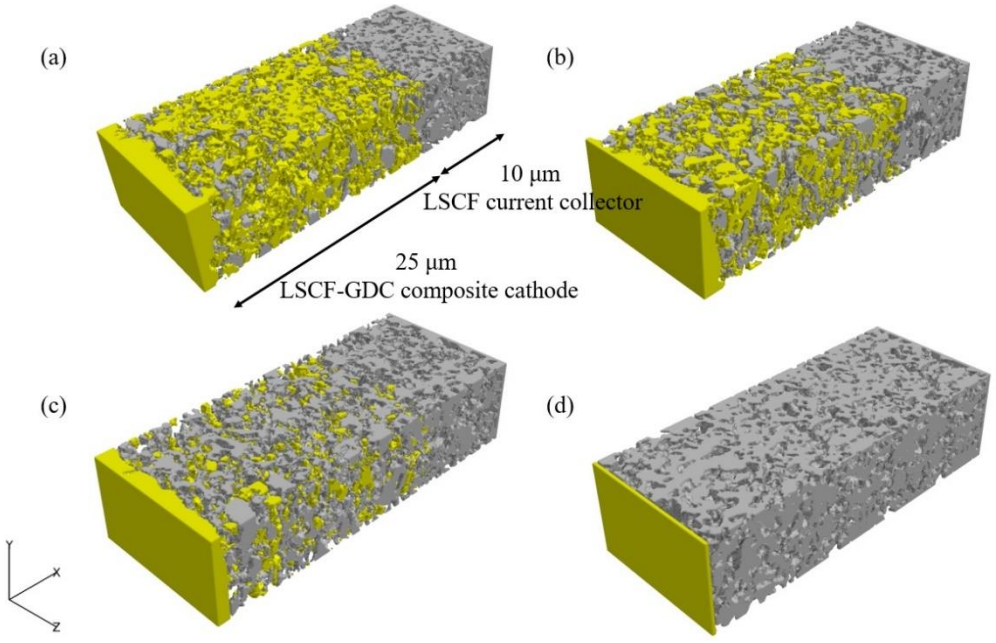

Fig. 3-10 Computational domains for LBM simulation with LSCF:GDC = (a) 30:70, (b) 50:50, (c) 70:30 and (d) 100:0 vol. %.

Isolated phases which do not connect to any boundary of the domain were considered as non-conducting phases in the simulation. There are unknown phases which appear at the boundaries but do not directly connect to the electrolyte and to the current collector. In the present study, two cases

for the unknown phase are considered. First, unknown phase is considered as a non-conducting phase. Second, the unknown phase is considered as a conducting phase. Figure 3-11 shows the unknown, the connected and the isolated phases of LSCF in the computational domain of LSCF:GDC = 30:70 vol. %.

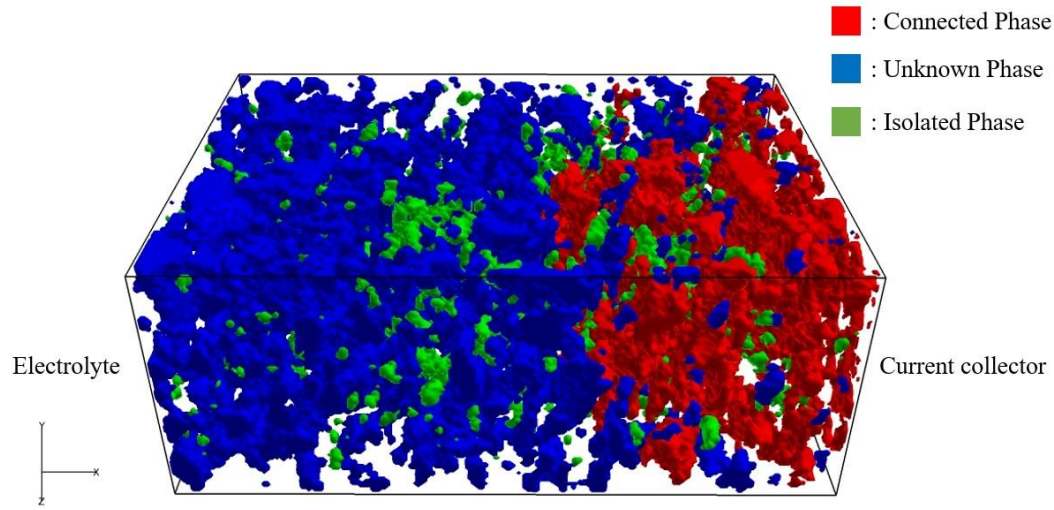

Fig. 3-11 Phases of LSCF in the LSCF:GDC = 30:70 vol. %.

3.2.2 Contributions from Two Reaction Mechanisms

In the present numerical simulation, two reaction mechanisms, i.e. LSCF surface reaction and TPB reaction, were considered as introduced in Chap. 2. Exchange current density for LSCF surface reaction was fitted using the experimental overpotential result of pure LSCF. Equation (3-2) shows the exchange current density for the LSCF surface reaction.

$$i_{0,\text{surface}} = 1.66315 \times 10^5 P_{O_2}^{0.2} \exp\left(-\frac{Q}{RT}\right) \tag{3.2}$$

To verify the surface reaction model, predicted overpotentials for pure LSCF with the experimental data are shown in Table 3-3. The simulation results show good agreement with the experimental data. This indicates that the surface reaction model works adequately for the pure LSCF case.

Table 3-3 Overpotential results for pure LSCF at different temperatures

Temperature	Experiment	Simulation
700°C	0.0198 V	0.0198 V
800°C	0.00680 V	0.00674 V

Exchange current density for the TPB reaction was chosen so that the prediction shows best agreement with the experimental overpotential results of all composite samples.

$$i_{0,\mathrm{TPB}} = 0.3968 P_{\mathrm{O_2}}^{0.2} \exp\left(-\frac{Q}{RT}\right) \tag{3.3}$$

In Fig. 3-12, the overpotential results of simulation for LSCF:GDC = 30:70, 50:50, 70:30, and 100:0 vol. % were compared with the experimental results. Here, unknown phase is considered as either conducting phase or non-conducting phase. The simulation results which consider only the surface reaction overpredict the experimental results as the LSCF surface area is decreased. The prediction can be greatly improved by introducing the TPB reaction. Therefore, it is considered that both surface and TPB reactions should be considered to explain the electrochemical reaction mechanisms of LSCF-GDC composite cathodes.

Simulations were also conducted for the cases in which the unknown phase is considered as a conducting phase or as a non-conducting phase. The results are shown in Fig. 3-12. The simulation overpotential results were improved when the unknown phase is considered as a connected phase. However, the discrepancy between the simulation and the experiment still remains especially for the cases of LSCF:GDC = 50:50 and 70:30 vol. %. It is considered that reason for this discrepancy can be partially attributed to the LSCF ionic conductivity which was used in the present study. The influence of ionic conductivities is shown in Fig. 3-13. The ionic conductivity proposed by Kudo et al. [108] which was used in the present study is larger than those from Refs. [44,120–122]. It can be considered that effect of GDC addition becomes more apparent by applying smaller LSCF ionic conductivity to the numerical simulation. Dependence of LSCF ionic conductivities on the numerical simulation will be investigated in the next chapter.

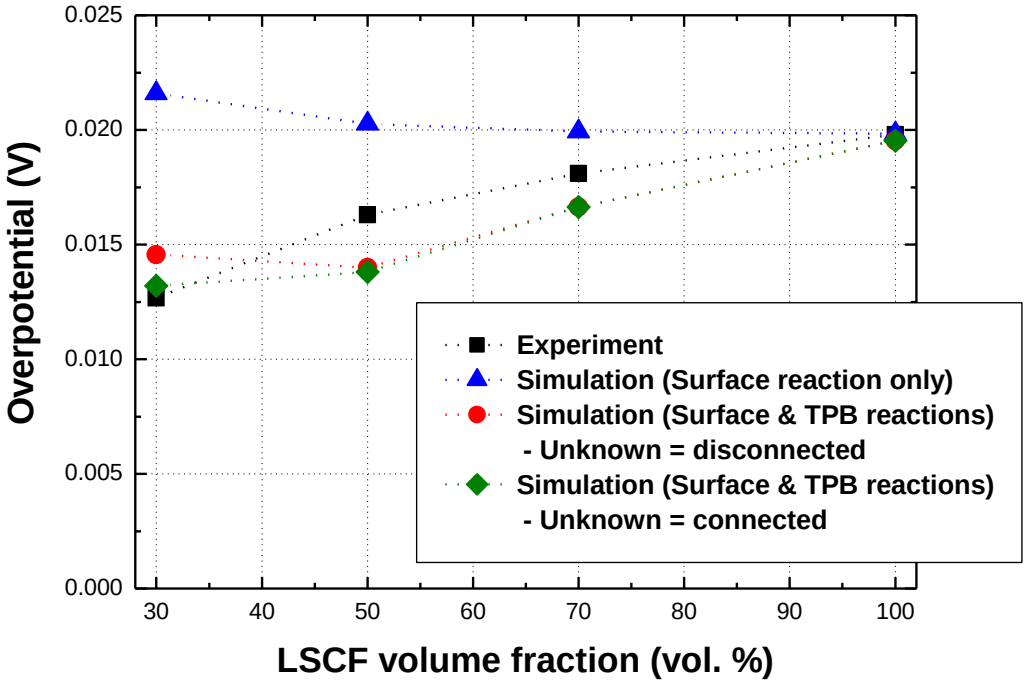

Fig. 3-12 Simulated overpotential results against LSCF volume fraction.

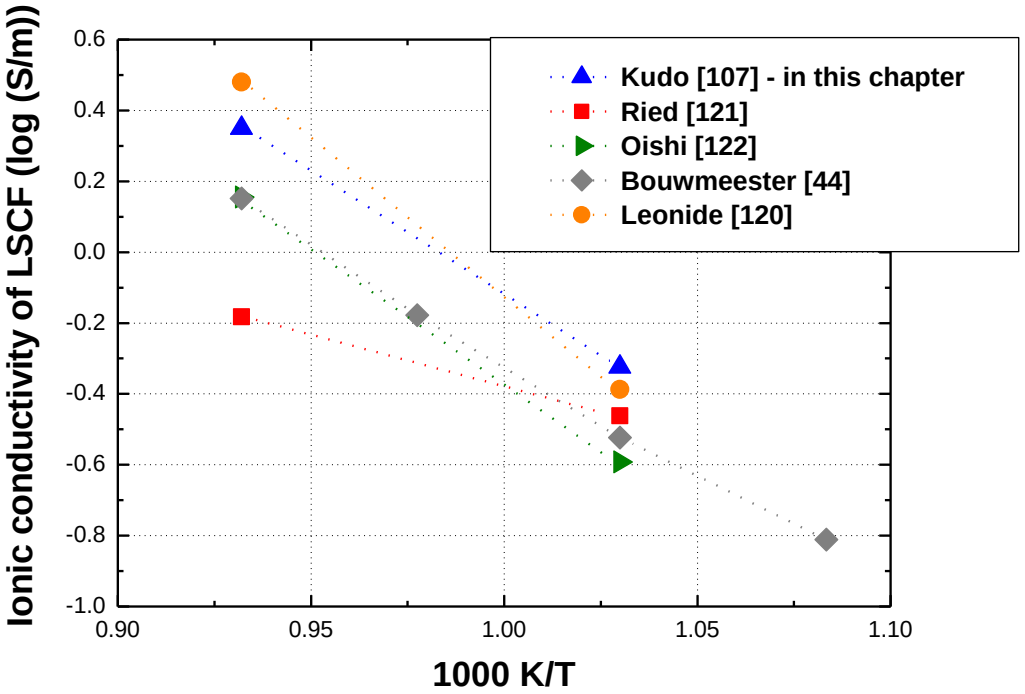

Fig. 3-13 Comparison of ionic conductivities from Refs. [44,120–122].

Figure 3-14 shows the reaction current distribution in the LSCF-GDC composite cathode. The blue lines represent the reaction current distribution arose from TPB reaction and the red lines represent reaction current distribution arose from both surface and TPB reactions. For the case of composites, significant contribution of TPB reactions can be seen. Contributions of surface and TPB reactions in the composite region of 25 μm are quantified in Fig. 3-15. The contribution of LSCF surface reaction is increased as the volume fractions of LSCF in the composite is increased. All LSCF-GDC composite cathodes show large contribution from TPB reaction. Especially, contribution of TPB reaction in LSCF:GDC = 30:70 vol. % cathode occupies 64.1 % of the total reaction current. It is considered that TPB reaction significantly contributes to LSCF-GDC cathode performance.

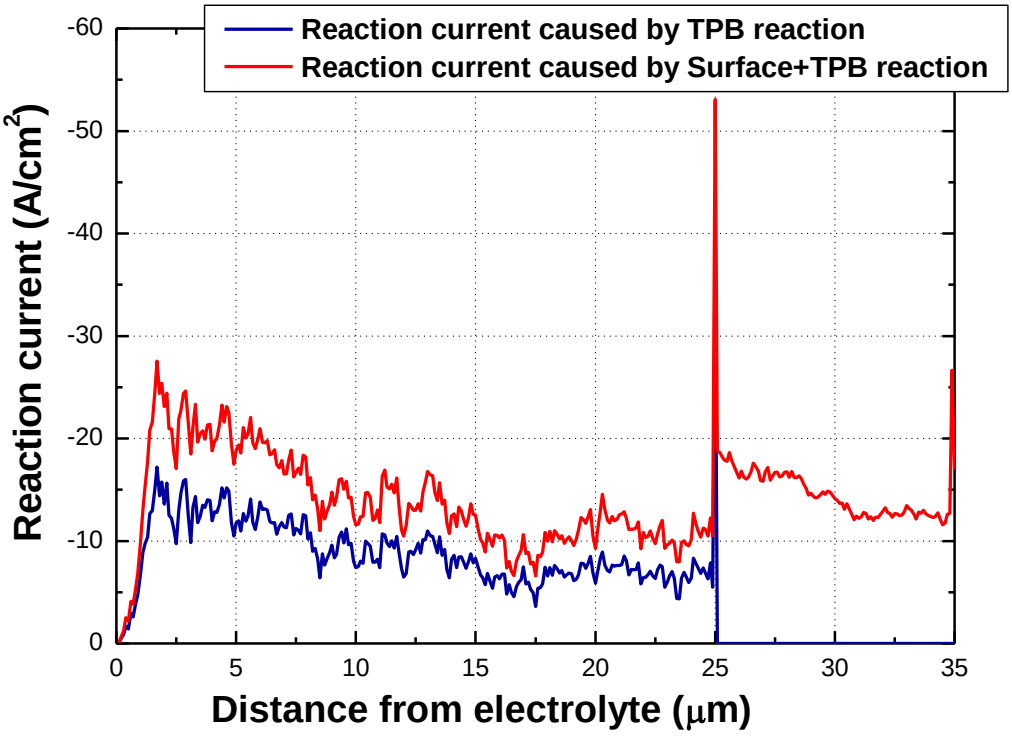

(a) LSCF:GDC = 30:70 vol. %.

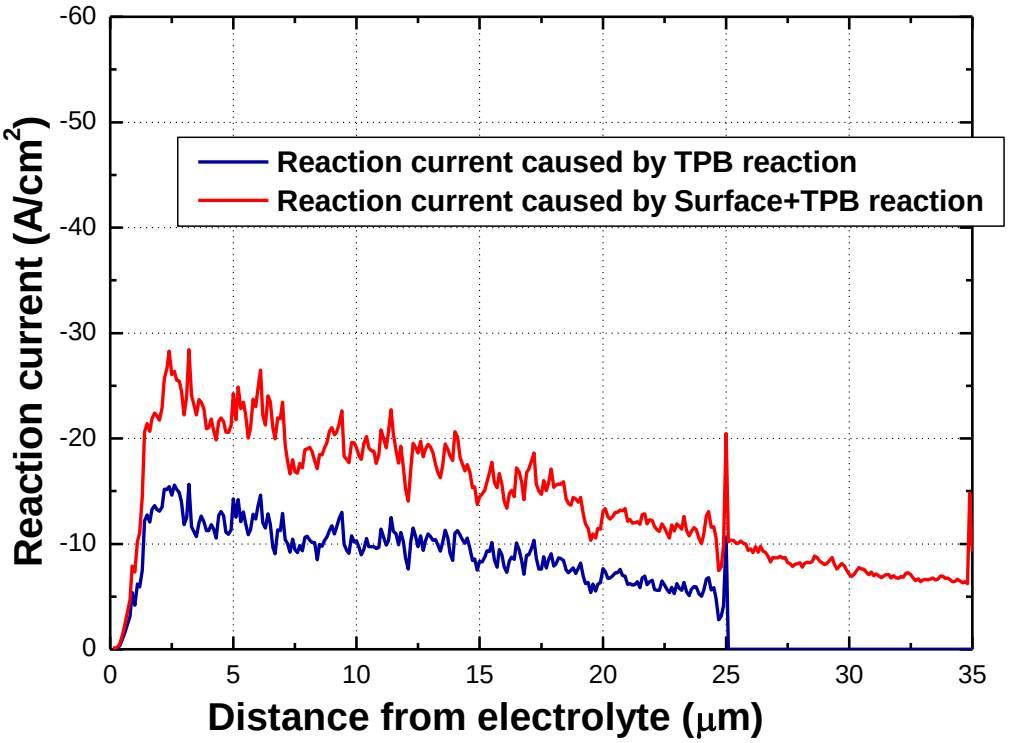

(b) LSCF:GDC 50:50 vol. %.

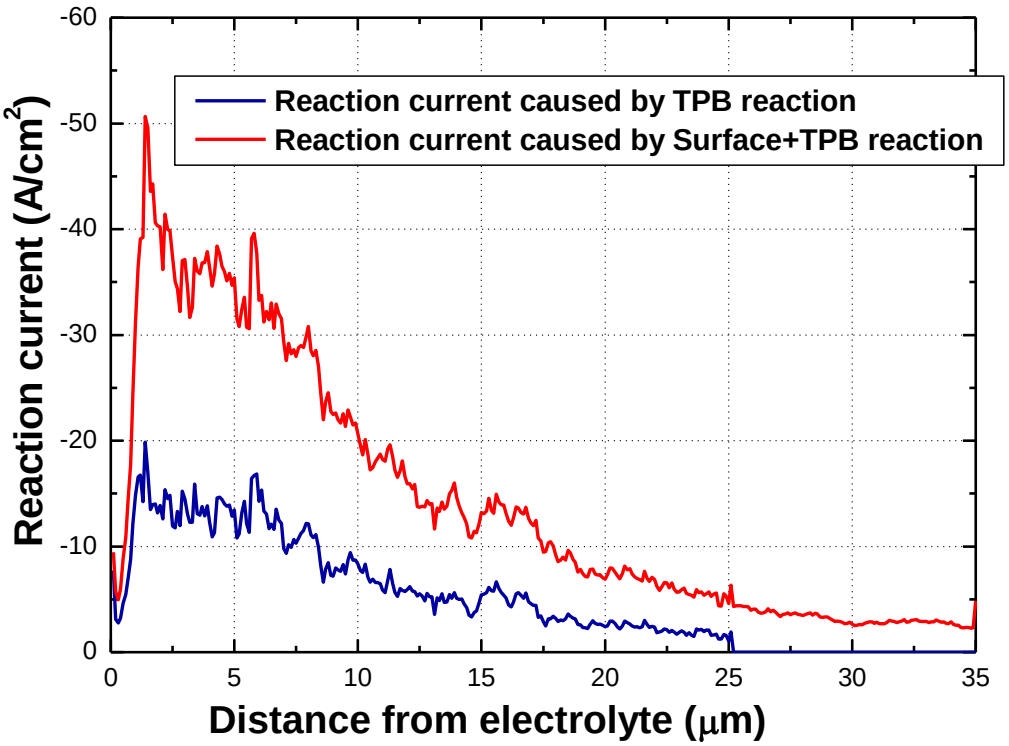

(c) LSCF:GDC = 70:30 vol. %.

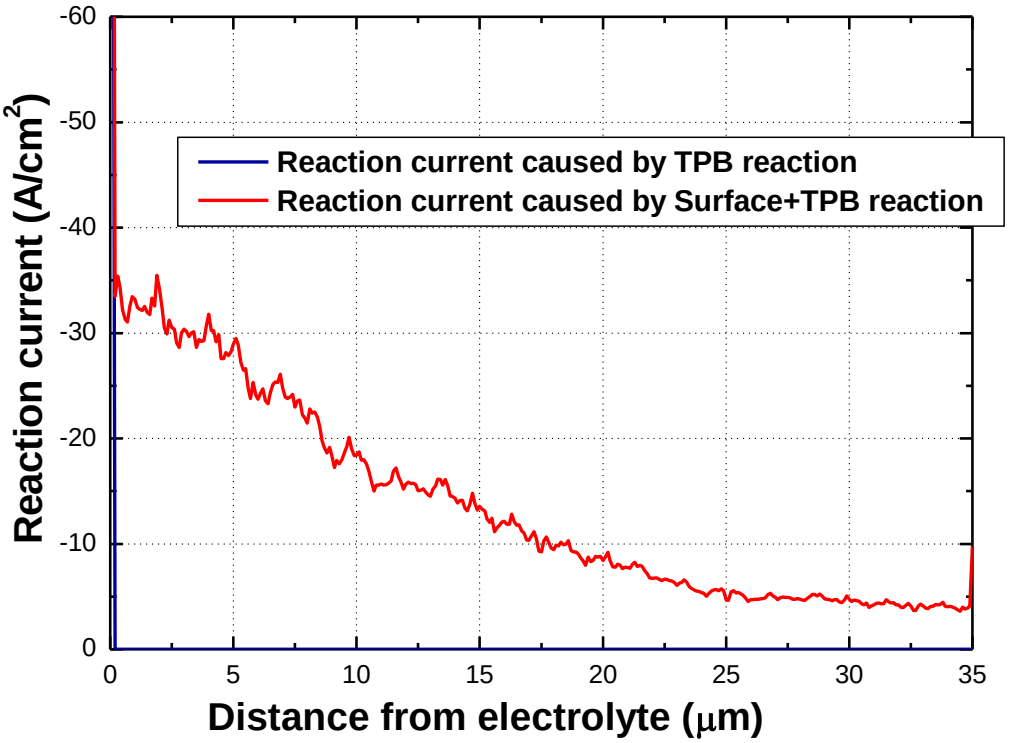

(d) LSCF:GDC = 100:0 vol. %.

Fig. 3-14 Reaction current distributions in the LSCF-GDC composite cathodes for LSCF:GDC = (a) 30:70, (b) 50:50, (c)70:30, and (d) 100:0 vol. %.

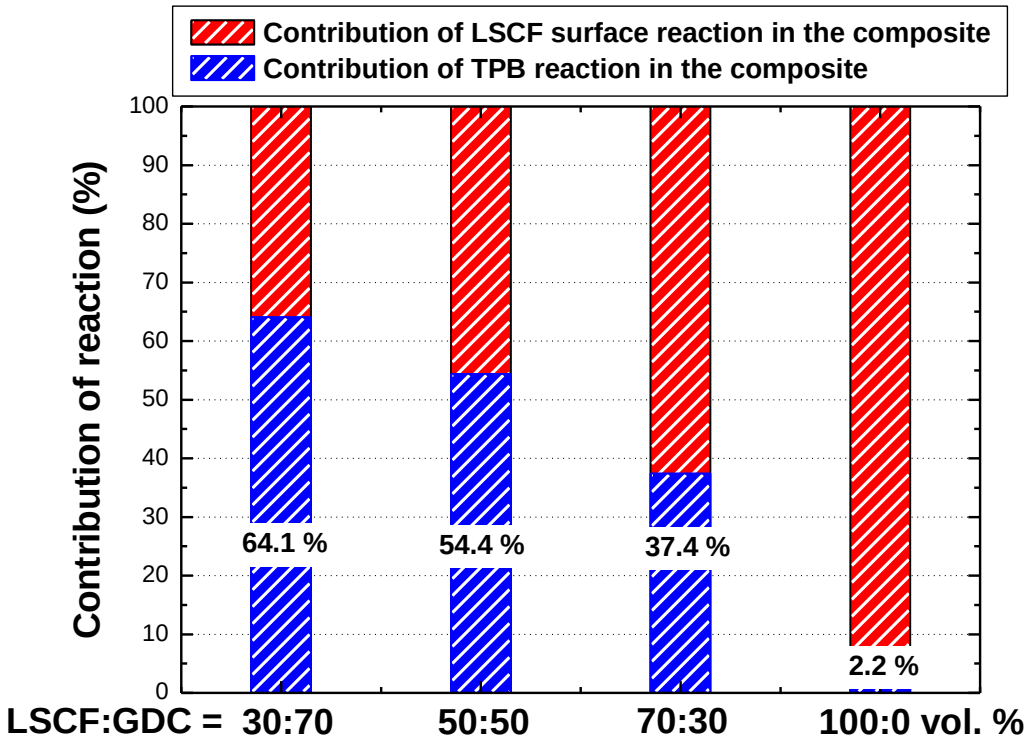

Fig. 3-15 Contribution of surface and TPB reactions in the composite of 25 μm.

3.2.3 Quantification of Ionic Conduction Losses

In this subsection, an electrochemical reaction ladder model as shown in Fig. 3-16 is introduced in order to investigate the contributions from ionic conduction and electrochemical reaction. Parallel activation overpotential resistances caused by the oxygen potential difference between the solid and the gas phases are connected to the electrolyte and the current collector. Ionic overptetential distributions against the distance from the electrolyte, *x*, are shown in Fig. 3-17. The ionic overpotential increased in the order of LSCF:GDC = 30:70, 50:50, 70:30 and 100:0 vol. %. The results show good accordance with the variations of cathode performance as shown in Section 3.3.1. It is considered that performance of LSCF-GDC composite cathode is enhanced by the reduction of local ionic conduction loss.

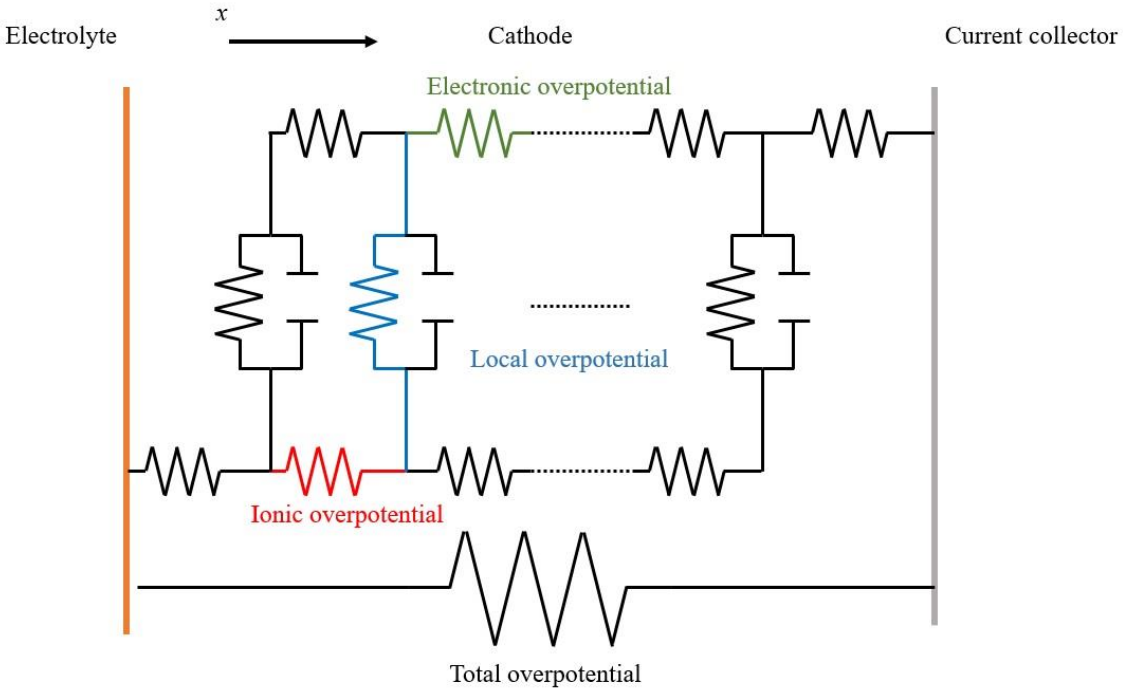

Fig. 3-16 An electrochemical reaction ladder model which is considered in the present numerical simulation.

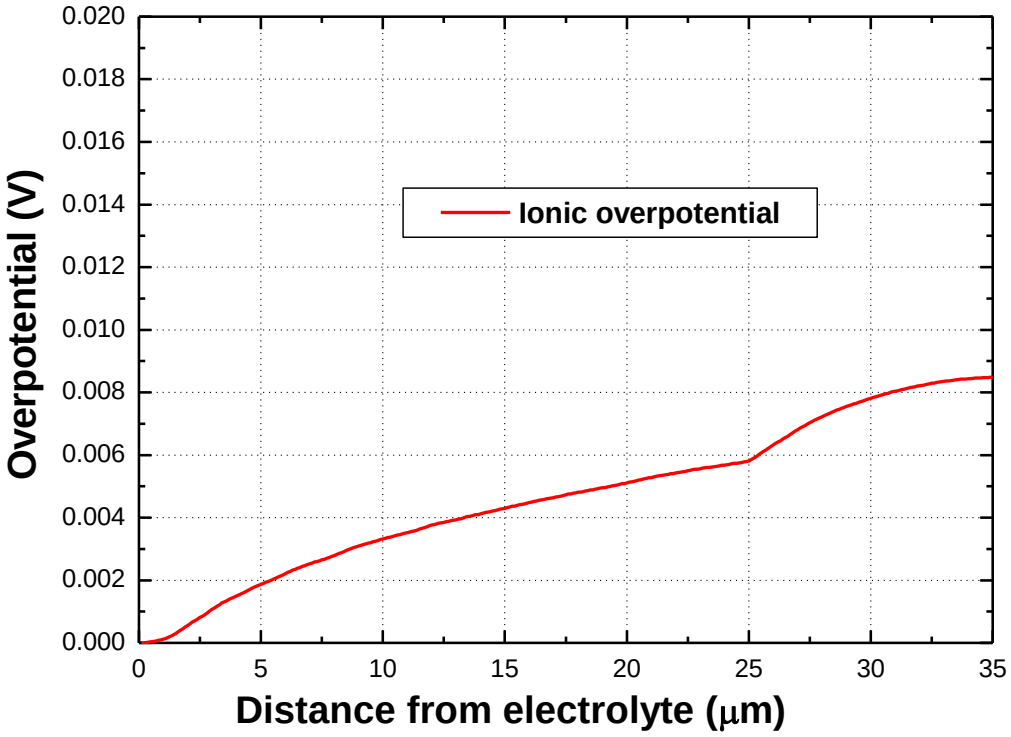

(a) LSCF:GDC = 30:70 vol. %.

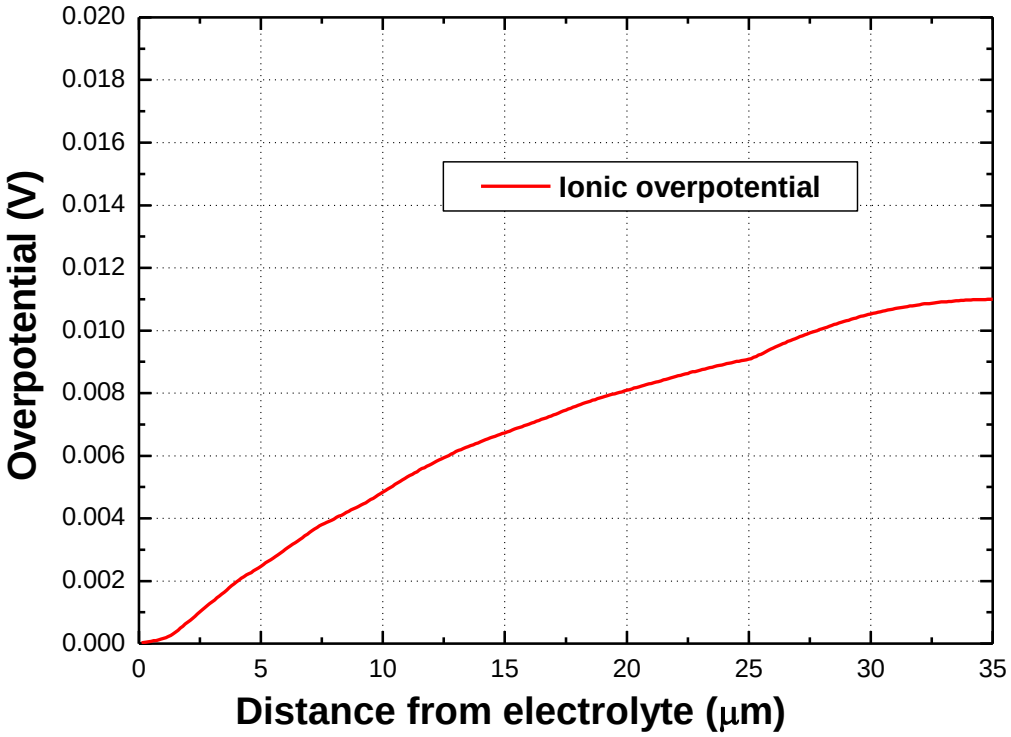

(b) LSCF:GDC = 50:50 vol. %.

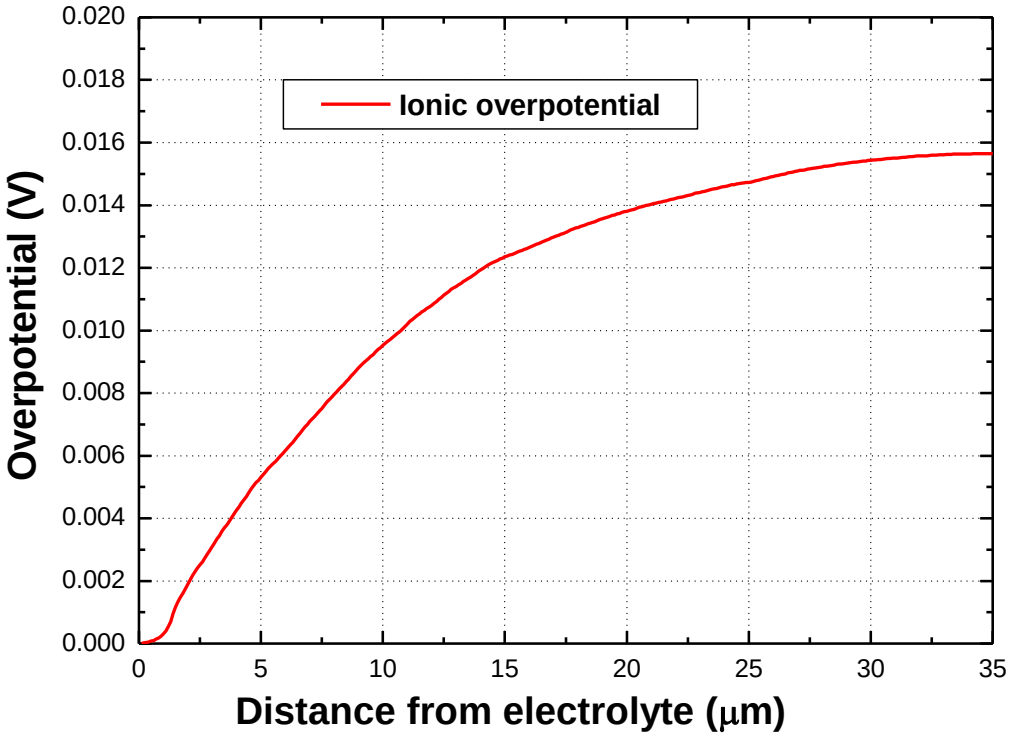

(c) LSCF:GDC = 70:30 vol. %.

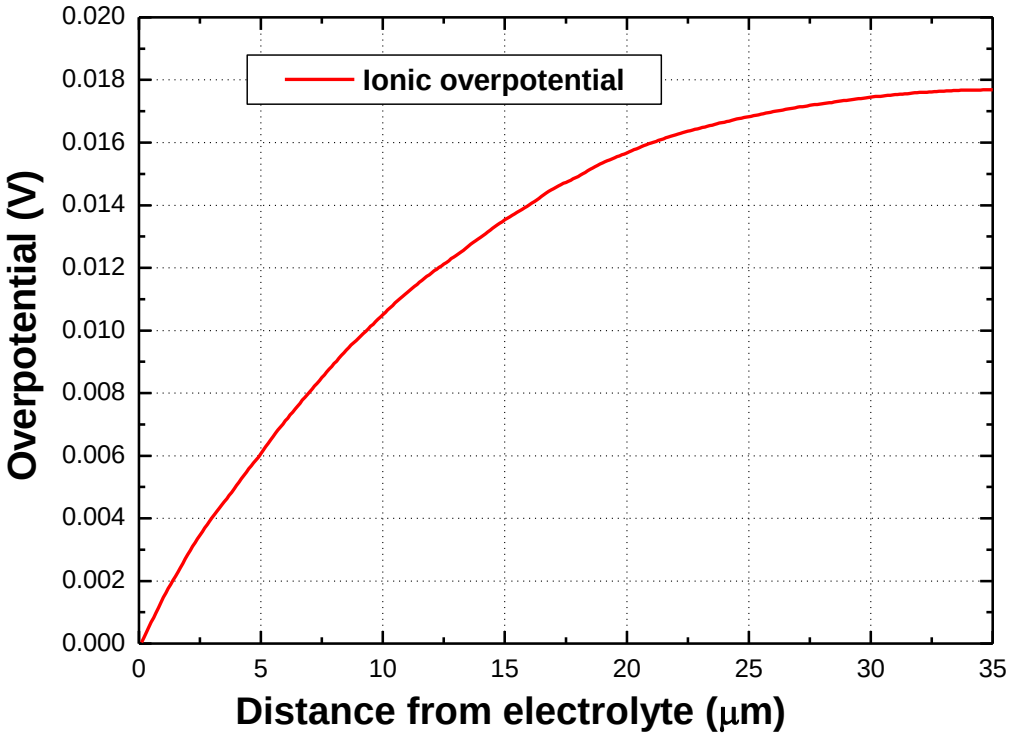

(d) LSCF:GDC = 100:0 vol. %.

Fig. 3-16 Ionic overpotential distributions in the composite cathode. The volume ratios of LSCF:GDC are (a) 30:70, (b) 50:50, (c) 70:30, and (d) 100:0 %.

3.2.4 Reactive Thickness

In this chapter, effective reaction thickness of LSCF-GDC composite cathodes were investigated. Figure 3-17 shows ionic and electronic current distributions when both unknown and connected phases are considered as conducting phases. For the cases of LSCF:GDC = 30:70 and 50:50 vol.%, exchange between the ionic and electronic currents continues far from the electrolyte to the current collector side compared to those in 70:30 and 100:0 vol.%. This indicates that the reactive thickness is elongated for LSCF:GDC = 30:70 and 50:50 vol.%.

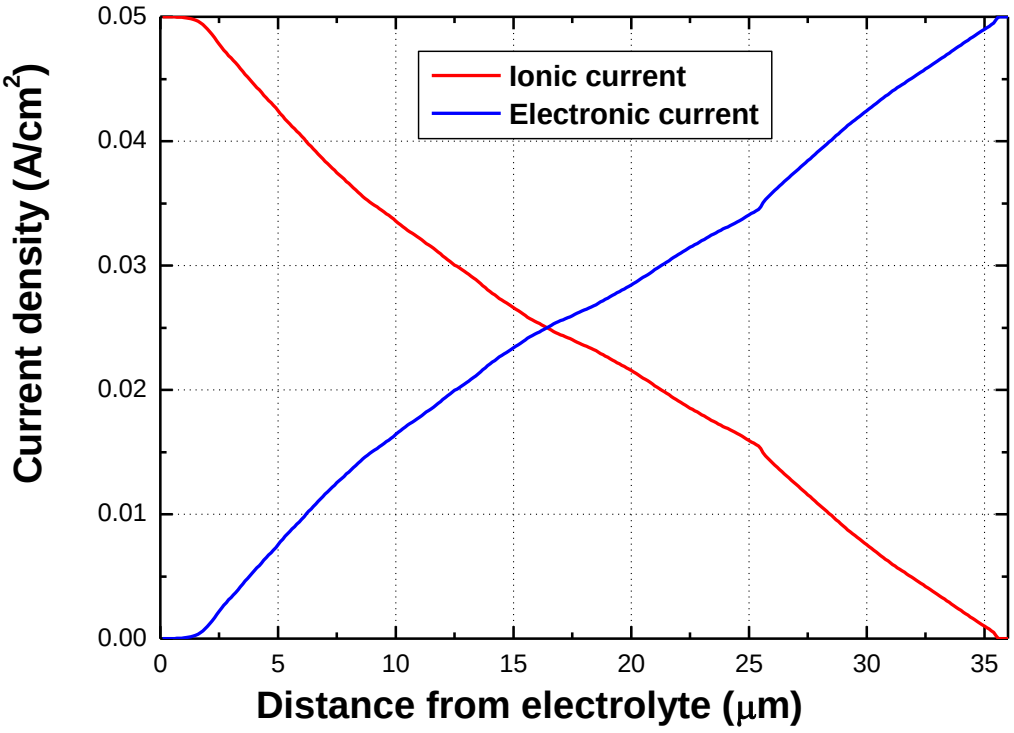

(a) LSCF:GDC = 30:70 vol. %.

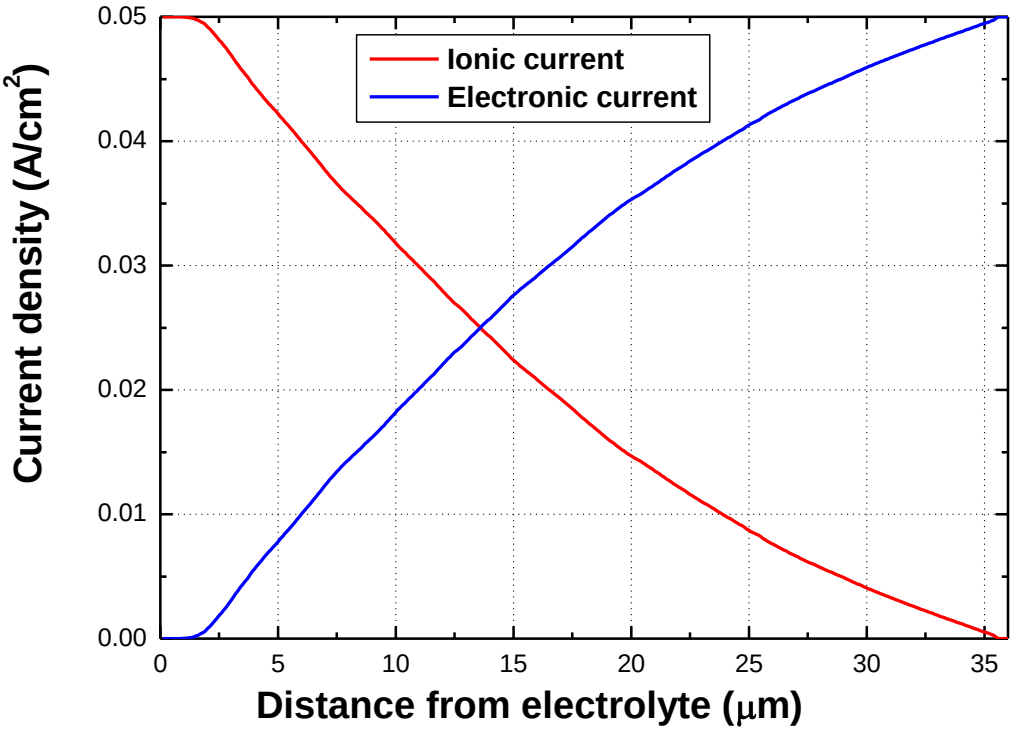

(b) LSCF:GDC 50:50 vol. %.

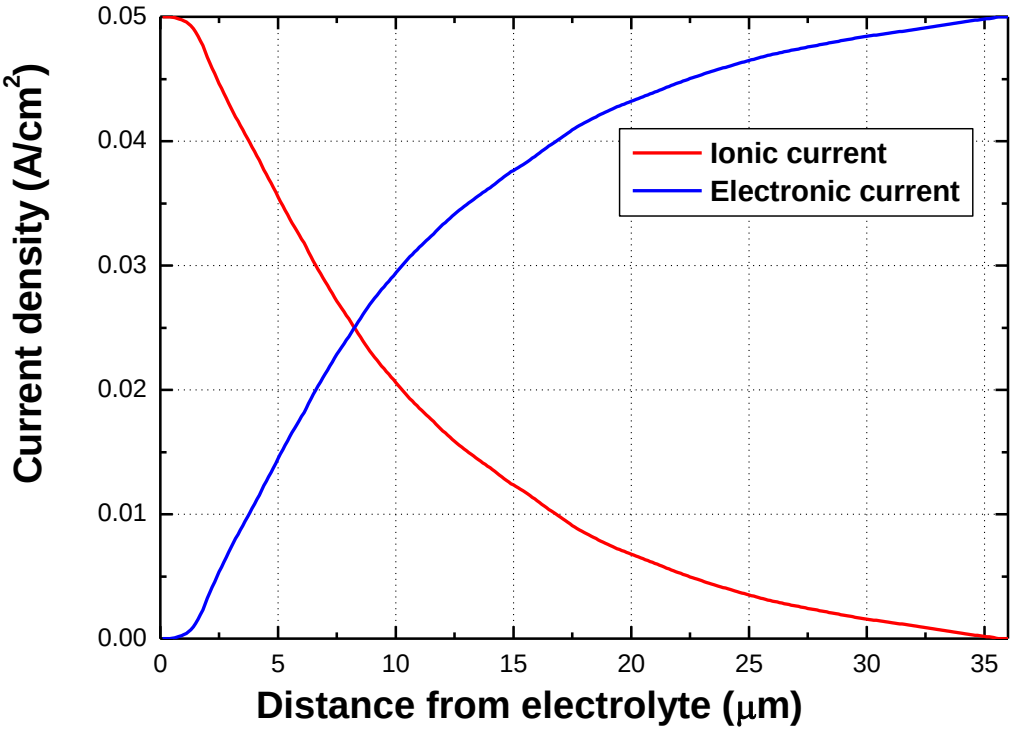

(c) LSCF:GDC = 70:30 vol. %.

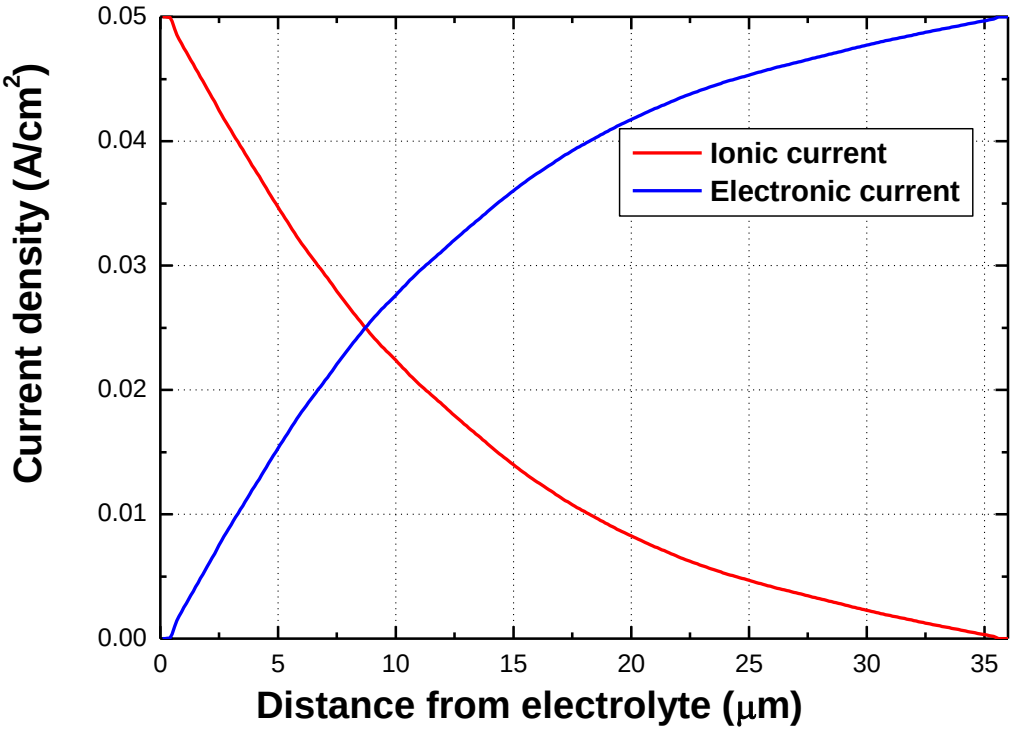

(d) LSCF:GDC = 100:0 vol. %.

Fig. 3-17 Current distributions in the LSCF-GDC composite cathodes for LSCF:GDC = (a) 30:70, (b) 50:50, (c)70:30, and (d) 100:0 vol. %.

Figure 3-18 represents the oxygen chemical potential distributions inside the LSCF phase. The dark blue part corresponds to the isolated LSCF in which oxygen chemical potential is in equilibrium with the gas phase. The oxygen chemical potential distributions become more uniform as GDC phase is increased. From the results above, it can be concluded that the increase of effective ionic conductivity due to the addition of GDC which has high ionic conductivity contributes to the performance enhancement of LSCF-GDC composite cathode by elongation of the reactive area. Optimal LSCF-GDC composite cathode thickness will be investigated in the next chapter.

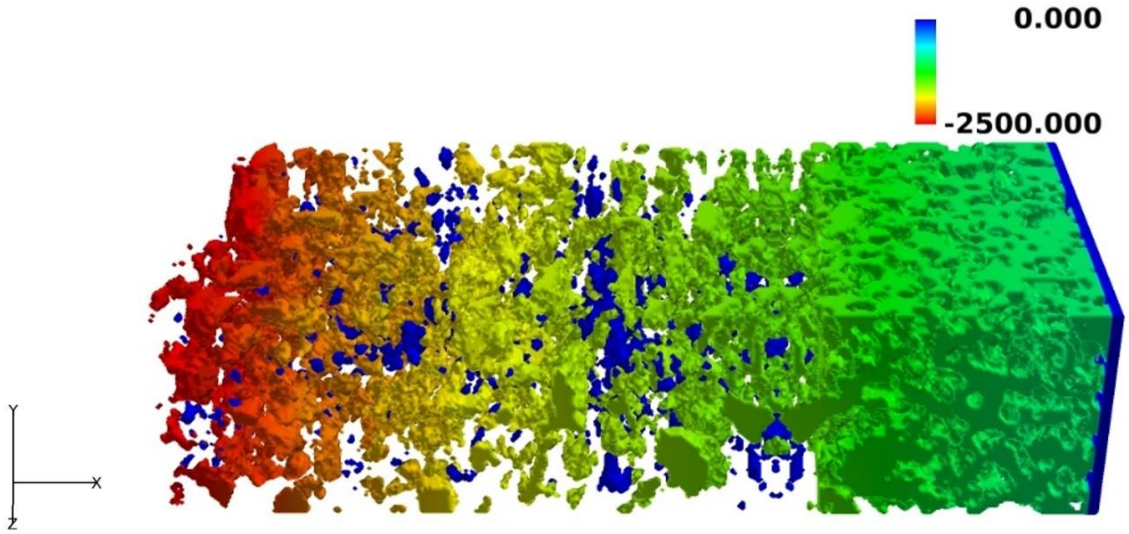

(a) LSCF:GDC = 30:70 vol. %.

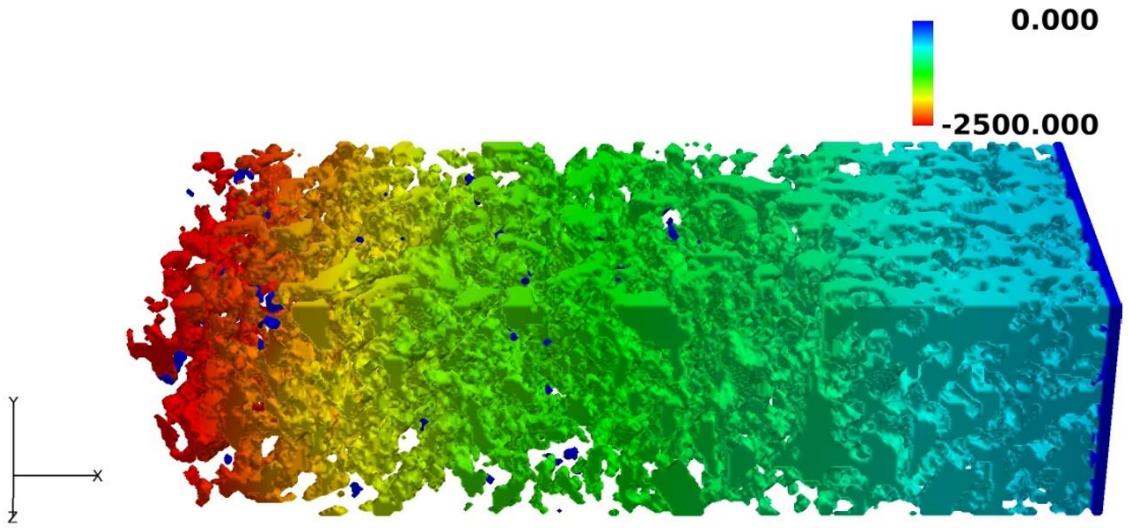

(b) LSCF:GDC = 50:50 vol. %.

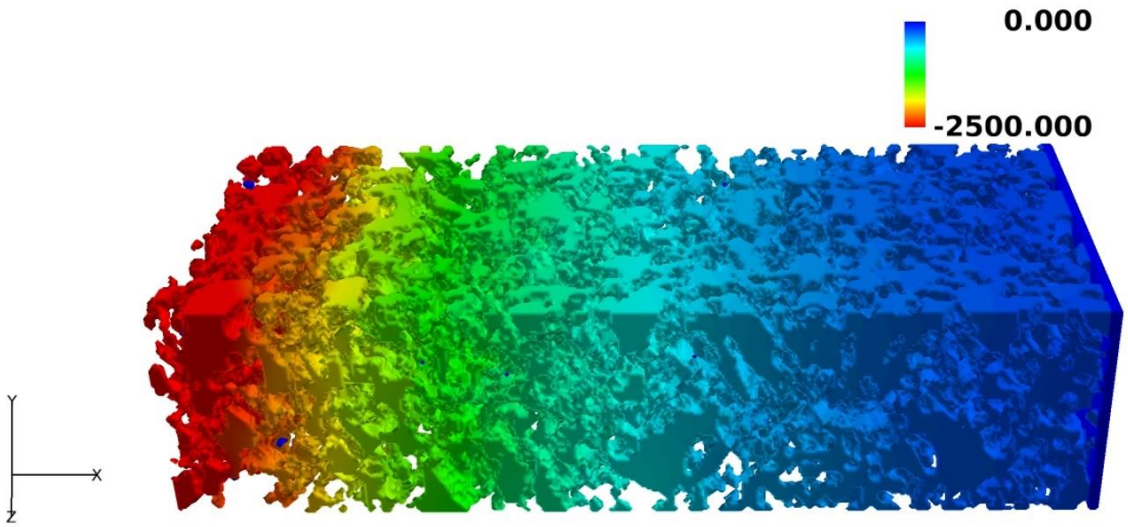

(c) LSCF:GDC = 70:30 vol. %.

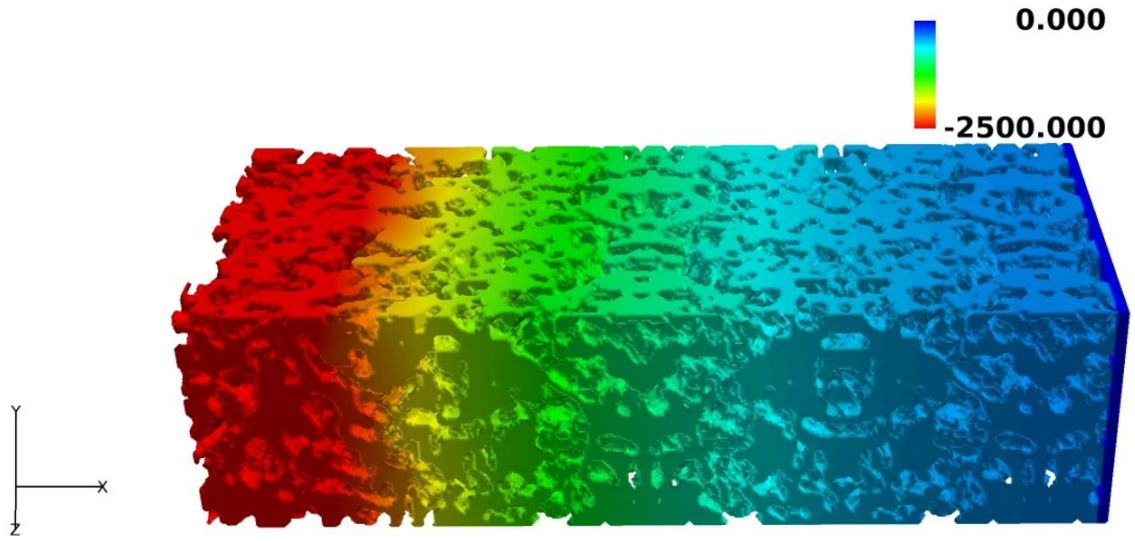

(d) LSCF:GDC = 100:0 vol. %.

Fig. 3-18 Oxygen chemical potential distributions in LSCF corresponding to Fig. 3-16 (a) to (d) (units: J/mol).

3.3 Summary of Chapter 3

In this section, evaluations of LSCF-GDC composite cathodes are summarized. LSCF-GDC composite cathodes with different volume ratios, 20:80, 30:70, 50:50, 70:30, and 100:0 %, were fabricated by screen printing method, and cathode performances were measured at 700°C in 100 % oxygen. The lowest overpotential was achieved at a volume ratio of LSCF:GDC = 30:70 %, and overpotentials were increased in the order of 50:50, 70:30, 100:0, and 20:80 vol. %. Microstructure parameters were calculated based on 3D reconstructed microstructures. Neither LSCF surface reaction nor TPB reaction alone could explain the performance enhancement of LSCF-GDC composite cathodes individually. It is considered that the increase of effective ionic conductivity due to the addition of high ionic conductor, GDC, contributes to the cathode performance enhancement. Electrochemical reaction mechanisms were simulated by LBM. Simulation overpotential results considering both LSCF surface reaction and TPB reaction showed better agreement with the experimental results. It can be concluded cathode performance of LSCF:GDC composites cannot be explained without TPB reaction. However, the slight discrepancies still remained. Reaction current distributions and oxygen chemical potential distributions were investigated. For the LSCF:GDC = 30:70, 50:50 vol. %, it is concluded that the cathode performance is partially enhanced by the elongation of the reactive thickness according to the improvement of ionic conduction kinetics due to the addition of GDC.

Chapter 4
Dependence on Ionic Conductivity

4.1 Ionic Conductivity

In this chapter, dependence of LSCF ionic conductivity on the numerical simulation was investigated using the microstructures of LSCF-GDC composite cathodes. The different ionic conductivities of LSCF from the literatures were introduced in the numerical simulation. Exchange current densities were re-fitted and contribution of surface reaction and TPB reaction were investigated. Computational domains which are introduced in Chap. 3 were applied.

4.1.1 Contribution of Surface Reaction

Figure 4-1 shows the comparison of overpotentials between experimental results and simulation results using different LSCF ionic conductivities. First, exchange currents for surface and TPB reactions introduced in Chap.3 are used. Ionic conductivities were calculated based on the experimental data suggested by Kudo et al. [108] and Bouwmeester et al. [44]. The value of ionic conductivity decreases in the order of Kudo et al. [108] and Bouwmeester et al. [44]. The simulated overpotential results increase as the ionic conductivity of LSCF is decreased.

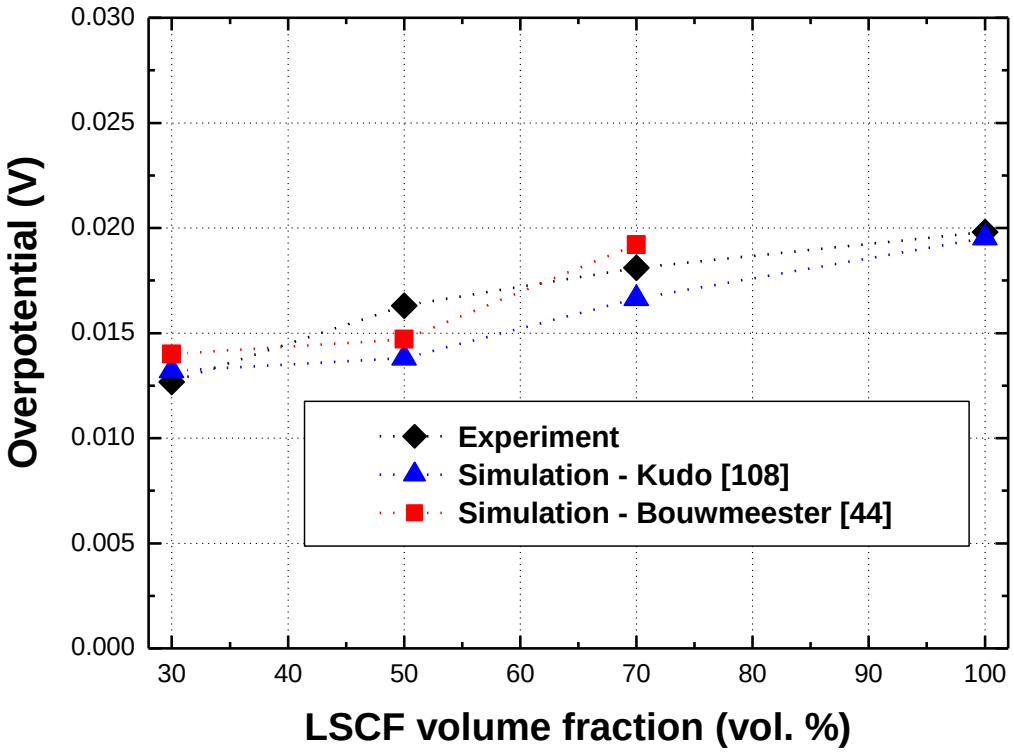

Fig. 4-1 Predicted overpotential results with different LSCF ionic conductivities.

It is seen that both cases show good agreement with the experimental results. However, it is considered that local activation is varied if ionic conductivity of LSCF is changed. In other words, it is thus necessary to re-fit the exchange current density i_0. As introduced in Chapters 2 and 3, the exchange current density for LSCF surface reactions was fitted with an experimental result of pure LSCF cathode, and the exchange current density for TPB reaction was fitted with the experimental results of other composite cathodes. In the present simulation, the ionic conductivity of LSCF which was calculated based on the experimental data in Bouwmeester et al. [44] was excluded because oxygen chemical diffusion coefficient in Bouwmeester et al. [44] drastically decreases under lower oxygen partial pressure. First, LSCF surface reaction was only considered in the numerical simulation in order to investigate the contribution of LSCF surface reaction with the different ionic conductivities of LSCF. Table 4-1 shows the fitted exchange current densities for LSCF surface reaction when different LSCF ionic conductivities are used.

Table 4-1 Fitted exchange current densities for LSCF surface reaction with different LSCF ionic conductivities (T = 973 K)

Ionic conductivity of LSCF	Fitted exchange current density for surface reaction
Oishi et al. (σ_{ion} = 0.25571 S/m) [122]	9.0578 A/m
Ried et al. (σ_{ion} = 0.34489 S/m) [121]	5.8993 A/m
Kudo et al. (σ_{ion} = 0.47383 S/m, Chap. 3) [108]	4.0880 A/m

Figure 4-2 represents the predicted overpotential results which consider only LSCF surface reaction. As the increase of LSCF ionic conductivity, the discrepancy with the experimental results is increased except for the case of Oishi. For the cases of Kudo and Ried, it can be considered that TPB reaction is needed in order to predict the LSCF-GDC cathode performance.

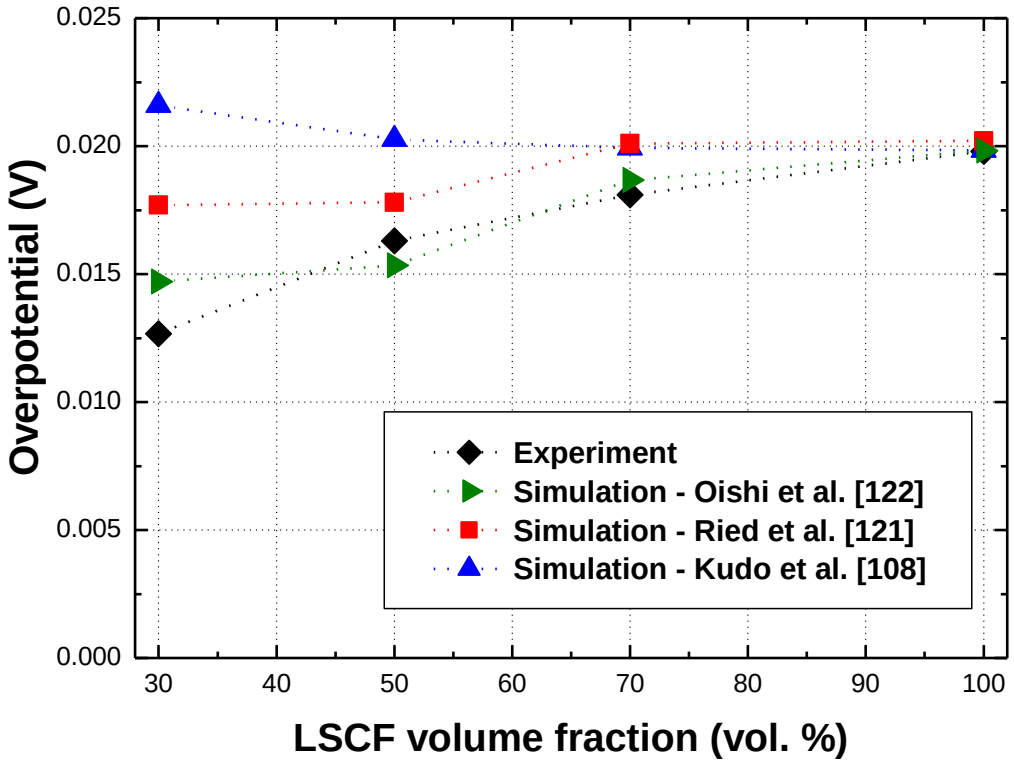

Fig. 4-2 Predicted overpotential results only considering surface reaction, i.e. without considering TPB reaction.

4.1.2 Contribution of TPB Reaction

It can be concluded that performances of LSCF-GDC composite cathodes cannot be explained without considering the TPB reaction except for the case of Oishi. Here, both LSCF surface and TPB reactions were considered with different ionic conductivities. Table 4-2 shows the fitted exchange current densities for TPB reaction with different conductivities.

Table 4-2 Fitted exchange current densities for TPB reaction with different LSCF ionic conductivities (T = 973 K)

Ionic conductivity of LSCF	Fitted exchange current density for TPB reaction
Oishi et al. (σ_{ion} = 0.25571 S/m) [122]	1.3953×10^{-6} A/m
Ried et al. (σ_{ion} = 0.34489 S/m) [121]	3.2955×10^{-6} A/m
Kudo et al. (σ_{ion} = 0.47383 S/m, Chap. 3) [108]	7.9533×10^{-6} A/m

Figure 4-3 shows the predicted overpotential results considering both LSCF surface and TPB reactions. The simulation results with low LSCF ionic conductivities well match with the experimental results. Especially, Oishi shows the best agreement with the experimental results.

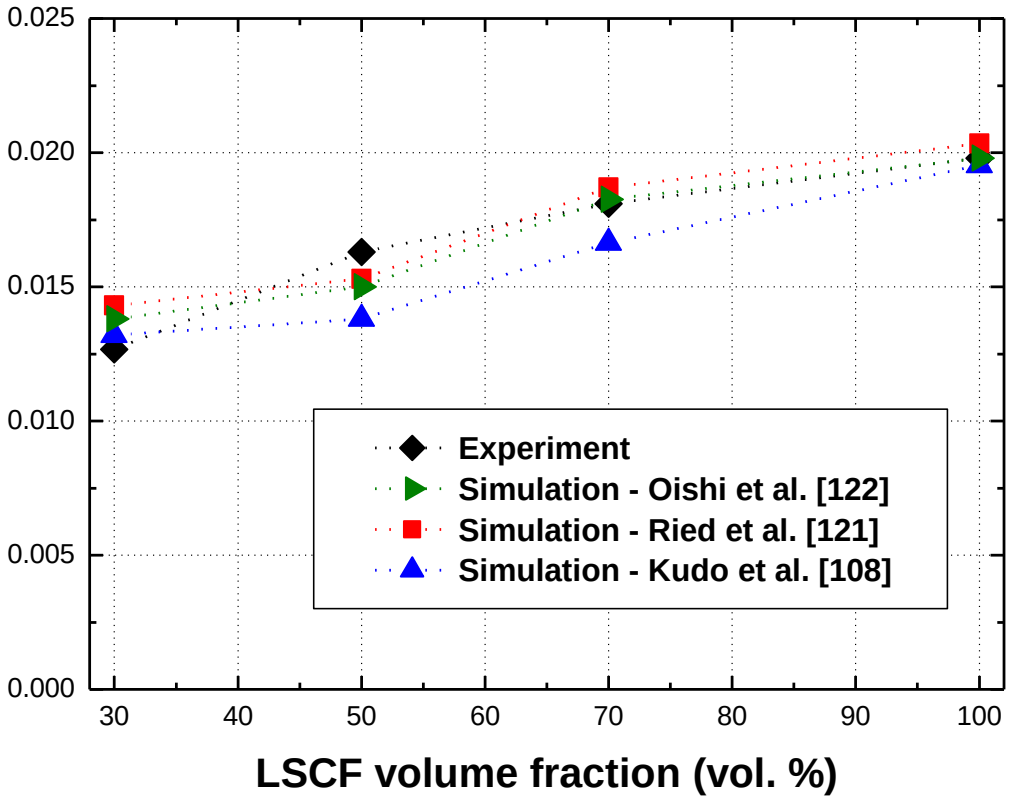

Fig. 4-3Predicted overpotential results considering both LSCF surface and TPB reactions.

Figures 4-4 and 4-5 represent the currents and the oxygen chemical potential distributions with the different ionic conductivities of LSCF. Region where ionic and electronic currents are exchanged becomes broader in the composite cathodes as the ionic conductivities of LSCF increases. Unevenly distributed oxygen chemical potential indicates that the reactive thickness is enlongated with the increase of LSCF ionic conductivities. On the other hand, oxygen chemical potentials are distributed uniformly as the GDC volume fraction increases. Especially for the case of LSCF:GDC = 30:70 vol. %, it is shown that the reactive thickness is elongated although the effective ionic conductivity is deteriorated by the decrease of LSCF ionic conductivity. Investigation of the effective thickness will be conducted with the experiments in the next section.

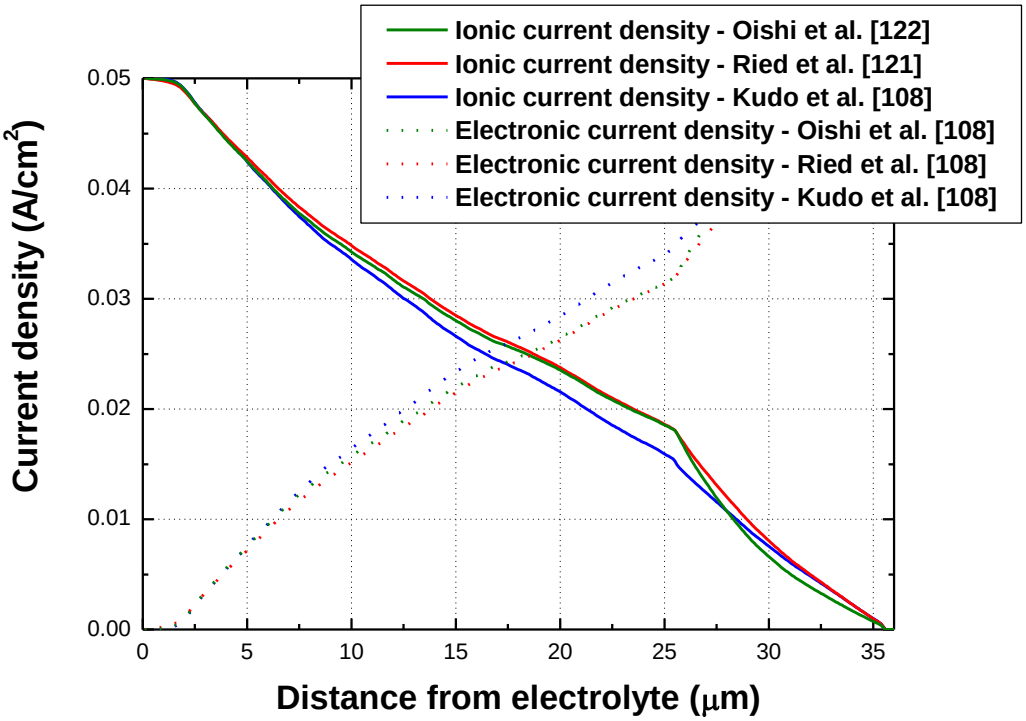

(a) LSCF:GDC = 30:70 vol. %

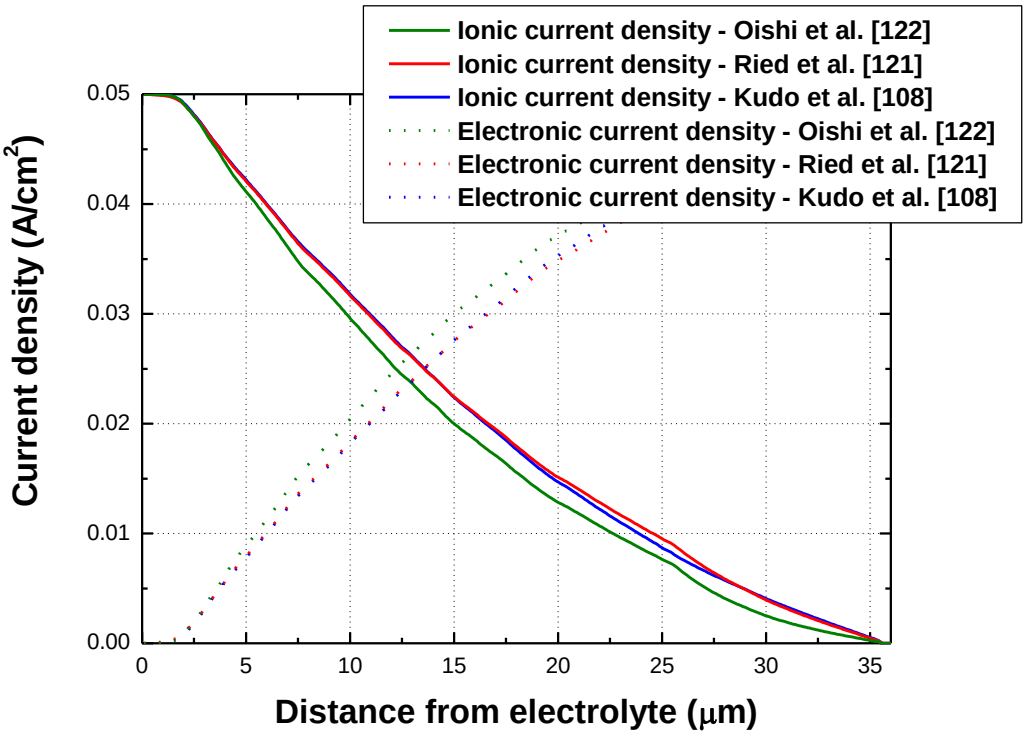

(b) LSCF:GDC = 50:50 vol. %

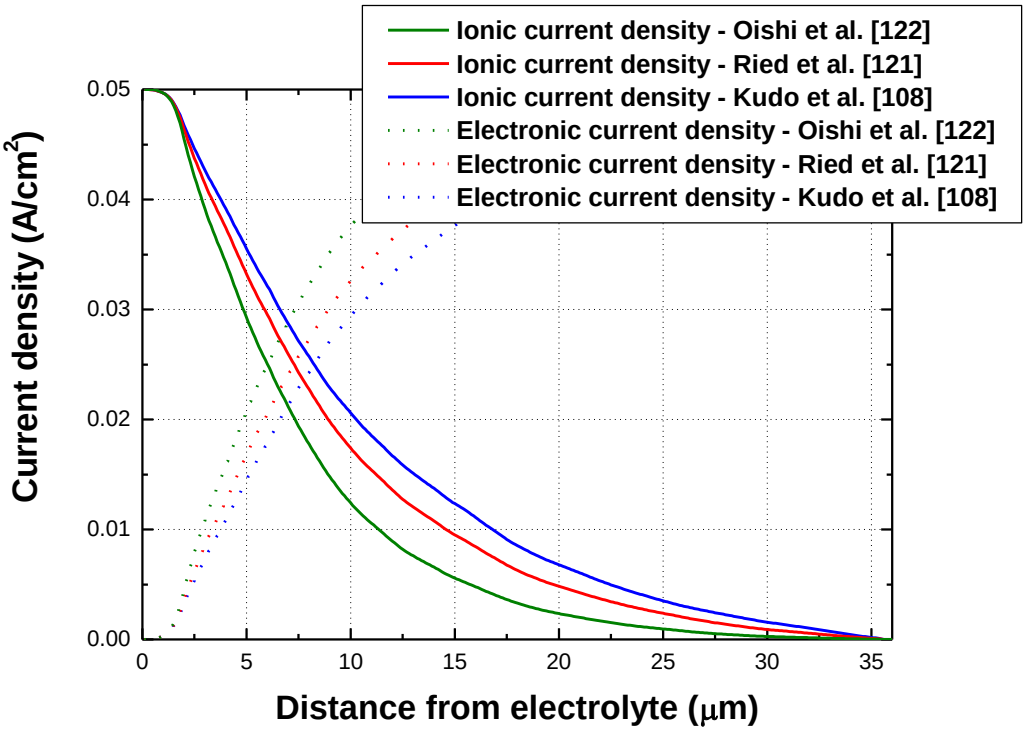

(c) LSCF:GDC = 70:30 vol. %

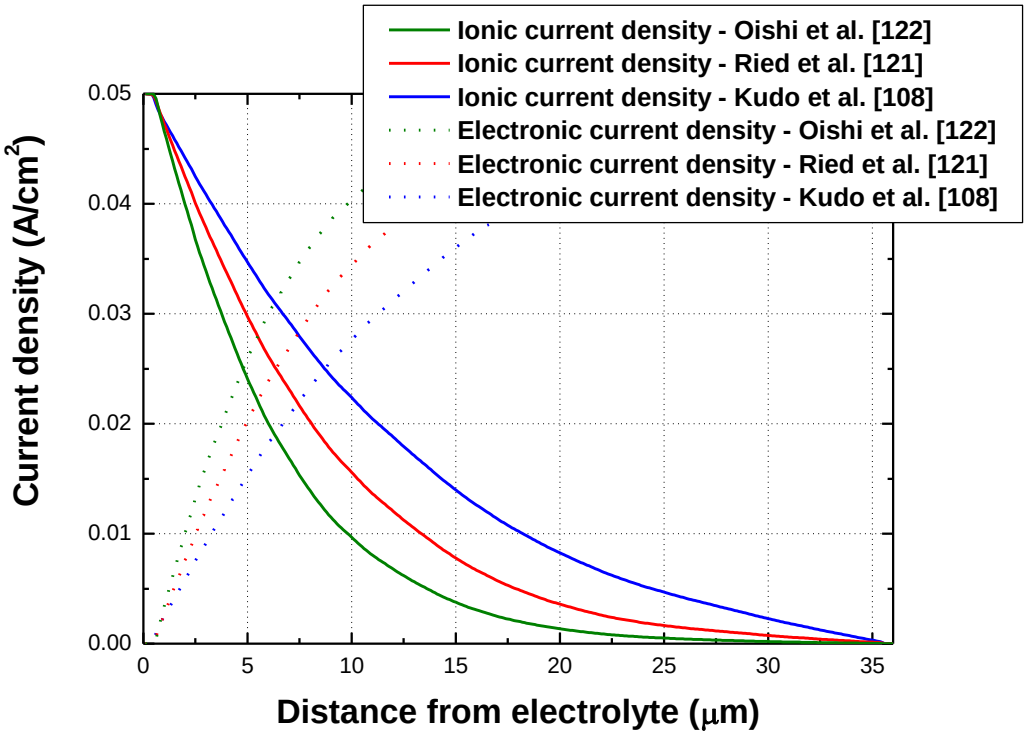

(d) LSCF:GDC = 100:0 vol. %

Fig. 4-4 Current distributions in the LSCF-GDC composite cathodes with different LSCF ionic conductivities. LSCF:GDC = (a) 30:70, (b) 50:50, (c) 70:30, and (d) 100:0 vol. %.

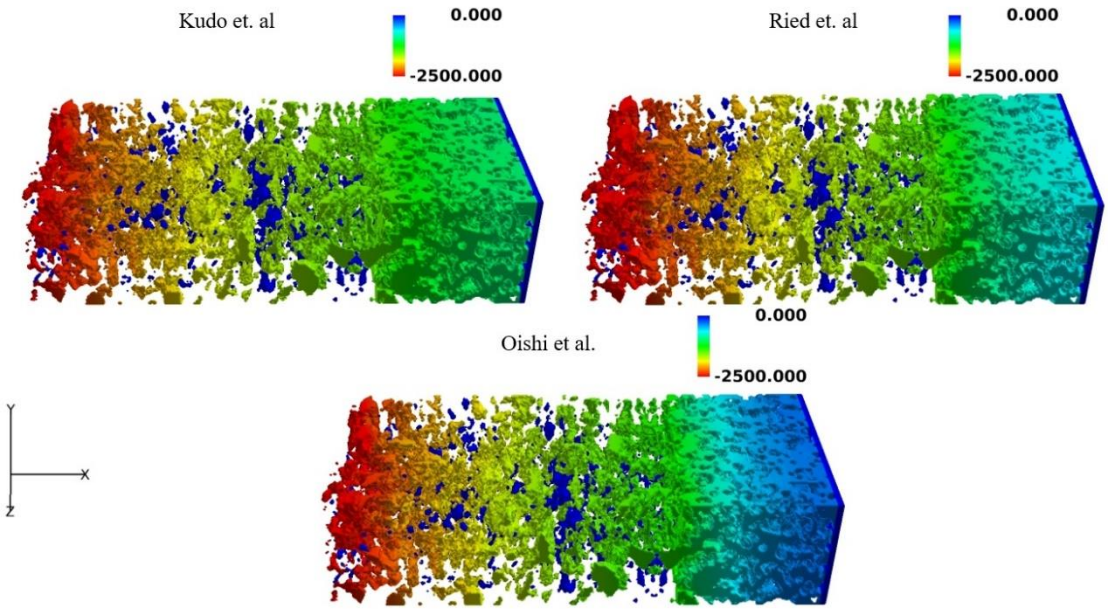

(a) LSCF:GDC = 30:70 vol. %.

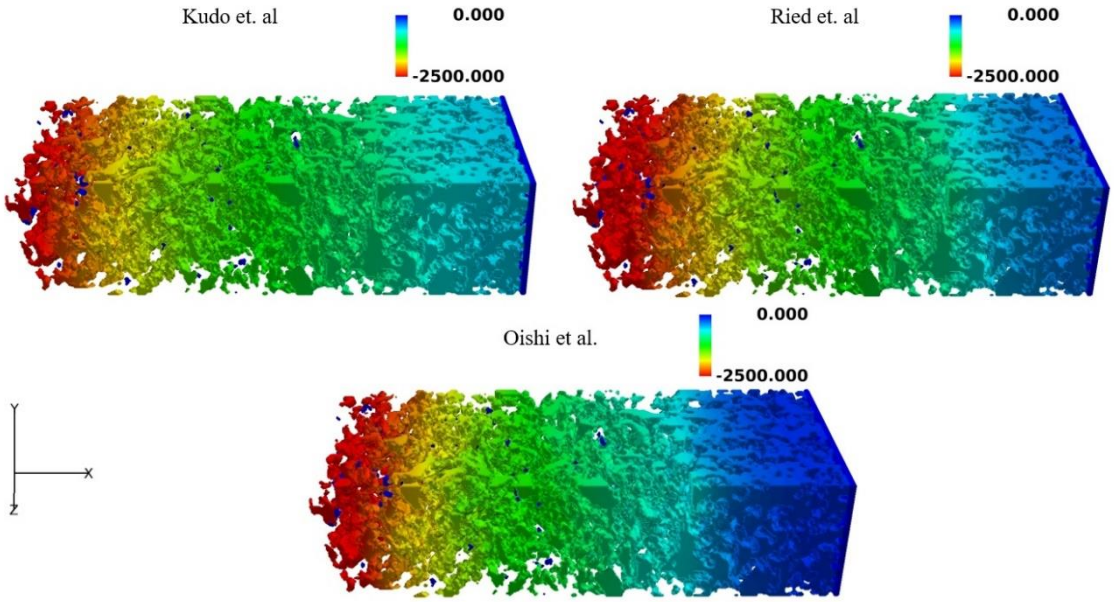

(b) LSCF:GDC = 50:50 vol. %.

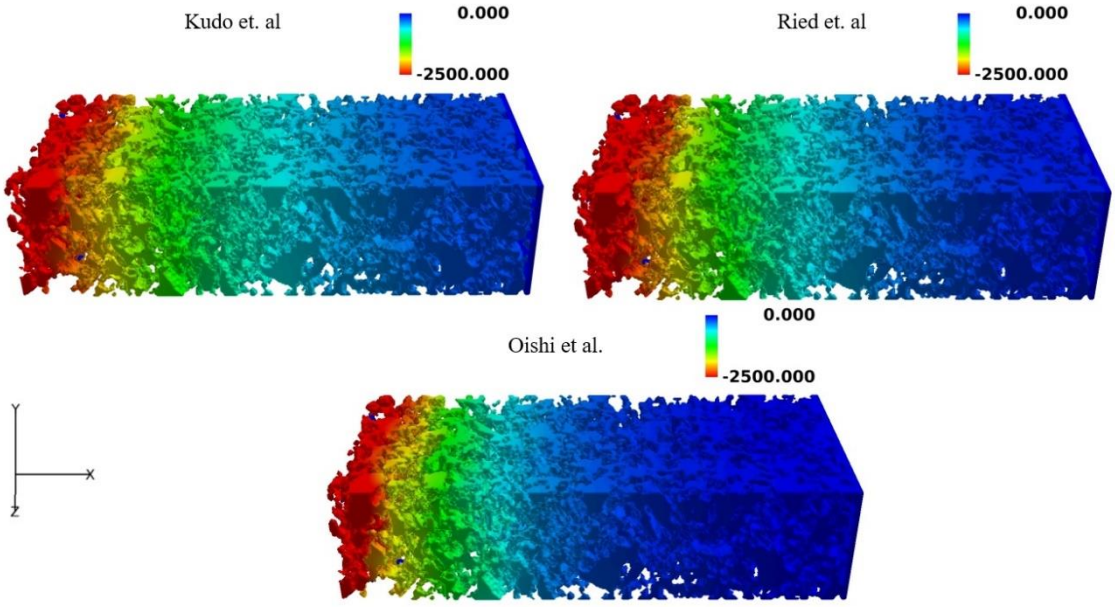

(c) LSCF:GDC = 70:30 vol. %.

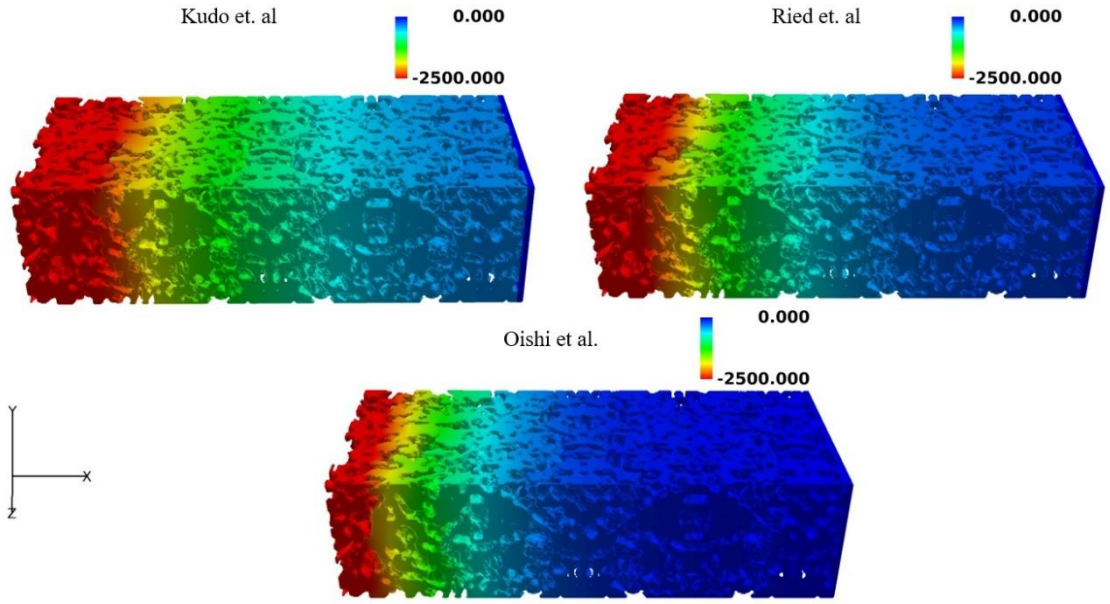

(d) LSCF:GDC = 100:0 vol. %.

Fig. 4-5 Oxygen chemical potential distributions in the LSCF phase with different LSCF ionic conductivities. LSCF:GDC = (a) 30:70, (b) 50:50, (c) 70:30, and (d) 100:0 vol. % (units: J/mol).

4.1.3 Verification of Ionic Conductivity

In this section, reliability of LSCF ionic conductivity was evaluated. First of all, validity of surface reaction models with different ionic conductivities of LSCF in the numerical simulations was investigated. Overpotentials of pure LSCF cathode were calculated with adequate exchange current densities for LSCF surface reaction. Only the surface reaction was considered and temperature in the numerical simulation was set at 700°C and 800°C. Table 4-3 shows the results.

Table 4-3 Overpotentials with different temperatures in the numerical simulations

	700°C	800°C
Experimentals	0.0198 V	0.0068 V
Oishi et al. (σ_{ion} = 1.4307 S/m at 800°C) [122]	0.0198 V	0.0057 V
Ried et al. (σ_{ion} = 0.6572 S/m at 800°C) [121]	0.0202 V	0.0108 V
Kudo et al. (σ_{ion} = 2.2387 S/m at 800°C) [108]	0.0198 V	0.0067 V

At the temperature of 700°C, exchange current densities for LSCF surface reaction were fitted with the experimental result. Therefore, all of the predicted overpotentials at 700°C show good agreement with an experimental result as shown in Table 4-3. However, the discrepancies were shown when the different temperature was applied into the numerical simulation except for the case of Kudo which is used in Chap. 3. It is indicated that the surface reaction model with Kudo is most reliable in

order to explain LSCF surface reaction kinetics compared to other cases. For the case of Oishi, the discrepancy between experimental and simulation is slightly small.

In the present study, ionic conductivities of LSCF were calculated by the correlation with oxygen chemical diffusion coefficient from several literatures as explained section 2.3.1. Therefore, adequacy of experimental methods which were used for quantification of oxygen chemical diffusion coefficient should be demonstrated. In Table 4-4, the experimental methods and the used catalysts corresponding to the literatures are shown, respectively.

Table 4-4 Experimental conditions to quantify oxygen chemical diffusion coefficient

Literature	Method	Catalyst	Ionic conductivity (T = 973 K, pO_2 = 1atm)
Kudo et al. [108]	Isotope exchanges and SIMS profile	Not used	0.47 S/m
Leonide [120]	AC impedance	Gold	0.41 S/m
Ried et al. [121]	Conductivity relaxation time	Gold	0.34 S/m
Oishi et al. [122]	Conductivity relaxation time	Platinum	0.26 S/m

When the isotope exchange method and the AC impedance methods are used for the quantification of oxygen chemical diffusion coefficient, the ionic conductivity values are larger. In Ref. [120], it is reported that when the conductivity relaxation time method is used, separation of surface exchange process and bulk transport process is difficult due to fast surface exchange reaction compared to the bulk diffusion when thick film electrode is used in the conductivity relaxation time method. Another problem of conductivity relaxation time method is that the gas change requires finite time. These problems result in the decrease of the measured oxygen diffusion coefficient. Furthermore, when platinum is used for the catalyst, oxygen chemical diffusion coefficients show the artificial pO_2 dependence [123]. Therefore, it can be concluded that ionic conductivity of LSCF calculated from Ref. [108] is reliable.

4.2 Reactive Thickness

In this chapter, reactive thickness of LSCF-GDC composite cathode was quantified by the experiment and the numerical simulation. A volume ratio of LSCF:GDC = 30:70 % was chosen for both experiment and simulation, because it shows the longest reactive thickness as described in section 3.2.3. The ionic conductivity of LSCF σ_{ion} = 0.25571 S/m (Oishi et al., [122]) was used in the numerical simulation.

4.2.1 Experimental Results

In the present study, cathode thickness was increased by increasing the number of screen printing process. Then, LSCF current collection layer was printed onto the top of the composite cathode. The thicknesses of the cathode were approximately 30, 40 and 50 μm. SEM micrographs of LSCF:GDC = 30:70 vol. % with different thicknesses are shown in Fig. 4-6. EsB detector with acceleration voltage of 5 keV was used for SEM observation.

Figure 4-7 shows the overpotentials at current density of 0.05 A/cm^2 and polarization resistance at OCV with different cathode thicknesses. The overpotential and polarization resistance decrease with the increase of cathode thickness, and the values become nearly unchanged at around the cathode thickness of approximately 40 μm. It is seen that the reactive thickness can be approximated to be around 40 μm for the LSCF:GDC = 30:70 vol. % cathode.

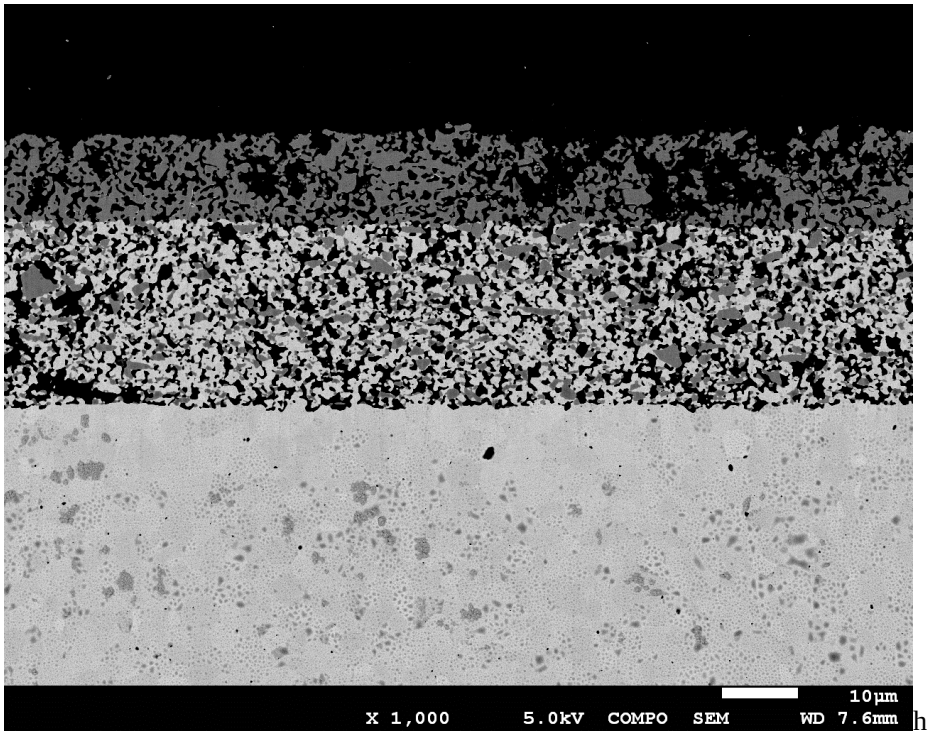

(a) Cathode thickness ≒ 30 μm.

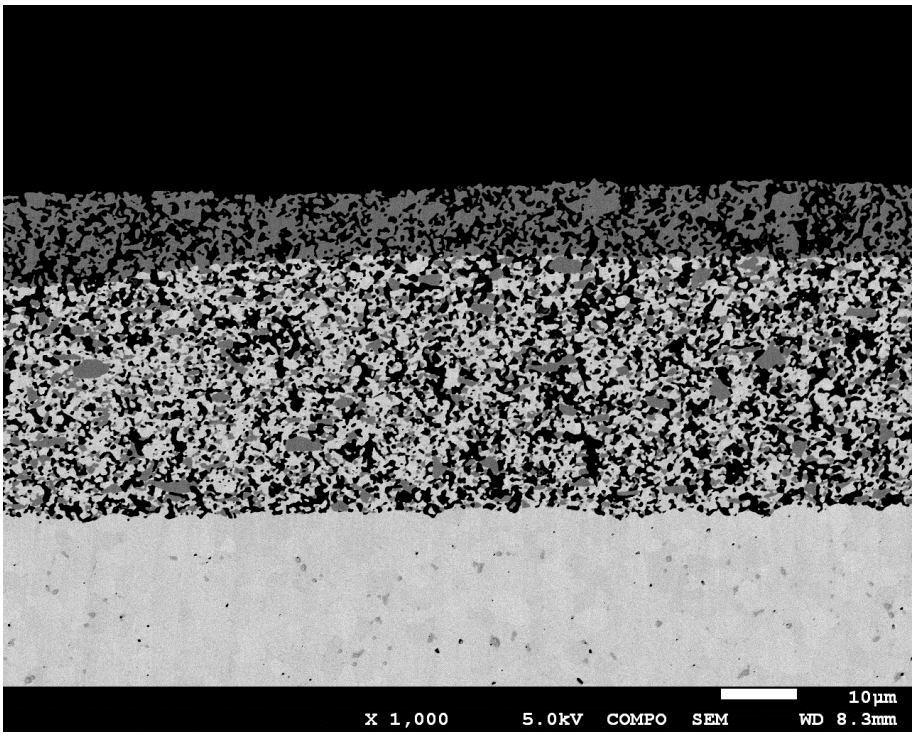

(b) Cathode thickness ≒ 40 μm.

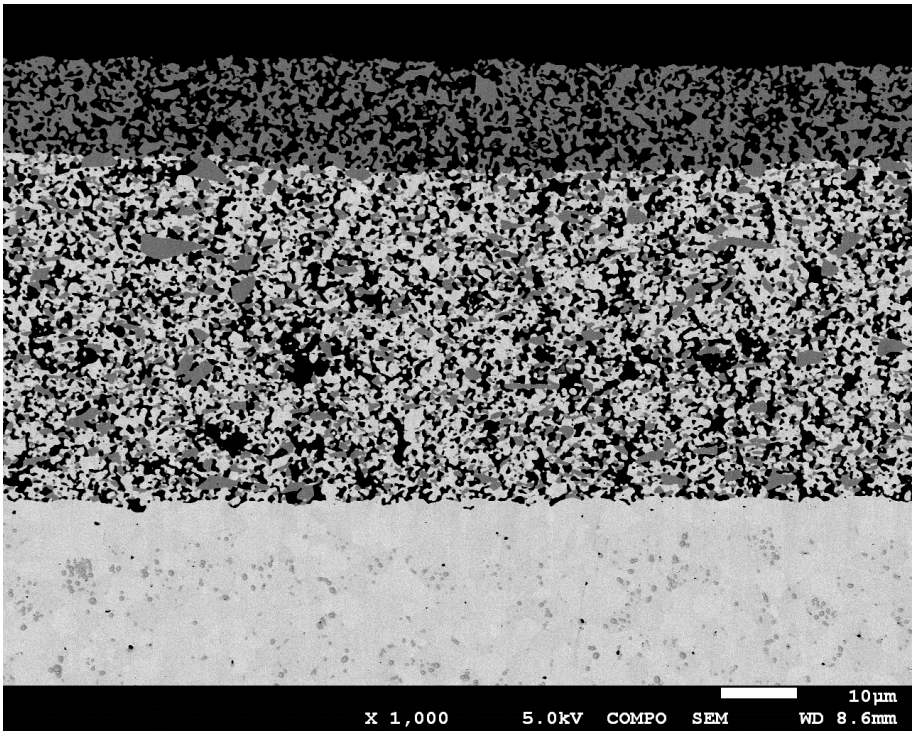

(c) Cathode thickness ≒ 50 μm.

Fig. 4-6 SEM images of LSCF:GDC = 30:70 vol. % cathode.

The thicknesses are (a) 30 μm, (b) 40 μm, and (c) 50μm.
(Dark solid phase: LSCF, Bright solid phase: GDC).

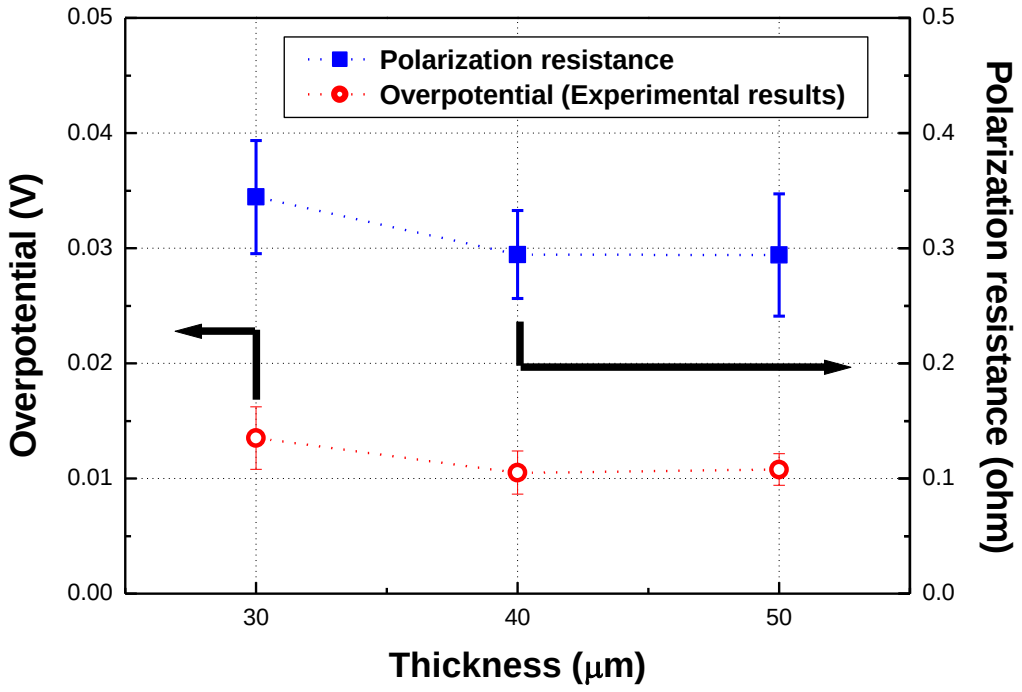

Fig. 4-7 Overpotentials and polarization resistance variations with different cathode thicknesses for LSCF:GDC = 30:70 vol. %.

4.2.2 Simulation Results

For the numerical simulation, a computational domain of LSCF:GDC = 30:70 vol. % which was used in Chap.3 was elongated in the thickness direction by mirroring. For the computational domain in the numerical simulation, composite cathode of 50 μm and LSCF current collector of 10 μm were introduced. Then dense electrolyte and current collector of 1 μm were additionally attached to the one end of the composite cathode and to the LSCF current collector. Computational domain is shown in Fig. 4-8.

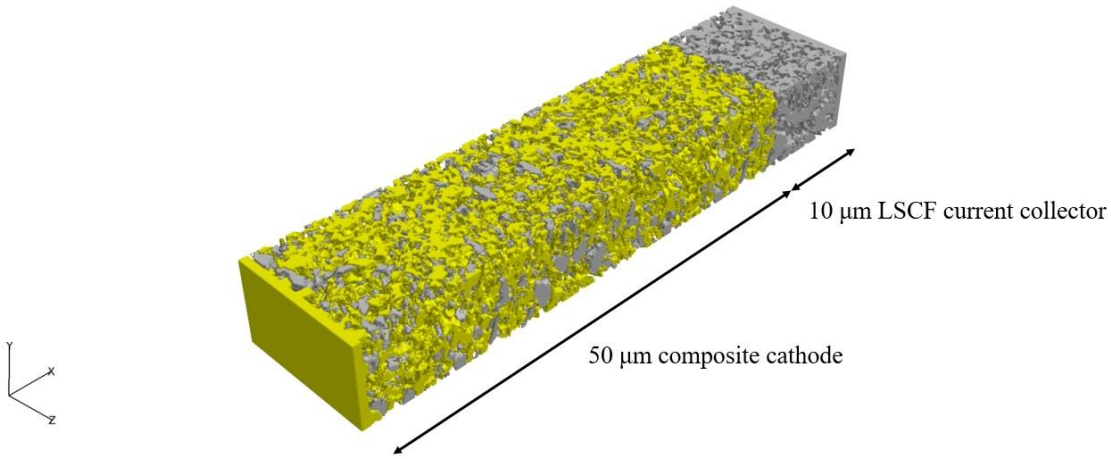

Fig. 4-8 Computational domain to investigate effective cathode thickness.
LSCF:GDC = 30:70 vol. % (Yellow: GDC, Gray: LSCF).

In the numerical simulation, fitted exchange current densities for Oishi" were used. Figure 4-9 shows the overpotential results of the experimental and the simulation with different cathode thicknesses. No significant difference can be seen as the cathode thickness is elongated in the simulation results. Current distribution in the composite cathode and oxide chemical potential distribution in the LSCF solid phases are shown in Figs. 4-10 and 4-11. It is shown that the ionic and electronic currents are exchanged at around of 20 μm computational domain. It is shown that the gradient of current distributions inside the LSCF current collector vary significantly. Similarly, oxygen chemical potential gradient is nearly uniform in the composite and it becomes zero in the LSCF current collector. Compared to the oxygen chemical distribution with 25 μm cathode thickness which is introduced in section 4.1.2, similar trend of the oxygen chemical potential distribution in the composite are seen. It is considered that small difference in electrochemical reaction kinetics in the composite results in the small discrepancy of overpotential when the cathode thickness is increased.

Figures 4-12 and 4-13 show the reaction current distribution and the ionic flux in the composite cathode, respectively. Both reaction current distribution and ionic flux show the rapid change near the LSCF current collector. The simulation results indicate that the electrochemical reaction progresses also inside the LSCF current collector and consumes oxygen chemical potential difference.

From the simulation results, effective thickness of LSCF:GDC = 30:70 vol. % composite cathode can be achieved at around 50 μm. However, the discrepancy between experiment and simulation results exists.

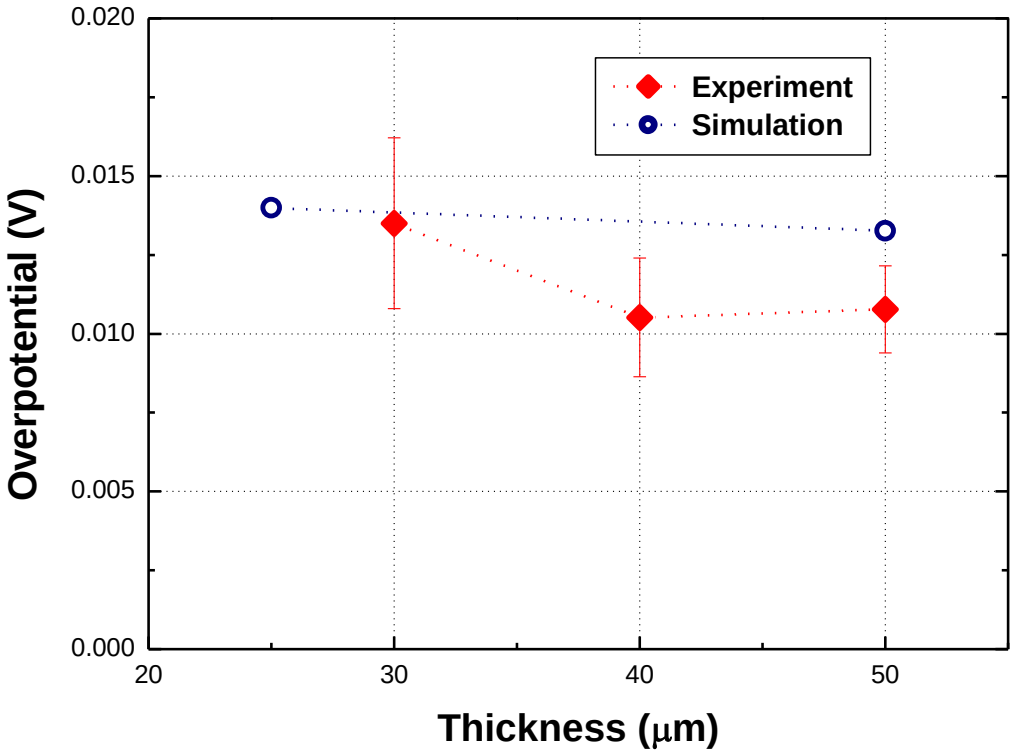

Fig. 4-9 Experimental and simulated overpotential results with different cathode thicknesses.

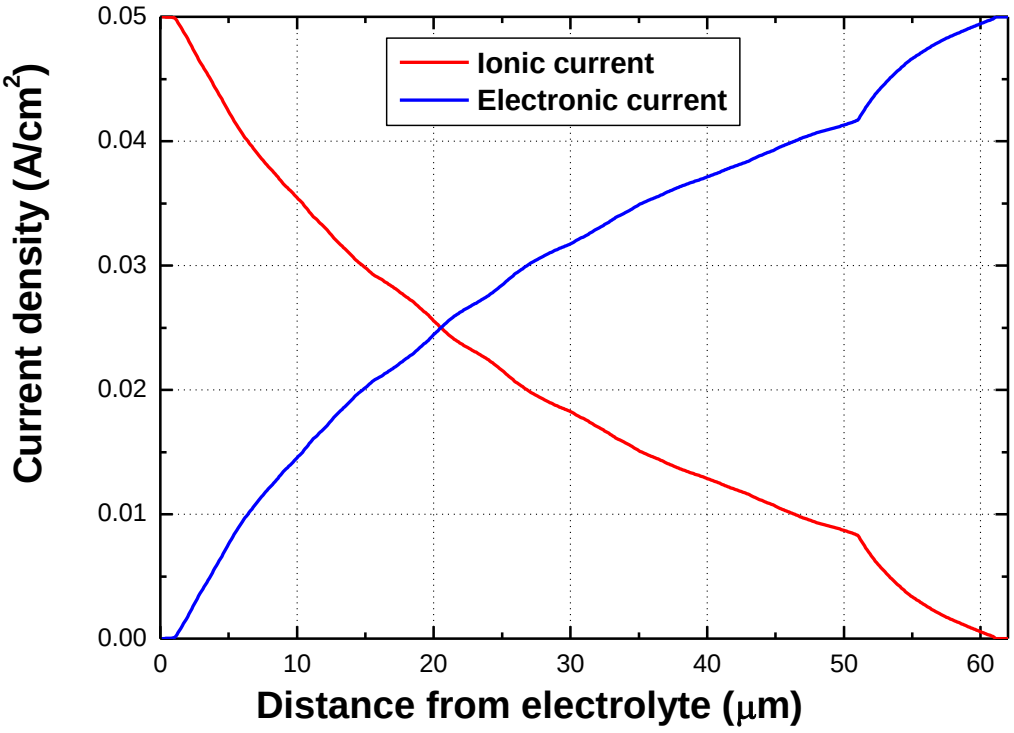

Fig. 4-10 Ionic and electronic current distributions in the LSCF:GDC = 30:70 vol. % composite cathode.

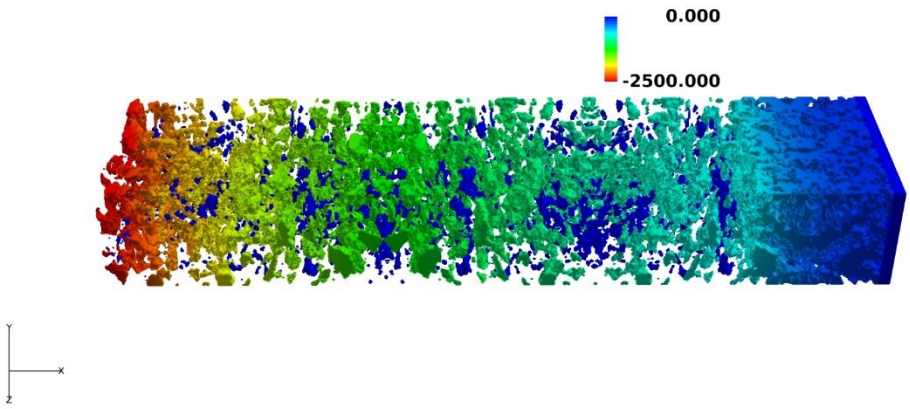

Fig. 4-11 Oxygen chemical potential in the LSCF phase (unit: J/mol).

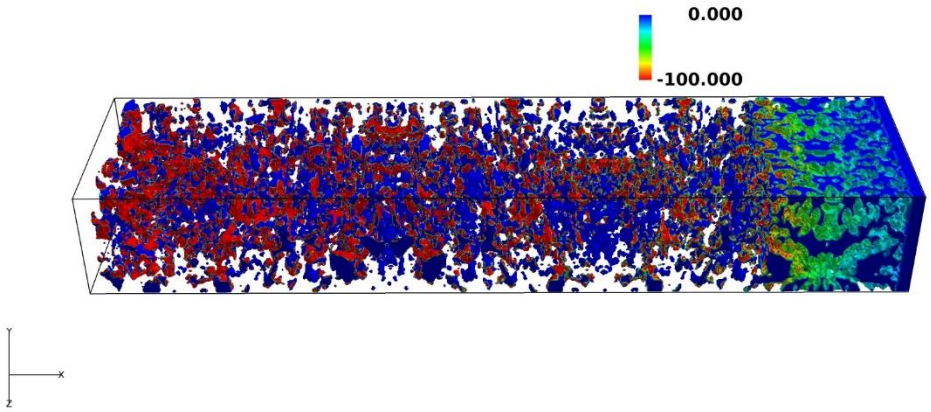

Fig. 4-12 Reaction current distribution in the LSCF phase (unit: A/cm^2).

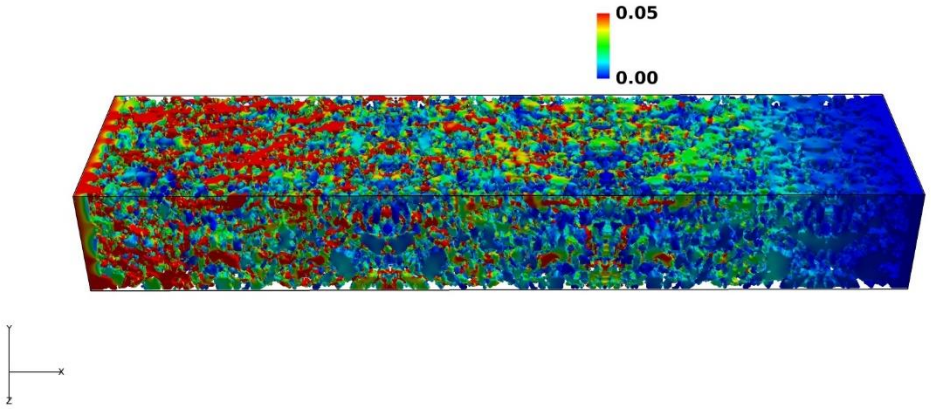

Fig. 4-13 Oxygen ionic flux in the composite cathode (unit: A/cm^2).

4.3 Summary of Chapter 4

In this chapter, dependence of the numerical simulation results on LSCF ionic conductivity was investigated. Various ionic conductivities from the literatures were applied. Exchange current densities corresponding to different ionic conductivities were re-fitted using the experimental results. When the lowest LSCF ionic conductivity is applied and the surface reaction is only considered, predicted overpotential show a good agreement with the experimental results. As the LSCF ionic conductivity is deteriorated, reactive thickness is decreased. However, the elongated reactive thickness was shown for the volume ratio of LSCF:GDC = 30:70 % even low LSCF ionic conductivities were applied. Validity of surface reaction models was investigated with different temperature in the numerical simulation. For the case of Kudo, an overpotential at temperature of 800°C is well-predicted compared to other cases. Reliability of LSCF ionic conductivities reported in the literature was evaluated by verifying their experimental methods. When conductivity relaxation time method is used for quantification of oxygen chemical diffusion coefficient, the ionic conductivity of LSCF decreases due to several problems. It is considered that ionic conductivities which are calculated by oxygen chemical diffusion coefficients from other experimental methods are reliable for the numerical simulation.

The reactive thickness was investigated by the experiment and by the numerical simulation. For the numerical simulation, LSCF ionic conductivity σ = 0.25571 S/m was applied. A volume ratio of LSCF:GDC = 30:70 % was chosen because it has the longest reactive thickness as introduced in Chap. 3. From the experimental results, it is indicated that the reactive thickness of LSCF:GDC = 30:70 vol. % can be approximated to be around 40 μm. For the numerical simulation, 50 μm composite cathode and 10 μm LSCF current collector was prepared by mirroring the original microstructures. Unlike the experimental results, very small dependence of overpotential on the cathode thickness was shown from the numerical simulation. Current and oxygen chemical potential distributions were investigated. The gradient of both current and oxygen chemical potential distributions changed drastically inside the LSCF current collector. It is considered that electrochemical reaction took place in the LSCF current collector as well. Electrochemical reaction kinetics in the composite were similar regardless of the cathode thickness. The discrepancy of reactive thickness between the experimental and simulation results was shown.

Chapter 5
LSC-GDC Composite Cathode with Different Volume Ratios

5.1 Experimental Results

In this chapter, LSC-GDC composite cathodes with different volume ratios of 20:80, 30:70, 50:50, 70:30, and 100:0 % were fabricated by screen printing method onto the dense GDC electrolyte. An electrolyte-supported cell was used for the measurement and cathode microstructures were reconstructed by FIB-SEM as explained in Chap. 2. Polarization characteristics were correlated with microstructure parameters.

5.1.1 Correlation between Performance and Microstructure

In the present study, electrochemical performance measurements were conducted three times for each volume ratio with three individual electrolyte-supported cells, and error bars correspond to the standard deviations of the three samples. Figure 5-1 represents the overpotential results. The lowest overpotential was achieved at a volume ratio of LSC:GDC = 30:70 %, and it increased in the order of LSC:GDC = 50:50, 70:30, 20:80 and 100:0 vol. %. The results show similar tendency with the LSCF-GDC composite cathode as reported in Chap. 3.

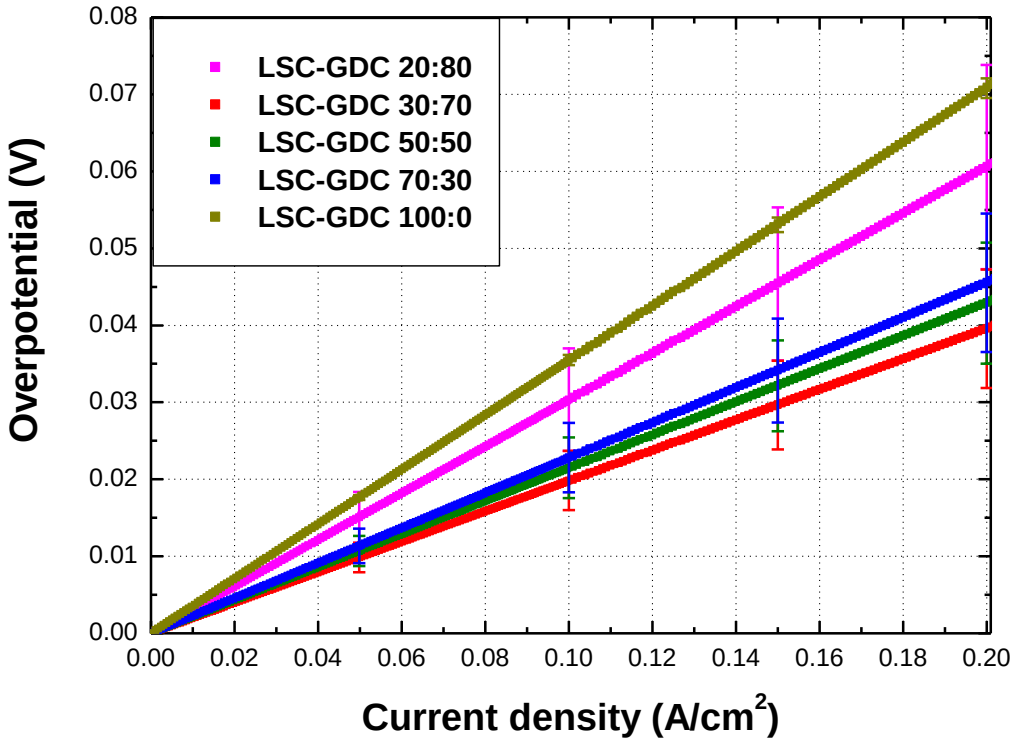

Fig. 5-1 Overpotentials of LSC-GDC composite cathodes.

Figure 5-2 shows the polarization resistances of LSC-GDC composite cathodes at OCV. The results show similar tendency with the overpotential results as shown in Fig. 5-1. Notable point is that the polarization resistance of LSC:GDC = 100:0 vol. % at OCV is lower than that of LSC:GDC = 70:30 and 20:80 vol. %, even it shows an increase in overpotential. The polarization characteristics can be different at OCV from those under polarization. For the cases of LSC:GDC = 30:70 and 50:50 vol. %, similar tendency with the overpotential results can be seen.

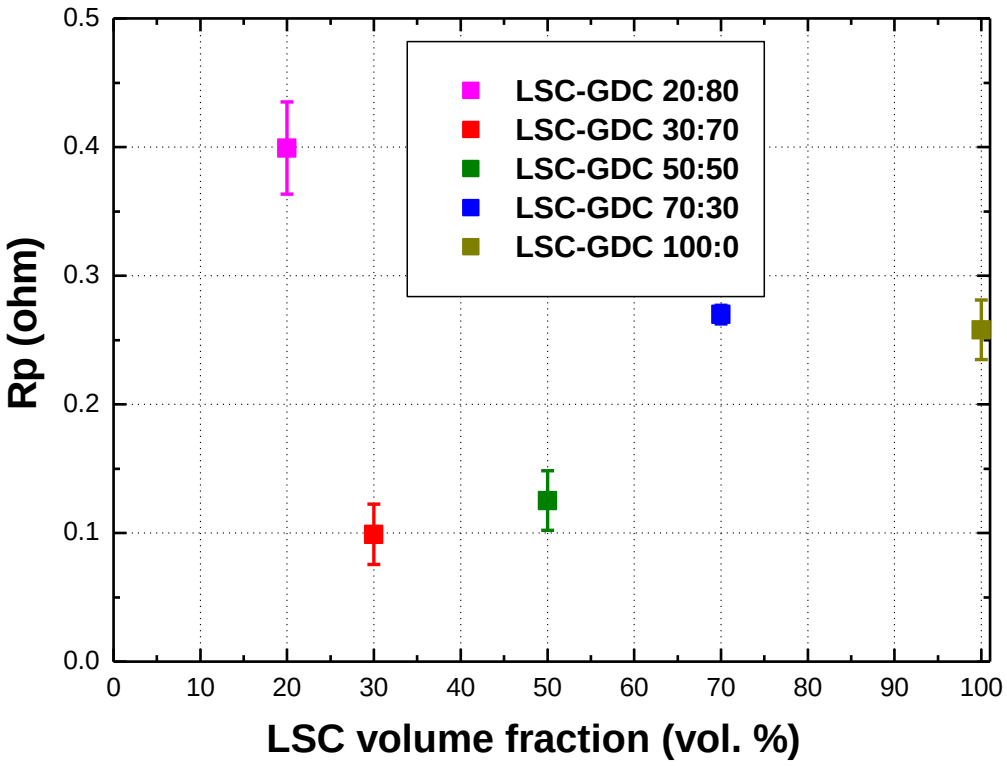

Fig. 5-2 Polarization resistances of LSC-GDC composite cathodes at OCV.

Microstructure parameters were calculated based on 3D reconstructed cathode microstructures. For the reconstruction of the LSC-GDC composite cathodes, energy selective backscatter (EsB) detector with an acceleration voltage of 5 keV was used for SEM observation. Sequential capturing of images with a pixel size of 25 nm was conducted with a *z*-axis slice pitch of 25 nm. In other words, all reconstructed microstructures have a voxel size of 25 nm. Figure 5-3 shows the SEM images during FIB-SEM measurement for the LSC-GDC composite cathodes.

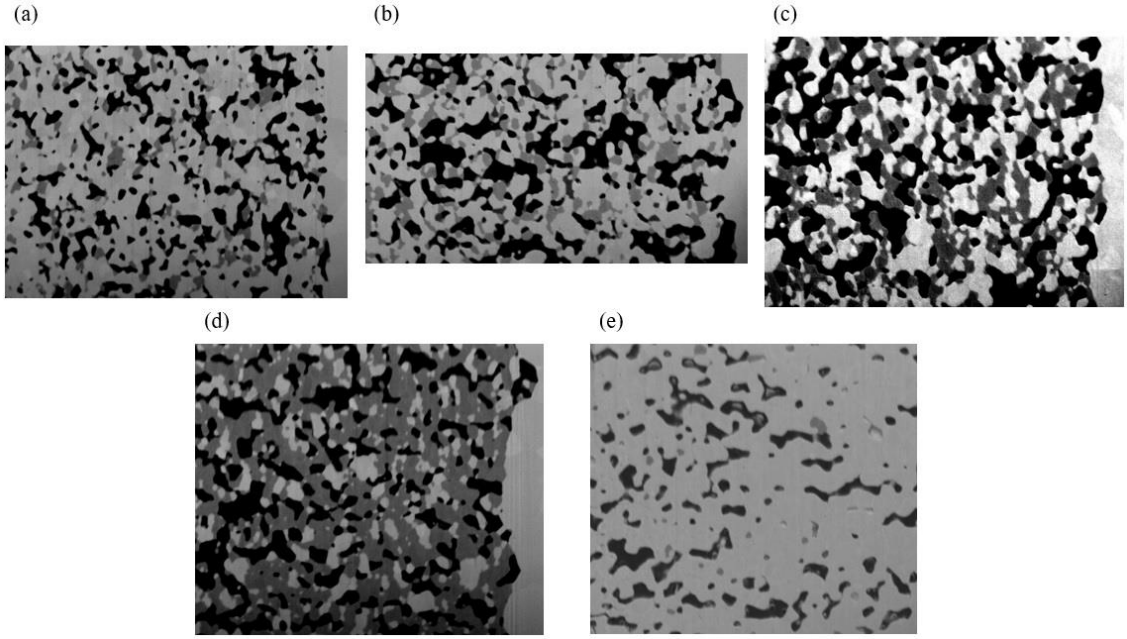

Fig. 5-3 SEM images from FIB-SEM measurement.
The volume ratios of LSC:GDC = (a) 20:80, (b) 30:70, (c) 50:50, (d) 70:30 and (e) 100:0 %.
(Black: pore, dark gray: LSC, light gray: GDC).

Table 5-1 and Figure 5-4 show the conditions and images of 3D reconstructed microstructures of LSC-GDC composite cathodes, respectively.

Table 5-1 Reconstructed sample conditions.

LSC:GDC	Number of pixels ($x \times y$)	Number of slices in z direction	Sample volume size
20:80 vol. %	716×596	360 slices	2400.39 μm^3
30:70 vol. %	820×516	331 slices	2189.65 μm^3
50:50 vol. %	712×592	345 slices	2273.49 μm^3
70:30 vol. %	752×668	348 slices	2764.16 μm^3
100:0 vol. %	832×740	291 slices	2801.34 μm^3

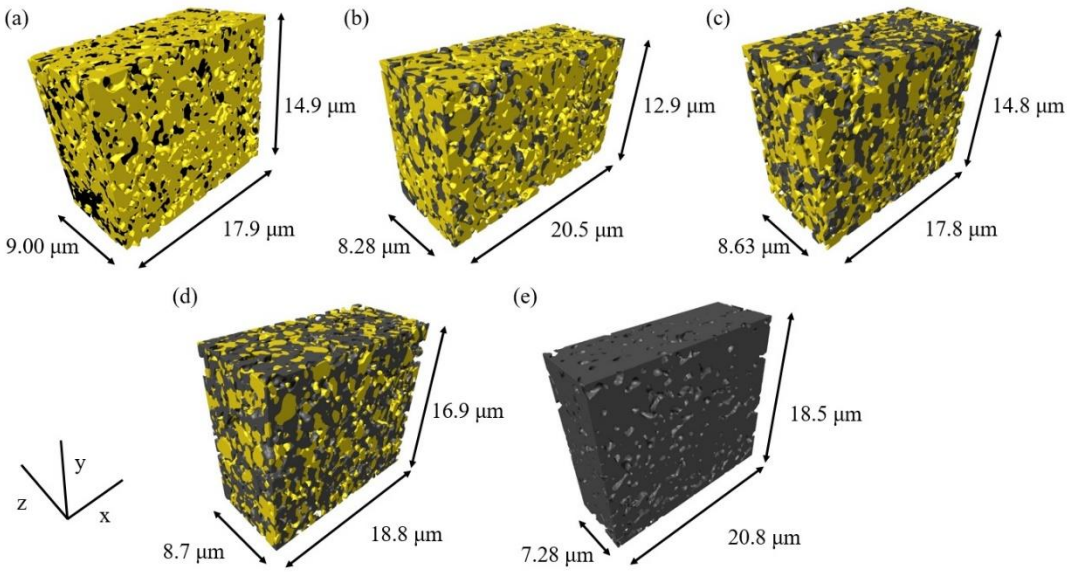

Fig. 5-4 3D reconstructed microstructures of LSC-GDC composite cathodes.
The volume ratios of LSC:GDC = (a) 20:80, (b) 30:70, (c) 50:50, (d) 70:30 and (e) 100:0 %.
(Yellow: GDC, dark gray: LSC).

For the microstructure parameter calculation, original resolution of 25 nm was used. Two electrochemical reaction mechanisms are also considered for the LSC-GDC composite cathode, i.e. LSC surface reaction and TPB reaction. In Fig. 5-5, LSC surface area densities and active TPB densities with the polarization resistances at OCV are shown. Closed symbols represent the polarization resistances and open symbols represent the microstructure parameters.

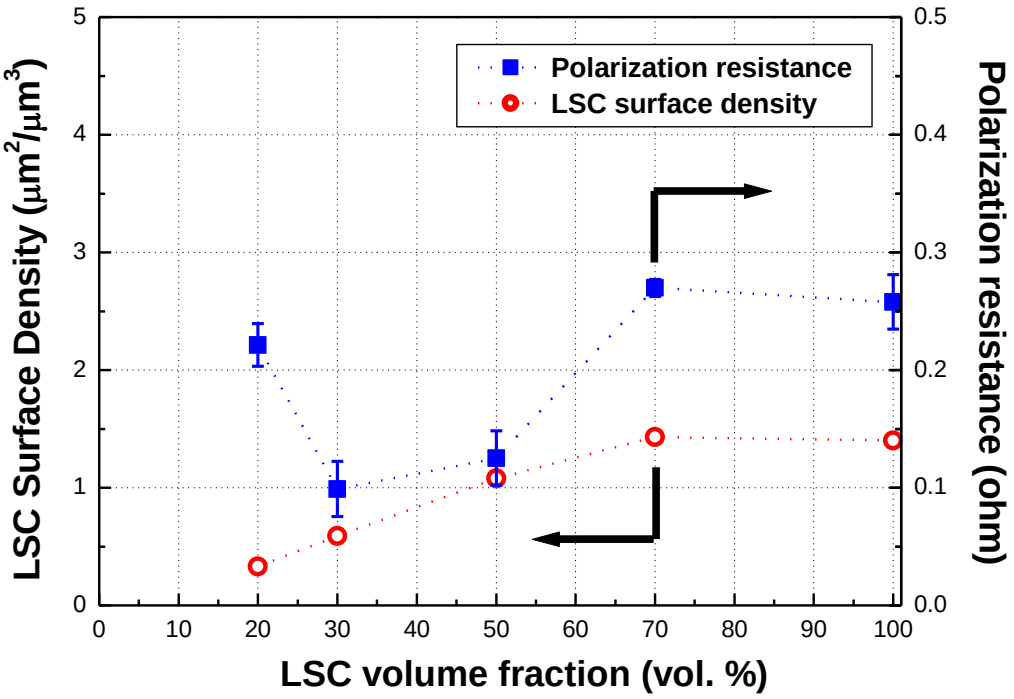

(a) LSC surface area densities and polarization resistances.

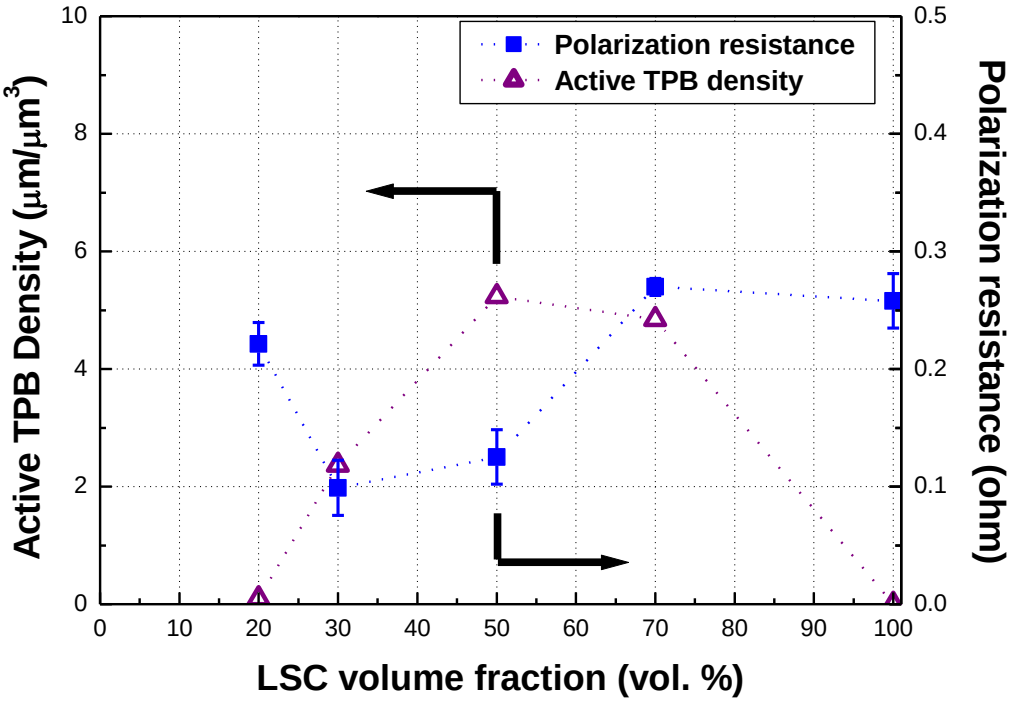

(b) Active TPB densities and polarization resistances.

Fig. 5-6 Comparison between reaction areas of LSC-GDC composite cathodes with polarization resistance.

As shown in Fig. 5-6, the surface area densities of LSC decrease monotonously with the decrease of LSC volume fraction. However, the pure LSC shows nearly the same surface area density as that of LSC:GDC = 70:30 vol. %. It can be considered that the rapid grain growth of LSC due to its high sinterability results in the decrease of surface area for the pure LSC cathode. The best performance at a volume ratio of LSC:GDC = 30:70 % which has small LSC surface area density implies that LSC surface reaction is not the single reaction mechanism of LSC-GDC composite cathode. On the other hand, the highest active TPB density was achieved at a volume ratio of LSC:GDC = 50:50 %, while the polarization resistance of LSC:GDC = 30:70 vol. % is the lowest. Therefore, TPB reaction alone also cannot explain the performance of LSC-GDC composite cathode as a single reaction mechanism. Correlation between the performance and the reaction area shows the similar tendency with the case of LSCF-GDC composite cathode as described in Chap. 3.

The other parameters are shown in Table 5-2. Notable point is that the porosity of pure LSC cathode is the lowest, 17.67 %. It can be considered that porosity decreases significantly due to the high sinterability of LSC for the case of pure LSC cathode, and it also causes the decrease of LSC surface area density as shown in Fig. 5-6 (a). Therefore, it can be considered that GDC in the composites suppresses the rapid grain growth of LSC.

The change in phase connectivity depends on the volume fraction. Compared to the LSCF-GDC composite cathode, both LSC and GDC phases are well-connected. The phase connectivity of LSC for the LSC:GDC = 20:80 vol. % is 20.21 %, while LSCF phase connectivity with the same volume ratio was only 10.91 %. For the case of 30 % GDC volume fraction, the phase connectivity of GDC is 79.29 % for the LSC-GDC composite cathode, while it is 6.67% for the LSCF-GDC composite cathode.

Table 5-2 Microstructure parameters from FIB-SEM reconstruction.

LSC:GDC =	20:80 vol.%	30:70 vol.%	50:50 vol.%	70:30 vol.%	100:0 vol.%
Porosity	33.88 %	36.70 %	33.96 %	32.48 %	17.67 %
GDC phase volume fraction	57.99 %	48.61 %	37.72 %	26.32 %	-
LSC phase volume fraction	8.13 %	14.69 %	28.32 %	41.20 %	68.84 %
GDC connectivity	99.98 %	99.90 %	99.56 %	79.29 %	-
LSC connectivity	20.21 %	70.37 %	98.91 %	99.87 %	99.98 %

Likewise to the LSCF-GDC composite cathode, contribution of effective ionic conductivity was investigated. As introduced in Eq. (3.1), tortuosity factor is a crucial parameter to determine the effective ionic conductivity. Figure 5-7 shows the tortuosity factors of GDC and LSC with the polarization resistances, respectively. In the graphs, the results located out of range due to the high tortuosity factor caused by the decrease of corresponding phases are excluded. As shown in Fig. 5-7, the tortuosity factors strongly depend on the volume fraction of each phase. It is considered that effective ionic conductivity will be increased monotonously as the volume fraction of GDC is increased due to its higher ionic conductivity compared to LSC. However, performance will be deteriorated due to the significant reduction of reaction areas for the case of a LSC:GDC = 20:80 vol. % as shown in Fig 5-6. Cathode performance will be determined by the trade-off between electrochemical reaction and ionic conduction kinetics. Present LSC-GDC composite cathode results show the similar tendency with the case of LSCF-GDC composite cathode which is investigated in Chap. 3. It is indicated that the reaction mechanism of LSC-GDC is the same as the LSCF-GDC

composite cathode.

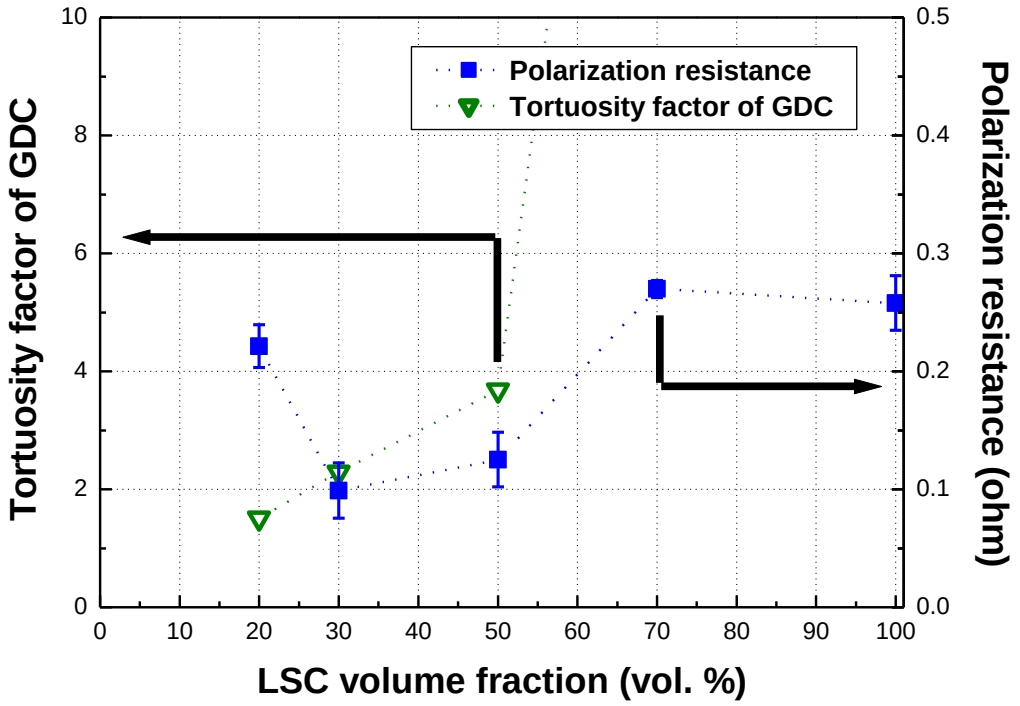

(a) Tortuosity factors of GDC with polarization resistances of LSC-GDC composite cathode.

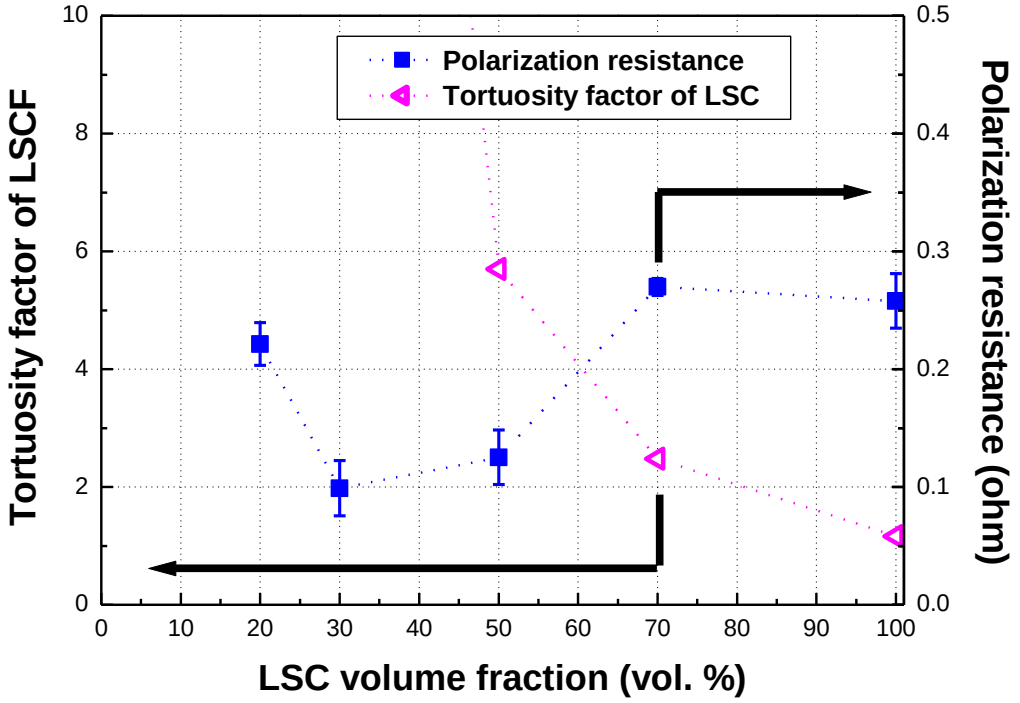

(b) Tortuosity factors of LSC with polarization resistances of LSC-GDC composite cathode.

Fig. 5-7 GDC tortuosity factors and LSC tortuosity factors of composite cathodes shown together with polarization resistances.

Representative volume element which was used in the present study was also considered in order to investigate the relevance of microstructure calculation of the LSC-GDC composite cathode. Microstructures of LSC-GDC composite cathodes were divided as introduced in section 3.1.2, and LSC surface area density and total TPB density were calculated using the divided microstructures. Figure 5-8 shows the comparison of microstructure parameters with divided microstructures.

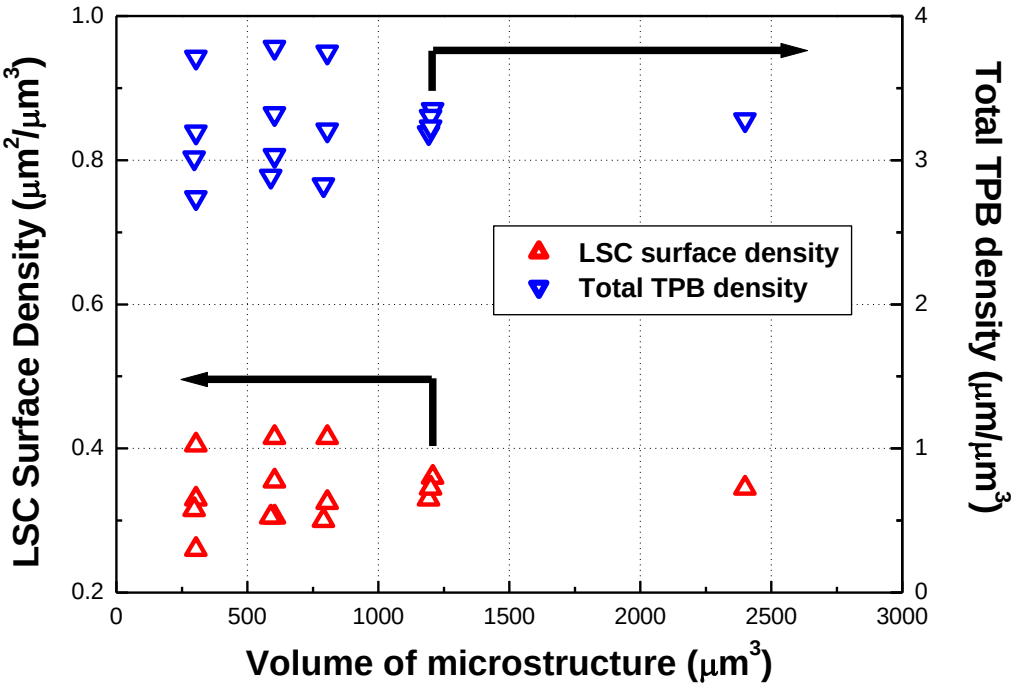

(a) LSC:GDC = 20:80 vol. %.

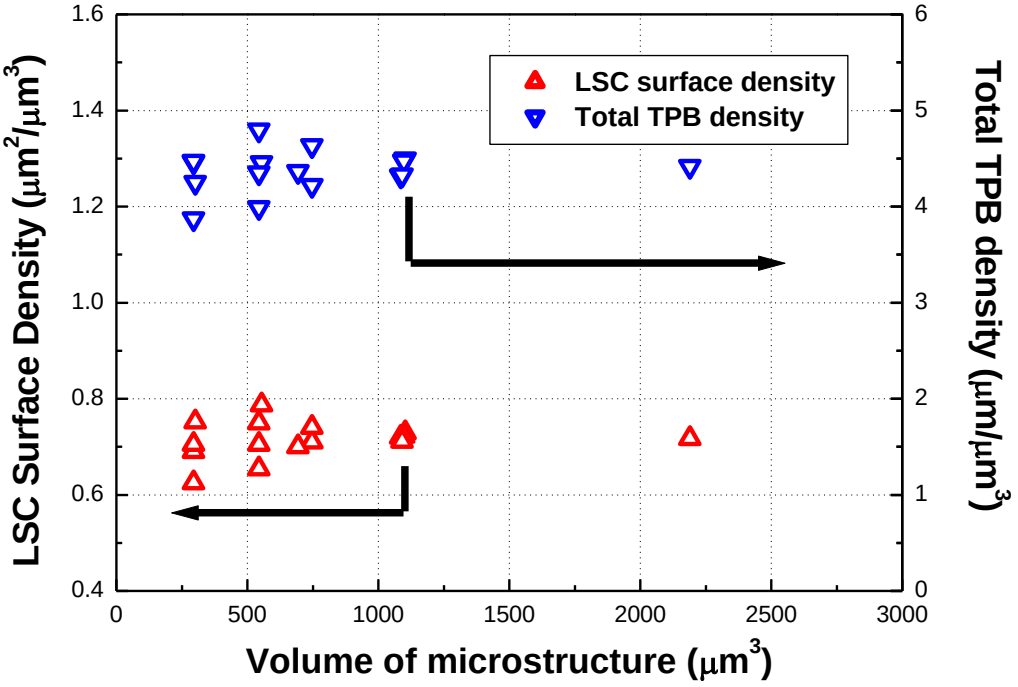

(b) LSC:GDC = 30:70 vol. %.

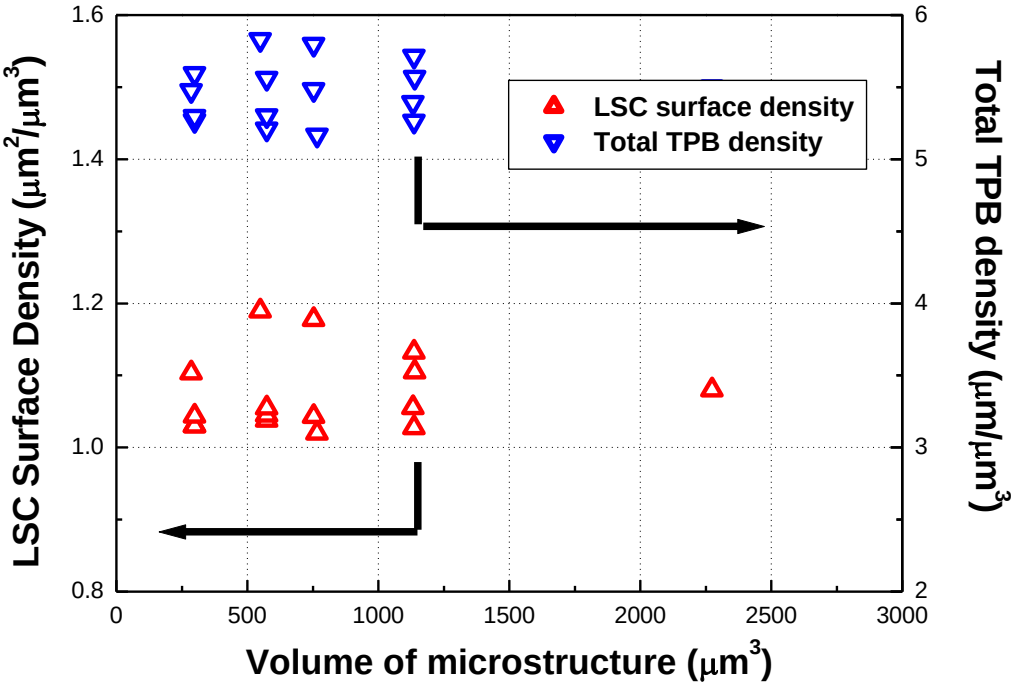

(c) LSC:GDC = 50:50 vol. %.

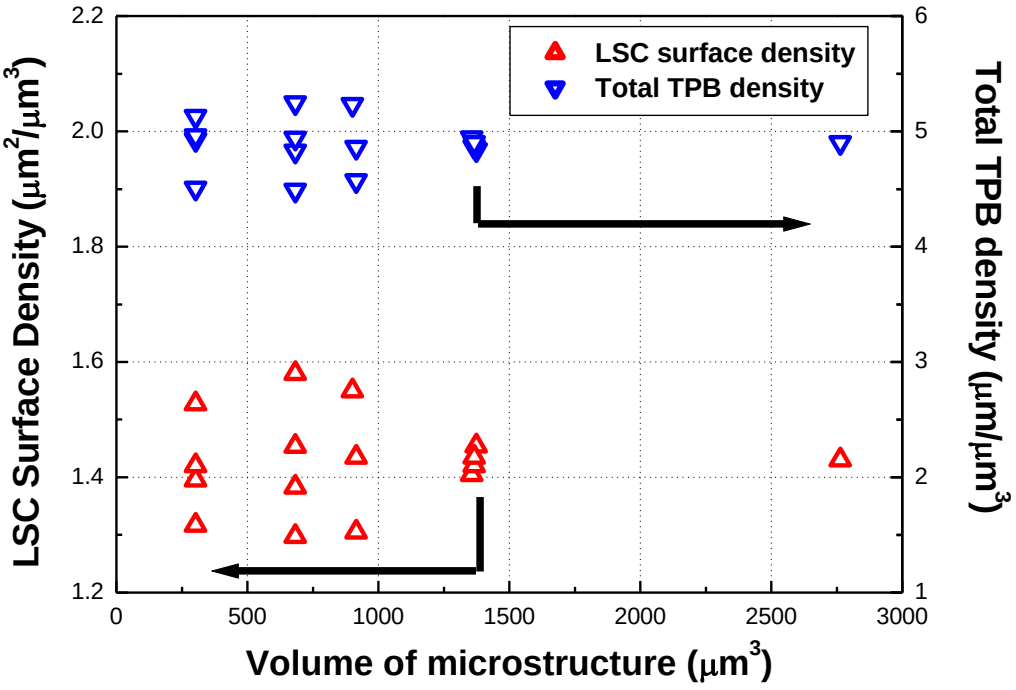

(d) LSC:GDC = 70:30 vol. %.

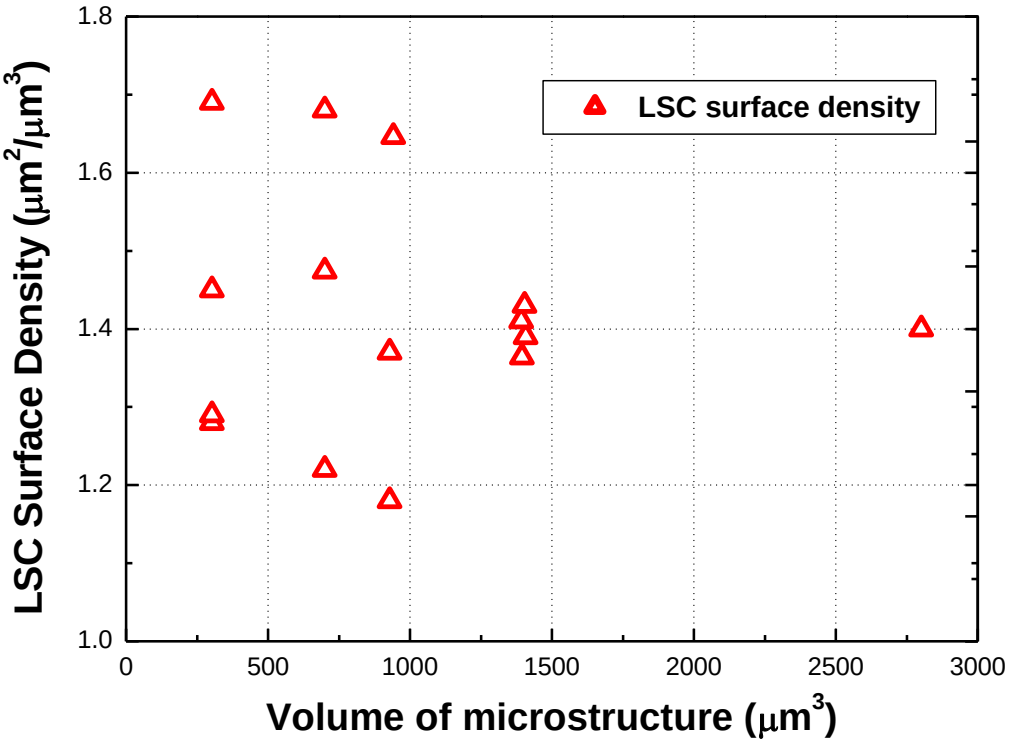

(e) LSC:GDC = 100:0 vol. %.

Fig. 5-8 Verification of RVE by calculations of LSC surface area density and total TPB density with LSC:GDC = (a) 20:80, (b) 30:70, (c) 50:50, (d) 70:30 and (e) 100:0 vol. %.

As seen in Fig. 5-8, the variations of parameters from small to big volume size become smaller, and the values seem to converge as the volume is increased. It is considered that the original microstructures which were used for calculation of microstructure parameters are reliable. It also shows the similar tendency with the LSCF-GDC composite cathode as shown in Fig. 3-9.

5.1.2 Cobalt Oxides

Seeharaj et al. [73] reported that the diffusion of lanthanum and strontium cation from LSC results in the formation of cobalt oxide in the LSC phase. Cobalt oxides can be observed by dark phases in SEM observation using EsB detector [73]. As shown in Table 2, the LSC volume fractions were lower than the target volume fraction. It can be considered that cobalt oxides in the LSC phase were distinguished as the pore phase during binarization process because of its similar atomic weight with carbon which is the main component of epoxy resin filled into the pore. Figure 5-9 shows the comparison of SEM observation between the second electron (SE) image and the EsB image for a

volume ratio of LSC:GDC = 50:50 %. Phase distinctions between SE and EsB images are marked by the circles

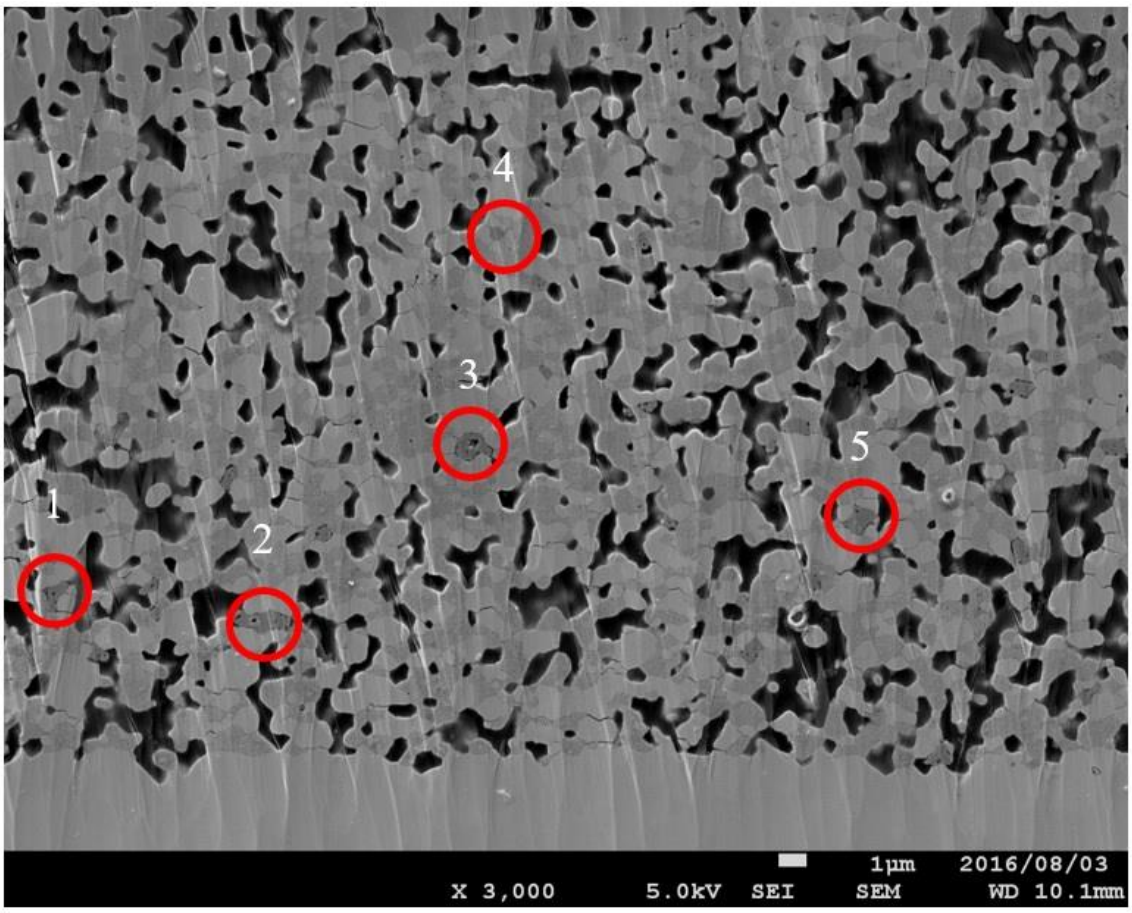

(a) Secondary electron image of LSC:GDC = 50:50 vol. %.

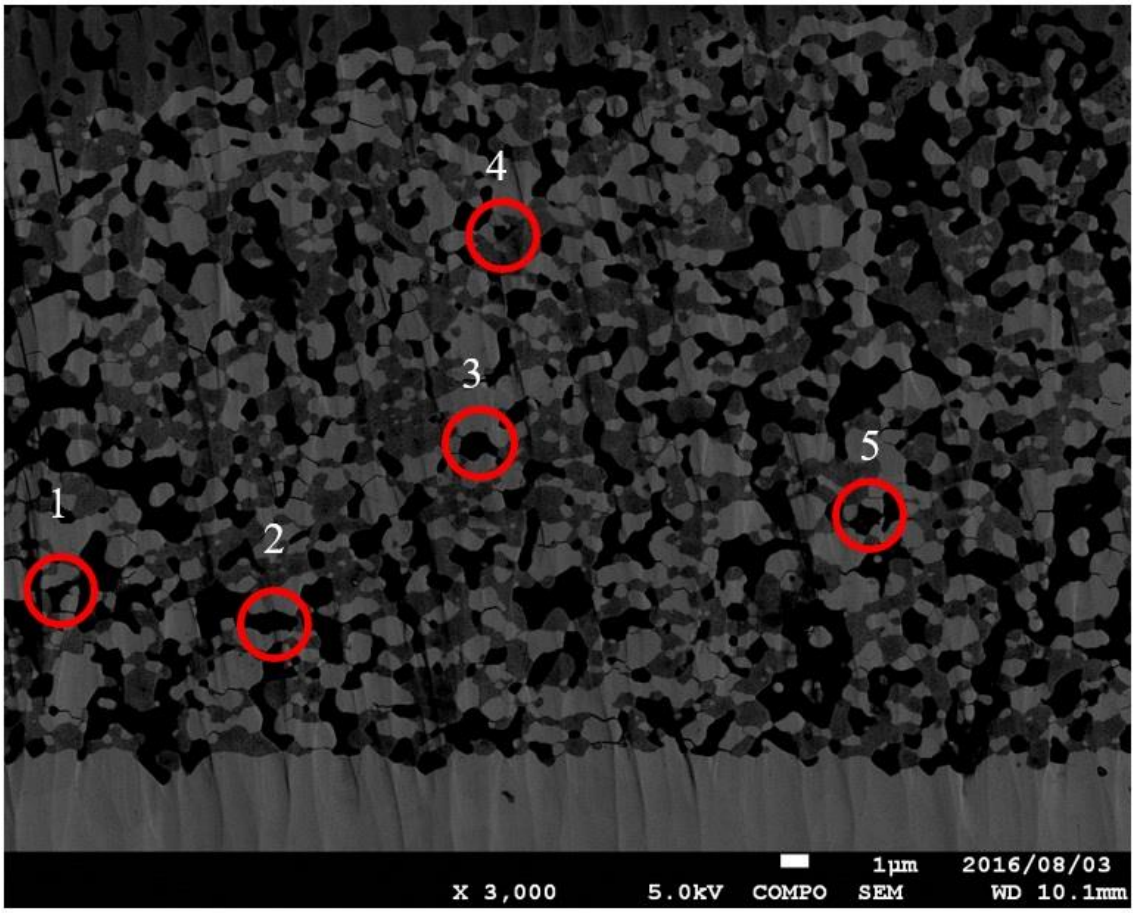

(b) Energy selective backscatter image of LSC:GDC = 50:50 vol. %.

Fig. 5-9 SEM images of LSC:GDC = 50:0 vol. % with (a) SE and (b) EsB detectors.

In the SE image, solid phases inside the circles are clearly seen, while these phases are observed as black phases in the EsB image. In other words, these solid phases are considered as pores in the EsB images. Element of the solid phase inside a circle which is marked by 5 in Fig. 5-9 was investigated by EDX as shown in Fig. 5-10. The result clearly shows that the solid phase is the cobalt oxide. Cobalt oxides are mainly distributed inside the LSC phases.

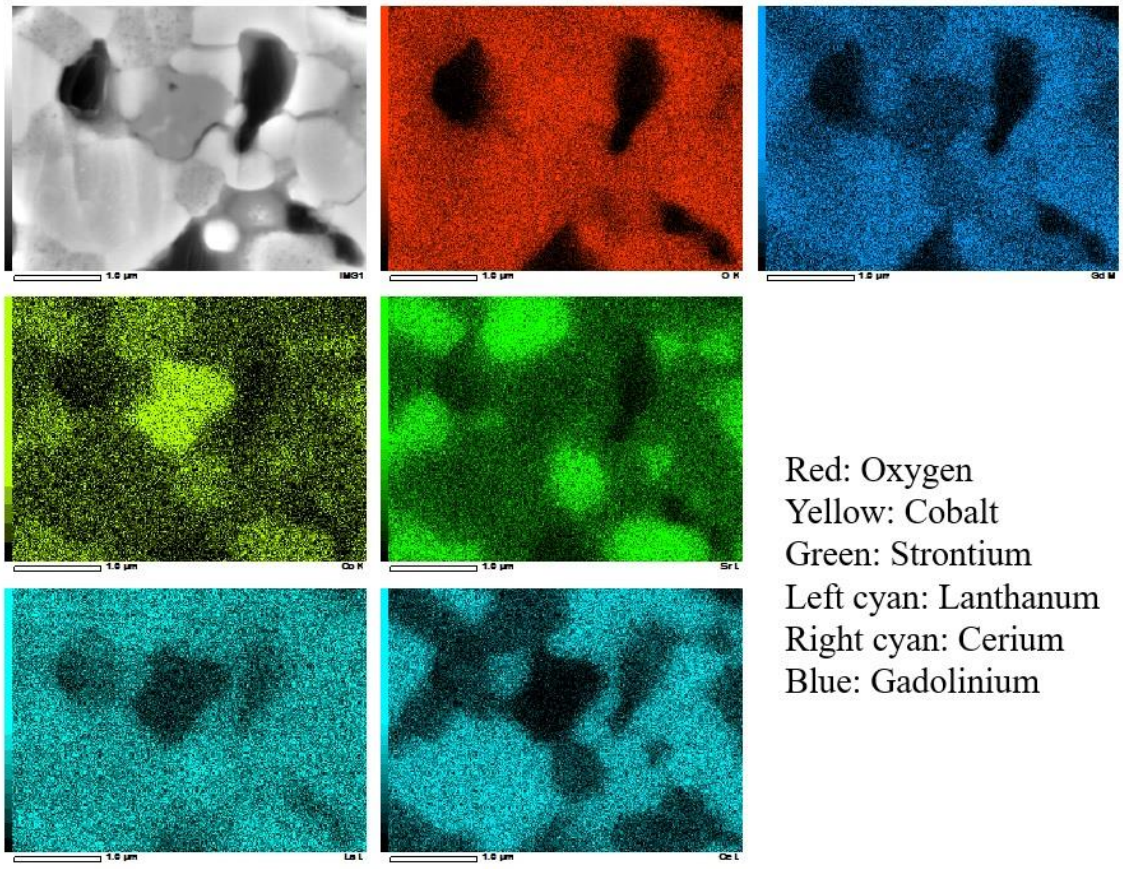

Fig. 5-10 EDX mapping results of the solid phase inside circle '5' in Fig. 5-9.

5.1.3 Comparison with LSCF-GDC Composite Cathodes

Figures 5-11 and 5-12 show the comparisons of the overpotentials and the polarization resistances at OCV between LSC-GDC and LSCF-GDC composite cathodes.

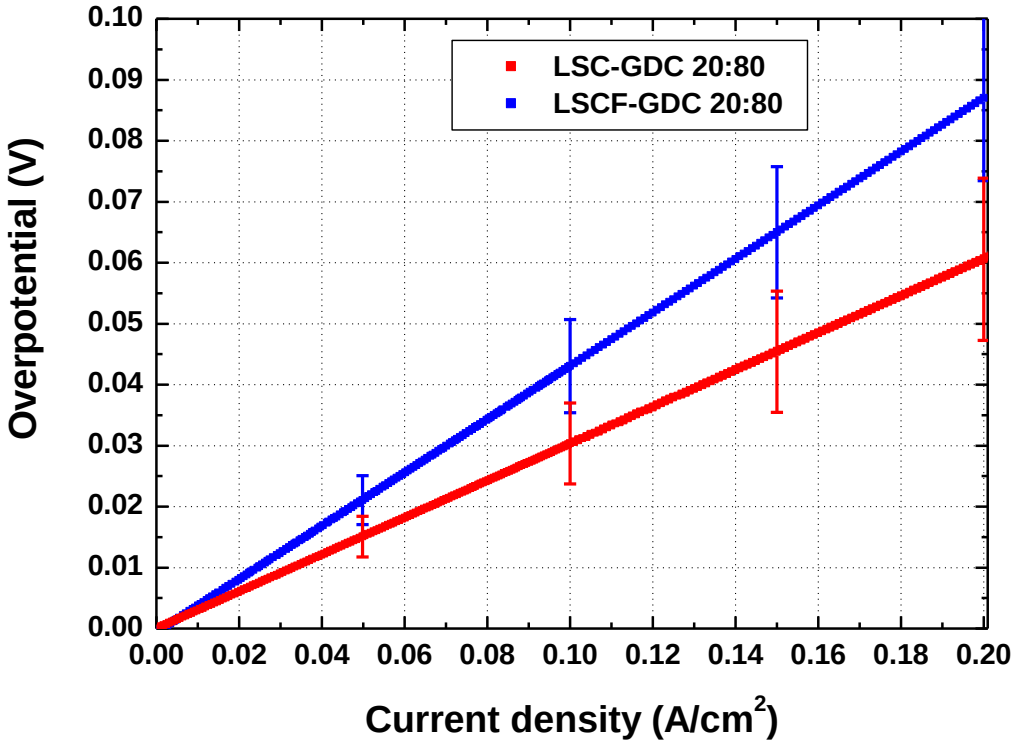

(a) LSC:GDC and LSCF:GDC = 20:80 vol. %.

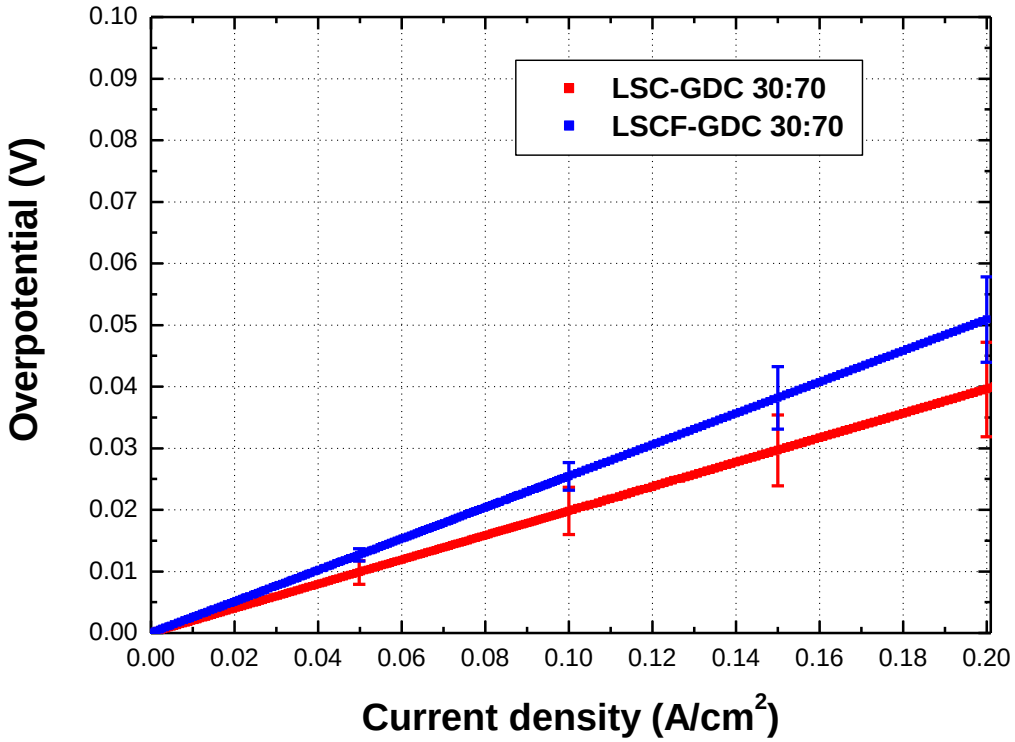

(b) LSC:GDC and LSCF:GDC = 30:70 vol. %.

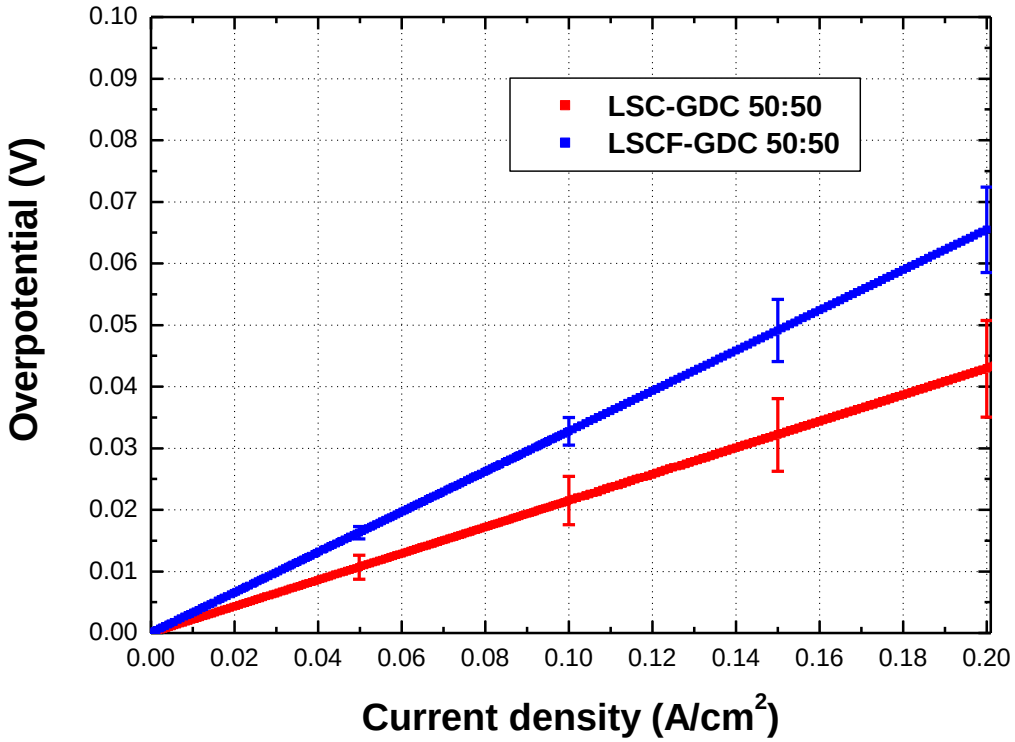

(c) LSC:GDC and LSCF:GDC = 50:50 vol. %.

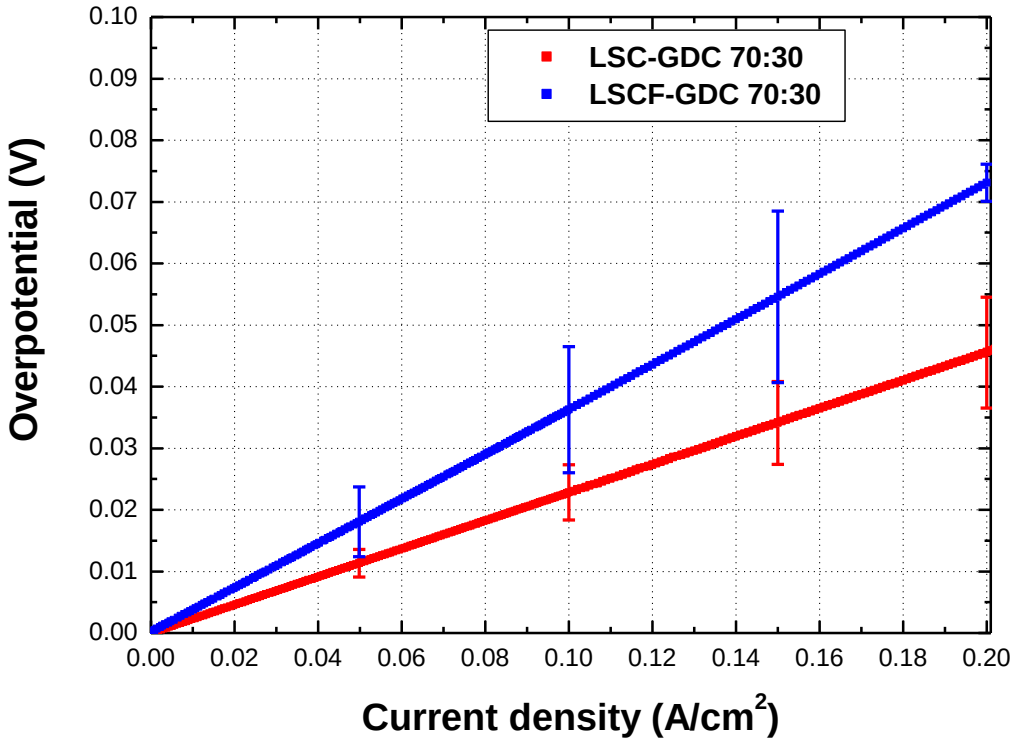

(d) LSC:GDC and LSCF:GDC = 70:30 vol. %.

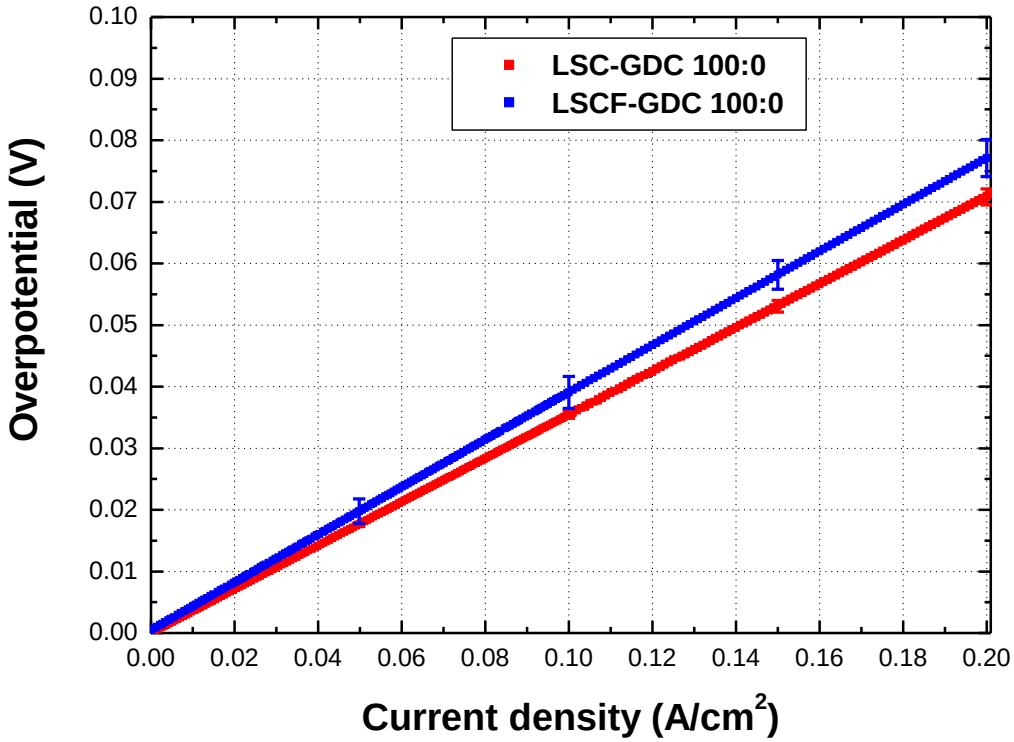

(e) LSC:GDC and LSCF:GDC = 100:0 vol. %.

Fig. 5-11 Comparisons of overpotentials between LSC-GDC and LSCF-GDC composite cathodes. Volume ratio is (a) 20:80, (b) 30:70, (c) 50:50, (d) 70:30 and (e) 100:0 %.

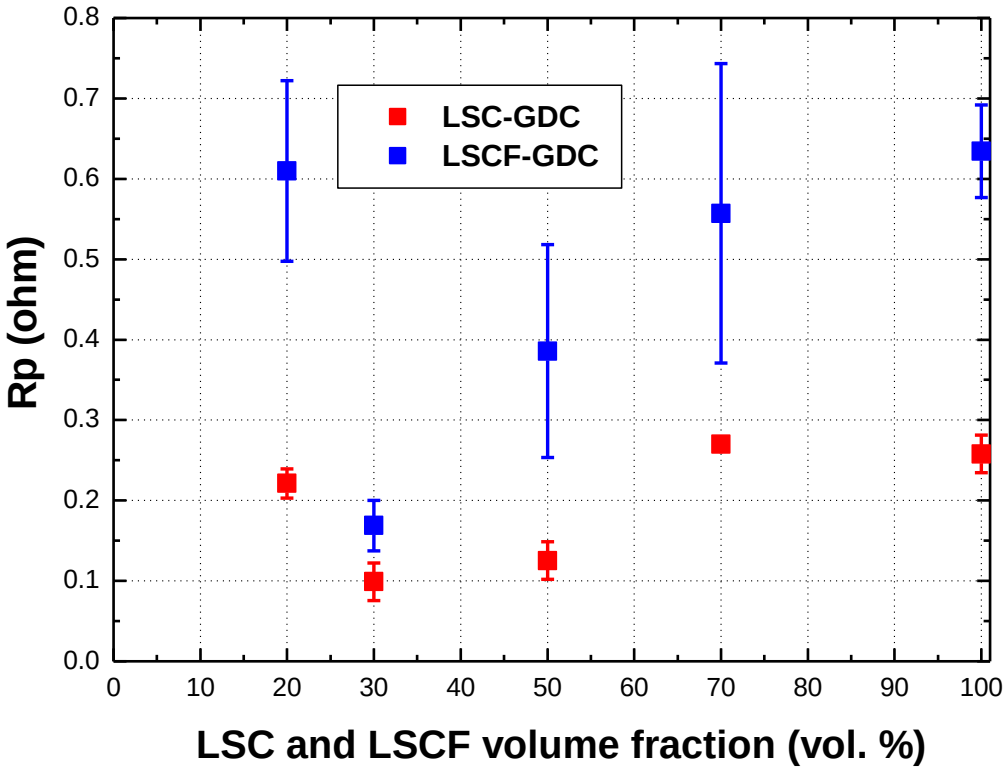

Fig. 5-12 Comparison of polarization resistances at OCV between LSC-GDC and LSCF-GDC composite cathodes.

Regardless of the volume ratios, LSC-GDC composite cathode always shows better performance than the LSCF-GDC composite cathode. The best performance was achieved at a volume ratio of 30:70 % for both LSC-GDC and LSCF-GDC composite cathodes. It is clarified that addition of GDC is also effective for the LSC cathode. Smaller ovepotential value of LSC:GDC = 20:80 vol. % than LSCF:GDC = 20:80 vol. % implies that high electronic conductivity and phase connectivity of LSC compensated the poor electronic connection of the LSC phase.

Microstructure parameters were also compared as shown in Fig. 5-13. For the parameter calculations of LSC-GDC, voxel size of 25 nm was used instead of voxel size of 50 nm which was used for the LSCF-GDC cases as described in Chap. 3. Therefore, microstructure parameters were also calculated with a re-meshed voxel of same 50 nm for the LSC-GDC composite cathode as well to see the dependence on resolution.

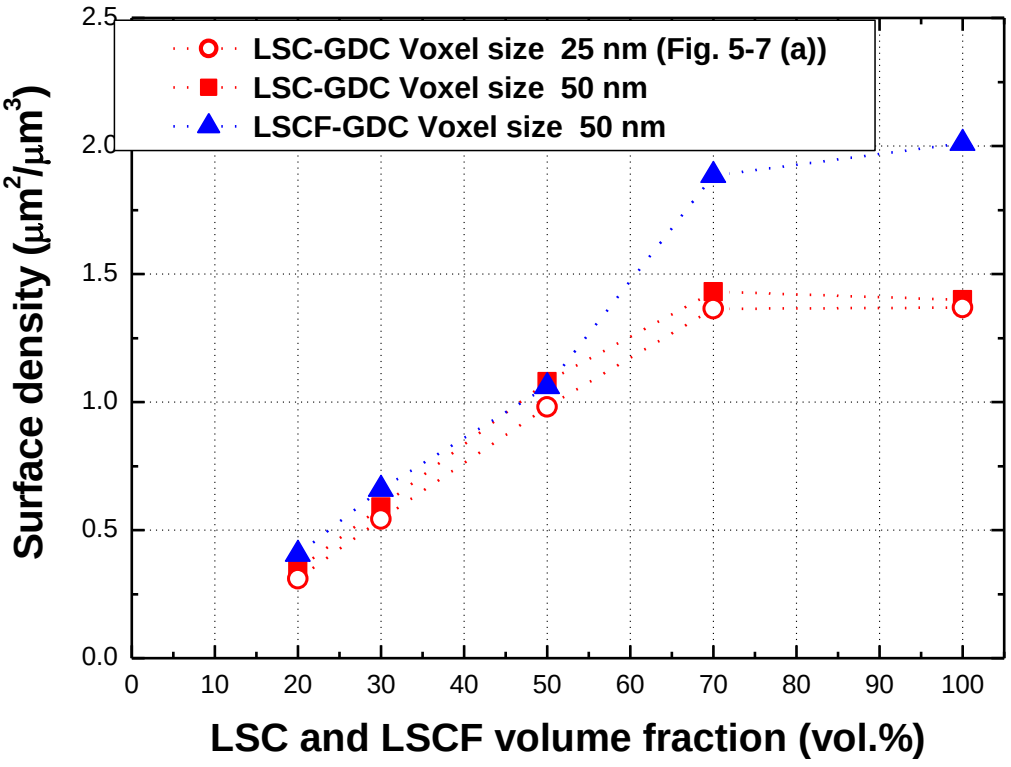

(a) Surface area densities of LSC and LSCF.

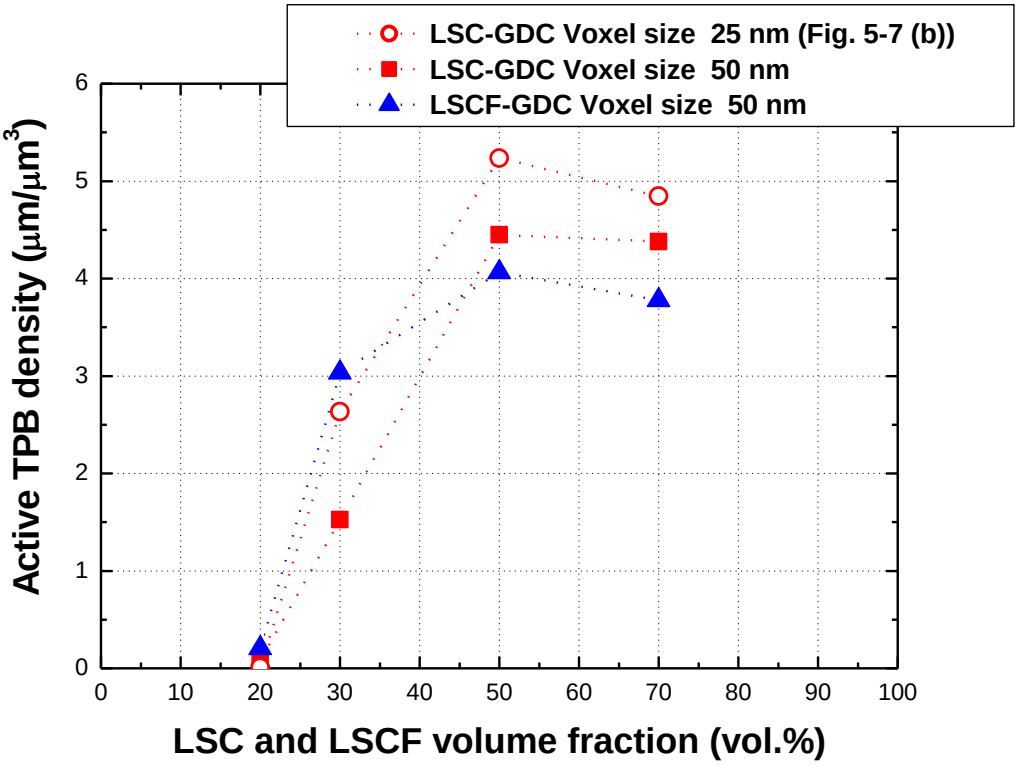

(b) Active TPB densities of LSC and LSCF.

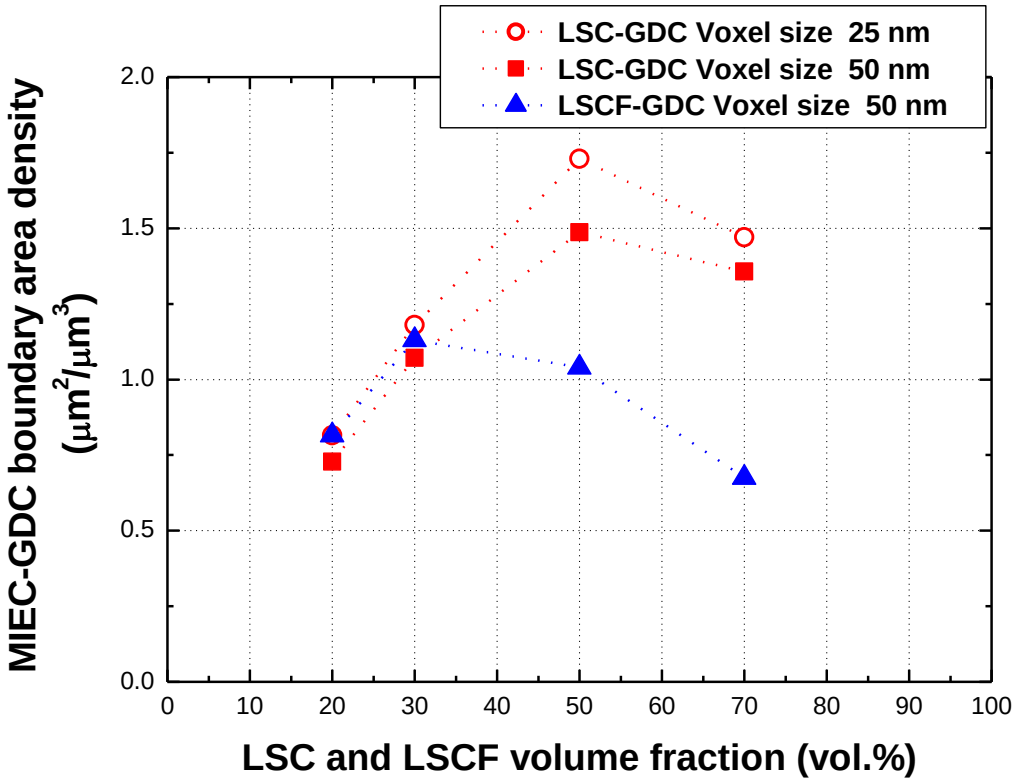

(c) MIEC-GDC boundary area densities of LSC-GDC and LSCF-GDC.

Fig. 5-13 Comparison of microstructure parameters between LSC-GDC and LSCF-GDC composite cathodes.

As shown in Fig. 5-13 (a), the surface area densities of LSC-GDC composite cathodes are smaller at lower GDC volume fraction compare to those of LSCF-GDC, due to the high sinterability of LSC. The active TPB densities of LSC-GDC are slightly lower than those of LSCF-GDC for the 20:80 and 30:70 vol. %. However, it becomes larger for the 50:50 and 70:30 vol. % as shown in Fig. 5-13 (b). It can be considered that the increase of LSC-GDC boundary area density as shown in Fig. 5-13 (c), caused by agglomeration of LSC, results in the increase of TPB length. The overpotential difference between pure LSC and LSCF cathodes was small as shown in Fig. 5-11(e). It is considered that the decrease of LSC surface area as shown in Fig. 5-13 (a) degrades the cathode performance for the pure LSC cathode.

5.2 Numerical Simulations

In this chapter, electrochemical reaction mechanisms of LSC-GDC composite cathodes with 30:70, 50:50, 70:30, and 100:0 vol. % were simulated by the Lattice Boltzmann Method (LBM). Simulation of a LSC:GDC = 20:80 vol. % case was excluded because of it did not converge due to the same reason with the case of LSCF-GDC composite cathodes.

5.2.1 Computational Domain

Computational domains of LSC-GDC composite cathodes are similar with those used for the LSCF-GDC composite cathodes which are described in details in Chap. 3. A resolution of 100 nm was used. For the LSC-GDC composite cathode, LSCF was set as the porous current collection layer in order to match with the experimental condition. Exchange current density and ionic conductivity of LSCF were introduced into the current collection layer as shown in Table 5-3. In other words, LSC-GDC composite cathode of 25 μm and LSCF of 10 μm were prepared for the computational domain. Then, 5 μm thick dense electrolyte and current collector were attached as introduced in Chap. 3. Figure 5-14 shows the computational domains.

Table 5-3 Reaction and diffusion parameters in the porous LSCF current collector.

Properties	Values
Exchange current density (A/m^2)	4.088
Ionic conductivity (S/m)	0.474

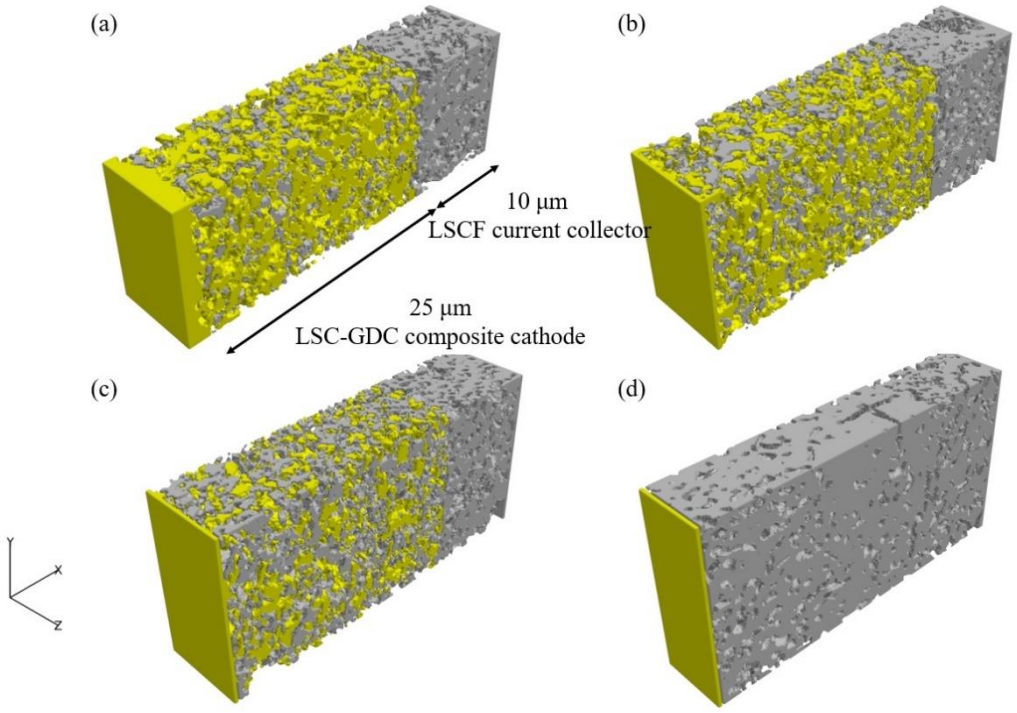

Fig. 5-14 Computational domains for LBM simulation with LSC:GDC = (a) 30:70, (b) 50:50, (c) 70:30, and (d) 100:0 vol. %.

In the present numerical simulations, isolated phases were considered as non-conducting phases and both unknown and connected phases were considered as conducting phases.

5.2.2 Contribution from Two reaction Mechanisms

For the numerical simulation of LSC-GDC composite cathode, contributions of surface and TPB reactions were considered in common with the case of LSCF-GDC composite cathode. Exchange current density for LSC surface reaction was fitted using an experimental result of pure LSC, and the exchange current density for TPB reaction was fitted using the experimental results of composites. Fitted exchange current density for LSC surface reaction and TPB reaction are shown in Table 5-4.

Table 5-4 Fitted exchange current densities.

	Exchange current density
Surface reaction (A/m^2)	5.484
TPB reaction (A/m)	9.884×10^{-6}

Figure 5-15 shows the predicted overpotentials with the experimental data.

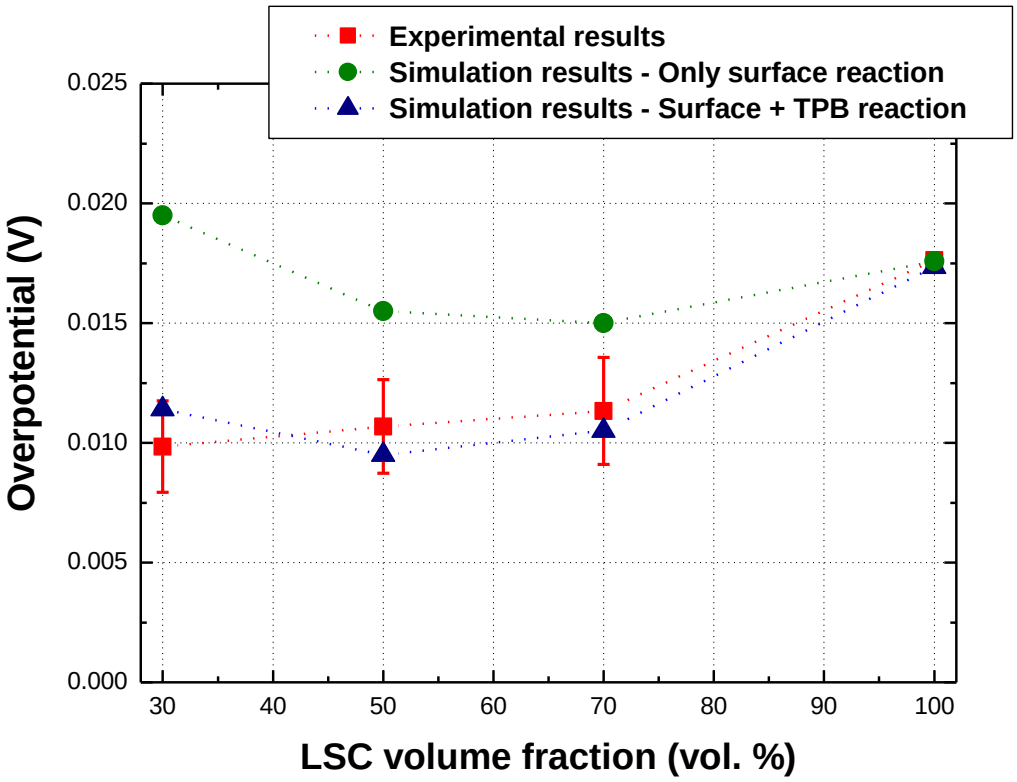

Fig. 5-15 Predicted overpotential results of LSC-GDC composite cathodes with the experimental results.

It is shown that predicted overpotential results are overestimated without considering TPB reaction. When both surface and TPB reactions are considered, simulation results show good agreement with the experimental results with the increase of LSCF volume fraction from 50 to 100 %. However, small discrepancy can be seen for the case of LSC:GDC = 30:70 vol. %. It is considered that expansion of voxel size from 25 to 100 nm in the numerical simulation has an influence on the simulation result. Variations of microstructure parameters with the change of voxel size is shown in Table 5-5.

Table 5-5 Variations of microstructure parameters with different voxel size

LSC:GDC =	30:70 vol. %	50:50 vol. %	70:30 vol. %	100:0 vol. %
Active TPB density (25 nm)	2.635 $\mu m/\mu m^3$	5.234 $\mu m/\mu m^3$	4.846 $\mu m/\mu m^3$	
Active TPB density (100 nm)	0.998 $\mu m/\mu m^3$	3.815 $\mu m/\mu m^3$	3.858 $\mu m/\mu m^3$	
LSC surface area density (25 nm)	0.59 $\mu m^2/\mu m^3$	1.08 $\mu m^2/\mu m^3$	1.43 $\mu m^2/\mu m^3$	1.40 $\mu m^2/\mu m^3$
LSC surface area density (100 nm)	0.49 $\mu m^2/\mu m^3$	0.91 $\mu m^2/\mu m^3$	1.32 $\mu m^2/\mu m^3$	1.33 $\mu m^2/\mu m^3$
Tortuosity factor of GDC (25 nm)	2.29	3.68	23.64	
Tortuosity factor of GDC (100 nm)	2.57	4.40	44.38	
Tortuosity factor of LSC (25 nm)	30.32	5.70	2.48	1.16
Tortuosity factor of LSC (100 nm)	105.10	7.17	2.87	1.20

The reaction area is decreased and the tortuosity factor is increased by the expansion of voxel size. Notable point is that the tortuosity factor of LSC drastically increases for the LSC:GDC = 30:70 vol. % from 30.32 to 105.10. It causes the deterioration of electronic conduction through the LSC phase. It is considered that increase of overpotential in the simulation result is possibly due to the disconnection of electronic path.

Reaction current distributions are shown in Fig. 5-16. Same as the case of LSCF-GDC composite cathodes, reaction current distributions due to TPB reaction are considerable. Figure 5-17 shows the quantified contribution rates of LSC surface and TPB reactions in the composite of 25 μm. All composite cathodes show over 40 % of contribution rates of TPB reaction except for a case of LSC:GDC = 100:0 vol. %. Similar with the case of LSCF-GDC composite cathode, TPB reaction occupies about 64 % of the reaction current for a LSC:GDC = 30:70 vol. % sample which shows the best cathode performance. It can be considered that TPB reaction dominates the electrochemical reactions in the LSC-GDC composite cathodes.

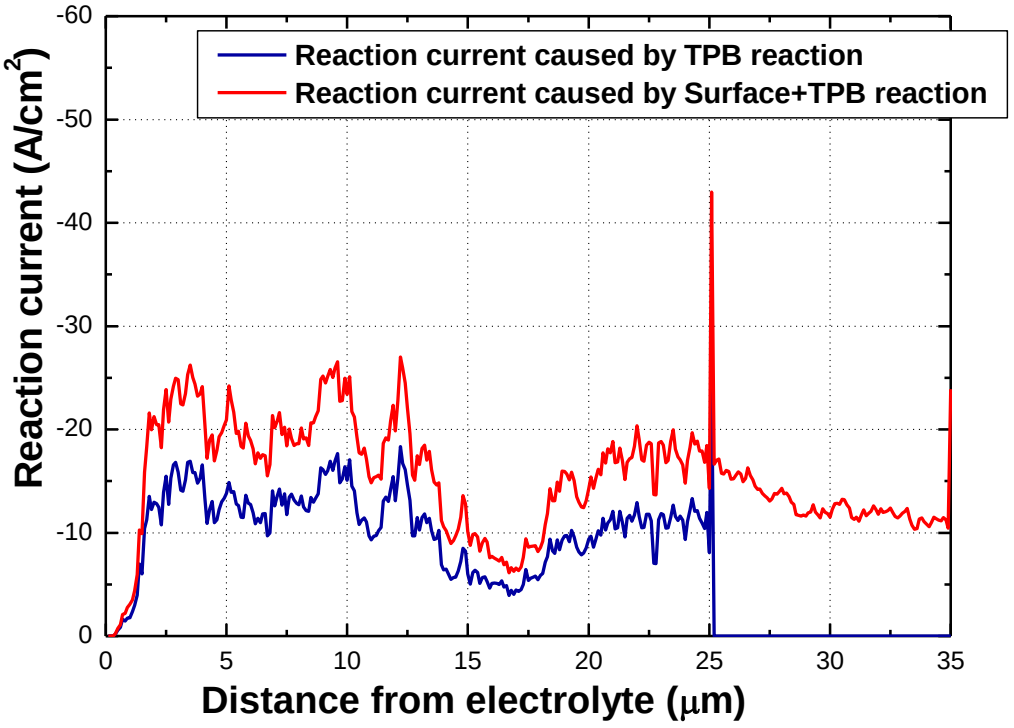

(a) LSC:GDC = 30:70 vol. %

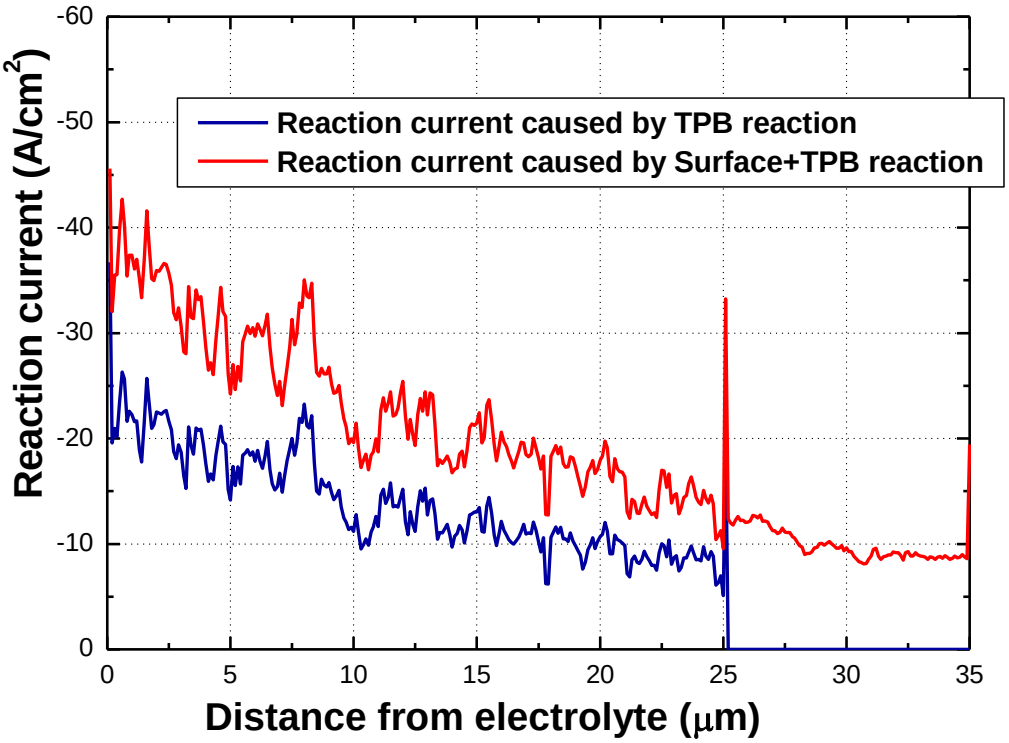

(b) LSC:GDC = 50:50 vol. %

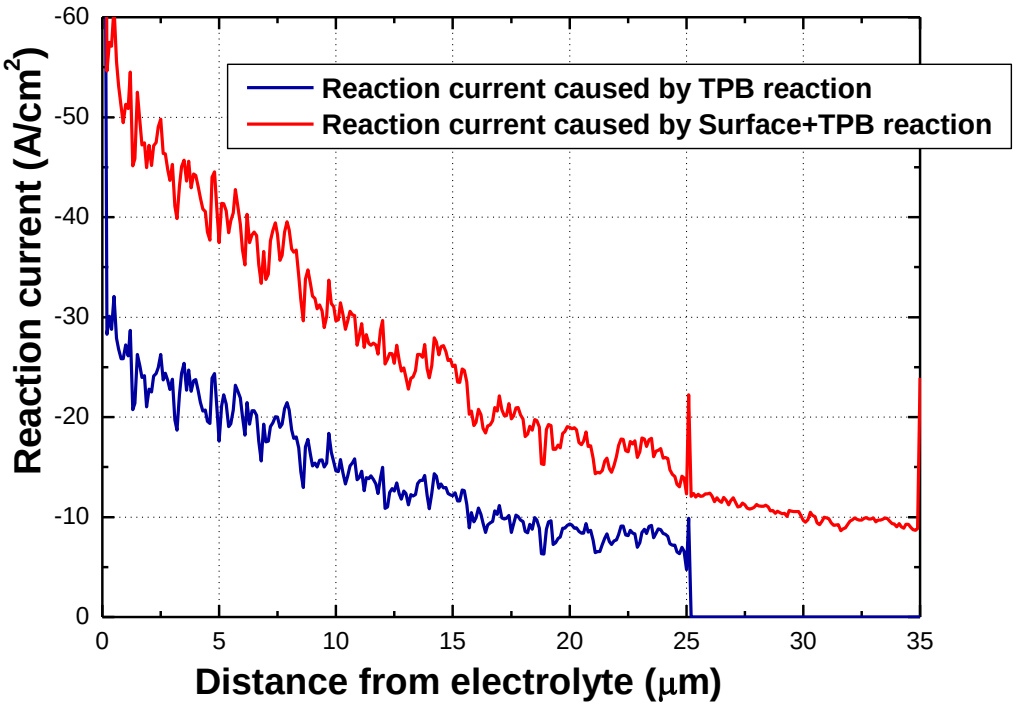

(c) LSC:GDC = 70:30 vol. %

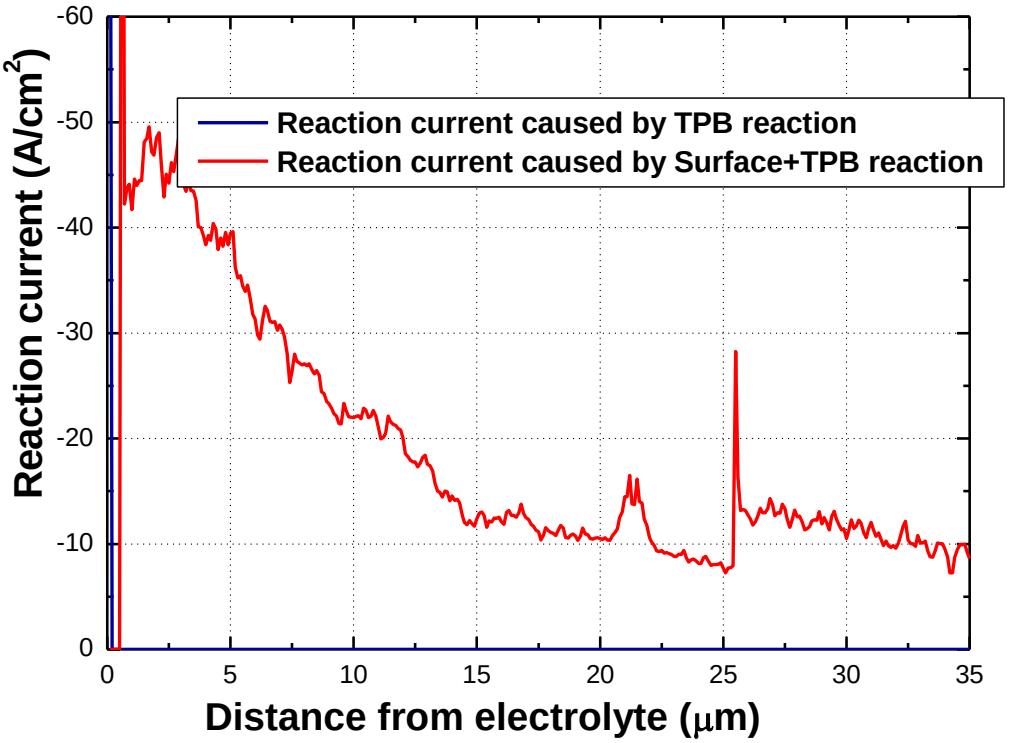

(d) LSC:GDC = 100:0 vol. %

Fig. 5-16 Reaction current distributions of LSC-GDC composite cathode. The volume ratio of LSC:GDC = (a) 30:70, (b) 50:50, (c) 70:30, and (d) 100:0 vol. %.

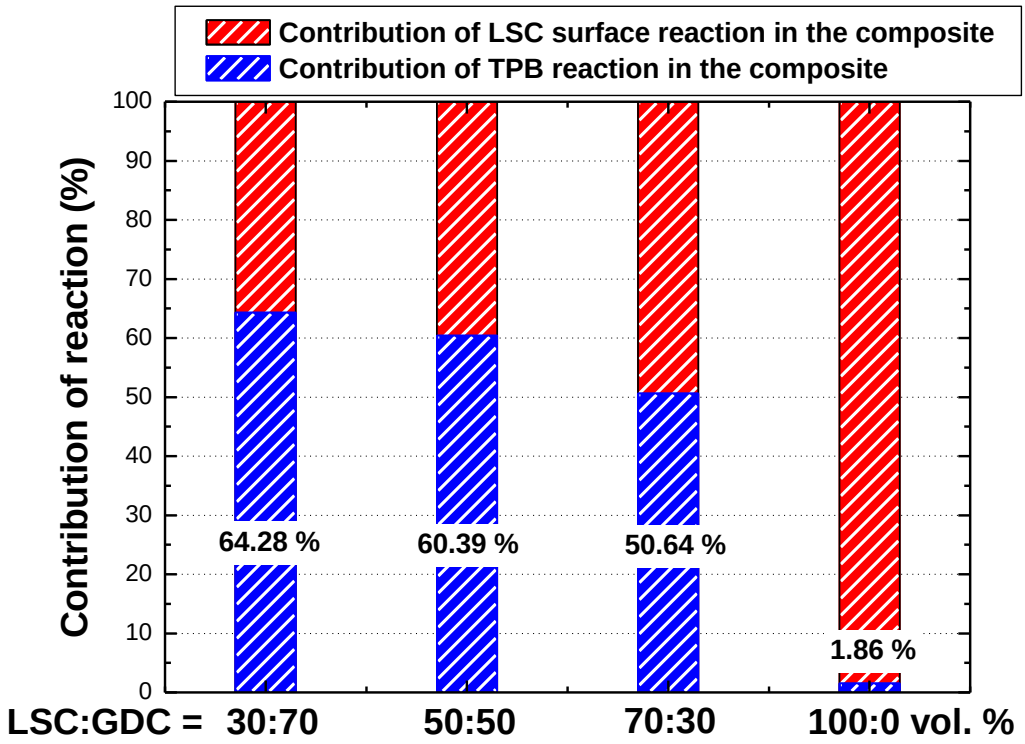

Fig. 5-17 Contribution of LSC surface and TPB reactions in the composite of 25 μm.

As introduced in Chapter 3, local activation overpotential and ionic conduction loss in the LSC-GDC composite cathodes are quantified using a ladder model. Figure 5-18 indicates the ionic overpotential distributions of LSC-GDC composite cathodes. Similar to the LSCF-GDC composite cathode, ionic overpotential is increased as the total overpotential is increased. It is considered that ionic conduction resistance affects the cathode performance for the LSC-GDC composite cathode.

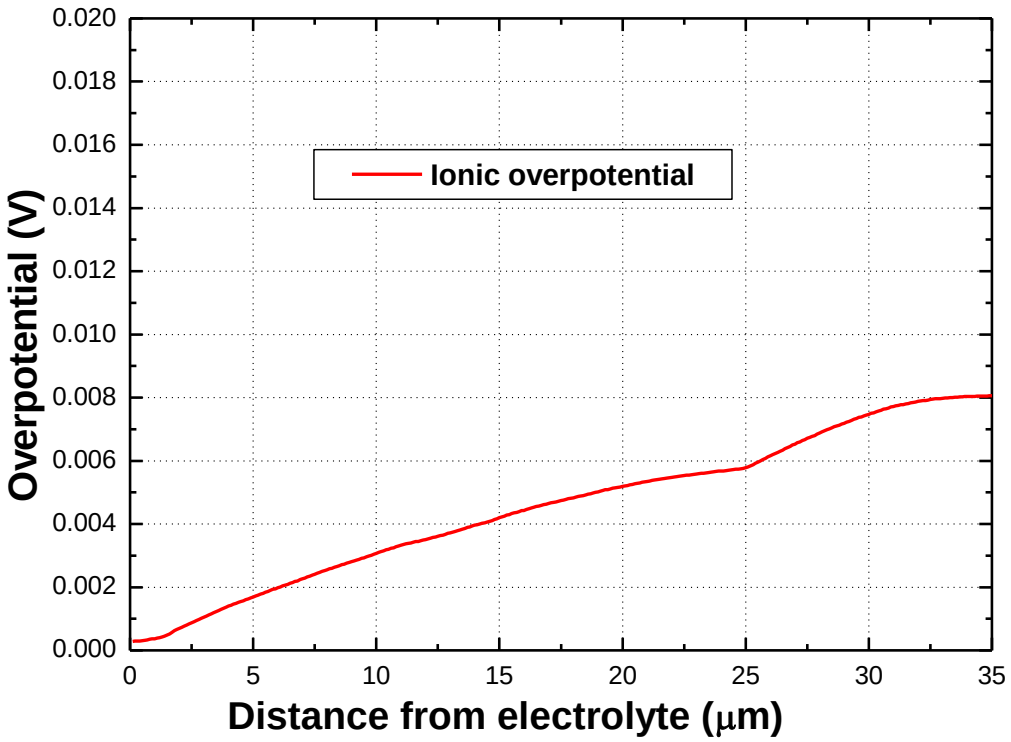

(a) LSC:GDC = 30:70 vol. %.

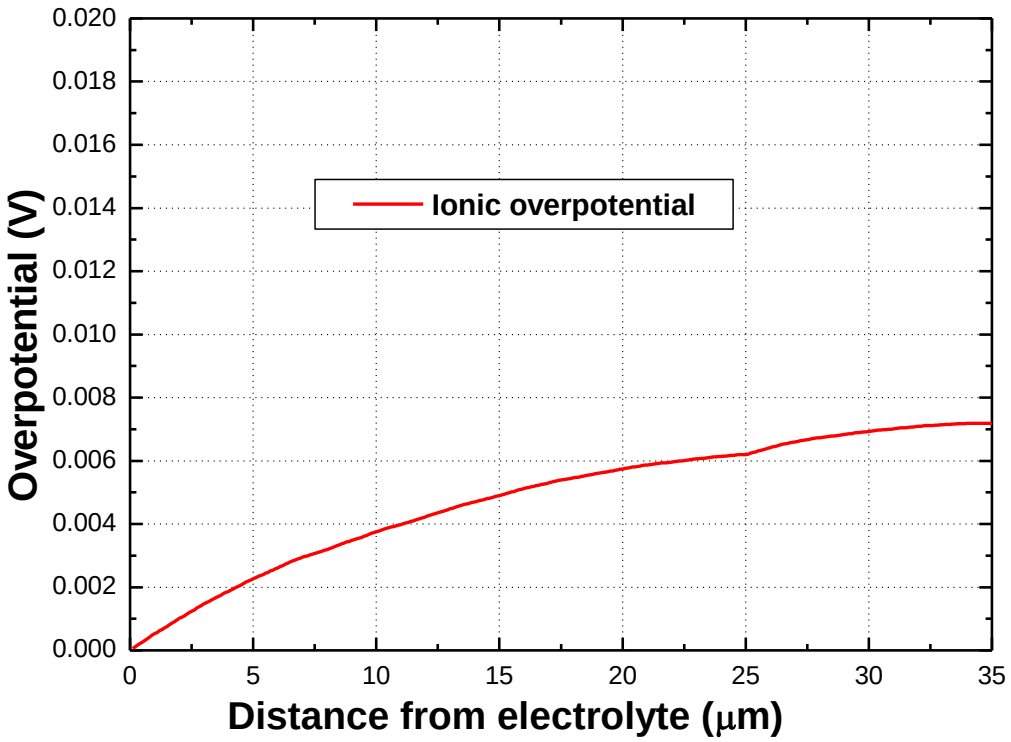

(b) LSC:GDC = 50:50 vol. %.

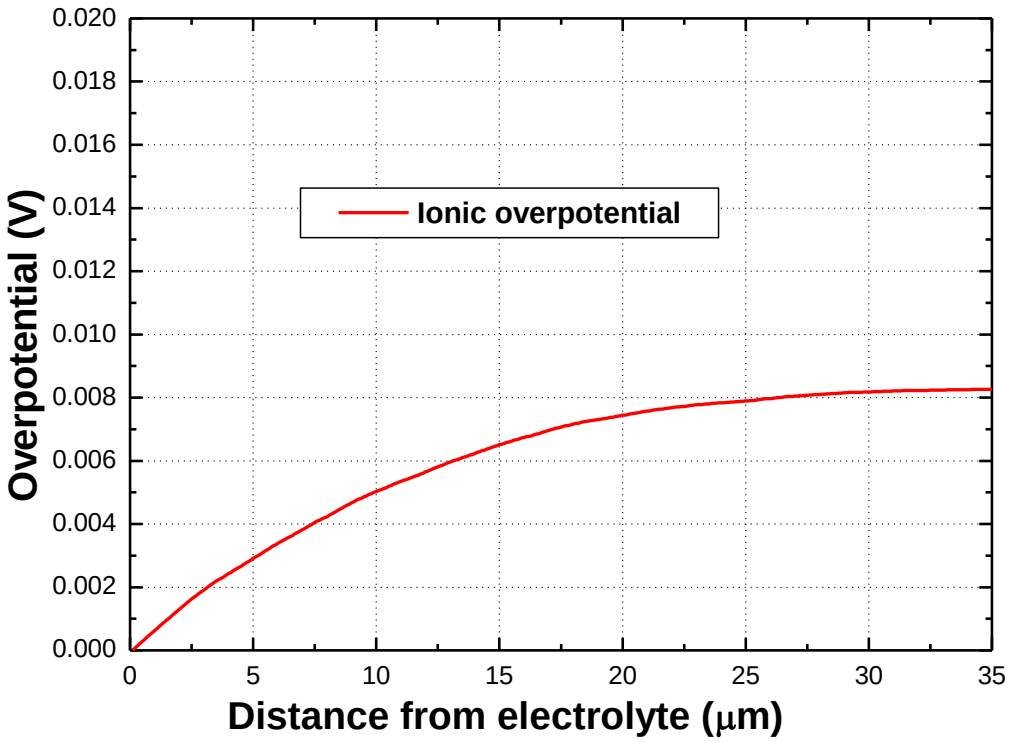

(c) LSC:GDC = 70:30 vol. %.

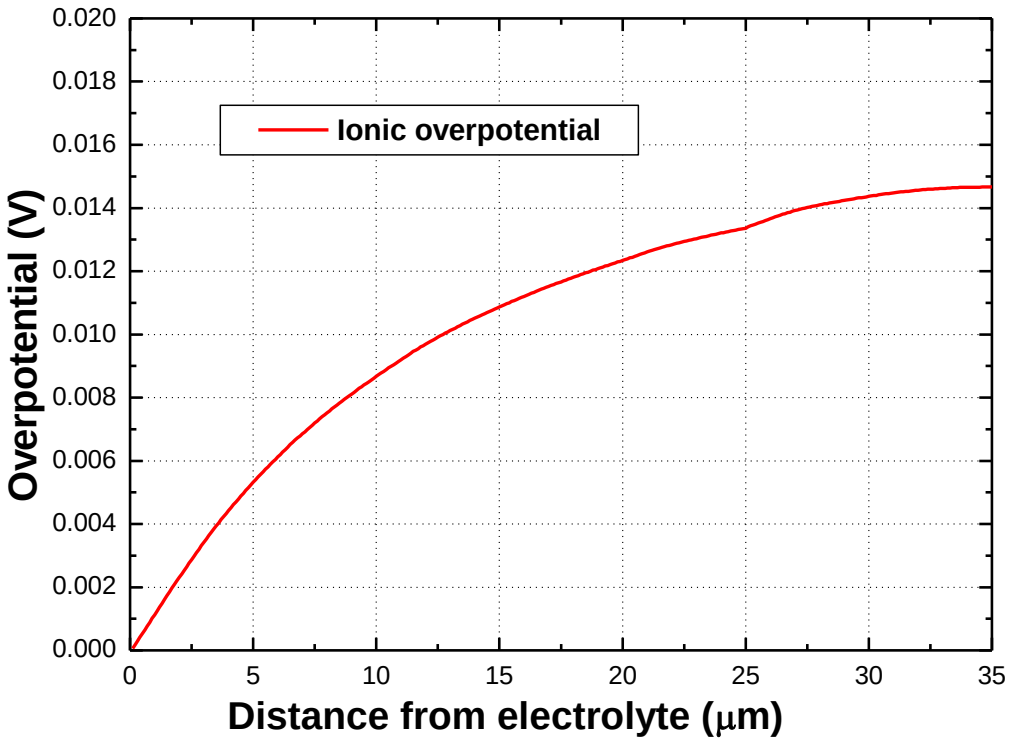

(d) LSC:GDC = 100:0 vol. %

Fig. 5-18 Ionic overpotential distributions in the composite cathode. The volume ratios of LSC:GDC are (a) 30:70, (b) 50:50, (c) 70:30, and (d) 100:0 %.

Figure 5-19 represents the ionic and electronic current distributions in the LSC-GDC composite cathodes. Exchange between ionic and electronic currents is distributed uniformly for all composite cathodes even close to the current collector. It indicates that reactive thickness of LSC-GDC composite cathode is elongated. Due to the poor surface reaction kinetics in the porous LSCF current collection layer, the gradient of current distribution is changed at cathode thickness = 25 μm.

Oxygen chemical potential distributions are shown in Fig. 5-20. As introduced in Chap. 3, the dark blue phase indicate that oxygen chemical potential is in equilibrium with the gas phase. With the increase of GDC volume fraction, the oxygen chemical potential is distributed more uniformly. It is considered that improvement of effective ionic conductivity by GDC addition contributes to the cathode performance, which is accompanied by the elongation of the reactive thickness as shown in Fig. 5-19. Polarization resistances at OCV with different cathode thicknesses are shown in Fig. 5-21. Only the volume ratios of LSC:GDC = 30:70 and 50:50 % were investigated. The polarization resistances decreased with the increase of cathode thickness for both cases. The experimental results

are also in accordance with the numerical simulation results.

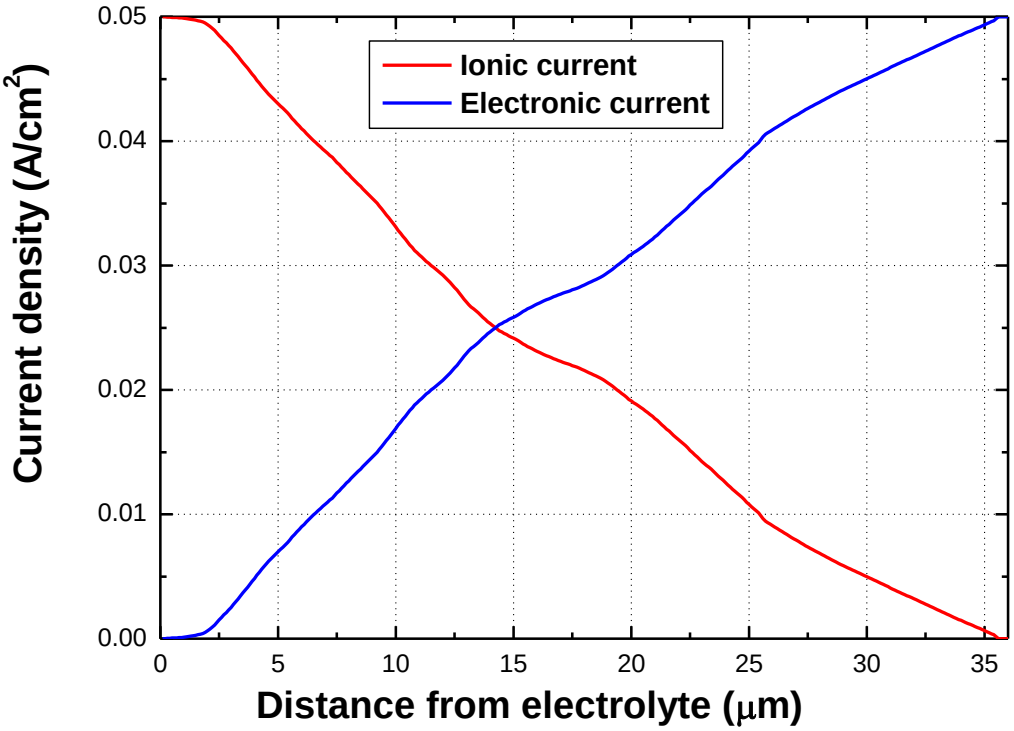

(a) LSC:GDC = 30:70 vol. %

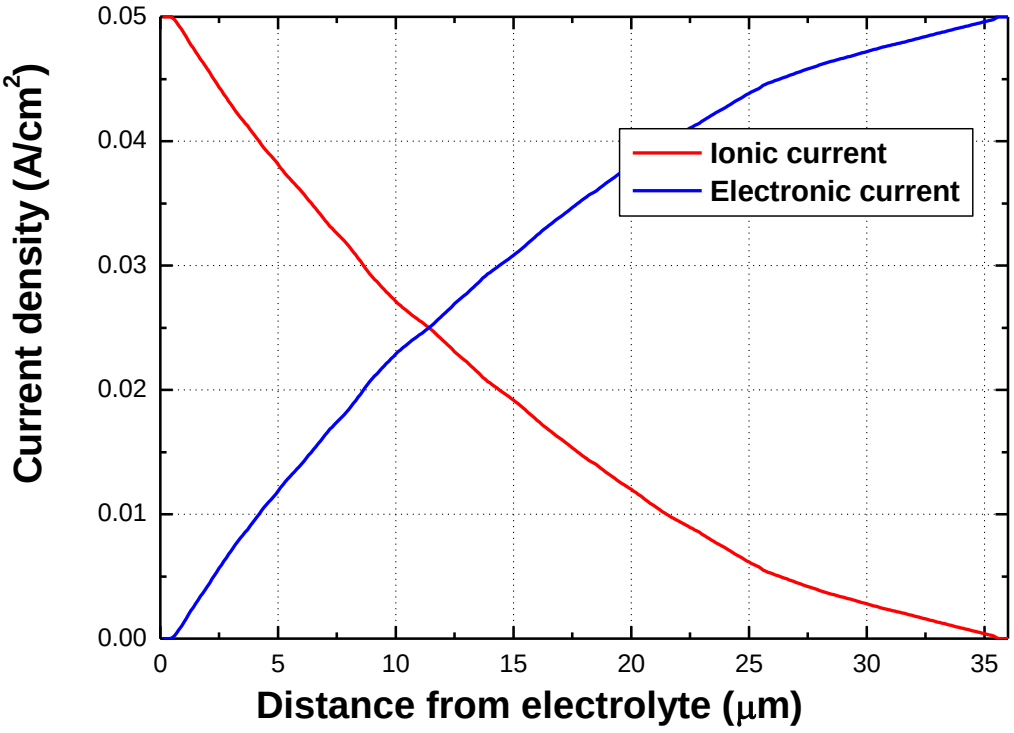

(b) LSC:GDC = 50:50 vol. %

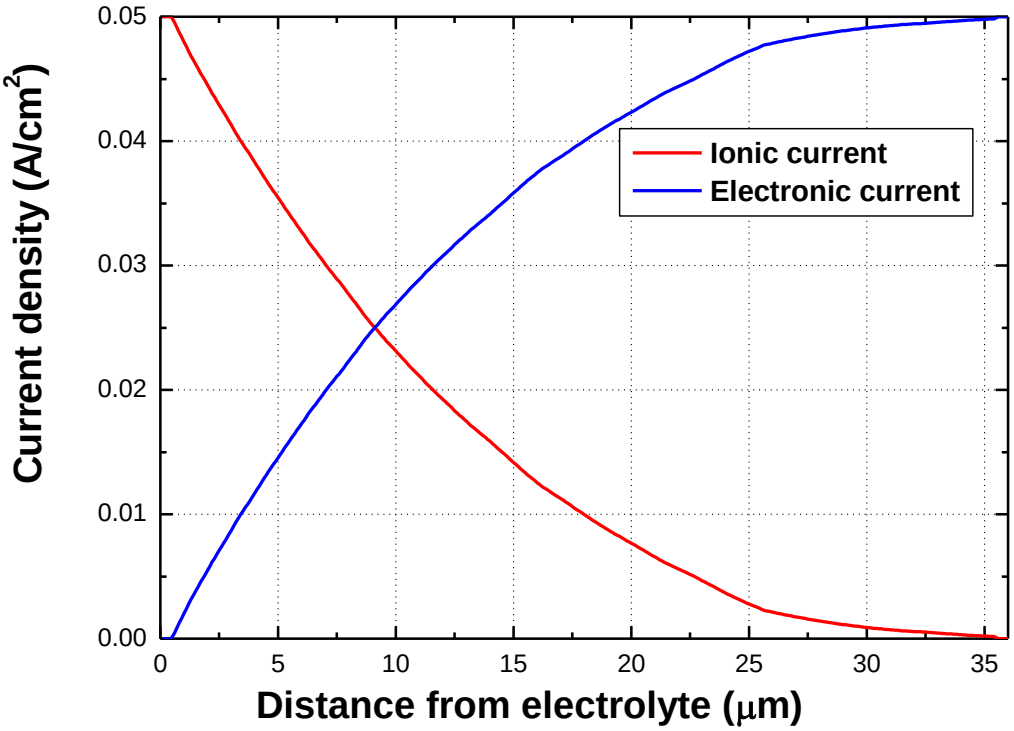

(c) LSC:GDC = 70:30 vol. %

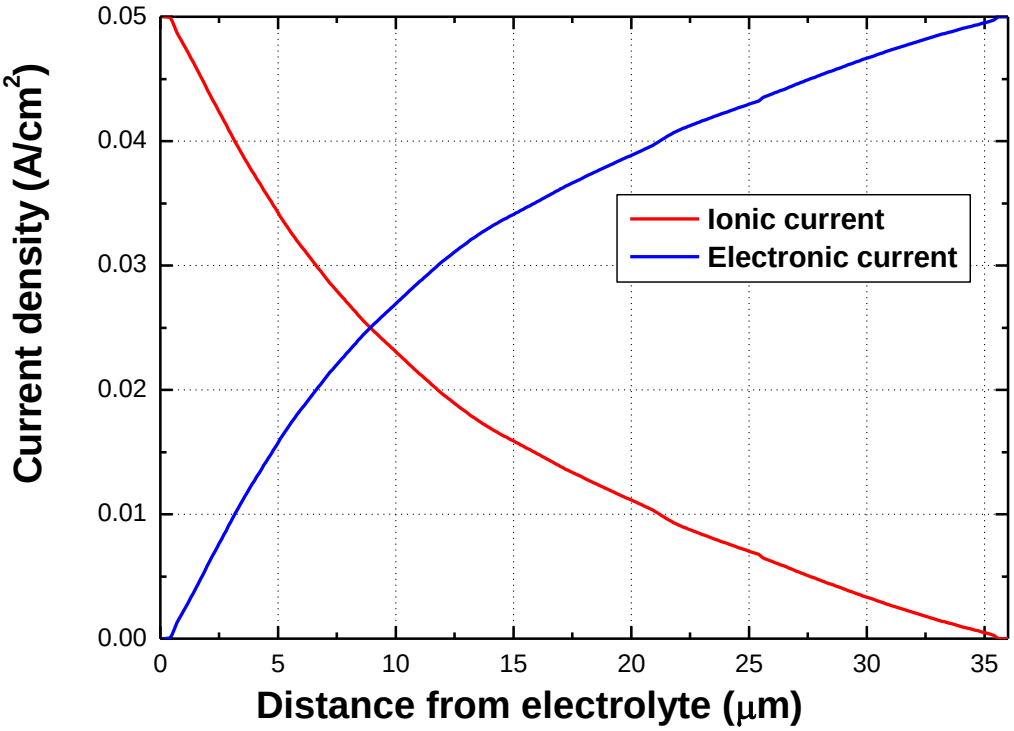

(d) LSC:GDC = 100:0 vol. %

Fig 5-19 Ionic and electronic current distributions in the LSC-GDC composite cathodes with LSC:GDC = (a) 30:70, (b) 50:50, (c) 70:30 and (d) 100:0 vol. %.

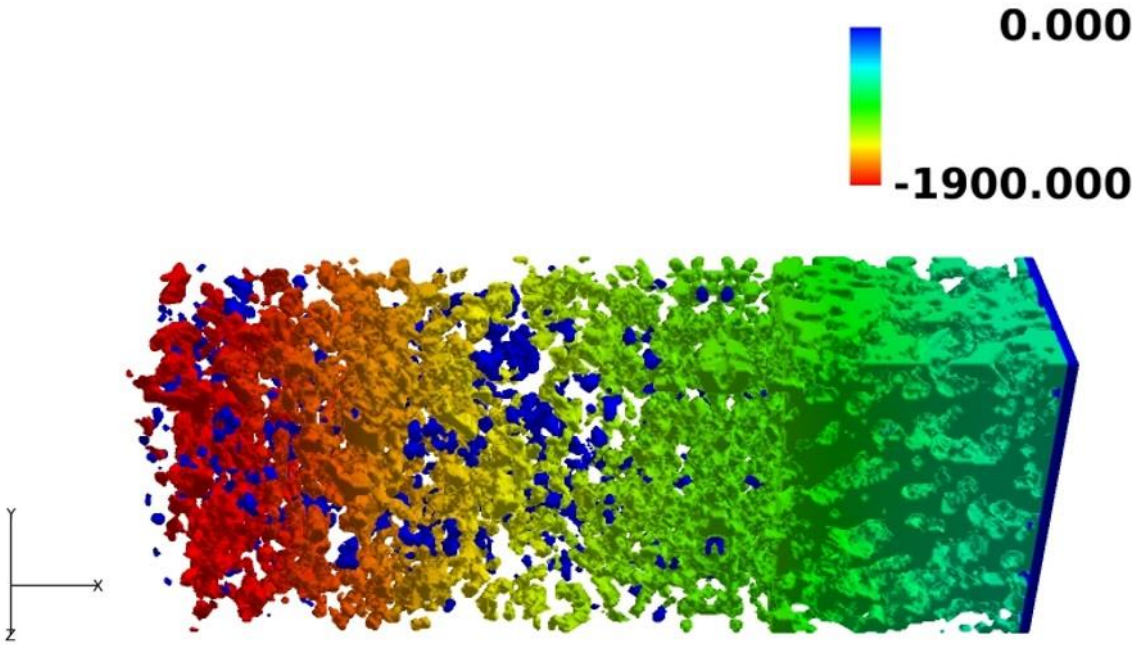

(a) LSC:GDC = 30:70 vol. %

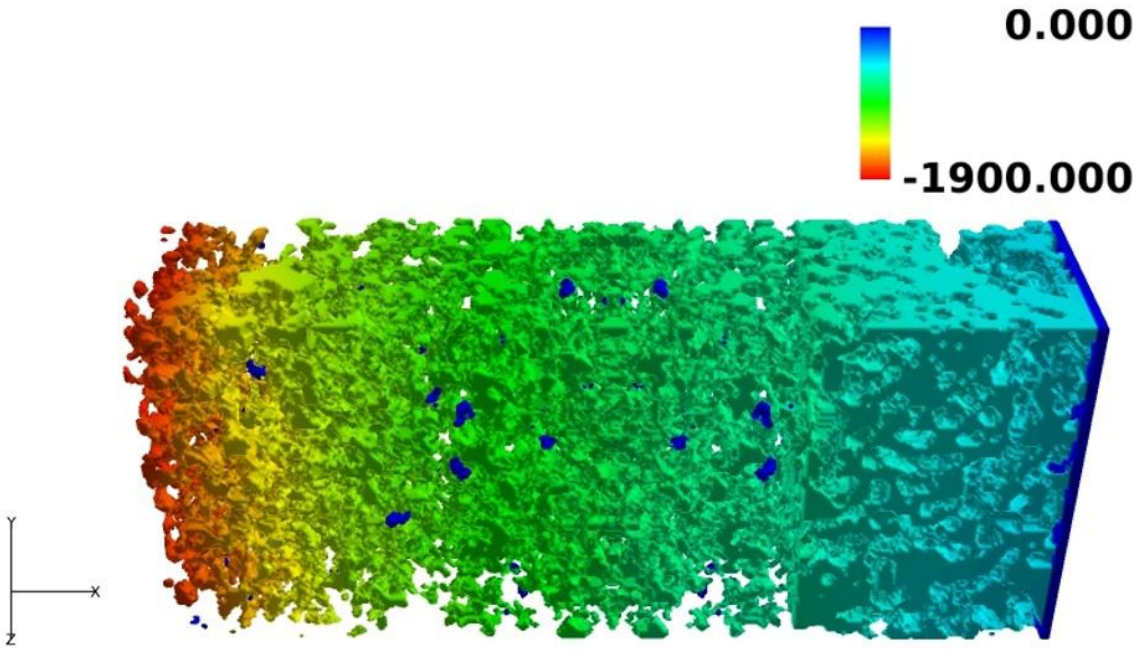

(b) LSC:GDC = 50:50 vol. %

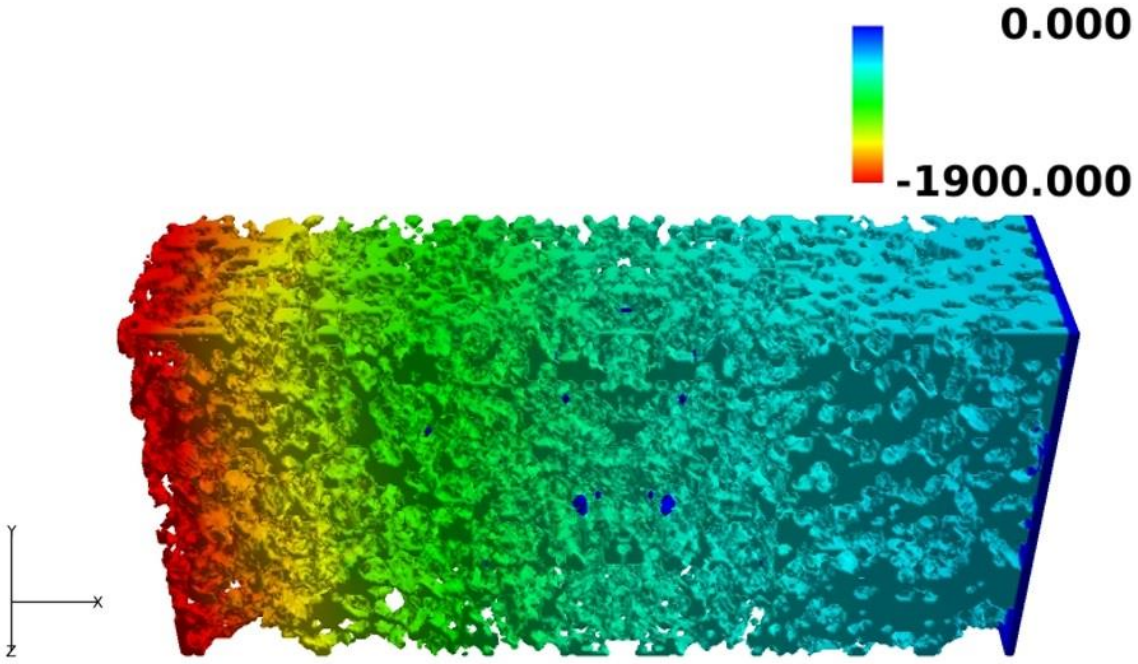

(c) LSC:GDC = 70:30 vol. %

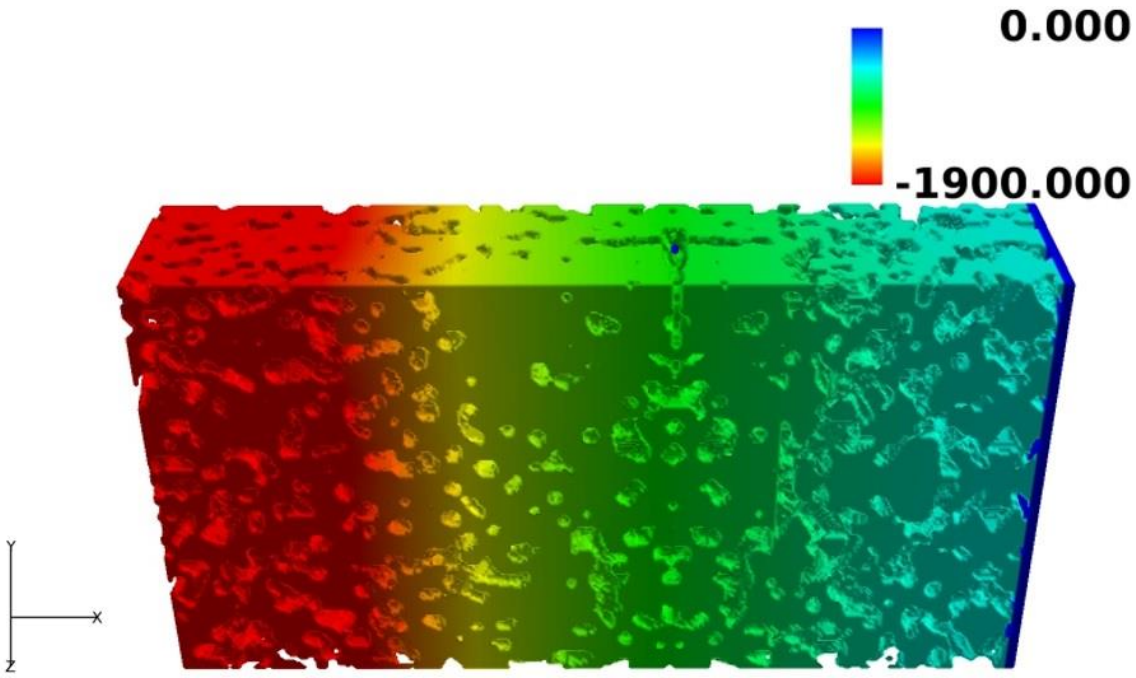

(d) LSC:GDC = 100:0 vol. %

Fig. 5-20 Oxygen chemical potential distributions in the LSC corresponding to Fig. 5-16 (a)-(d). (Current density i = 0.05 A/cm^2. Left is the electrolyte side, and right is the current collector side, units: J/mol).

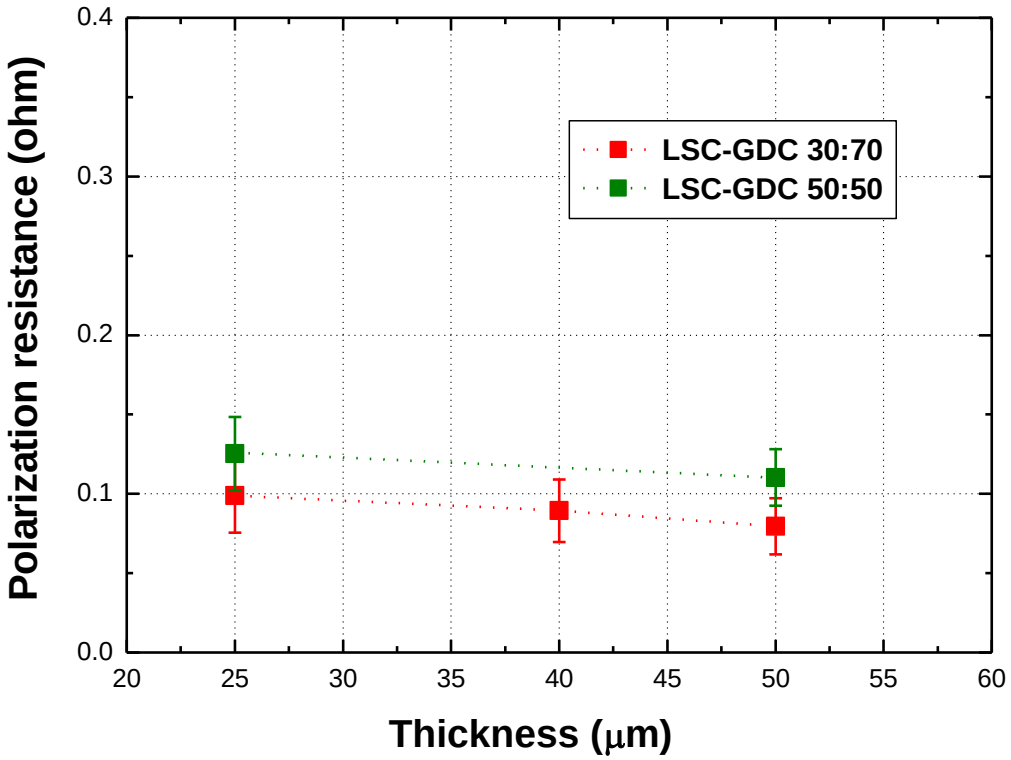

Fig. 5-21 Polarization resistances at OCV with different cathode thicknesses.

5.2.3 Comparison with LSCF-GDC Composite Cathodes

In this section, the numerical simulation results were compared with the results of LSCF-GDC composite cathodes which are shown in Chap. 3. Both experimental and simulation results of overpotential are smaller for the LSC-GDC composite cathodes. In the numerical simulation, both exchange current densities of LSC-GDC composite cathodes for surface and TPB reactions had similar values with those of LSCF-GDC, i.e. 5.484 A/m^2 and 9.884$\times 10^{-6}$ A/m for LSC-GDC and 4.088 A/m^2 and 7.953$\times 10^{-6}$ A/m for LSCF-GDC. It can be considered that local activation has less influence on the performance enhancement of LSC-GDC composite cathodes. Reaction current distributions in the solid LSCF and LSC phases are shown in Figs. 5-22 and 5-23, respectively.

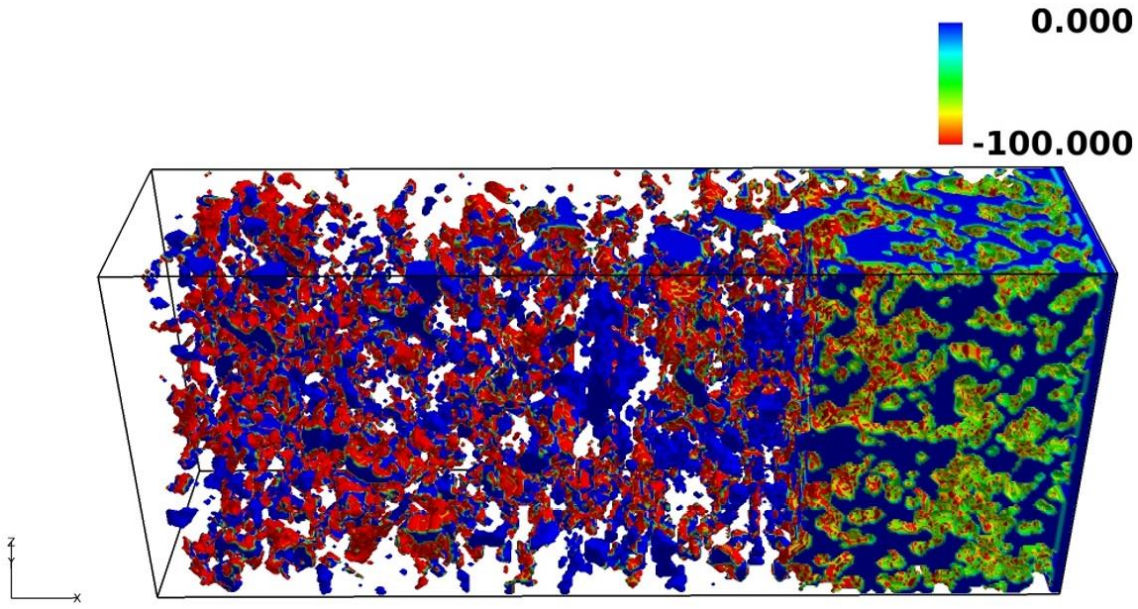

(a) LSCF:GDC = 30:70 vol. %

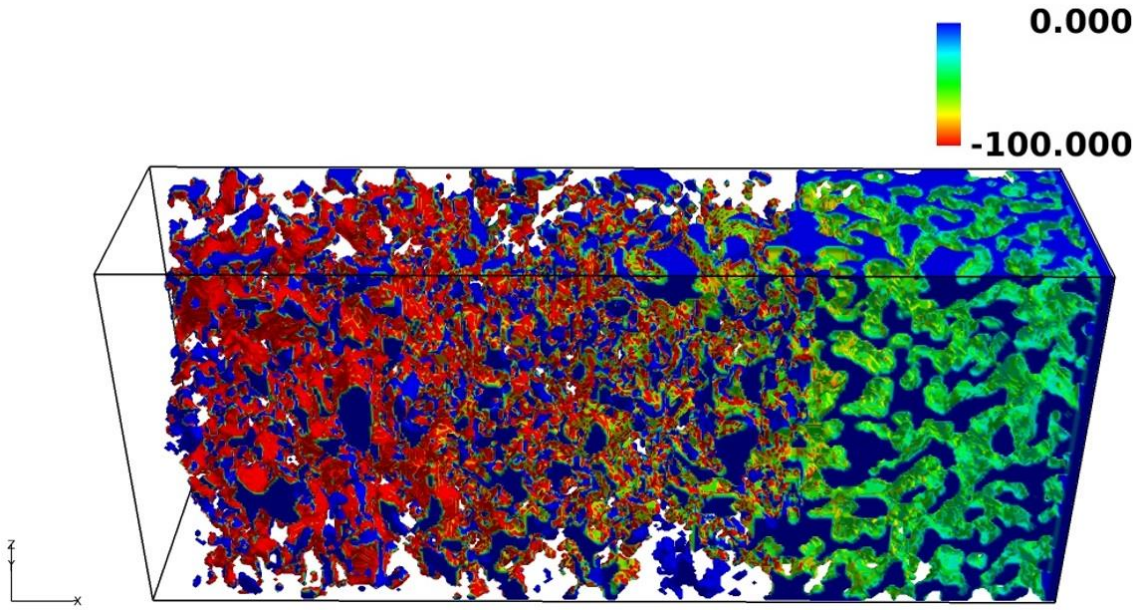

(b) LSCF:GDC = 50:50 vol. %

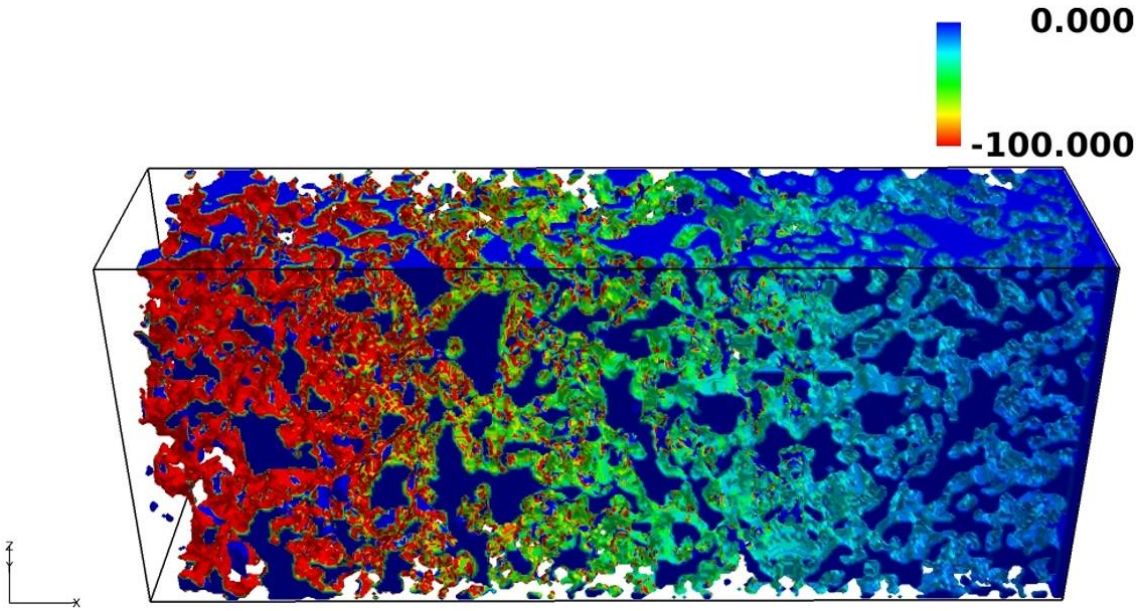

(c) LSCF:GDC = 70:30 vol. %

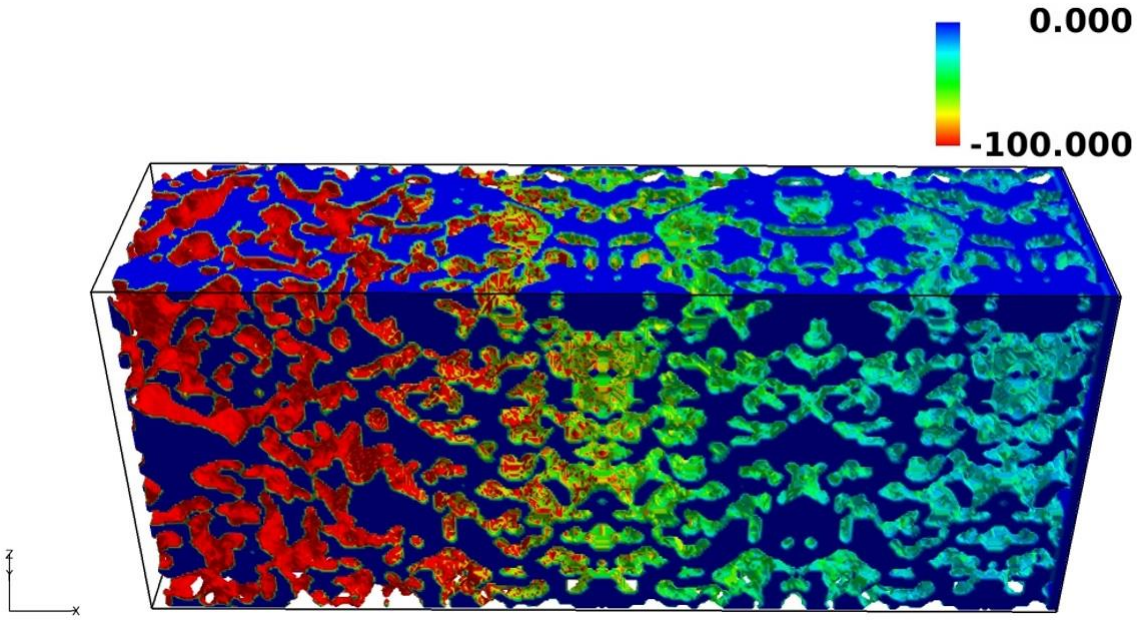

(d) LSCF:GDC = 100:0 vol. %

Fig. 5-22 Reaction current distributions inside the LSCF phases with LSCF:GDC = (a) 30:70, (b) 50:50, (c) 70:30 and (d) 100:0 vol. %. (Left is the electrolyte side, and right is the current collector side, units: A/cm^2).

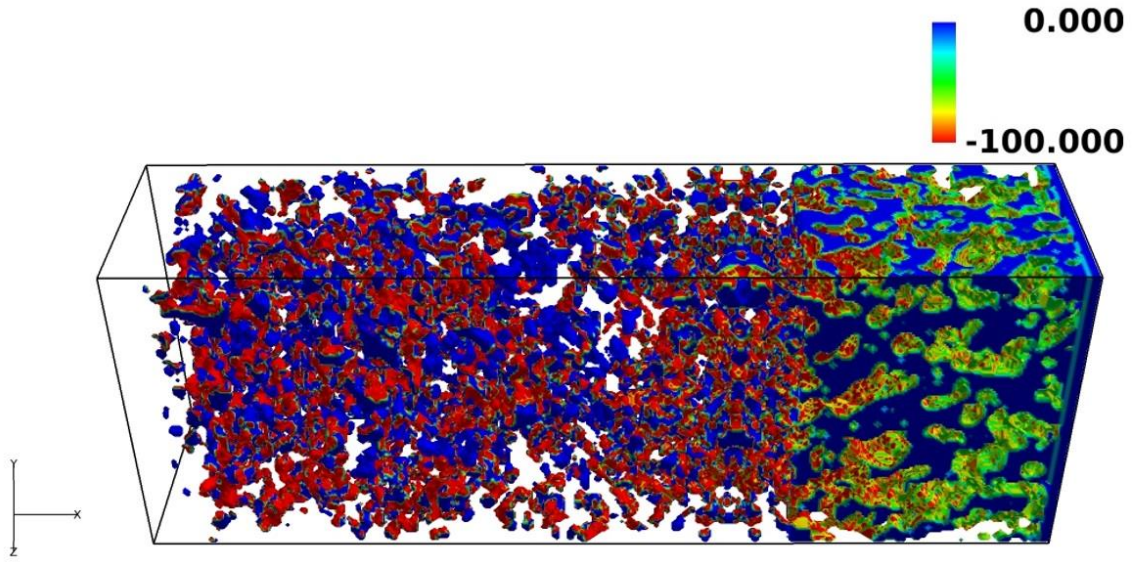

(a) LSC:GDC = 30:70 vol. %

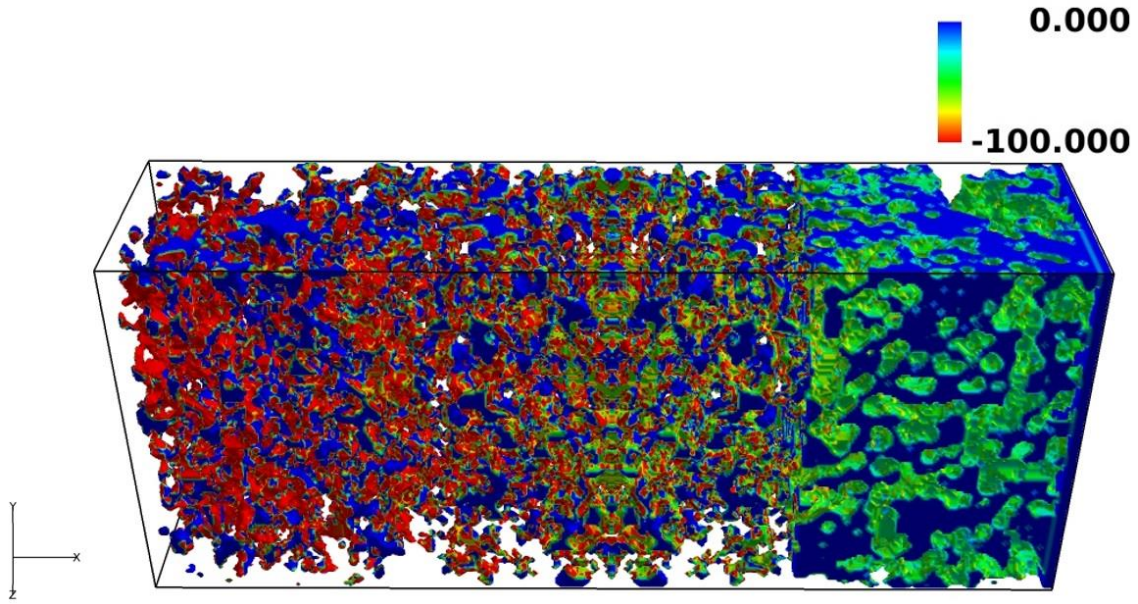

(b) LSC:GDC = 50:50 vol. %

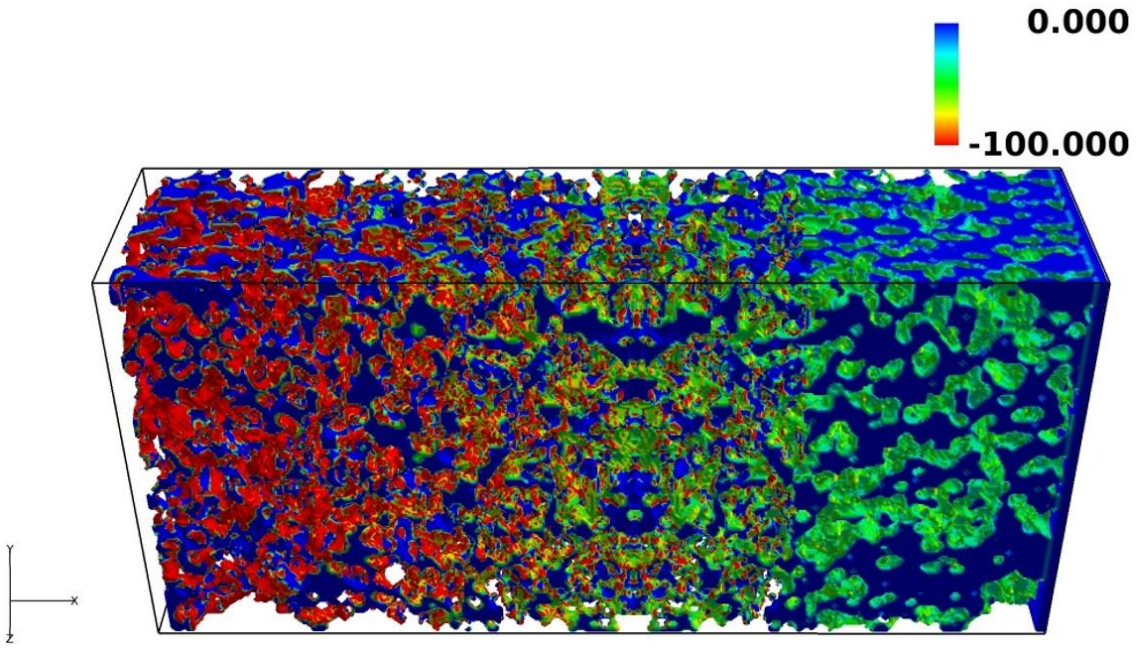

(c) LSC:GDC = 70:30 vol. %

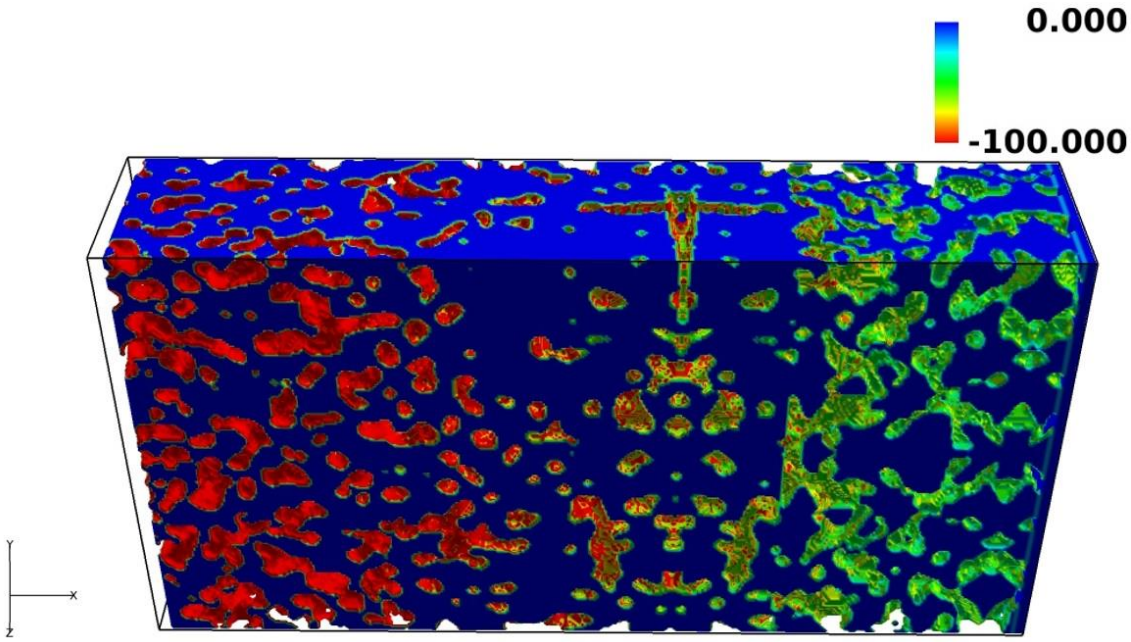

(d) LSC:GDC = 100:0 vol. %

Fig. 5-23 Reaction current distributions inside the LSC phases with LSC:GDC = (a) 30:70, (b) 50:50, (c) 70:30 and (d) 100:0 vol. %. (Left is the electrolyte side, and right is the current collector side, units: A/cm^2).

For LSC-GDC composite cathodes, the reaction current is more uniformly distributed compared

to the LSCF-GDC composite cathodes. It is considered that the increase of effective reaction area contributed to the performance enhancement of LSC-GDC composite cathodes. Figures 5-24 and 5-25 represent the ionic current flux inside the LSCF-GDC and LSC-GDC composite cathodes, respectively. Slightly higher ionic flux can be seen for the LSC-GDC composite cathodes. It is thus considered that performance of LSC-GDC composite cathode is enhanced due to the improvement of ionic conduction characteristics by higher ionic conductivity of LSC compared to LSCF, which resulted in the increase of effective reaction area.

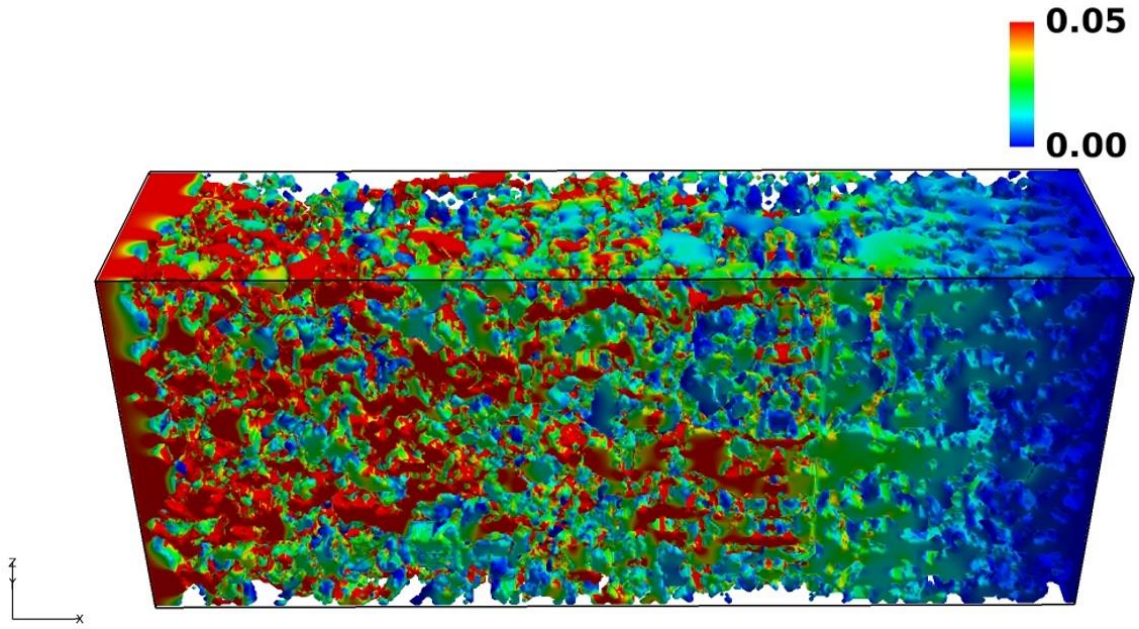

(a) LSCF:GDC = 30:70 vol. %

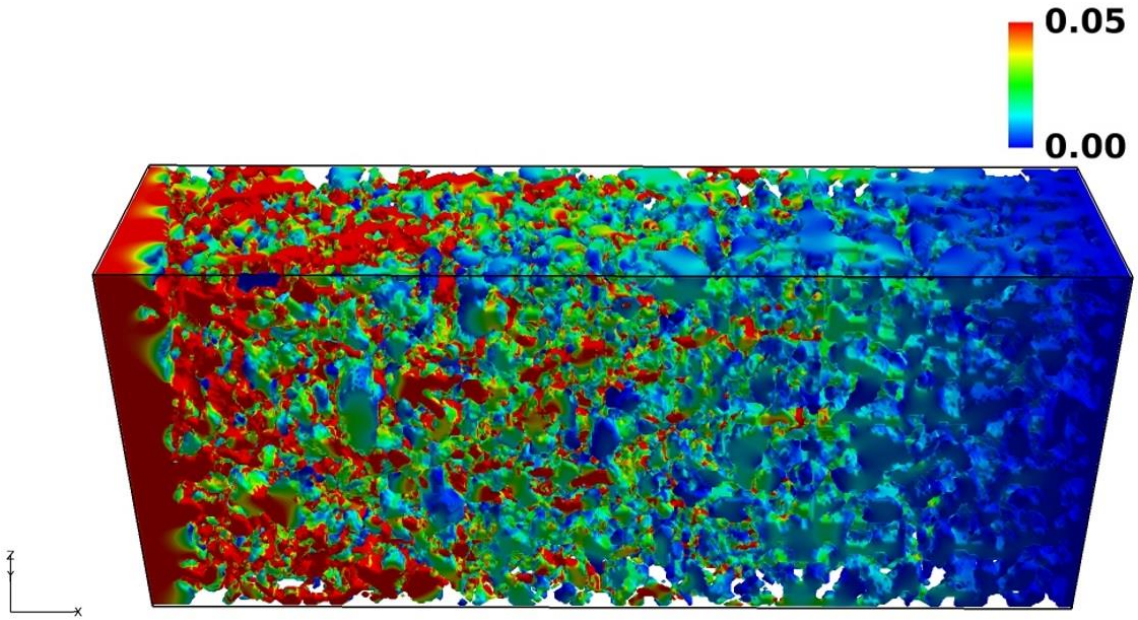

(b) LSCF:GDC = 50:50 vol. %

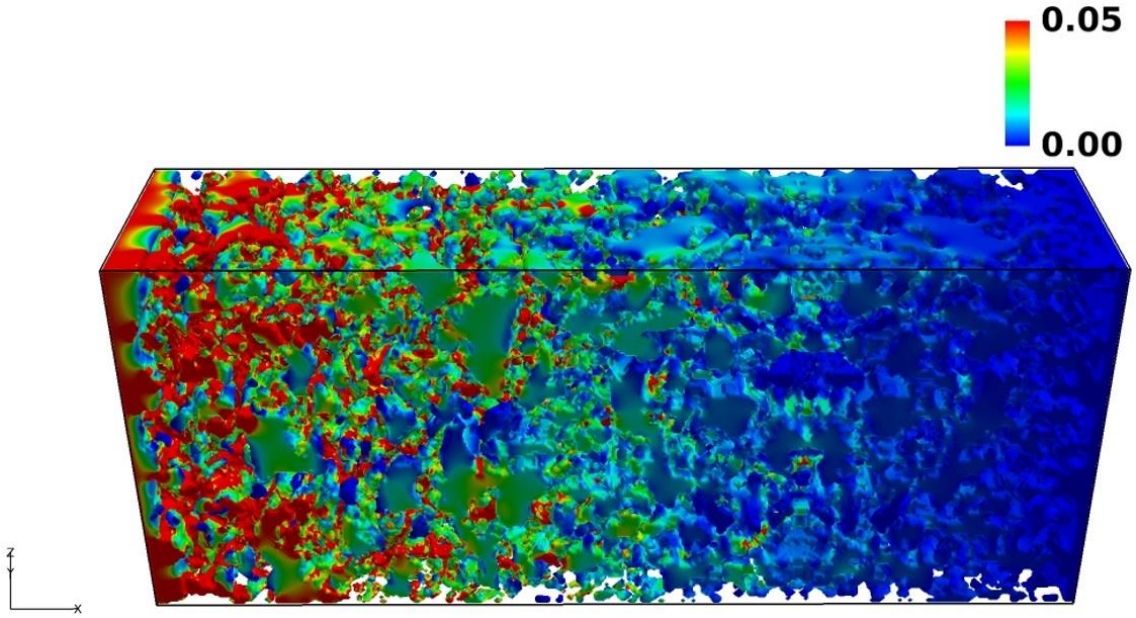

(c) LSCF:GDC = 70:30 vol. %

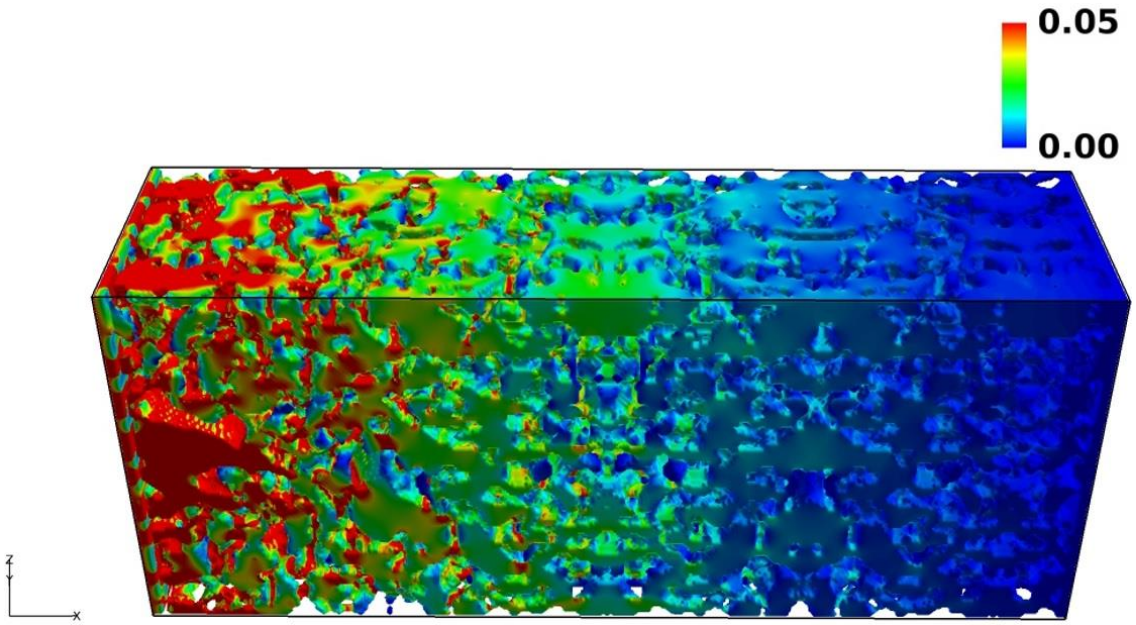

(d) LSCF:GDC = 100:0 vol. %

Fig 5-24 Ionic current flux inside the LSCF-GDC composite cathodes. The volume ratio of LSCF:GDC = (a) 30:70, (b) 50:50, (c) 70:30 and (d) 100:0 vol. %. (Left is the electrolyte side, and right is the current collector side, units: A/cm^2).

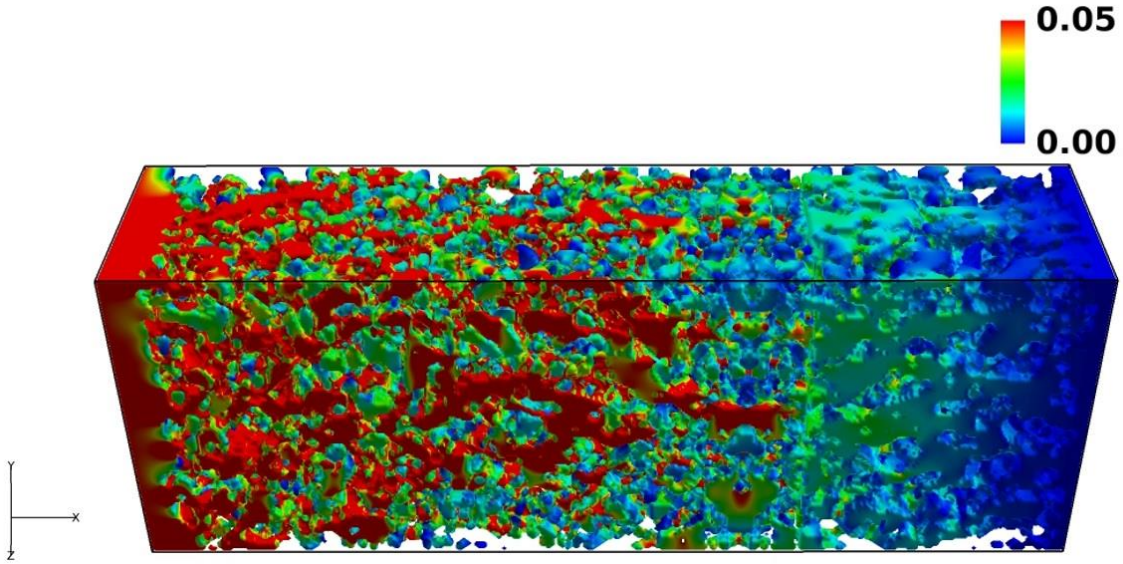

(a) LSC:GDC = 30:70 vol. %

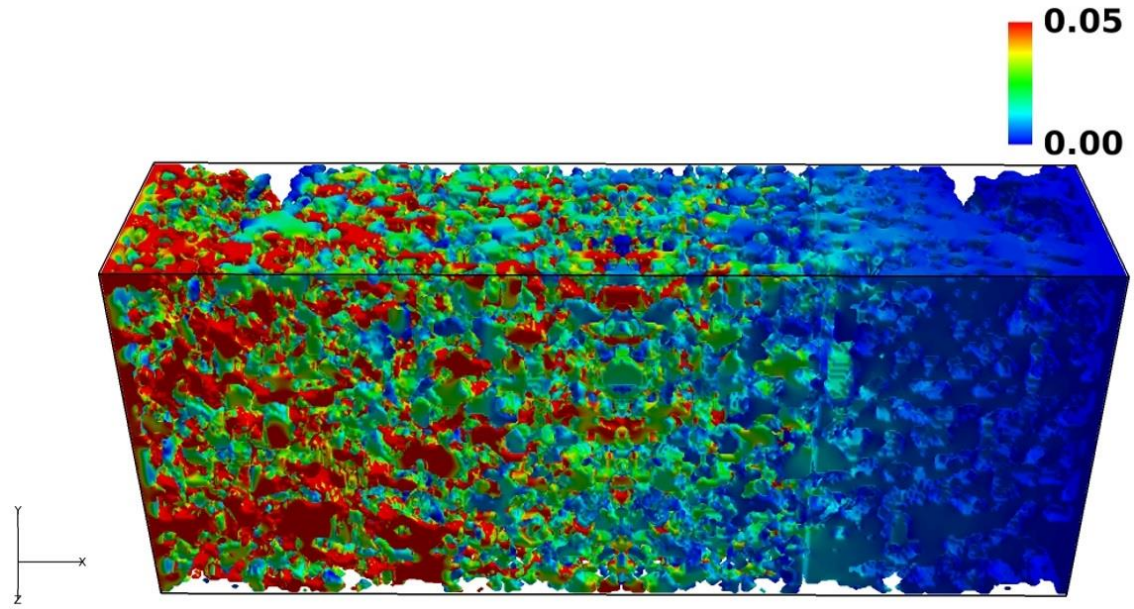

(b) LSC:GDC = 50:50 vol. %

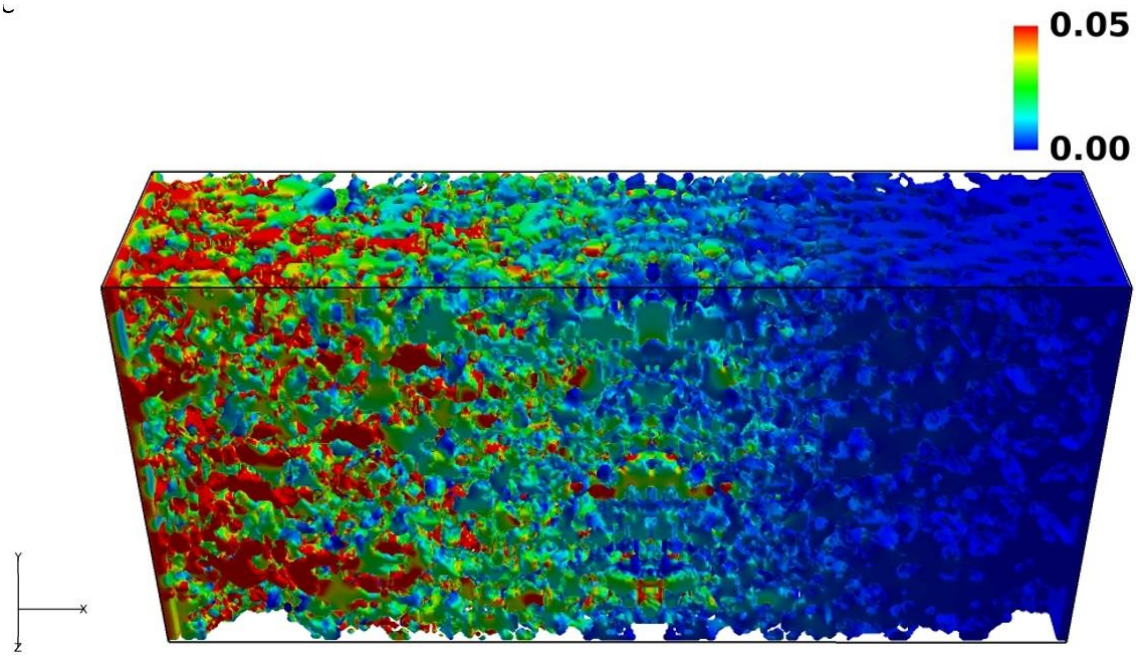

(c) LSC:GDC = 70:30 vol. %

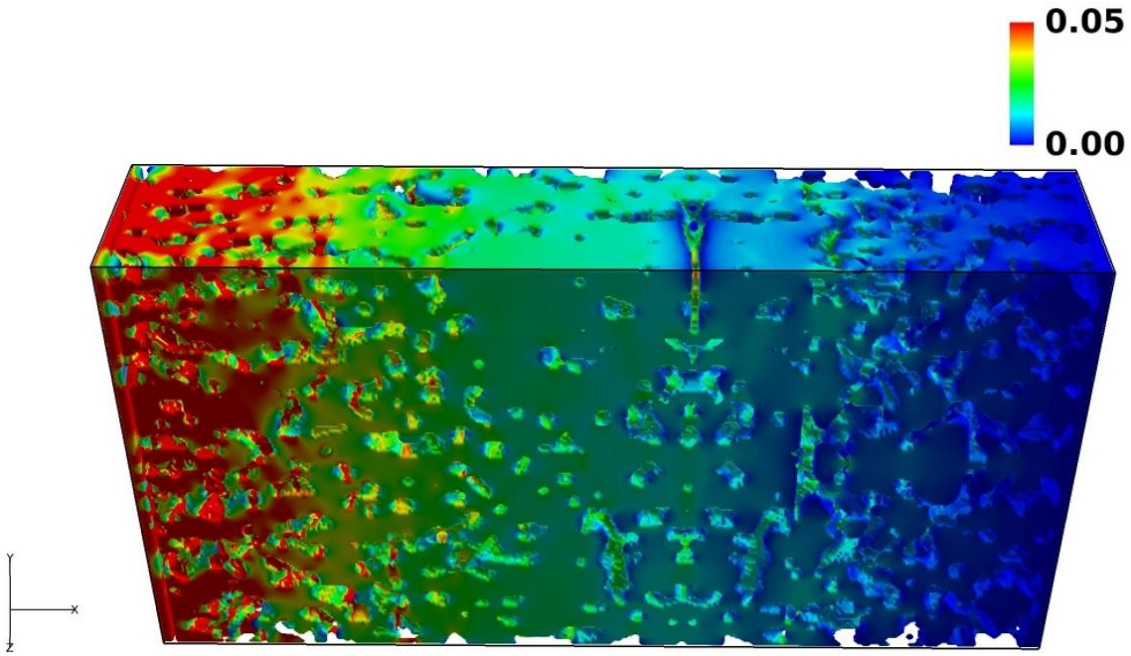

(d) LSC:GDC = 100:0 vol. %

Fig. 5-25 Ionic current flux inside the LSC-GDC composite cathodes. The volume ratio of LSC:GDC = (a) 30:70, (b) 50:50, (c) 70:30 and (d) 100:0 vol. %. (Left is the electrolyte side, and right is the current collector side, units: A/m^2).

5.3 Summary of Chapter 5

In this chapter, LSC-GDC composite cathodes with different volume fractions were investigated. Different volume ratios of LSC:GDC = 20:80, 30:70, 50:50, 70:30 and 100:0 % composite cathodes were prepared by screen printing method. Cathode performance measurements were conducted at 700°C with 100 % of oxygen pressure. The lowest overpotential was achieved at a volume ratio of LSC:GDC = 30:70 %, and it increased in the order of 50:50, 70:30, 20;80 and 100:0 vol. % The results of cathode performance showed the similar tendency with the case of LSCF-GDC composite cathodes. Microstructure parameters were calculated based on 3D reconstructed microstructures. Neither LSC surface nor TPB reactions could explain the performance of LSC-GDC composite cathodes by their individual reaction mechanisms alone. It is considered that the improvement of effective ionic conductivity by GDC addition contributes to the cathode performance. The results of microstructure calculation also show the similar tendency with the LSCF-GDC composite cathodes. It is considered that reaction mechanisms of LSC-GDC composite cathode are the same as the LSCF-GDC. The performance and microstructural changes of LSC-GDC composite cathodes were compared to the case of LSCF-GDC composites. Regardless of the composition, all LSC-GDC composite cathodes showed better performance than the LSCF-GDC. It is seen that performance of LSC-GDC is enhanced due to higher ionic conductivity of LSC compared to LSCF. Surface area densities of LSC are smaller at lower GDC volume fractions compared to LSCF due to the high sinterablitiy of LSC. Active TPB density of LSC-GDC is lower for the volume ratios of 20:80 and 30:70 %. However, it becomes larger for the volume ratios of 50:50 and 70:30 %. It is considered that the increase of LSC-GDC boundary area results in the increase of TPB length. Electrochemical reaction mechanism of LSC-GDC composite cathodes was investigated by numerical simulation. The simulation results of LSC:GDC = 50:50, 70:30 and 100:0 vol. % show good agreement with the experimental data. However, slight discrepancy was shown in the case of LSC:GDC = 30:70 vol. %. It is considered that the disconnection of the electron path due to the expansion of voxel size in the simulation possibly resulted in the increase of predicted overpotential. Contribution of TPB reactions was quantified. It is considered that TPB reactions contribute to the cathode performance of LSC-GDC composites significantly. Similar with the LSCF-GDC composite cathode, it is shown that reactive thickness of LSC-GDC composite cathodes is elongated. The simulation results were compared to the case of LSCF-GDC composite cathodes. It can be concluded that the performance of LSC-GDC composite cathodes is partly enhanced due to the improved effective ionic conductivity by higher ionic conducting LSC, which was accompanied by the increase of the reaction area.

Chapter 6
Effect of Powder Size

6.1 Correlation between Performance and Microstructure

In this chapter, original powder sizes of LSC and GDC were varied in order to investigate the contributions of LSC surface reactions and ionic conduction kinetics of the GDC on the cathode performance. LSC of 0 .5 μm and GDC of 3 μm, LSC of 3 μm and GDC of 0.5 μm were mixed with a volume ratio of 50:50 %. It is expected that two cathodes have the similar TPB length, but have different LSC surface areas and GDC tortuosity factors. In this chapter, the composite cathodes with the combination of small LSC and big GDC denoted as GDC3 and the contrary case denoted as LSC3 are investigated experimentally.

6.1.1 Performance Evaluation with Different Powder Sizes

Figure 6-1 shows the SEM images of the original powders which were used in the present study. Difference of particle size is clearly seen. Therefore, it is expected that LSC surface area will be increased for the GDC3, and tortuosity factor of GDC will be decreased for the LSC3.

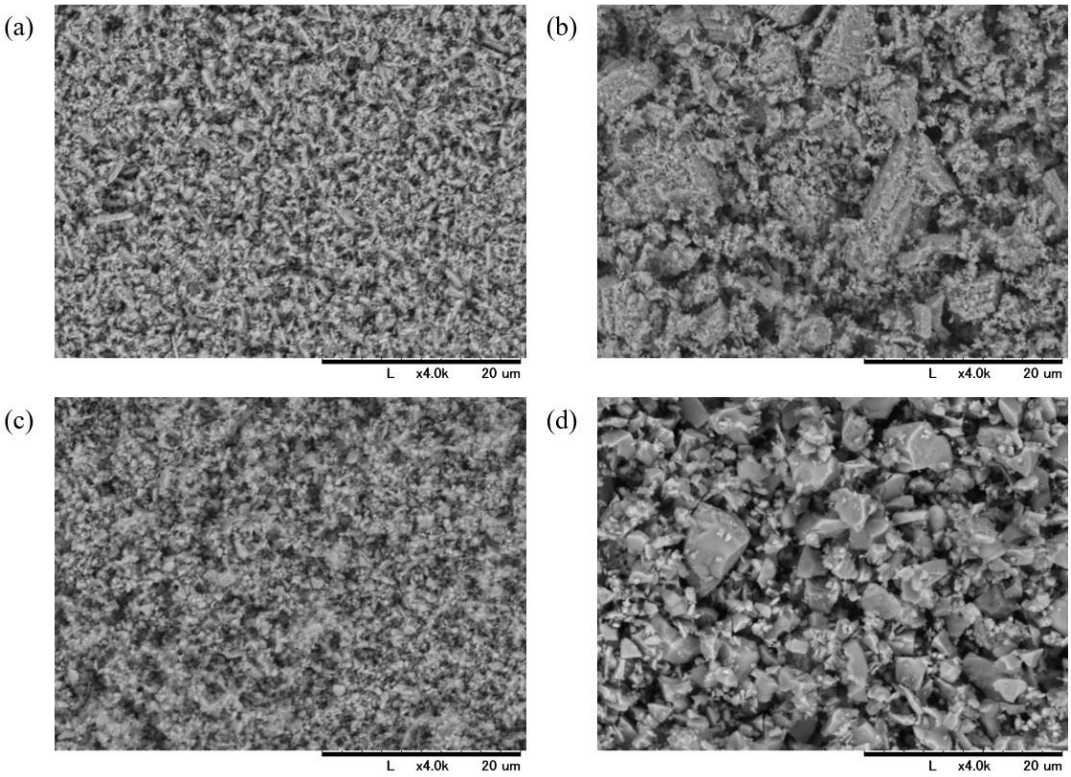

Fig. 6-1 SEM images of the starting particles.
Particle size of (a) GDC = 0.5 μm, (b) GDC = 3 μm, (c) LSC = 0.5 μm, (d) LSC = 3 μm.

Measured overpotential results and polarization resistances at OCV are shown in Figs. 6-2 and 6-3, respectively.

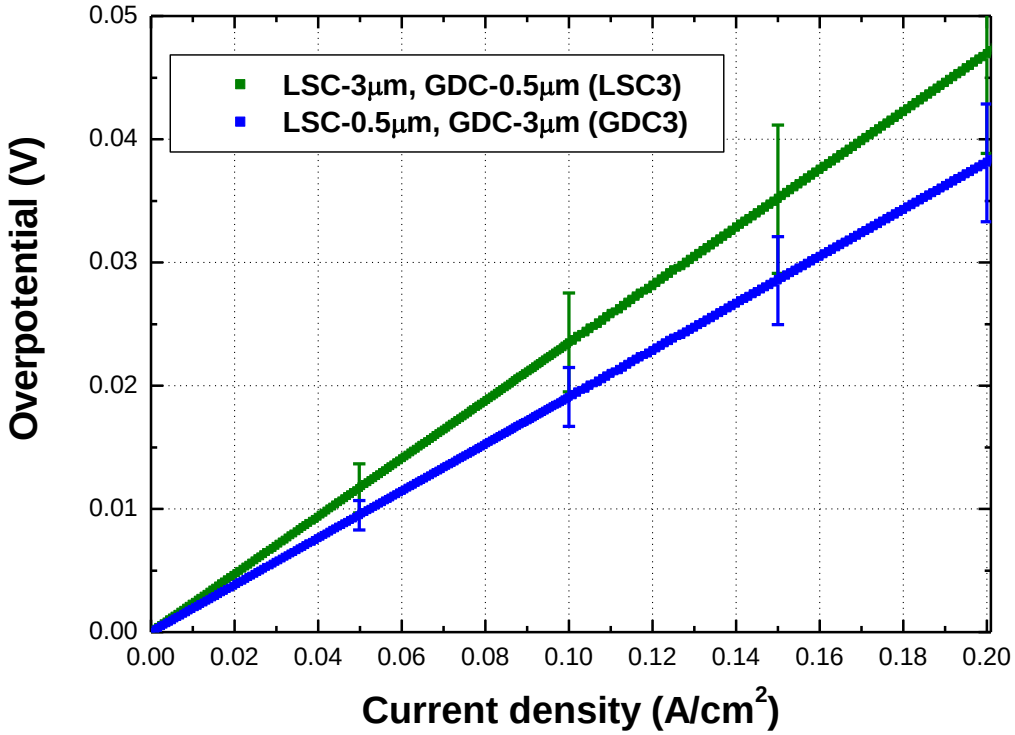

Fig. 6-2 Overpotential results of LSC:GDC = 50:50 vol. % with different combinations of particle sizes.

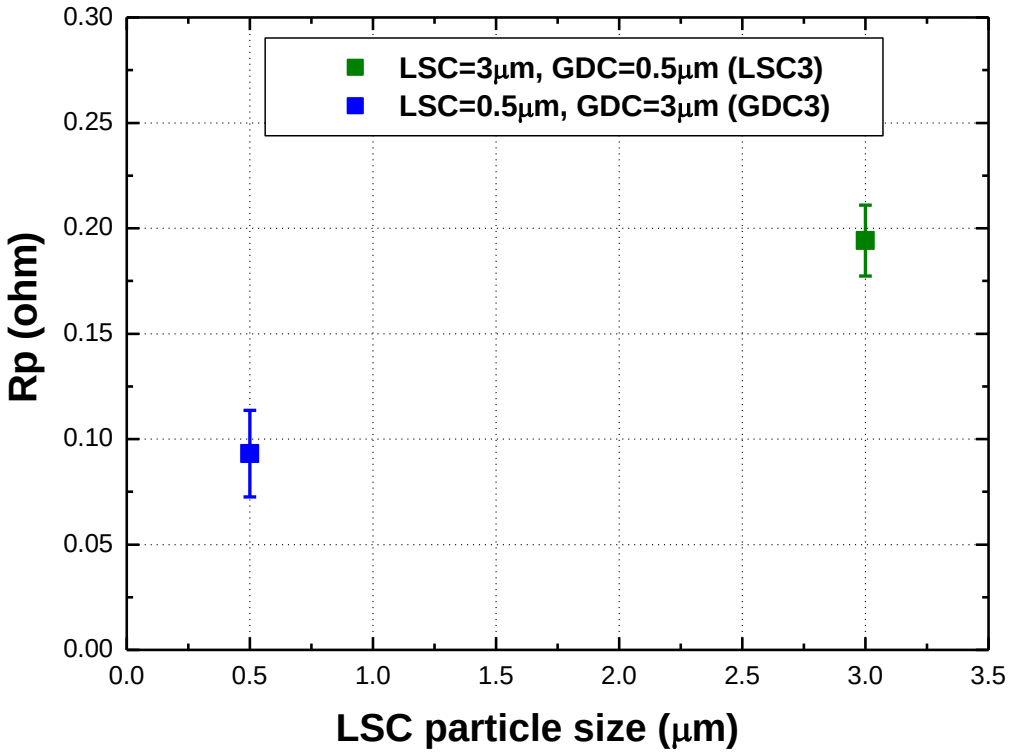

Fig. 6-3 Polarization resistances of LSC:GDC = 50:50 vol. % at OCV with different combinations of particle sizes.

From the results, GDC3 shows better performance than LSC3. It is expected that the LSC surface reaction more contributes to the cathode performance compared to the ionic conduction of GDC.

6.1.2 Microstructure Parameters

It is expected that only LSC surface area and GDC tortuosity factor will be varied as explained in section 6.1.1. In order to verify this assumption, microstructure parameters were calculated based on 3D reconstructed cathode microstructures. As introduced in Chap. 5, EsB detector with an acceleration voltage of 5 keV was used for the SEM observation, and all reconstructed microstructures have voxel size of 25 nm. Figure 6-4 shows the SEM images during FIB-SEM measurement.

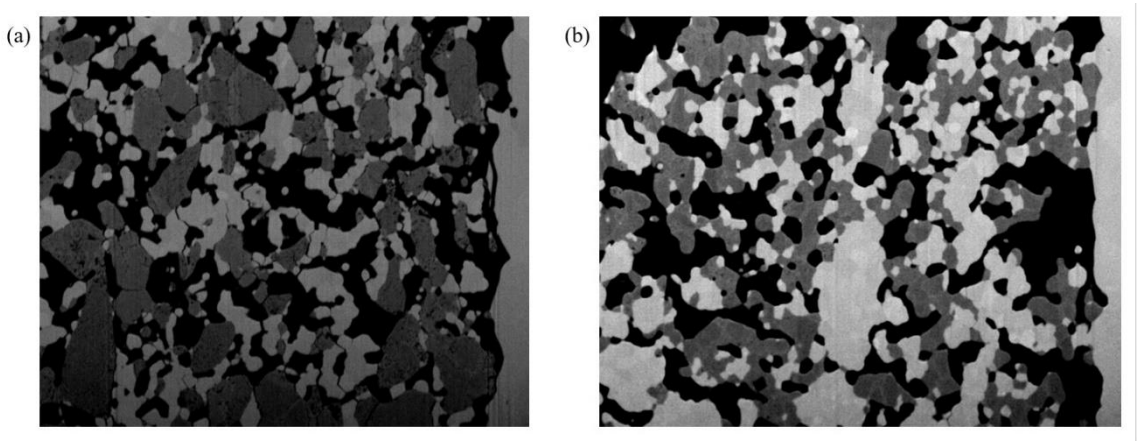

Fig. 6-4 SEM images from FIB-SEM measurement. (a) LSC3 and (b) GDC3. (Black: pore, dark gray: LSC, light gray: GDC).

It is clearly seen that the original powder sizes remain in the sintered structure. Table 6-1 and Fig. 6-5 show the condition of FIB-SEM reconstruction and the 3D reconstructed microstructures, respectively.

Table 6-1 Reconstructed sample information.

	Number of pixels ($x \times y$)	Number of slices in z direction	Sample volume size
LSC3	780×716	364 slices	3176.36 μm^3
GDC3	752×632	366 slices	2717.92 μm^3

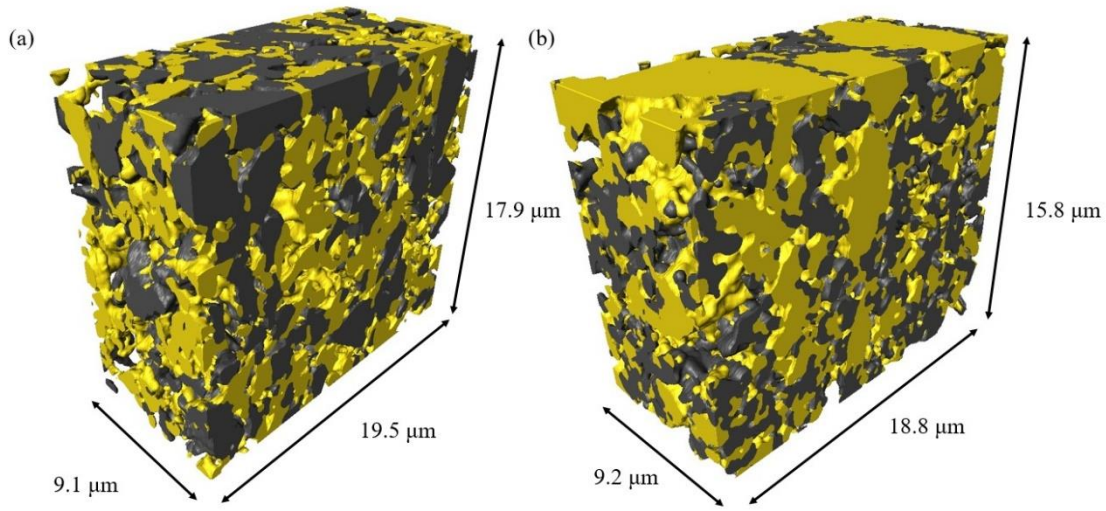

Fig. 6-5 3D reconstructed microstructures of LSC-GDC composite cathodes.

(a) LSC3 and (b) GDC3. (Yellow: GDC, dark gray: LSC).

The microstructure parameters are calculated at a resolution of 25 nm. Figure 6-6 shows the LSC surface area densities and the total and active TPB densities with polarization resistances at OCV.

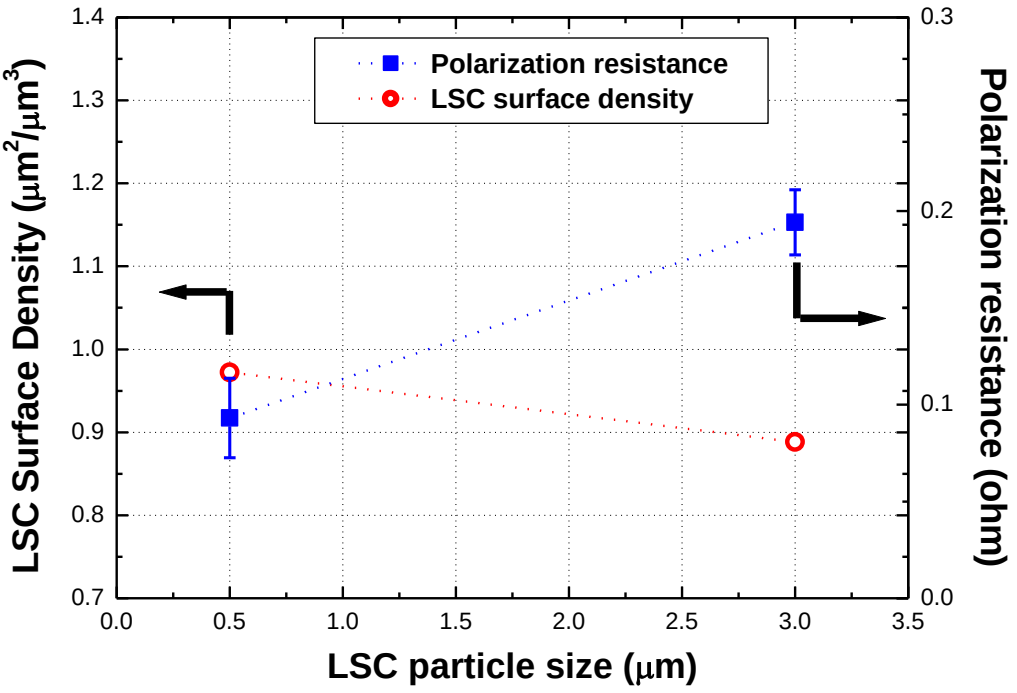

(a) LSC surface densities and polarization resistances.

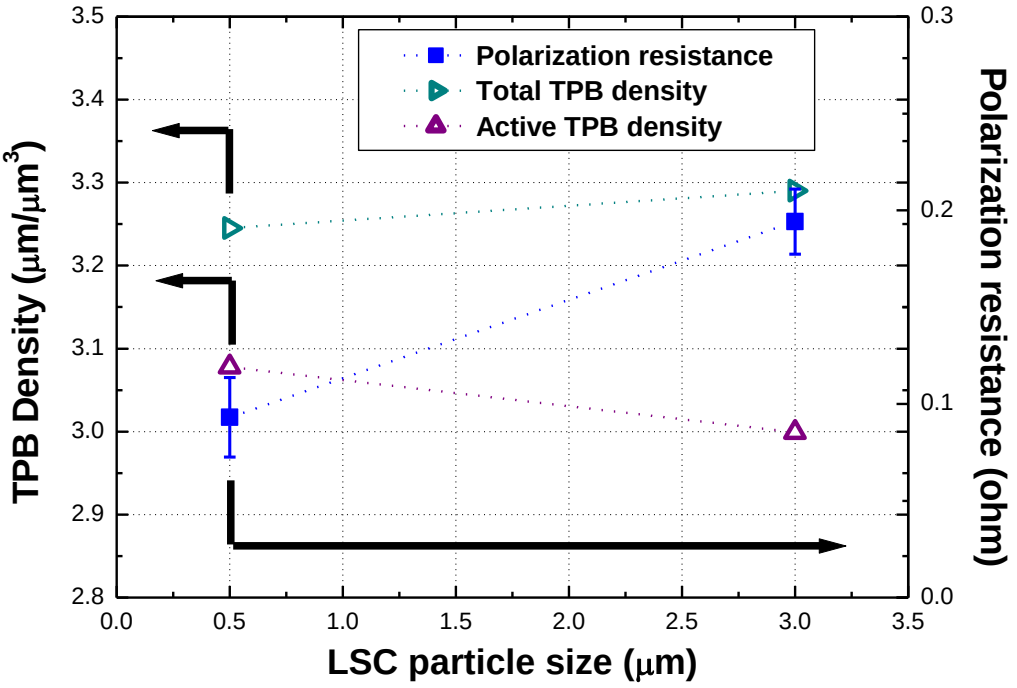

(b) Total and active TPB densities and polarization resistances.

Fig. 6-6 (a) LSC surface densities and (b) total and active TPB densities plotted with the polarization resistance of composite cathodes with the different particle sizes.

For GDC3 cathode, the LSC surface density is increased. Unlike the total TPB density, the active TPB density is increased for the GDC3 cathode. In general, it is considered that small particle size of phase in the electrode accelerates the sintering of the corresponding phase. It is seen that the increase of active TPB density is attributed to the sintering of LSC compared to GDC. From the results, it is considered that the increase of reaction area contributed to the performance enhancement of GDC3 cathode. Figure 6-7 represents the tortuosity factors of LSC and GDC with the polarization resistance at OCV.

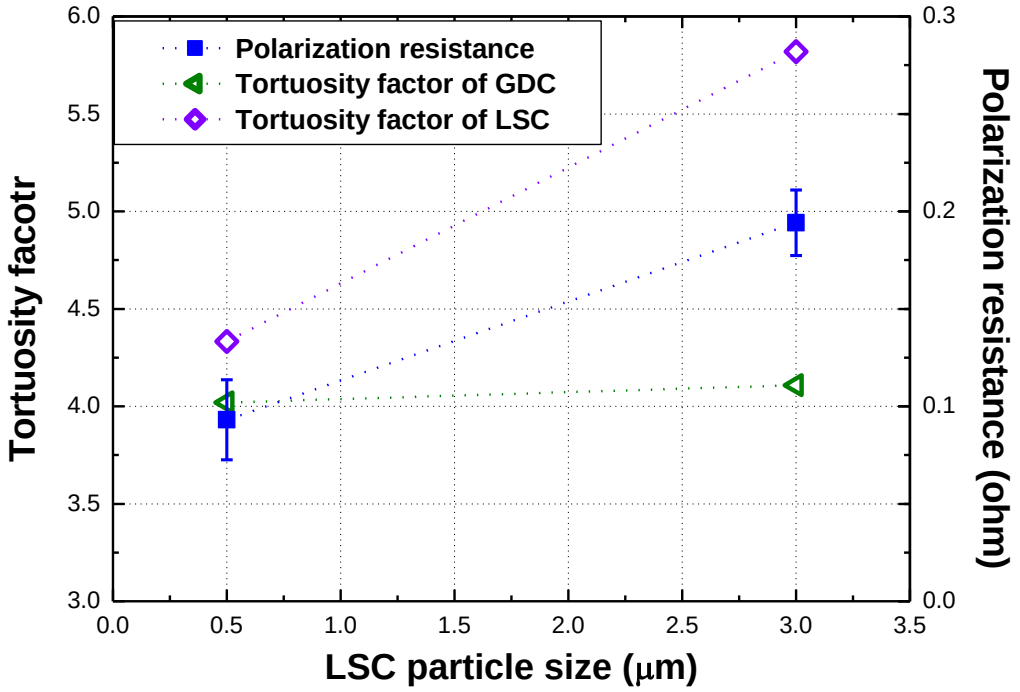

Fig. 6-7 Tortuosity factors of LSC and GDC with polarization resistance at OCV.

Compared to the GDC tortuosity factor, the change of LSC tortuosity factor is more remarkable. The GDC tortuosity factor shows nearly the same values for cathodes with different original GDC particle sizes. It implies that tortuosity factor is drastically decreased due to higher sinterability for LSC. Therefore, it can be considered that performance enhancement of GDC3 is attributed to the improvement of ionic conduction of LSC compared to GDC.

The other microstructure parameters are shown in Table 6-2. Porosity and phase connectivity for both composites are similar. Volume fraction of each phase increases with the increase of particle size for each phase. From the investigation of microstructure parameters, it can be concluded that not only the increase of reaction area, but also the improvement of effective ionic diffusivity inside the LSC phases contribute to the performance enhancement for the GDC3 cathode.

Table 6-2 Microstructure parameters from FIB-SEM reconstruction.

	LSC3	GDC3
Porosity	34.05 %	31.52 %
GDC phase volume fraction	30.83 %	41.67 %
LSC phase volume fraction	35.12 %	26.81 %
GDC connectivity	98.89 %	98.49 %
LSC connectivity	98.16 %	98.93 %

The relevance of microstructure volume size which is used in the present study was also evaluated by the same dividing method as the LSCF-GDC and the LSC-GDC composite cathodes shown in Chapters 3 and 5. LSC surface area density and total TPB density with different volume sizes were calculated as shown in Fig. 6-8.

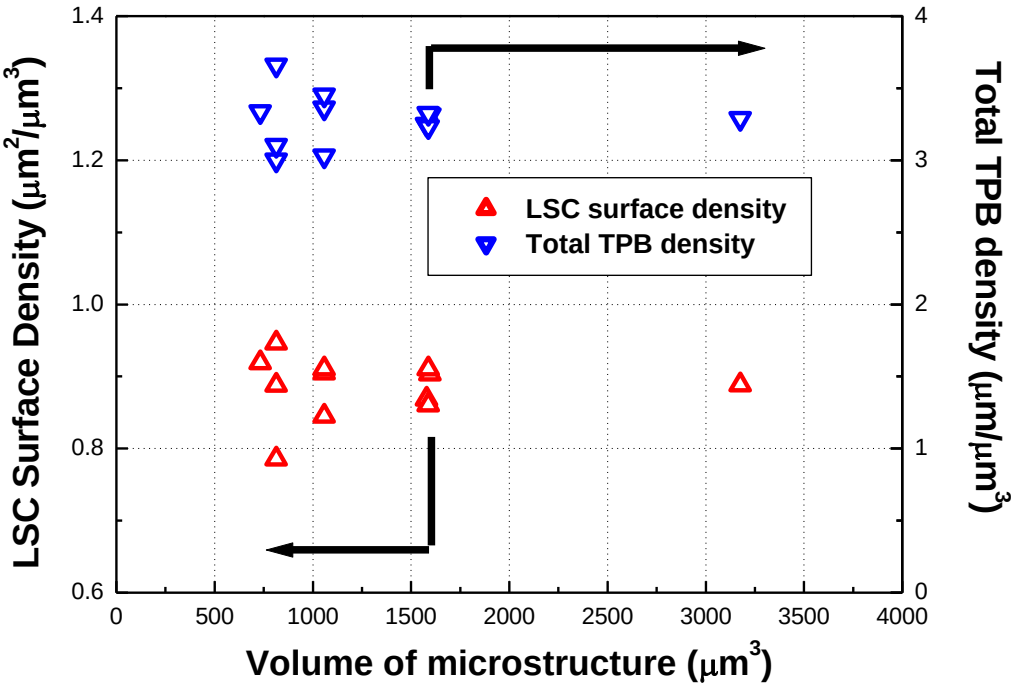

(a) LSC3.

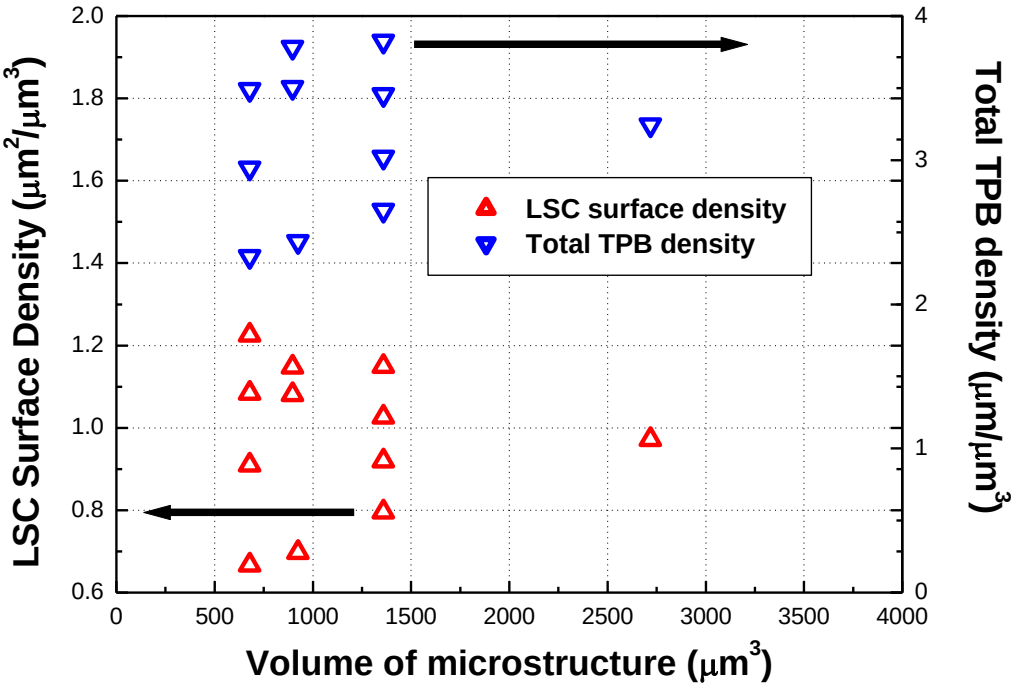

(b) GDC3.

Fig. 6-8 Verification of RVEs by LSC surface area density and total TPB density with (a) LSC3 (b) GDC3.

As shown in Fig. 6-8, variations of parameters with smaller volume sizes are significant and it converges at the biggest volume sizes which were used in the microstructure parameters calculation. It can be considered that the volume sizes are reasonable. The results show similar tendency with the LSCF-GDC and the LSC-GDC composite cathodes with different volume ratios as introduced in Chapters 3 and 5.

6.2 Numerical Simulation

In this chapter, electrochemical reaction mechanism of composite cathode with different powder sizes were investigated by LBM. Same exchange current densities were introduced into the numerical simulation as explained in Chap. 5.

6.2.1 Computational Domain

For the computational domains, 25 μm LSC-GDC composite cathodes and 10 μm LSCF current collector were prepared by mirroring as shown in Fig. 6-9. In the numerical simulation, resolution of 100 nm was used due to the computational limitation. 5 μm thick dense electrolyte and current collector were attached to both side of the domains.

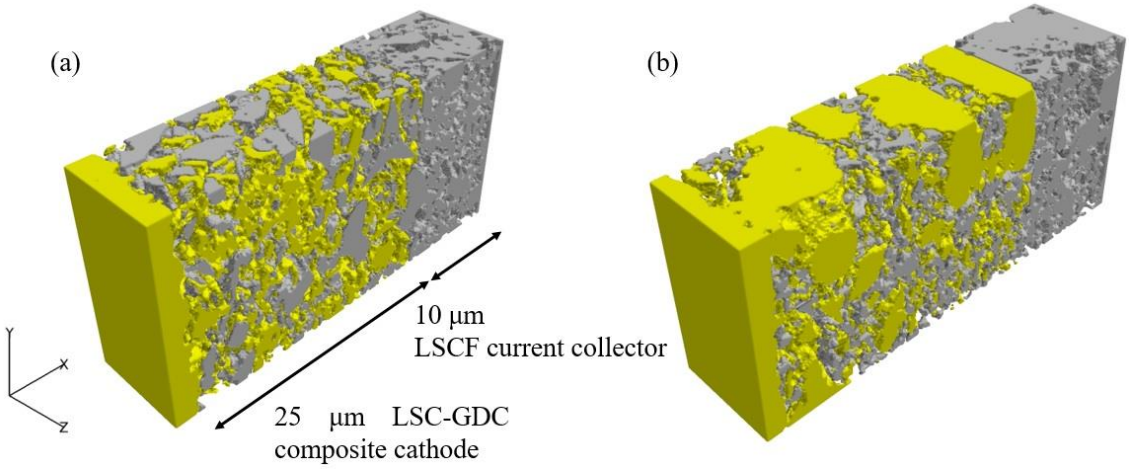

Fig. 6-9 Computational domains of (a) LSC3 and (b) GDC3 cathodes (Yellow: GDC, gray: LSC).

6.2.2 Overpontential and Electrochemical Reaction Mechanisms

Figure 6-10 shows the comparison of overpotential results between experimental and simulation. The discrepancy between the experimental and the simulation is small for both cathodes. It is indicated that electrochemical reaction model which was considered in the present study is reliable. Current distributions in the composite cathodes are shown in Fig. 6-11. The difference between two cathodes were insignificant. Figure 6-12 shows the oxygen chemical potential distributions in the LSC phase. It is indicated that the oxygen chemical potential is uniformly distributed in both LSC3 and GDC3 cathodes. Reaction current distributions in the LSC phase are shown in Fig. 6-13. For the GDC3 cathode, finer distribution of reaction current can be seen compared to the LSC3. It is considered that the predicted overpotential result decreases due to the increase of reaction area for the GDC3 cathode as introduced in section 6.1.2.

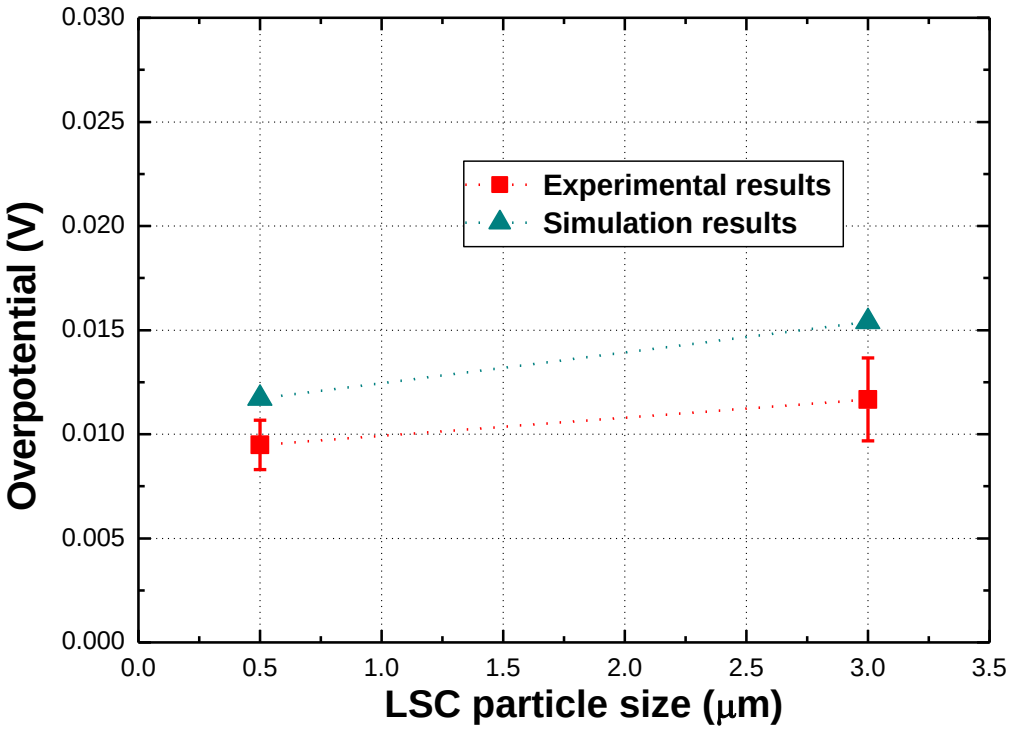

Fig. 6-10 Overpotential results of experimental and simulation.

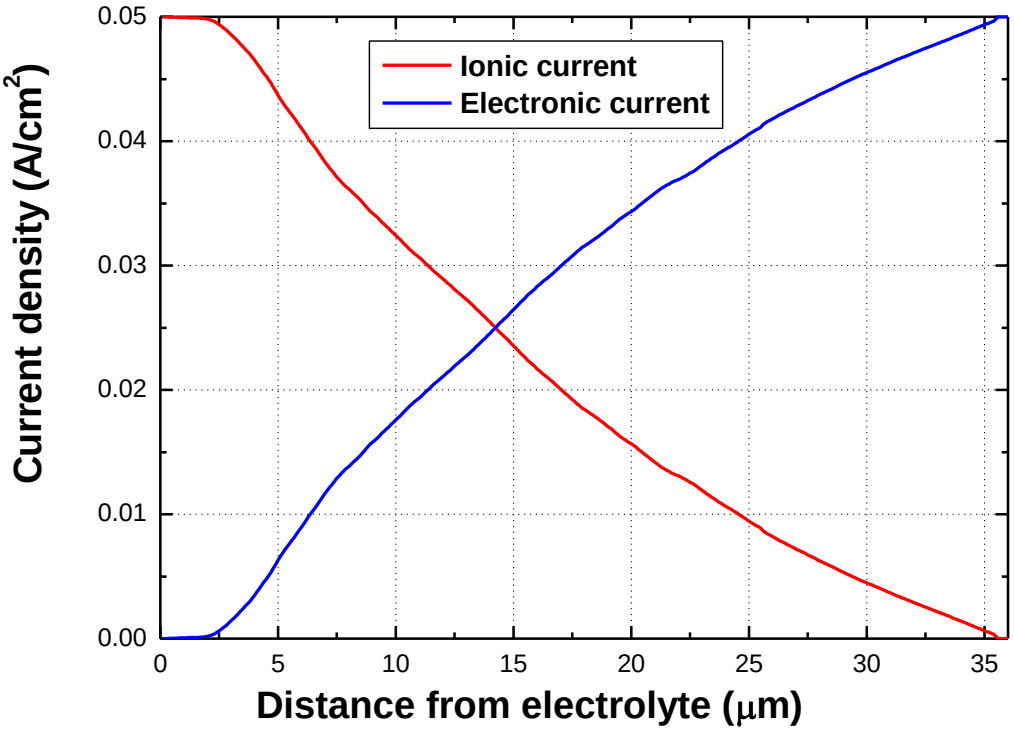
Ionic current
Electronic current
Current density (A/cm^2)
Distance from electrolyte (μm)
0.00
0.01
0.02
0.03
0.04
0.05
0
5
10
15
20
25
30
35

(a) LSC3.

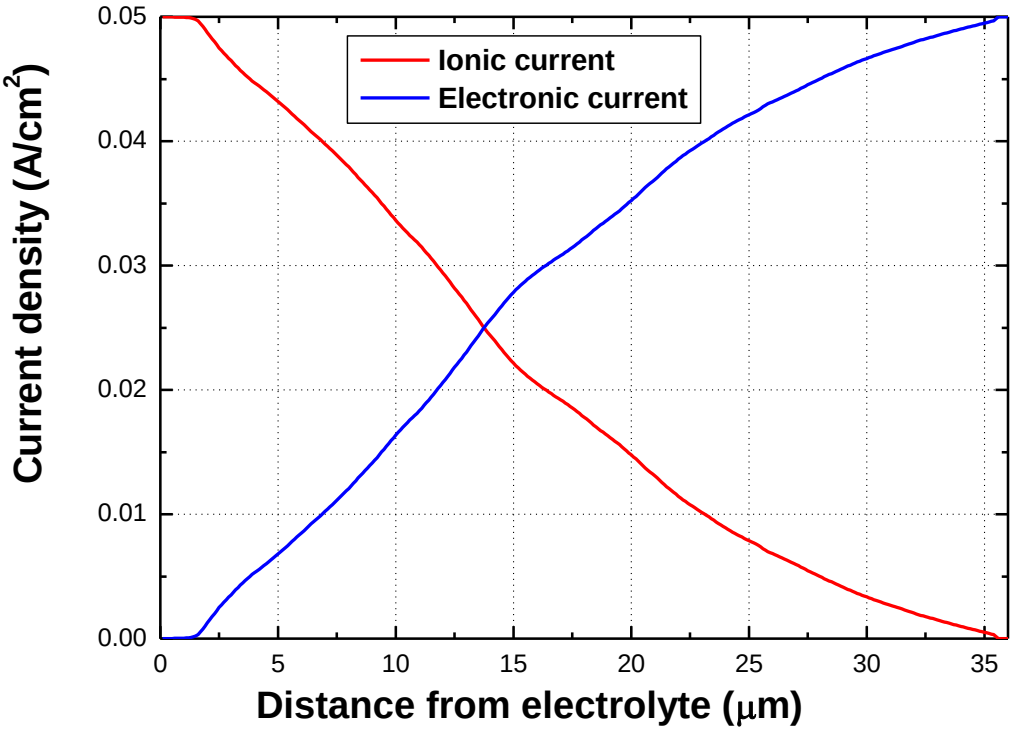

(b) GDC3

Fig. 6-11 Current distributions in (a) LSC3 and (b) GDC3 composite cathodes.

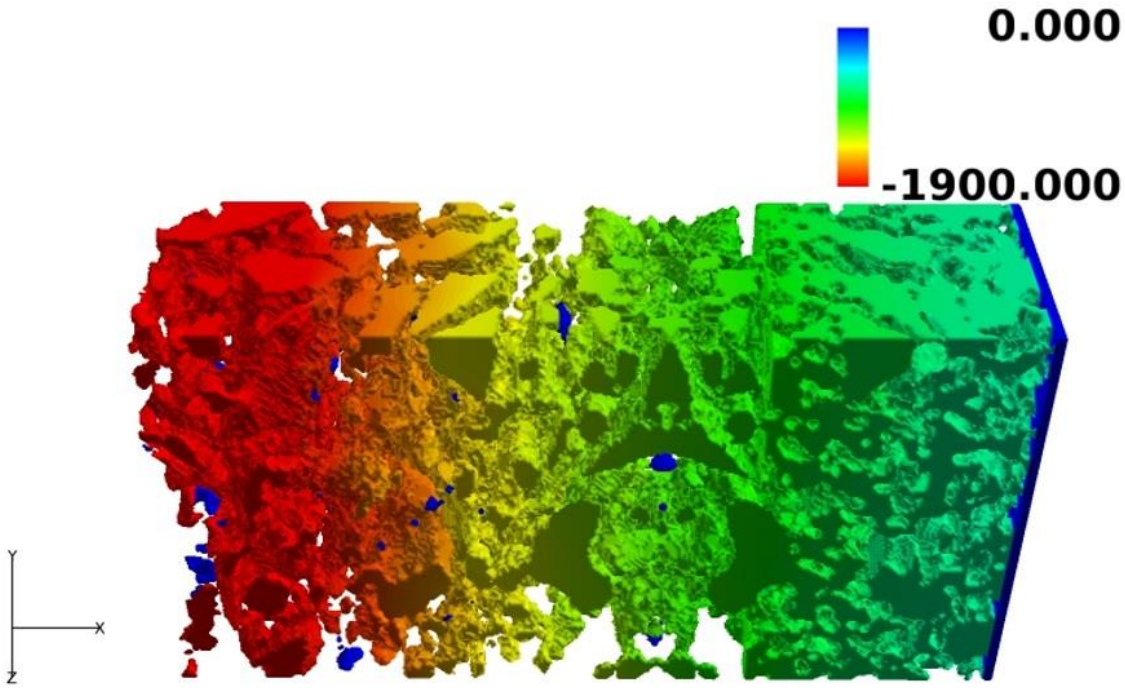

(a) LSC3

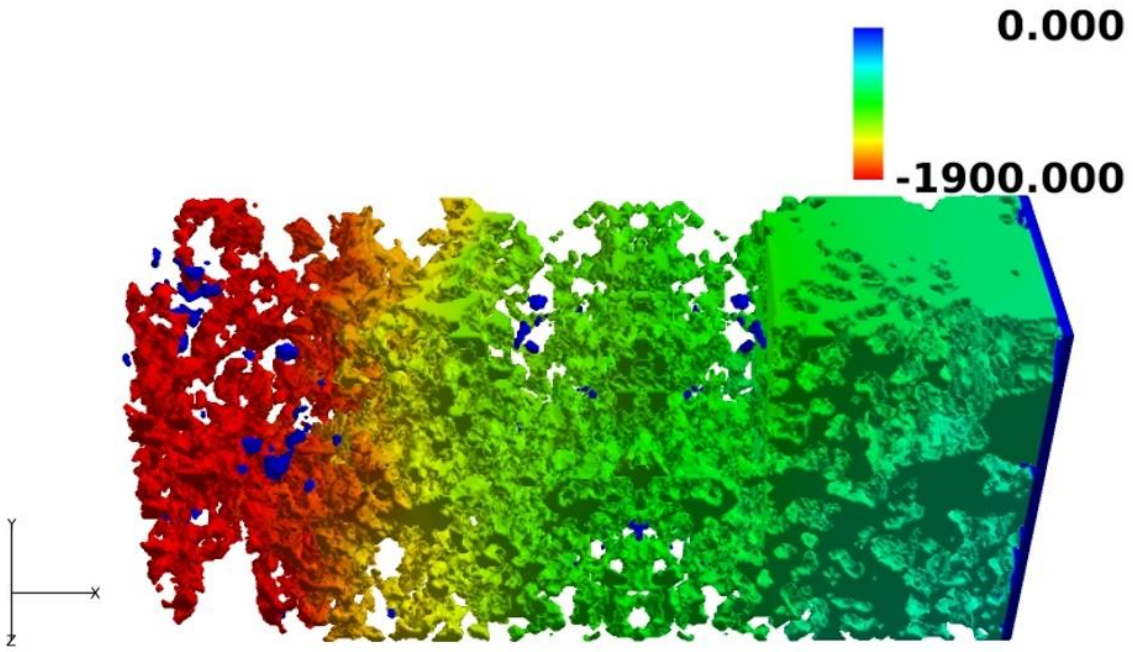

(b) GDC3

Fig. 6-12 Oxygen chemical potential distributions in the LSC phase. (a) LSC3 and (b) GDC3.

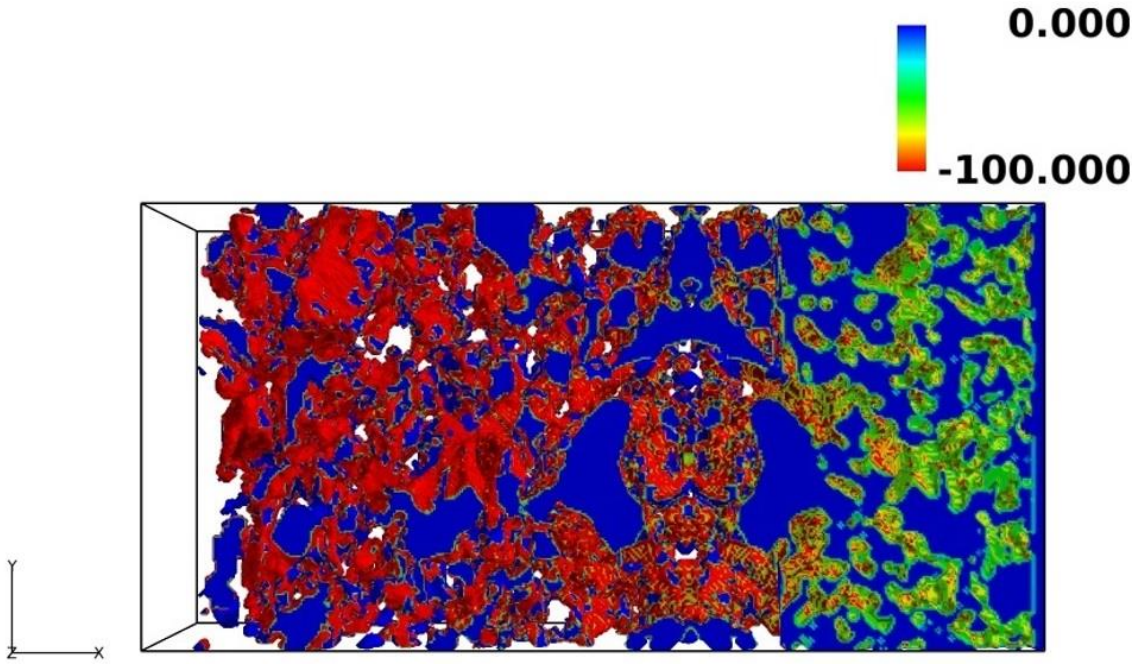

(a) LSC3

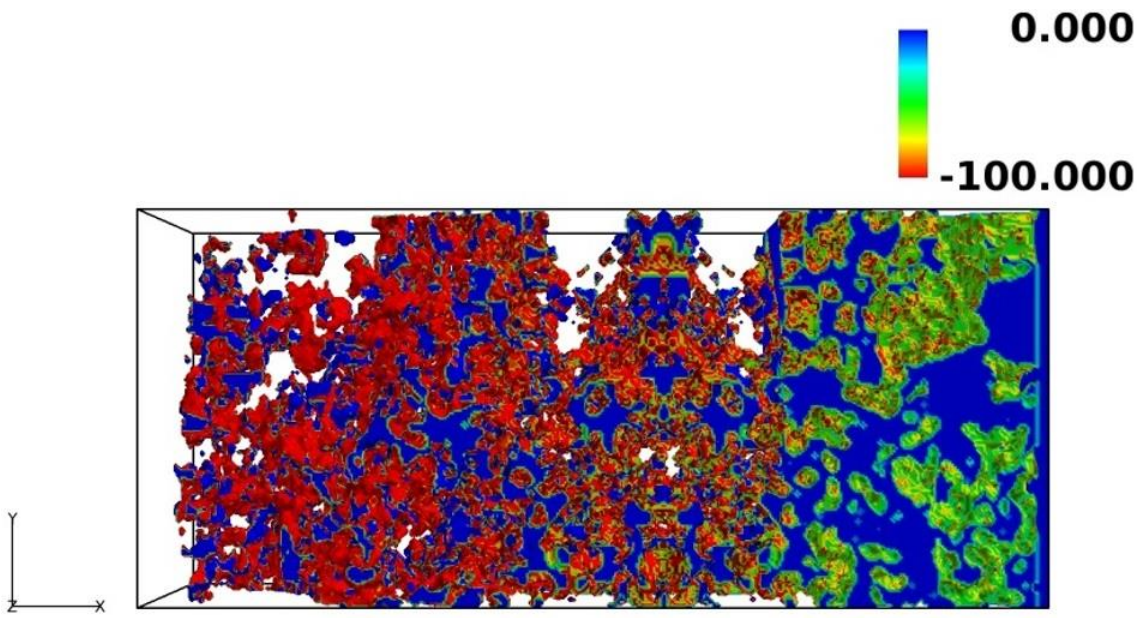

(b) GDC3

Fig. 6-13 Reaction current distributions inside the LSC phases with (a) LSC3 and (b) GDC3 cathodes (Left is the electrolyte side, and right is the current collector side, units: A/cm^2).

6.3 Summary of Chapter 6

In this chapter, microstructure parameters of LSC-GDC composite cathode were controlled by using different particle sizes of the starting powders. LSC = 0.5 μm and GDC = 3 μm of composite cathode (GDC3) and LSC = 3 μm and GDC = 0.5 μm composite cathode (LSC3) were used with a volume ratio of 50:50 %. It is expected that the increase of LSC surface area can be achieved by small LSC particle size with big GDC particle size (GDC3), and the improvement of effective ionic conductivity by the GDC connectivity can be achieved for contrary case (LSC3). For both cathodes, TPB length is assumed to be almost the same since same volume fraction was used. Both overpotential and polarization resistance are smaller for GDC3 cathode. Three dimensional cathode microstructures were reconstructed by FIB-SEM. Both LSC surface area and active TPB density increased for the GDC3 cathode, while similar total TPB density is obtained for both cathodes. Tortuosity factor of LSC is drastically decreased when smaller LSC original powder size is used. On the other hand, GDC tortuosity factor showed small difference. It is indicated that the microstructural change due to particle size is more significant because of its higher sinterability of LSC compared to GDC. It is considered that performance of GDC3 cathode is enhanced due to not only the increase of reaction area, but also the improvement of ionic conduction kinetics in the LSC phase. Electrochemical reaction mechanisms of composite cathodes were investigated by LBM. Overpotential results of simulation showed good agreement with the experimental result. It is considered that electrochemical reaction model which is used in the present study is reasonable to analyze the reaction mechanisms of LSC-GDC composite cathodes. Exchange of ionic and electronic currents and oxygen chemical potential are distributed uniformly for both LSC3 and GDC3 cathodes. It is concluded that the decrease of overpotential for GDC3 cathode is due to the improvement of effective ionic conductivity of LSC.

Chapter 7
Durability of LSC-GDC Composite Cathodes

7.1 Durability Test

In this chapter, LSC-GDC composite cathodes with volume ratios of 30:70, 50:50 and 70:30 % were operated at a current density of i = 0.2 A/cm^2 for 100 hrs. I-V characteristics and impedance spectroscopy were measured with the interval of 20 hrs operation. Cathode microstructures were reconstructed by FIB-SEM and microstructure parameters were correlated with the polarization characteristics.

7.1.1 Cathode Performance Variations

Figure 7-1 shows the voltage drops of LSC:GDC = 30:70, 50:50, and 70:30 vol. % in 100 hrs cell operation. The voltage is decreased during cell operation and the decrease rate becomes higher as the increase of LSC volume fraction from 30 to 70 % in the composites. For the all composite cathodes, the significant voltage drops during initial 20 hrs operation are shown. It can be considered that cathode performance degradation is caused by LSC phases. Overpotential results with the interval of 20 hrs cell operation are shown in Fig. 7-2.

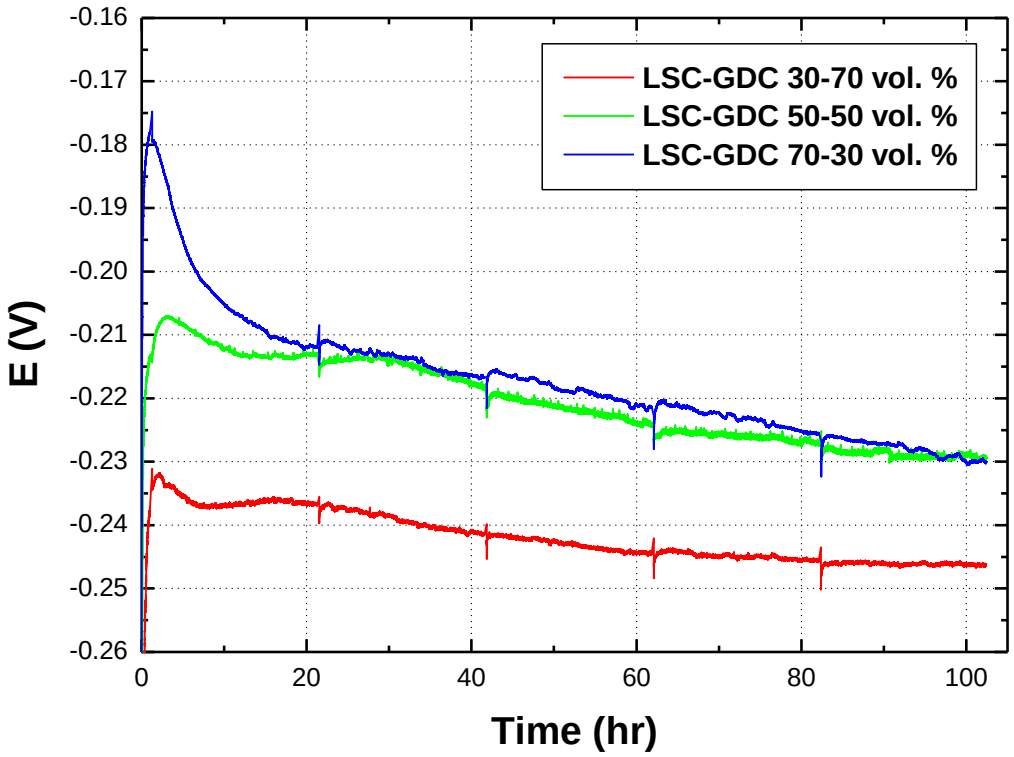

Fig. 7-1 Voltage drop of LSC-GDC composite cathodes during 100 hrs operation.

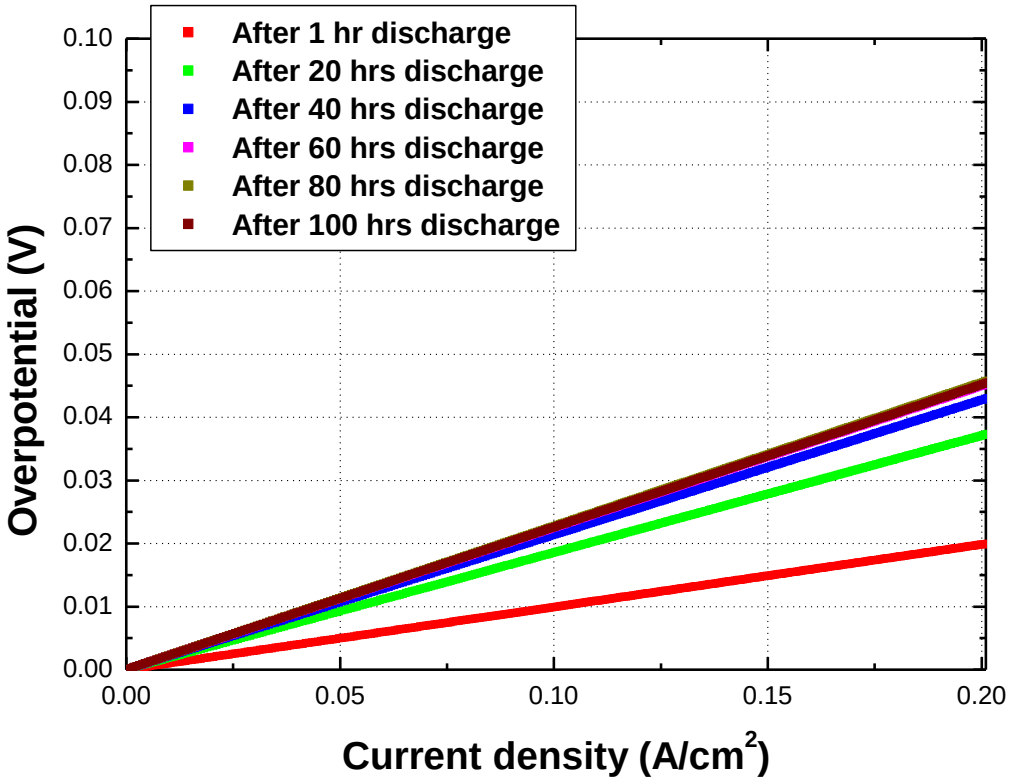

(a) LSC:GDC = 30:70 vol. %.

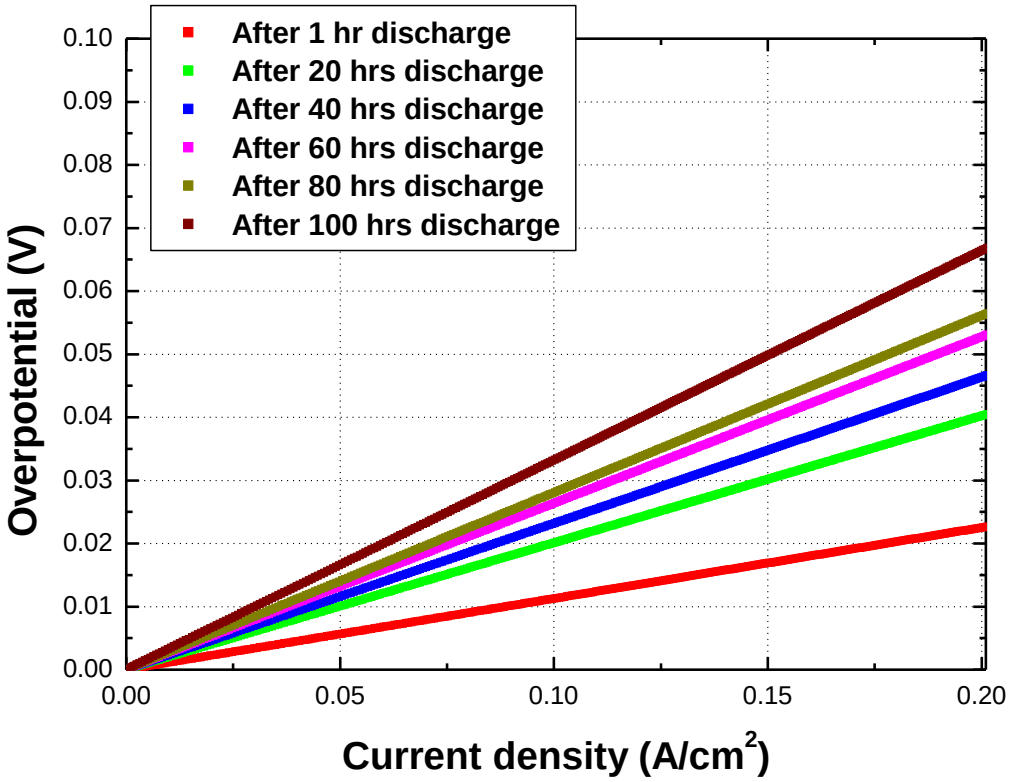

(b) LSC:GDC = 50:50 vol. %.

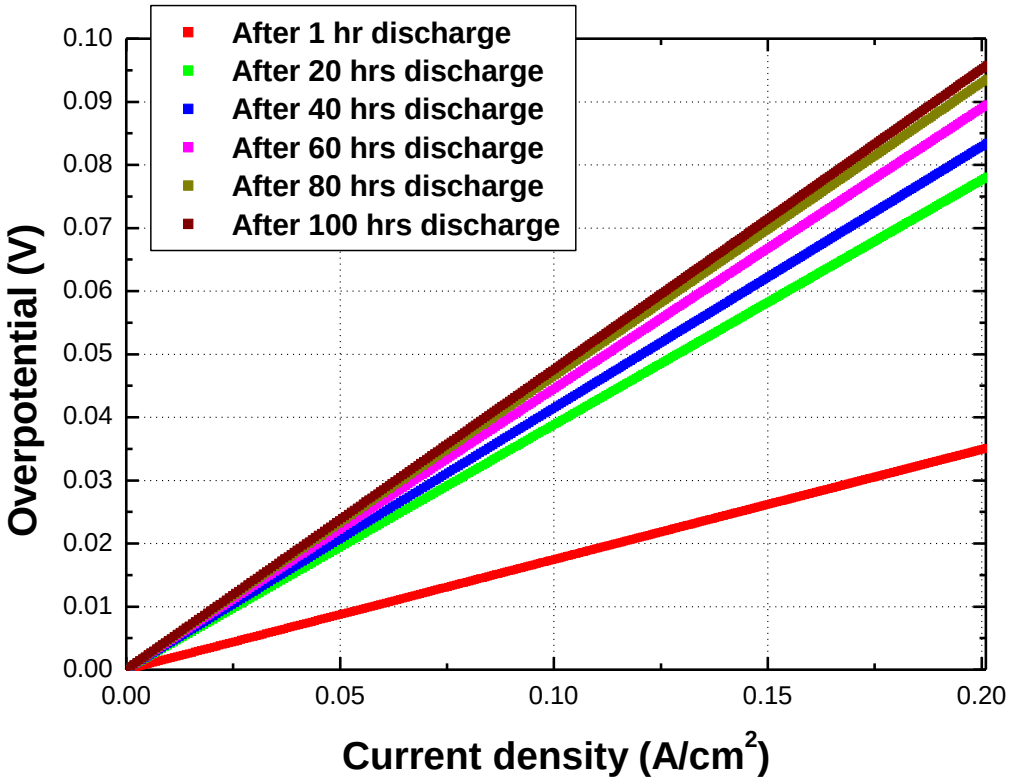

(c) LSC:GDC = 70:30 vol. %.

Fig. 7-2 Overpotential results during 100 hrs cell operation with the interval of 20 hrs.

Overpotential is increased mainly during initial 20 hrs cell operation for all composite cathodes. The results show good agreement with the voltage drops as shown in Fig. 7-1. After 100 hrs operation, it is shown that the overpotentials are increased more significantly as the volume fraction of LSC increases. For the case of LSC:GDC = 70:30 vol. %, the significant increase of overpotential after 100 hrs operation is shown compared to other cases of composite. It can be considered that cathode performance degradation of LSC-GDC composites depends on the LSC phases. Figure 7-3 shows the change of polarization resistances at OCV with cell operation.

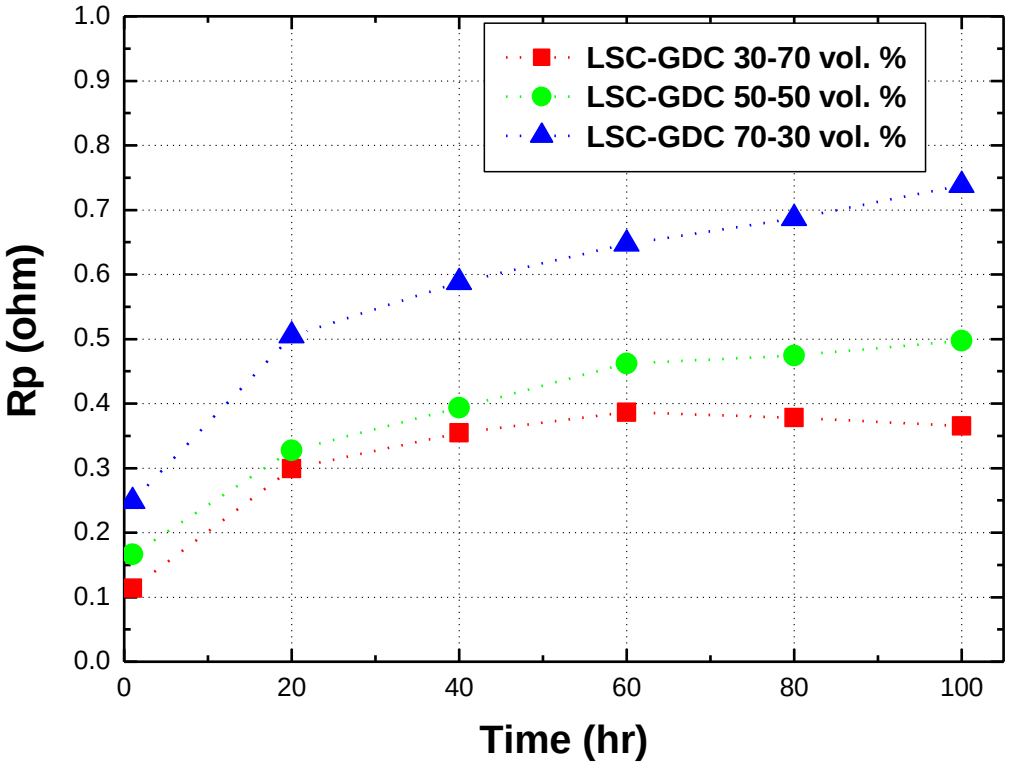

Fig. 7-3 Polarization resistances at OCV after 100 hrs cell operation with the interval of 20 hrs operation time.

Polarization resistances at OCV also show the similar tendency with the variations of voltage and overpotentials as shown in Figs. 7-1 and 7-2. The slight discrepancies of experimental results between the results which are introduced in this chapter and in Chap. 5 are shown. It is considered that variations in experimental conditions such as slurry viscosity or environmental room conditions cause the discrepancies. Note that the cathode performance degradation with the different volume fraction of LSC and GDC is clear.

7.1.2 Microstructure Parameters

Cathode microstructures were reconstructed by FIB-SEM in order to investigate the variations of microstructural parameters after 100 hrs operation. Figure 7-4 shows the SEM images. EsB detector with an acceleration voltage of 5 keV was used for SEM observation. All microstructures have a voxel size of 25 nm. All conditions and images of 3D reconstructed microstructures of LSC-GDC composite cathodes are shown in Table 7-1 and Fig. 7-5, respectively.

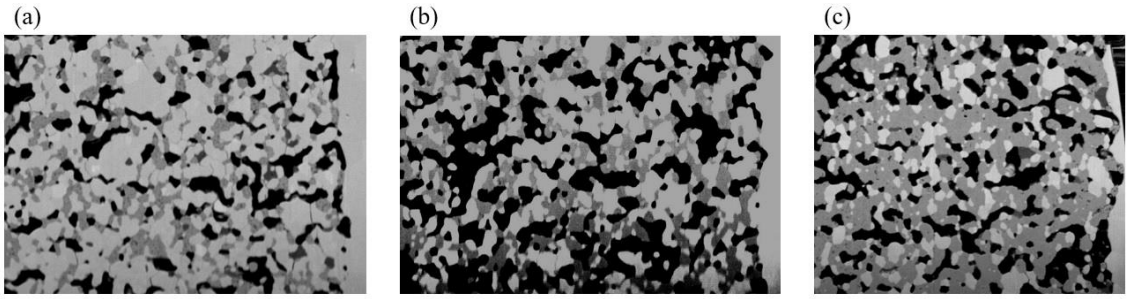

Fig. 7-4 SEM images for FIB-SEM technique.
The volume ratios of LSC:GDC = (a) 30:70, (b) 50:50, and (c) 70:30.
(Black: pore, dark gray: LSC, light gray: GDC).

Table 7-1 Reconstructed sample conditions.

LSC:GDC	Number of pixels ($x \times y$)	Number of slices in z direction	Sample volume size
30:70 vol. %	788×612	257 slices	1938.07 μm^3
50:50 vol. %	860×624	392 slices	3286.92 μm^3
70:30 vol. %	804×736	267 slices	2470.53 μm^3

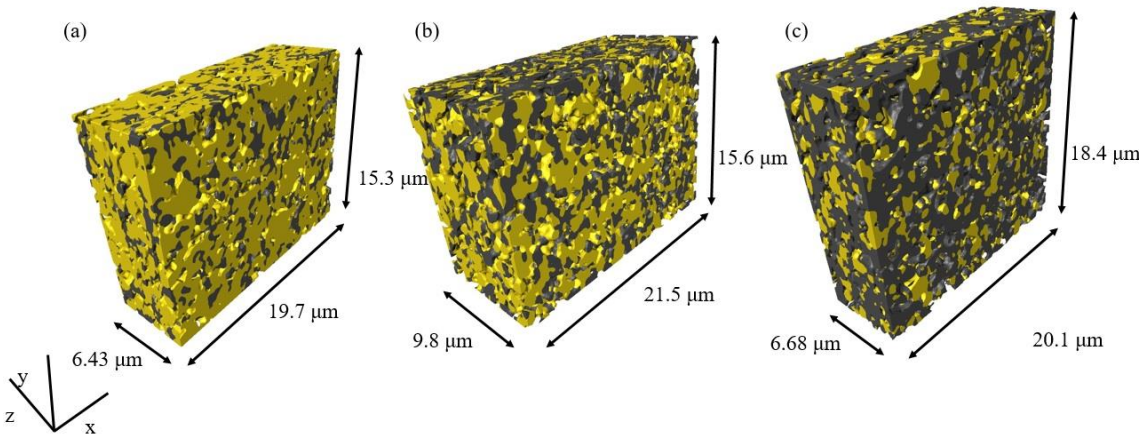

Fig. 7-5 3D reconstructed microstructures of LSC-GDC composite cathodes after 100 hrs operation.
The volume ratio of LSC:GDC = (a) 30:70, (b) 50:50, and (c) 70:30 %.
(Yellow: GDC, Dark gray: LSC).

Microstructure parameters were calculated based on the 3D reconstructed cathode microstructures. For the SEM observation as shown in Fig. 7-4, inhomogeneous phase distributions in the LSC phases can be shown. In the microstructure parameter calculation, these phases were considered to the homogeneous LSC phases. Figure 7-6 represents the variations of LSC surface area

densities and active TPB densities between initial and after 100 hrs operation.

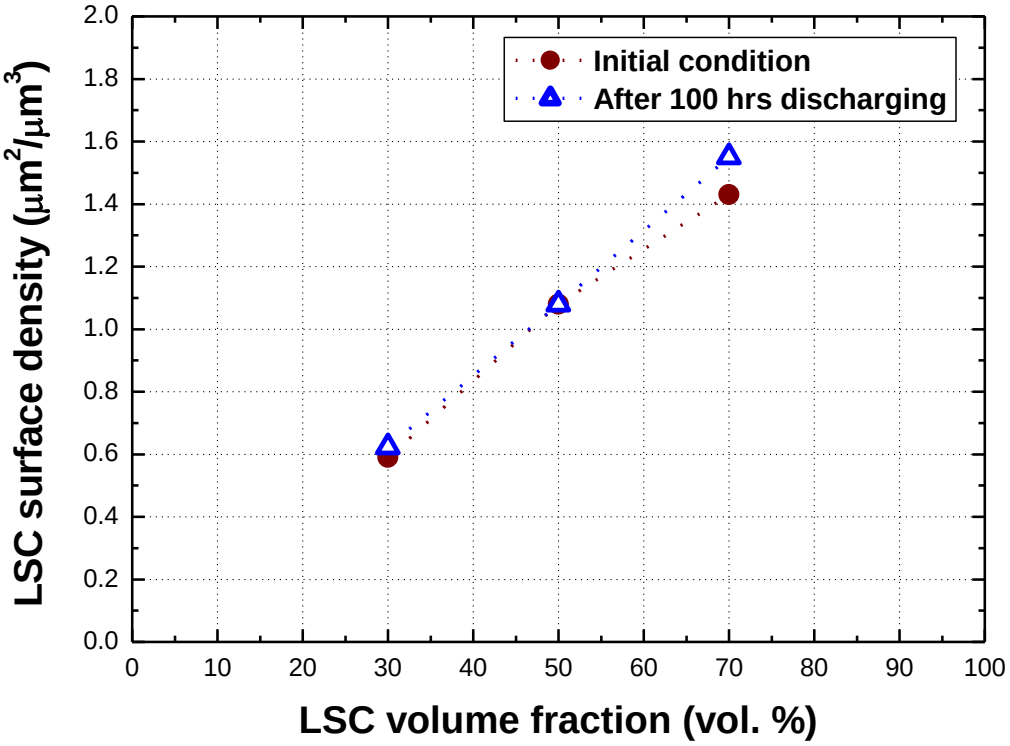

(a) LSC surface area densities

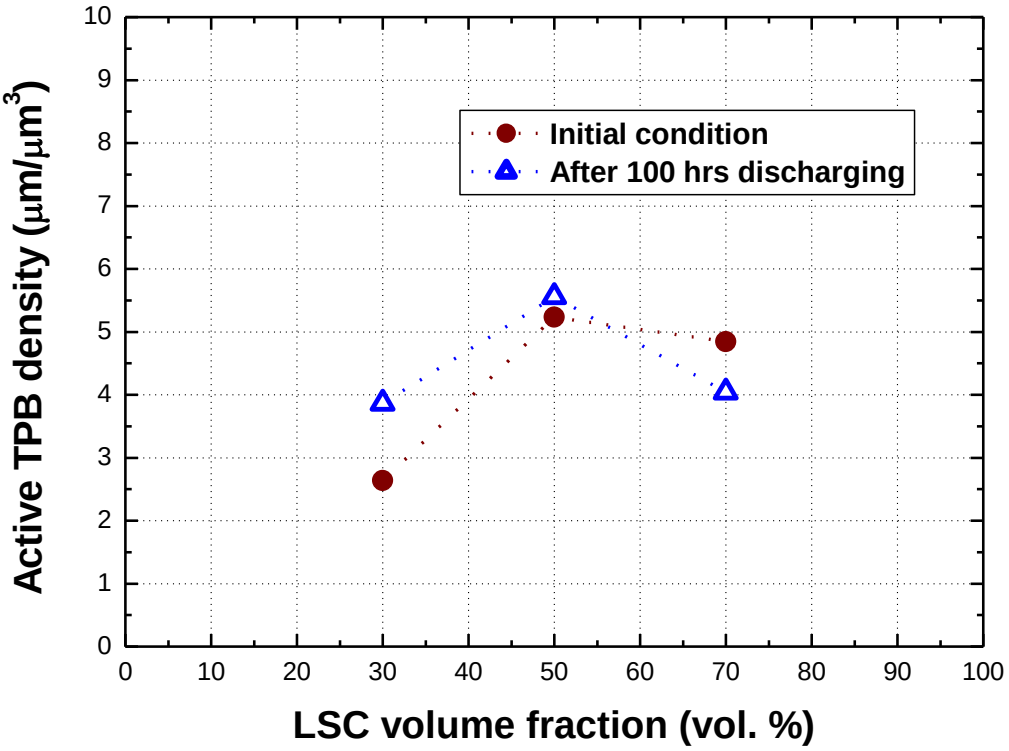

(b) Active TPB densities

Fig. 7-6 Reaction area variations of LSC-GDC composite cathodes between initial and after 100 hrs operation. (a) LSC surface area densities and (b) Active TPB densities.

In Fig. 7-6, similar LSC surface area densities and active TPB densities before and after 100 hrs operation are shown. It indicates that the variations of reaction area cannot explain the cathode performance degradation during cell operation. The other microstructure parameters are shown in Table 7-2. About 30 % porosities are maintained for all cases except for the LSC:GDC = 30:70 vol. %. The variations of tortuosity factors do not show the consistent pattern before and after cell operation. It can be concluded that cathode performance degradation with cell operation cannot be explained by the variations of microstructure characteristics.

Table 7-2 Microstructure parameters before and after 100 hrs operation.

LSC:GDC =	30:70 vol.%	50:50 vol.%	70:30 vol.%
Porosity (initial)	36.70 %	33.96 %	32.48 %
Porosity (after 100 hrs opration)	24.69 %	36.49 %	30.95 %
Tortuosity factor of GDC (initial)	2.290	3.682	23.640
Tortuosity factor of GDC (after 100 hrs operation)	1.893	3.785	44.158
Tortuosity factor of LSC (initial)	30.320	5.698	2.480
Tortuosity factor of LSCC (after 100 hrs operation)	16.425	6.600	2.115

As mentioned, cathode performance was deteriorated more significantly as the volume fraction of LSC increases. It can be predicted that LSC phase in the composites affect the cathode performance degradation more than GDC phase. Variations in the LSC phases between initial and after operation will be investigated.

7.2 Investigation of LSC Phase

In this chapter, phase variations inside the LSC between initial and after 100 hrs cell operation were investigated. It is anticipated that cathode performance with cell operation is degraded due to the LSC, not GDC in the composites. Microstructure variations of LSC were observed by SEM.

7.2.1 Inner Structures

Figures 7-7 and 7-8 show the SEM micrographs of LSC:GDC = 30:70 vol. % before and after 50 hrs cell operation. EsB and SE detectors with an acceleration voltage of 5 keV were used.

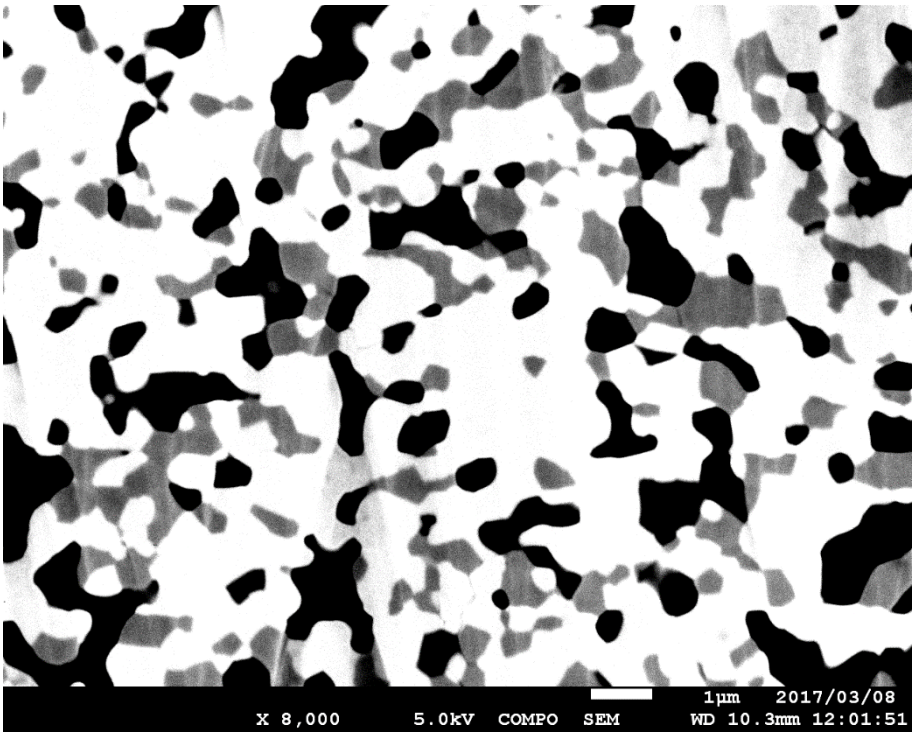

(a) LSC:GDC = 30:70 vol. % before operation.

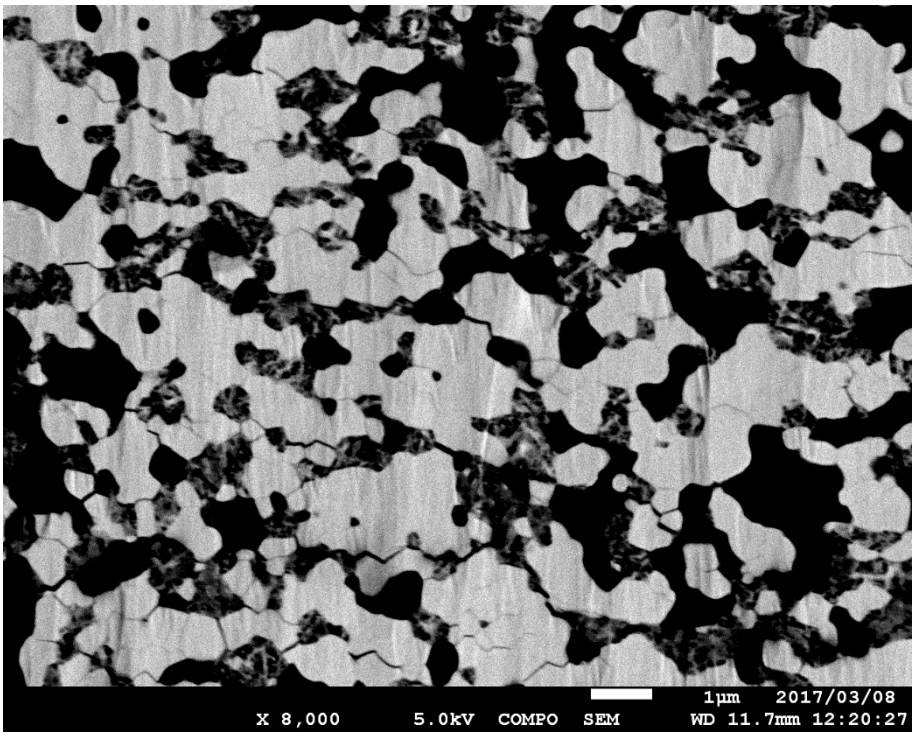

(b) LSC:GDC = 30:70 vol. % after 50 hrs operation.

Fig. 7-7 SEM micrographs with a EsB detector.

A volume ratio of LSC:GDC = 30:70 % (a) before and (b) after 50 hrs operation.

(Dark gray: LSC, light gray: GDC)

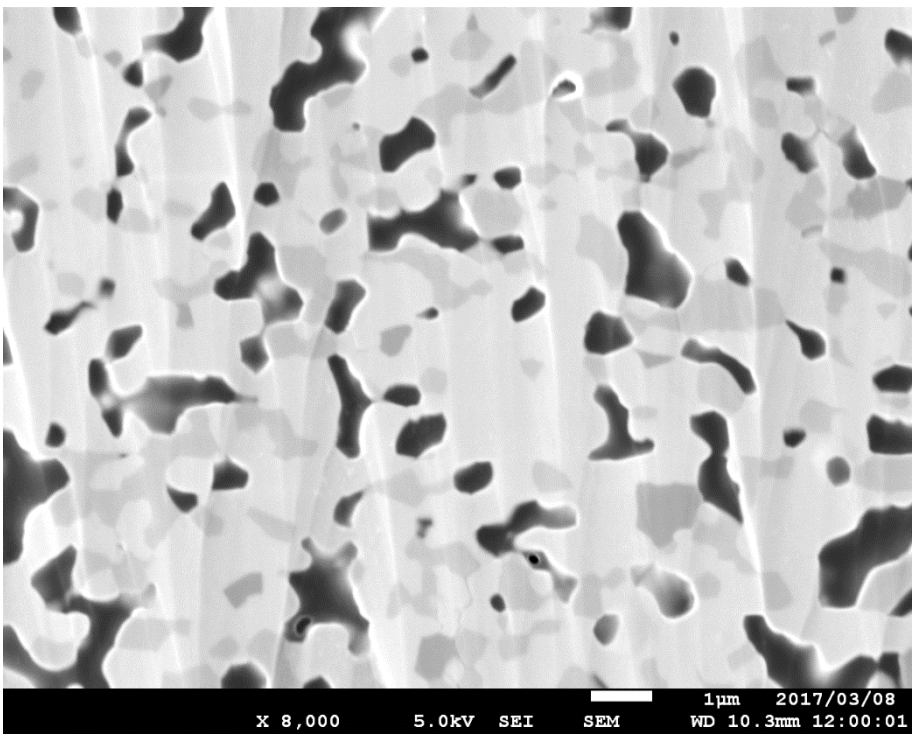

(a) LSC:GDC = 30:70 vol. % before operation.

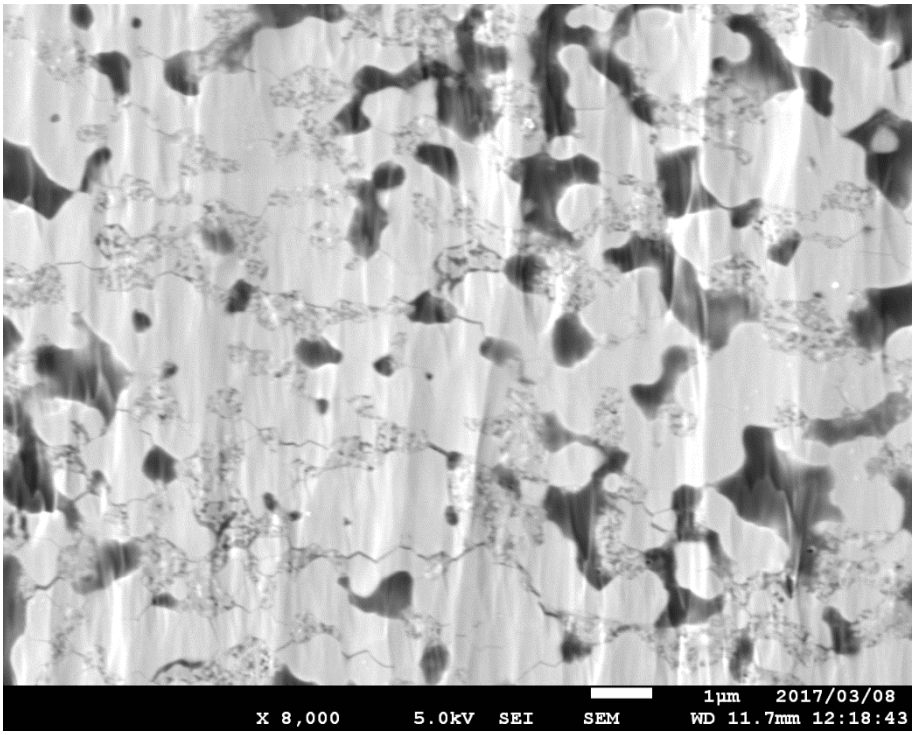

(b) LSC:GDC = 30:70 vol. % before operation.

Fig. 7-8 SEM micrographs with a SE detector.
A volume ratio of LSC:GDC = 30:70 % (a) before and (b) after 50 hrs operation.
(Dark gray: LSC, light gray: GDC)

Inhomogeneous LSC phases are clearly seen after cell operation. Many nano-sized inner pores can be observed in the LSC. It is considered that LSC phases become inhomogeneous under cathode polarization. As the volume fraction of LSC increases in the composites, it is considered that performance degradation of cathode will be exacerbated by the increase of inhomogeneous LSC phases.

7.2.2 TEM observation

In order to investigate the variations of LSC phases more details, transmission electron microscopy (TEM, JEM-2010F, JEOL, Japan) observation was conducted. A LSC:GDC = 30:70 vol. % cathode specimen after 50 hrs discharge was prepared by FIB (FB-2000A, Hitach Co., Ltd, Japan) with an acceleration voltage of 30 kV. For the TEM observation, an acceleration voltage of 200 kV was used. EDX (JED-2300T, JEOL, Japan) mapping was conducted with an acceleration voltage of 200 kV and a beam radius of 1.0 nm to investigate the variations of elements distribution in the

LSC phases. Figure 7-9 shows the STEM micrographs with low and high magnification, respectively. Fig 7-9 (b) corresponds to the spot inside a red circle in Fig. 7-9 (a). In Fig. 7-9 (b), a red circle indicates the nano-sized inner pore in the LSC phase. It is shown that a lot of nano-sized inner pores in the LSC phase were observed after 50 hrs cell operation. No change of GDC phases were observed.

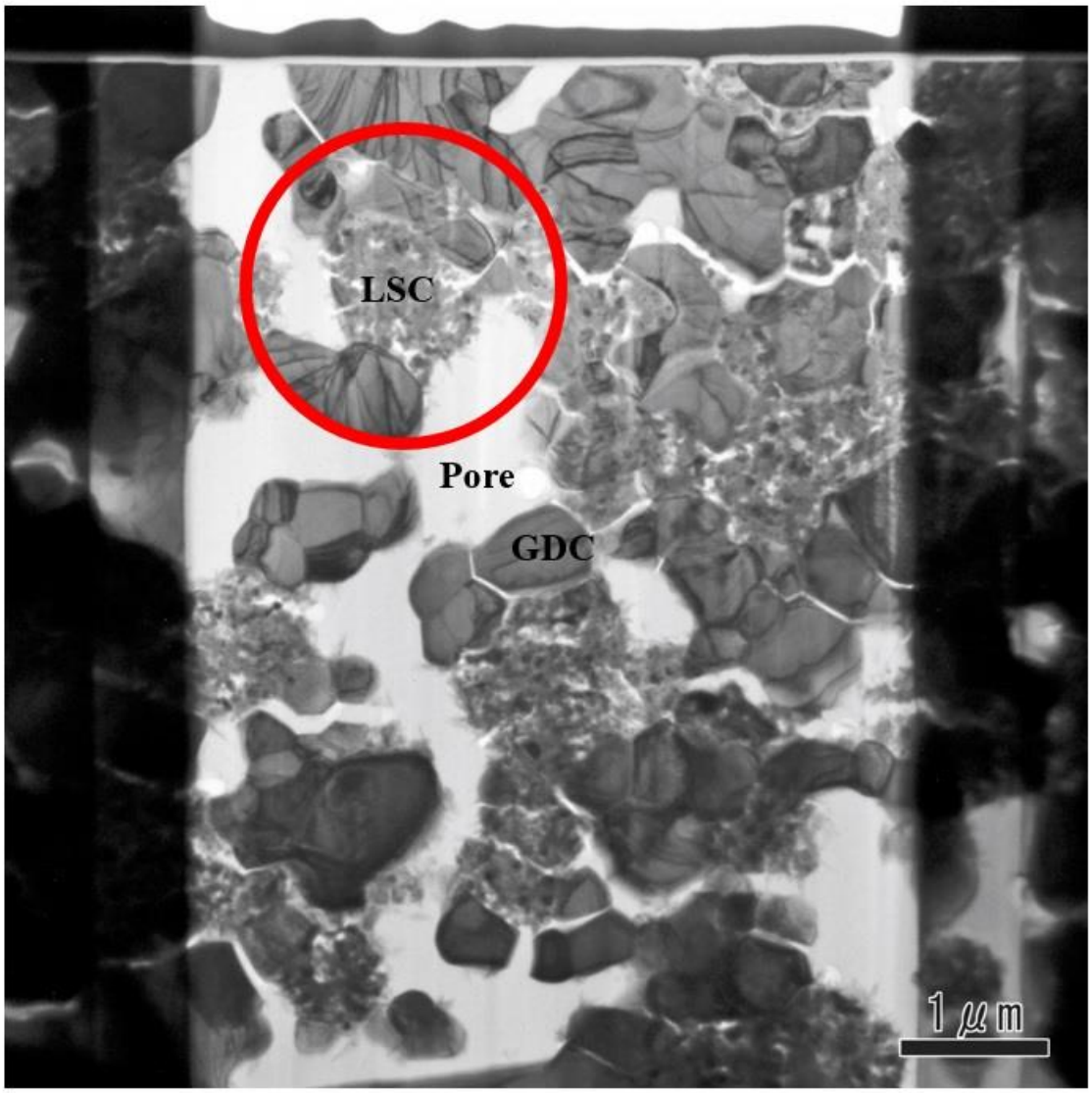

(a) A STEM micrograph with low magnification.

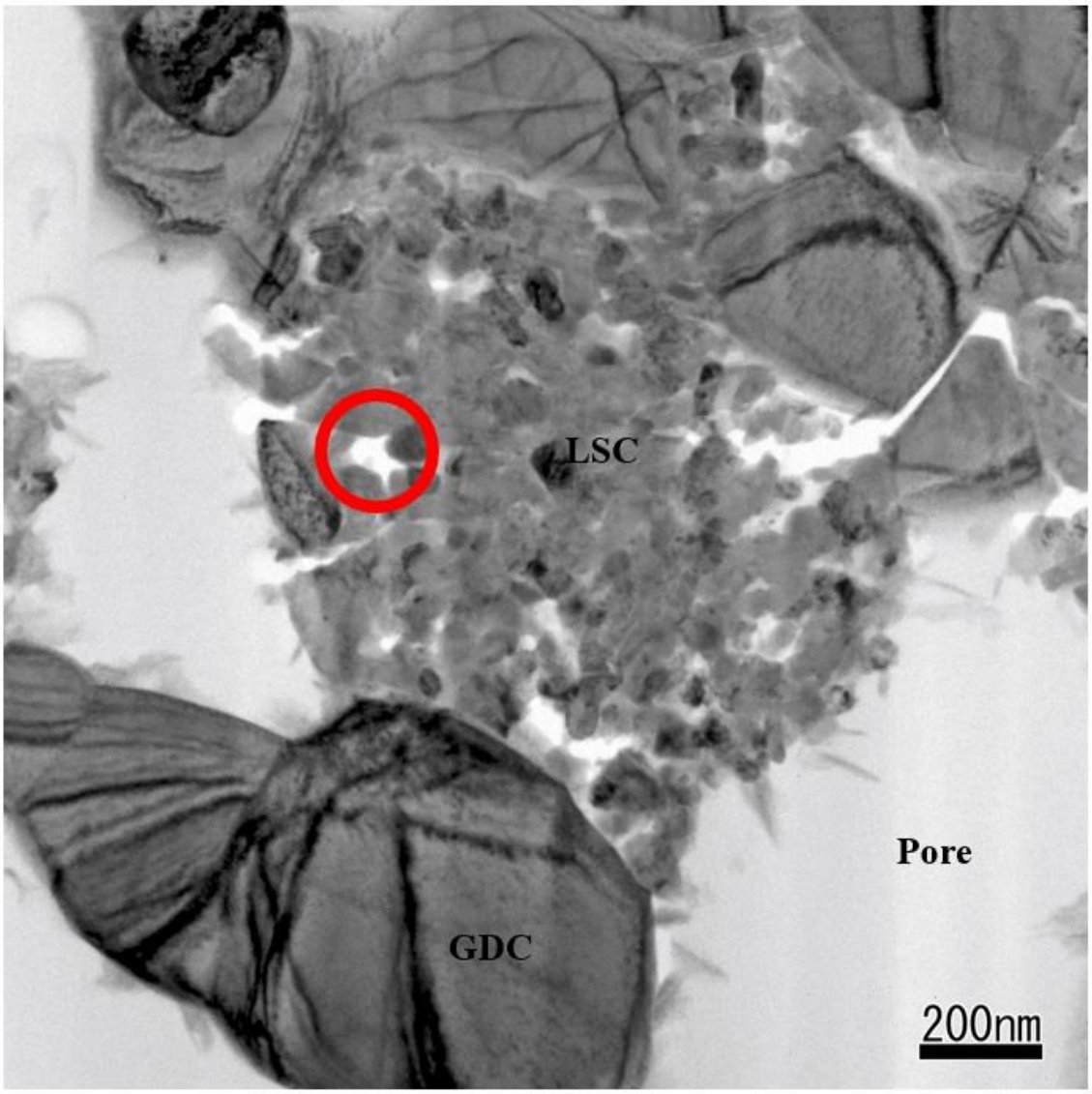

(b) A STEM micrograph with high magnification.

Fig. 7-9 STEM micrographs of LSC:GDC = 30:70 vol. % cathode after 50 hrs operation.

Figure 7-10 shows the EDX mapping results corresponding to the LSC phases in Fig. 7-9 (b). The nano-sized cobalt agglomeration is observed. It is considered that cobalt in the LSC agglomerates at several spots under polarization and this phenomena coincides with a lot of nano-sized inner pores generation. It is considered that severe performance degradation as the increase of LSC volume fraction with cell operation arises from the nano-sized cobalt agglomerations in the LSC phases.

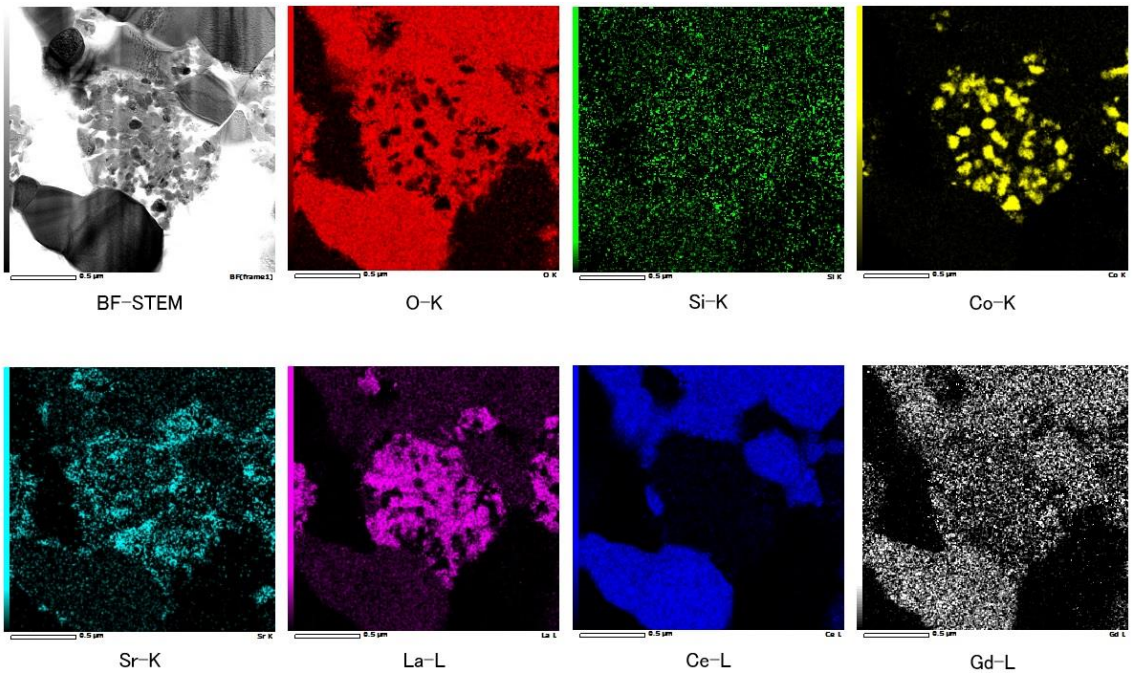

Fig. 7-10 Mapping results of LSC after 50 hrs operation.

7.3 Summary of Chapter 7

In this chapter, cell operation effect was investigated. LSC-GDC composite cathodes with volume ratios of 30:70, 50:50, and 70:30 % were discharged at a current density of i = 0.2 A/cm^2 for 100 hrs. Cathode performances were degraded during cell operation. All composite cathodes show high degradation rates after initial 20 hrs operation. As the volume fractions of LSC increase, cathode performance was degraded more significantly. It is considered that performance degradations of LSC-GDC composite cathode are caused by the variations of LSC phases. After 100 hrs operation, microstructure parameters of cathode were calculated based on 3D reconstructed cathode microstructures. No distinct differences in microstructural characteristics between before and after cell operation were observed. It is seen that performance degradation with cell operation is not related with the whole microstructural variations, directly. Microstructures of LSC:GDC = 30:70 % at initial and after 50 hrs operation were observed by SEM. Inhomogeneous distributions of LSC phase were observed after 50 hrs cell operation. It is considered that cathode performance of LSC-GDC is deteriorated by the decomposition of LSC phases under polarization. TEM and EDX observations of LSC were conducted. After 50 hrs cell operation, small inner pores are generated and nano-sized cobalt agglomerations were observed. It is considered that performance degradation of LSC-GDC composite cathode is caused by the decomposition in the LSC phases. From the results, a LSC:GDC = 30:70 vol. % can be regarded as the most promising volume fraction of LSC-GDC composite cathode due to the lowest degradation rate.

Chapter 8
Conclusions

MIEC-GDC composite is one of the most promising cathode materials for low to intermediate temperature operation of SOFCs due to the significant enhancement of cathode performance. Different from conventional cathodes, two electrochemical reaction mechanisms should be considered including electrochemical reactions on MIEC surface and at TPBs. It is considered that electrochemical reaction at TPB contributes to the performance enhancement of MIEC-GDC composite cathodes. In the present study, mechanisms of performance enhancement are quantitatively investigated based on the cathode performance evaluation and microstructure characteristics. LSCF-GDC and LSC-GDC composite cathodes with different volume ratios were fabricated. An electrolyte-supported cell was used for the measurement. The composite cathodes were fabricated by screen printing method onto the GDC electrolyte. Cathode-reference voltage measurements were conducted. I-V characteristics and electrochemical impedance spectroscopy were measured at 700°C with 100 % of pure oxygen. Cathode microstructures were reconstructed by FIB-SEM using the post-tested cells. Microstructure parameters were calculated by several methods and correlated with polarization characteristics. Electrochemical reaction mechanisms were investigated by LBM based on the 3D reconstructed microstructures. The conclusions are shown below:

- For the LSCF-GDC composite cathodes with different volume ratios, the best performance was achieved at a volume ratio of LSCF:GDC = 30:70 %. Neither LSCF surface and TPB reactions could explain the performance of LSCF-GDC composite cathodes by individual reaction mechanisms. Improvement of ionic conduction kinetics by GDC in the composite contributes to the cathode performance enhancement by elongation of reactive thickness.

- Dependence on ionic conductivity of LSCF in the numerical simulation was investigated. As the ionic conductivity of LSCF decreases, the reactive thickness of LSCF-GDC composite cathode became shorten. For the case of LSCF:GDC = 30:70 vol. %, reactive thickness was elongated even low LSCF ionic conductivity was applied. As lower LSCF ionic conductivity in applied in the numerical simulation, overpotentials were well-matched with the experimental results although only surface reaction was considered. Reliability of LSCF ionic conductivities was evaluated. The ionic conductivities which were calculated by using experimental data based on conductivity relaxation time are lower than those calculated based on the other methods. It is considered that to use the conductivity relaxation method for calculation of ionic conductivity lacks validity due to several problems of that method. Effective thickness of LSCF-GDC composite cathode was investigated by both experimentally and numerically using a volume ratio of LSCF:GDC = 30:70 %. The effective thickness of LSCF:GDC = 30:70 vol. % was found to be around 40 μm from the experiment. However, in the numerical simulation, effective thickness was around 50 μm.

- For the LSC-GDC composite cathodes, the best performance was achieved at a volume ratio of 30:70 %. The results from both performance and microstructure evaluations show similar tendency with that of the LSCF-GDC composite cathode. From the comparison of microstructure parameters with LSCF-GDC, it is found that LSC shows higher sinterability compared to LSCF. The LSC-GDC composite cathodes show better performance compared to the LSCF-GDC for all volume fractions. Performance of LSC-GDC composite cathodes were enhanced not only by the increase of reaction area, but also by the improvement of effective ionic conductivity due to higher ionic conductivity of LSC than LSCF.

- Contributions of LSC surface reaction and ionic conduction in the GDC were investigated by using different original powder sizes. It was assumed that TPB length do not change significantly because same volume ratio of LSC:GDC = 50:50 % was used. LSC of 0.5 μm -with GDC of 3 μm (GDC3), and LSC of 3 μm with GDC of0.5 μm (LSC3) composites were prepared. It was expected that higher LSC surface area can be achieved by the GDC3, and lower tortuosity factor of GDC can be achieved by the LSC3 cathode. GDC3 showed better cathode performance compared to LSC3. From the microstructure parameters, higher LSC surface area density and active TPB density were observed for the GDC3 cathode. The tortuosity factor of LSC is decreased for the GDC3 cathode and the tortuosity factor of GDC were nearly the same for LSC3 and GDC3 cathodes. It is concluded that performance enhancement of GDC3 cathode have relevance to the high sinterability of LSC compared to the GDC.

- Durability of the LSC-GDC composite cathodes were investigated. LSC-GDC composite cathodes with different volume ratios of 30:70, 50:50, and 70:30 % were discharged at a current density of i = 0.2 A/cm^2 for 100 hrs. Cathode performance was degraded during cell operation. As the increase of LSC volume fractions from 30 to 70 %, degradation rate becomes noticeable. It is considered that performance of LSC-GDC composite cathodes is deteriorated by variations of LSC phases. Microstructure parameters were calculated based on 3D reconstruction. Correlation between performance degradation and microstructural variations is unapparent. Phase variations of LSC before and after 50 hrs operation were observed by SEM. Inhomogeneous LSC phase after 50 hrs operation was observed. It is predicted that performance degradation of LSC-GDC composite cathode is caused by the formation of inhomogeneous LSC phase. Many inner pores and nano-sized cobalt agglomeration were observed by TEM and EDX analysis. It is considered that performance of LSC-GDC composite cathode is deteriorated by the decomposition of the LSC phase. It is concluded that a volume ratio of LSC:GDC = 30:70 % is most promising in terms of durability.

Reference

[1] Singer, L. E., and Peterson, D., 2016, “International Energy Outlook 2016.”

[2] International Energy Agency, 2015, “Oil Market Report,” *Int. Energy Agency* [Online]. Available: https://www.iea.org/oilmarketreport/reports/2015/0815/.

[3] 2016, “Annual Global Fossil-Fuel Carbon Emmisions - Graphics” [Online]. Available: http://cdiac.ornl.gov/trends/emis/glo_2013.html.

[4] 2017, “Monthly Electricity Statistics.”

[5] Harrington, R., 2016, “These 10 Countries Are Leading the World in Solar Energy,” *Bus. Insid.* [Online]. Available: http://www.businessinsider.com/best-solar-power-countries-2016-3/#2-china-28330-megawatts-9. [Accessed: 01-Feb-2016].

[6] Liang, B., Suzuki, T., Hamamoto, K., Yamaguchi, T., Sumi, H., Fujishiro, Y., Ingram, B. J., and Carter, J. D., 2012, “A Reduced Temperature Solid Oxide Fuel Cell with Three-Dimensionally Ordered Macroporous Cathode,” *J. Power Sources*, **212**, pp. 86–92.

[7] Liu, Y., Wang, F., Chi, B., Pu, J., Jian, L., and Jiang, S. P., 2013, “A Stability Study of Impregnated LSCF–GDC Composite Cathodes of Solid Oxide Fuel Cells,” *J. Alloys Compd.*, **578**, pp. 37–43.

[8] Wang, X., Chen, Z., and Atkinson, A., 2013, “Crack Formation in Ceramic Films Used in Solid Oxide Fuel Cells,” *J. Eur. Ceram. Soc.*, **33**(13–14), pp. 2539–2547.

[9] Simner, S. P., Anderson, M. D., Engelhard, M. H., and Stevenson, J. W., 2006, “Degradation Mechanisms of La–Sr–Co–Fe–O_3 SOFC Cathodes,” *Electrochem. Solid-State Lett.*, **9**(10), p. A478.

[10] Leng, Y., Chan, S., and Liu, Q., 2008, “Development of LSCF–GDC Composite Cathodes for Low-Temperature Solid Oxide Fuel Cells with Thin Film GDC Electrolyte,” *Int. J. Hydrogen Energy*, **33**(14), pp. 3808–3817.

[11] Muhammad, Z. K., Muhammad, T. M., Song, R. H., Lee, J. W., Lee, S. B., Lim, T. H., and Park, S. J., 2016, “Effect of GDC Interlayer Thickness on Durability of Solid Oxide Fuel Cell Cathode,” *Ceram. Int.*, **42**(6), pp. 6978–6984.

[12] Wang, F., Brito, M. E., Yamaji, K., Cho, D. H., Nishi, M., Kishimoto, H., Horita, T., and Yokokawa, H., 2014, “Effect of Polarization on Sr and Zr Diffusion Behavior in LSCF/GDC/YSZ System,” *Solid State Ionics*, **262**, pp. 454–459.

[13] Jamale, A. P., Bhosale, C. H., and Jadhav, L. D., 2016, “Effect of Screen-Printing Mesh Opening Diameter on Microstructural and Electrical Properties of $La_{0.6}Sr_{0.4}Co_{0.2}Fe_{0.8}O_{3-\delta}$ Thick Films,” *J. Electron. Mater.*, **45**(1), pp. 509–514.

[14] Chen, K., Ai, N., Zhao, L., and Jiang, S. P., 2013, “Effect of Volatile Boron Species on the

Electrocatalytic Activity of Cathodes of Solid Oxide Fuel Cells: II. (La,Sr)(Co,Fe)O_3 Based Electrodes," *J. Electrochem. Soc.*, **160**(3), pp. F301–F308.

[15] Hu, B., Wang, Y., and Xia, C., 2015, "Effects of Ceria Conductivity on the Oxygen Incorporation at the LSCF-SDC-Gas Three-Phase Boundary," *J. Electrochem. Soc.*, **162**(1), pp. F33–F39.

[16] Liu, Y., Cao, Y., Yang, S., Yan, D., Chi, B., Pu, J., and Jian, L., 2015, "Effects of Oxygen Partial Pressure on the Performance Stability of Impregnated La0.6Sr0.4Co0.2Fe0.8O3−δ–Sm0.2Ce0.8O2 Cathodes of Solid Oxide Fuel Cells," *Fuel Process. Technol.*, **135**, pp. 203–206.

[17] Constantin, G., Rossignol, C., Briois, P., Billard, A., Dessemond, L., and Djurado, E., 2013, "Efficiency of a Dense Thin CGO Buffer Layer for Solid Oxide Fuel Cell Operating at Intermediate Temperature," *Solid State Ionics*, **249**–**250**, pp. 98–104.

[18] Chen, J., Liu, Y., Chi, B., Pu, J., and Li, J., 2014, "Electrocatalytic Performance Enhancement of $La_{0.6}Sr_{0.4}Co_{0.2}Fe_{0.8}O_{3-\delta}$–$Y_2O_3$ Stabilized ZrO_2 Cathodes Prepared by an Impregnation Technique," *J. Power Sources*, **256**, pp. 312–318.

[19] Fu, C., Sun, K., Zhang, N., Chen, X., and Zhou, D., 2007, "Electrochemical Characteristics of LSCF–SDC Composite Cathode for Intermediate Temperature SOFC," *Electrochim. Acta*, **52**(13), pp. 4589–4594.

[20] Murray, E. P., Sever, M. J., and Barnett, S. A., 2002, "Electrochemical Performance of (La ,Sr)(Co,Fe)O_3 –(Ce,Gd)O_3 Composite Cathodes," *Solid State Ionics*, **148**, pp. 27–34.

[21] DiGiuseppe, G., and Sun, L., 2011, "Electrochemical Performance of a Solid Oxide Fuel Cell with an LSCF Cathode under Different Oxygen Concentrations," *Int. J. Hydrogen Energy*, **36**(8), pp. 5076–5087.

[22] Hwang, H. J., Moon, J. W., Lee, S., and Lee, E. A., 2005, "Electrochemical Performance of LSCF-Based Composite Cathodes for Intermediate Temperature SOFCs," *J. Power Sources*, **145**(2), pp. 243–248.

[23] Nie, L., Liu, Z., Liu, M., Yang, L., Zhang, Y., and Liu, M., 2010, "Enhanced Performance of $La_{0.6}Sr_{0.4}Co_{0.2}Fe_{0.8}O_{3-\delta}$ (LSCF) Cathodes with Graded Microstructure Fabricated by Tape Casting," *J. Electrochem. Sci. Technol.*, **1**(1), pp. 50–56.

[24] Petric, A., Huang, P., and Tietz, F., 2000, "Evaluation of La-Sr-Co-Fe-O Perovskites for Solid Oxide Fuel Cells and Gas Separation Membranes," *Solid State Ionics*, **135**(1–4), pp. 719–725.

[25] Lu, Z., Hardy, J., Templeton, J., and Stevenson, J., 2012, "Extended Reaction Zone of $La_{0.6}Sr_{0.4}Co_{0.2}Fe_{0.8}O_{3-\delta}$ Cathode for Solid Oxide Fuel Cell," *J. Power Sources*, **198**, pp. 90–94.

[26] Sun, L. P., Rieu, M., Viricelle, J. P., Pijolat, C., and Zhao, H., 2014, "Fabrication and Characterization of Anode-Supported Single Chamber Solid Oxide Fuel Cell Based on $La_{0.6}Sr_{0.4}Co_{0.2}Fe_{0.8}O_{3-\delta}$–$Ce_{0.9}Gd_{0.1}O_{1.95}$ Composite Cathode," *Int. J. Hydrogen Energy*, **39**(2), pp. 1014–1022.

[27] Sumi, H., Yamaguchi, T., Hamamoto, K., Suzuki, T., and Fujishiro, Y., 2013, "High Performance

of $La_{0.6}Sr_{0.4}Co_{0.2}Fe_{0.8}O_3$–$Ce_{0.9}Gd_{0.1}O_{1.95}$ Nanoparticulate Cathode for Intermediate Temperature Microtubular Solid Oxide Fuel Cells," *J. Power Sources*, **226**, pp. 354–358.

[28] Leonide, A., Rüger, B., Weber, A., Meulenberg, W. A., and Ivers-Tiffée, E., 2010, "Impedance Study of Alternative (La,Sr)$FeO_{3-\delta}$ and (La,Sr)(Co,Fe)$O_{3-\delta}$ MIEC Cathode Compositions," *J. Electrochem. Soc.*, **157**(2), p. B234.

[29] Druce, J., and Kilner, J. A., 2013, "Improvement of Oxygen Surface Exchange Kinetics for CGO with Surface Treatment," *J. Electrochem. Soc.*, **161**(1), pp. F99–F104.

[30] Xie, J., Ju, Y. W., and Ishihara, T., 2013, "Influence of Sulfur Impurities on the Stability of $La_{0.6}Sr_{0.4}Co_{0.2}Fe_{0.8}O_3$ Cathode for Solid Oxide Fuel Cells," *Solid State Ionics*, **249**–**250**, pp. 177–183.

[31] Sakai, N., Kishimoto, H., Yamaji, K., Horita, T., Brito, M. E., and Yokokawa, H., 2007, "Interface Stability of Perovskite Cathodes and Rare-Earth Doped Ceria Interlayer in SOFCs," *J. Electrochem. Soc.*, **154**(12), p. B1331.

[32] Izuki, M., Brito, M. E., Yamaji, K., Kishimoto, H., Cho, D.-H., Shimonosono, T., Horita, T., and Yokokawa, H., 2011, "Interfacial Stability and Cation Diffusion across the LSCF/GDC Interface," *J. Power Sources*, **196**(17), pp. 7232–7236.

[33] Jung, H. G., Sun, Y. K., Jung, H. Y., Park, J. S., Kim, H. R., Kim, G. H., Lee, H. W., and Lee, J.-H., 2008, "Investigation of Anode-Supported SOFC with Cobalt-Containing Cathode and GDC Interlayer," *Solid State Ionics*, **179**(27–32), pp. 1535–1539.

[34] Shen, F., and Lu, K., 2015, "$La_{0.6}Sr_{0.4}Co_{0.2}Fe_{0.8}O_3$ Cathodes Incorporated with $Sm_{0.2}Ce_{0.8}O_2$ by Three Different Methods for Solid Oxide Fuel Cells," *J. Power Sources*, **296**, pp. 318–326.

[35] Xiong, C., Taillon, J. A., Pellegrinelli, C., Huang, Y. L., Salamanca-Riba, L. G., Chi, B., Jian, L., Pu, J., and Wachsman, E. D., 2016, "Long-Term Cr Poisoning Effect on LSCF-GDC Composite Cathodes Sintered at Different Temperatures," *J. Electrochem. Soc.*, **163**(9), pp. 1091–1099.

[36] Perz, M., Bucher, E., Gspan, C., Waldhäusl, J., Hofer, F., and Sitte, W., 2016, "Long-Term Degradation of $La_{0.6}Sr_{0.4}Co_{0.2}Fe_{0.8}O_{3-X}$ IT-SOFC Cathodes due to Silicon Poisoning," *Solid State Ionics*, **288**, pp. 22–27.

[37] Lee, S., Song, H. S., Hyun, S. H., Kim, J., and Moon, J., 2010, "LSCF–SDC Core–shell High-Performance Durable Composite Cathode," *J. Power Sources*, **195**(1), pp. 118–123.

[38] Wang, H., Yakal-kremski, K. J., Yeh, T., Rupp, G. M., Limbeck, A., and Barnett, S. A., 2016, "Mechanisms of Performance Degradation of (La,Sr)(Co,Fe)$O_{3-\delta}$ Solid Oxide Fuel Cell Cathodes," *J. Electrochem. Soc.*, **163**(6), pp. 581–585.

[39] Murata, K., Fukui, T., Abe, H., Naito, M., and Nogi, K., 2005, "Morphology Control of La(Sr)Fe(Co)O_{3-a} Cathodes for IT-SOFCs," *J. Power Sources*, **145**(2), pp. 257–261.

[40] Chen, J., Liang, F., Liu, L., Jiang, S., Chi, B., Pu, J., and Li, J., 2008, "Nano-Structured (La, Sr)(Co, Fe)O_3+YSZ Composite Cathodes for Intermediate Temperature Solid Oxide Fuel Cells,"

J. Power Sources, **183**(2), pp. 586–589.

[41] Raj, I. A., Nesaraj, A. S., Kumar, M., Tietz, F., Buchkremer, H. P., and Stoever, D., 2004, "On the Suitablity of $La_{0.60}Sr_{0.40}Co_{0.20}Fe_{0.80}O_3$ Cathode for the Intermediate Temperature Solid Oxide Fuel Cell (ITSOFC)," *J. New Mater. Electrochem. Syst.*, **151**, pp. 145–151.

[42] Dusastre, V., and Kilner, J. A., 1999, "Optimisation of Composite Cathodes for Intermediate Temperature SOFC Applications," *Solid State Ionics*, **126**, pp. 163–174.

[43] Hu, B., Wang, Y., and Xia, C., 2014, "Oxygen Incorporation at the Three-Phase Boundary of LSCF–SDC Composite," *J. Power Sources*, **269**, pp. 180–188.

[44] Bouwmeester, H. J. M., Otter, M. W., and Boukamp, B. A., 2004, "Oxygen Transport in $La_{0.6}Sr_{0.4}Co_{1-y}Fe_yO_{3-\delta}$," *J. Solid State Electrochem.*, **8**(9), pp. 599–605.

[45] Tietz, F., Haanappel, V. A. C., Mai, A., Mertens, J., and Stöver, D., 2006, "Performance of LSCF Cathodes in Cell Tests," *J. Power Sources*, **156**(1), pp. 20–22.

[46] Liu, Y., Chen, K., Zhao, L., Chi, B., Pu, J., Jiang, S. P., and Jian, L., 2014, "Performance Stability and Degradation Mechanism of $La_{0.6}Sr_{0.4}Co_{0.2}Fe_{0.8}O_{3-\delta}$ Cathodes under Solid Oxide Fuel Cells Operation Conditions," *Int. J. Hydrogen Energy*, **39**, pp. 15868–15876.

[47] Möbius, A., Henriques, D., and Markus, T., 2009, "Sintering Behaviour of $La_{1-x}Sr_xCo_{0.2}Fe_{0.8}O_{3-\delta}$ ($0.3 < X < 0.8$) Mixed Conducting Materials," *J. Eur. Ceram. Soc.*, **29**(13), pp. 2831–2839.

[48] Shah, M., and Barnett, S. A., 2008, "Solid Oxide Fuel Cell Cathodes by Infiltration of $La_{0.6}Sr_{0.4}Co_{0.2}Fe_{0.8}O_{3-\delta}$ into Gd-Doped Ceria," *Solid State Ionics*, **179**(35–36), pp. 2059–2064.

[49] Oh, M. Y., Unemoto, A., Amezawa, K., and Kawada, T., 2012, "Stability of $La_{0.6}Sr_{0.4}Co_{0.2}Fe_{0.8}O_{3-\delta}$ as SOFC Cathode," *J. Electrochem. Soc.*, **159**(10), pp. F659–F664.

[50] Chen, Z., Wang, X., Giuliani, F., and Atkinson, A., 2014, "Surface Quality Improvement of Porous Thin Films Suitable for Nanoindentation," *Ceram. Int.*, **40**(3), pp. 3913–3923.

[51] Endler-Schuck, C., Joos, J., Niedrig, C., Weber, A., and Ivers-Tiffée, E., 2015, "The Chemical Oxygen Surface Exchange and Bulk Diffusion Coef Fi Cient Determined by Impedance Spectroscopy of Porous $La_{0.58}Sr_{0.4}Co_{0.2}Fe_{0.8}O_{3-\delta}$ (LSCF) Cathodes," *Solid State Ionics*, **269**, pp. 67–79.

[52] Fleig, J., and Maier, J., 2004, "The Polarization of Mixed Conducting SOFC Cathodes: Effects of Surface Reaction Coefficient, Ionic Conductivity and Geometry," *J. Eur. Ceram. Soc.*, **24**(6), pp. 1343–1347.

[53] Sar, J., Celikbilek, O., Villanova, J., Dessemond, L., Martin, C. L., and Djurado, E., 2015, "Three Dimensional Analysis of $Ce_{0.9}Gd_{0.1}O_{1.95}$-$La_{0.6}Sr_{0.4}Co_{0.2}Fe_{0.8}O_{3-\delta}$ Oxygen Electrode for Solid Oxide Cells," *J. Eur. Ceram. Soc.*, **35**(16), pp. 4497–4505.

[54] Xu, Q., Huang, D., Chen, W., Wang, H., Wang, B., and Yuan, R., 2004, "X-Ray Photoelectron Spectroscopy Investigation on Chemical States of Oxygen on Surfaces of Mixed Electronic–ionic Conducting $La_{0.6}Sr_{0.4}Co_{1-y}Fe_yO_3$ Ceramics," *Appl. Surf. Sci.*, **228**(1–4), pp. 110–114.

[55] Zhao, F., Peng, R., and Xia, C., 2008, "A $La_{0.6}Sr_{0.4}CoO_{3-\delta}$-Based Electrode with High Durability for Intermediate Temperature Solid Oxide Fuel Cells," *Mater. Res. Bull.*, **43**(2), pp. 370–376.

[56] Yasumoto, K., Inagaki, Y., Shiono, M., and Dokiya, M., 2002, "An (La,Sr)(Co,Cu)$O_{3-\delta}$ Cathode for Reduced Temperature SOFCs," *Solid State Ionics*, **148**(3–4), pp. 545–549.

[57] Ko, M., and Hwang, J., 2016, "Application of Sonochemical Processing to LSC($La_{0.6}Sr_{0.4}CoO_3$)/SDC(Sm_2O_3-Doped CeO_2) Composite Cathodes for Solid Oxide Fuel Cells Involving CeO2-Based Electrolytes," *Ceram. Int.*, **42**, pp. 11548–11553.

[58] Huang, Y., Ahn, K., Vohs, J. M., and Gorte, R. J., 2004, "Characterization of Sr-Doped $LaCoO_3$-YSZ Composites Prepared by Impregnation Methods," *J. Electrochem. Soc.*, **151**(10), pp. 1592–1597.

[59] Egger, A., Bucher, E., Yang, M., and Sitte, W., 2012, "Comparison of Oxygen Exchange Kinetics of the IT-SOFC Cathode Materials $La_{0.5}Sr_{0.5}CoO_{3-\delta}$ and $La_{0.6}Sr_{0.4}CoO_{3-\delta}$," *Solid State Ionics*, **225**, pp. 55–60.

[60] Ullmann, H., Trofimenko, N., Tietz, F., Stöver, D., and Ahmad-Khanlou, A., 2000, "Correlation between Thermal Expansion and Oxide Ion Transport in Mixed Conducting Perovskite-Type Oxides for SOFC Cathodes," *Solid State Ionics*, **138**(1–2), pp. 79–90.

[61] Bucher, E., Gspan, C., and Sitte, W., 2015, "Degradation and Regeneration of the SOFC Cathode Material $La_{0.6}Sr_{0.4}CoO_{3-\delta}$ in SO_2-Containing Atmospheres," *Solid State Ionics*, **272**, pp. 112–120.

[62] Su, Q., Yoon, D., Kim, Y. N., Gong, W., Chen, A., Cho, S., Manthiram, A., Jacobson, A. J., and Wang, H., 2012, "Effects of Interlayer Thickness on the Electrochemical and Mechanical Properties of Bi-Layer Cathodes for Solid Oxide Fuel Cells," *J. Power Sources*, **218**, pp. 261–267.

[63] Takeshita, A., Miyoshi, S., Yamaguchi, S., Kudo, T., and Sato, Y., 2014, "High Surface Reactivity of La/Sr-Co Perovskite Based Cathode with Cation Nonstoichiometry," *Solid State Ionics*, **262**(3), pp. 378–381.

[64] Tsvetkov, N., Lu, Q., Sun, L., Crumlin, E. J., and Yildiz, B., 2016, "Improved Chemical and Electrochemical Stability of Perovskite Oxides with Less Reducible Cations at the Surface," *Nat. Mater.*, (June), pp. 1–8.

[65] Moller, P., Kanarbik, R., Kivi, I., Nurk, G., and Lust, E., 2013, "Influence of Microstructure on the Electrochemical Behavior of LSC Cathodes for Intermediate Temperature SOFC," *J. Electrochem. Soc.*, **160**(11), pp. F1245–F1253.

[66] Pecho, O., Holzer, L., Yáng, Z., Martynczuk, J., Hocker, T., Flatt, R. J., and Prestat, M., 2015, "Influence of Strontium-Rich Pore-Filling Phase on the Performance of $La_{0.6}Sr_{0.4}CoO_{3-\delta}$ Thin-Film Cathodes," *J. Power Sources*, **274**, pp. 295–303.

[67] Matsuda, M., Ihara, K., and Miyake, M., 2004, "Influences of Ga Doping on Lattice Parameter, Microstructure, Thermal Expansion Coefficient and Electrical Conductivity of La0.6Sr0.4CoO3-

Y," *Solid State Ionics*, **172**(1–4), pp. 57–61.

[68] Kivi, I., Aruvali, J., Kirsimae, K., Heinsaar, A., Nurk, G., and Lust, E., 2015, "Kinetic Response of $La_{0.6}Sr_{0.4}CoO_{3-\delta}$ Lattice Parameters to Electric Potential Change in Porous Cathode at In Situ Solid Oxide Fuel Cell Conditions," *J. Electrochem. Soc.*, **162**(3), pp. F354–F358.

[69] Wei, F., Cao, H., and Chen, X., 2016, "$La_{0.6}Sr_{0.4}CoO_{3-\delta}$-$Ce_{0.8}Gd_{0.2}O_{2-\delta}$ Nanocomposites Prepared by a Sol – Gel Process for Intermediate Temperature Solid Oxide Fuel Cell Cathode Applications," *J. Mater. Sci.*, **51**(4), pp. 2160–2167.

[70] Zhan, W., Zhou, Y., Chen, T., Miao, G., Ye, X., Li, J., Zhan, Z., and Wang, S., 2015, "Long-Term Stability of Infiltrated $La_{0.8}Sr_{0.2}CoO_{3-\delta}$, $La_{0.58}Sr_{0.4}Co_{0.2}O_{3-\delta}$ and $SmBa_{0.5}Sr_{0.5}CoO_{5+\delta}$," *Int. J. Hydrogen Energy*, **40**, pp. 16532–16539.

[71] Adler, S. B., 1998, "Mechanism and Kinetics of Oxygen Reduction on Porous $La_{1-x}Sr_xCoO_{3-\delta}$ Electrodes," *Solid*, **111**, pp. 125–134.

[72] Dieterle, L., Bockstaller, P., Gerthsen, D., Hayd, J., and Ivers-tiffée, E., 2011, "Microstructure of Nanoscaled $La_{0.6}Sr_{0.4}CoO_{3-\delta}$ Cathodes for Intermediate-Temperature Solid Oxide Fuel Cells," *Adv. Energy Mater.*, **1**, pp. 249–258.

[73] Seeharaj, P., Berenov, A., Raj, E., Rudkin, R., and Atkinson, A., 2011, "Mixed-Conducting LSC/CGO Composites for Passive Oxygen Separation Membranes," *Solid State Ionics*, **192**(1), pp. 638–641.

[74] Nurk, G., Vestli, M., Moller, P., Jaaniso, R., Kodu, M., Mandar, H., Romann, T., Kanarbik, R., and Lust, E., 2016, "Mobility of Sr in Gadolinia Doped Ceria Barrier Layers Prepared Using Spray Pyrolysis, Pulsed Laser Deposition and Magnetron Sputtering Methods," *J. Electrochem. Soc.*, **163**(2), pp. 88–96.

[75] Hayd, J., Dieterle, L., Guntow, U., Gerthsen, D., and Ivers-Tiffée, E., 2011, "Nanoscaled $La_{0.6}Sr_{0.4}CoO_{3-\delta}$ as Intermediate Temperature Solid Oxide Fuel Cell Cathode: Microstructure and Electrochemical Performance," *J. Power Sources*, **196**(17), pp. 7263–7270.

[76] Tao, Y., Shao, J., Wang, W. G., and Wang, J., 2009, "Optimisation and Evaluation of $La_{0.6}Sr_{0.4}CoO_{3-\delta}$ Cathode for Intermediate Temperature Solid Oxide Fuel Cells," *Fuel Cells*, **9**(5), pp. 679–683.

[77] Kuhn, M., Hashimoto, S., Sato, K., Yashiro, K., and Mizusaki, J., 2013, "Oxygen Nonstoichiometry and Thermo-Chemical Stability of $La_{0.6}Sr_{0.4}CoO_{3-\delta}$," *J. Solid State Chem.*, **197**, pp. 38–45.

[78] Horita, T., Yamaji, K., Sakai, N., Yokokawa, H., and Ivers-tiffe, E., 2001, "Oxygen Reduction Mechanism at Porous $La_{1-x}Sr_xCoO_{3-d}$/$La_{0.8}Sr_{0.2}Ga_{0.8}Mg_{0.2}O_{2.8}$ Electrolyte Interface for Solid Oxide Fuel Cells," *Electrochim. Acta*, **46**(12), pp. 1837–1845.

[79] Berenov, A. V., Atkinson, A., Kilner, J. A., Bucher, E., and Sitte, W., 2010, "Oxygen Tracer Diffusion and Surface Exchange Kinetics in $La_{0.6}Sr_{0.4}CoO_{3-\delta}$," *Solid State Ionics*, **181**(17–18), pp.

819–826.

[80] Choi, H. J., Bae, K., Jang, D. Y., Kim, J. W., and Shim, J. H., 2015, "Performance Degradation of Lanthanum Strontium Cobaltite after Surface Modification," *J. Electrochem. Soc.*, **162**(6), pp. F622–F626.

[81] Park, J. H., Hong, W. S., Yoon, K. J., Lee, J. H., Lee, H. W., and Son, J. W., 2013, "Physical and Electrochemical Characteristics of Pulsed Laser Deposited $La_{0.6}Sr_{0.4}CoO_{3-\delta}$-$Ce_{0.9}Gd_{0.1}O_{2-\delta}$ Nanocomposites as a Function of the Mixing Ratio," *J. Electrochem. Soc.*, **161**(1), pp. F16–F22.

[82] Miyoshi, S., Takeshita, A., Okada, S., and Yamaguchi, S., 2016, "Rate-Determining Elementary Step of Oxygen Reduction Reaction at (La,Sr)CoO_3-Based Cathode Surface," *Solid State Ionics*, **285**, pp. 202–208.

[83] Hwang, J., Lee, H., Yoon, K. J., Lee, H. W., Kim, B. K., Lee, J. H., and Son, J. W., 2012, "Study on the Electrode Reaction Mechanism of Pulsed-Laser Deposited Thin-Film $La_{1-x}Sr_xCoO_{3-\delta}$ (X = 0.2. 0.4) Cathodes," *J. Electrochem. Soc.*, **159**(10), pp. F639–F643.

[84] Benel, C., Darbandi, A. J., Djenadic, R., Evans, A., Tolke, R., Prestat, M., and Hahn, H., 2009, "Synthesis and Characterization of Nanoparticulate $La_{0.6}Sr_{0.4}CoO_{3-\delta}$ Cathode for Thin-Film Solid Oxide Fuel Cells," *Solid State Ionics*, **180**(4–5), pp. 424–430.

[85] Park, J. H., Hong, W. S., Kim, G. C., Chang, H. J., Lee, J. H., Yoon, K. J., and Son, J. W., 2013, "The Effect of Post-Annealing on the Properties of a Pulsed-Laser-Deposited $La_{0.6}Sr_{0.4}CoO_{3-\delta}$-$Ce_{0.9}Gd_{0.1}O_{2-\delta}$ Nano-Composite Cathode," *J. Electrochem. Soc.*, **160**(9), pp. 1027–1032.

[86] Fujimaki, Y., Mizuno, K., Shindo, Y., Nakamura, T., Yashiro, K., Nitta, K., Terada, Y., Iguchi, F., Yugami, H., Kawada, T., and Asezawa, K., 2016, "Evaluation of Reaction Distribution in SOFC Cathodes by Using Patterned Dense Thin Film Electrodes," *The 25th Symposium on Solid Oxide Fuel Cells in Japan*, The Solid Oxide Fuel Cell Society of Japan, ed., The Solid Oxide Fuel Cell Society of Japan, Tokyo.

[87] Chen, Z., Wang, X., Giuliani, F., and Atkinson, A., 2015, "Analyses of Microstructural and Elastic Properties of Porous SOFC Cathodes Based on Focused Ion Beam Tomography," *J. Power Sources*, **273**, pp. 486–494.

[88] Scott Cronin, J., Muangnapoh, K., Patterson, Z., Yakal-Kremski, K. J., Dravid, V. P., and Barnett, S. A., 2012, "Effect of Firing Temperature on LSM-YSZ Composite Cathodes: A Combined Three-Dimensional Microstructure and Impedance Spectroscopy Study," *J. Electrochem. Soc.*, **159**(4), p. B385.

[89] Gunda, N. S. K., Choi, H. W., Berson, A., Kenney, B., Karan, K., Pharoah, J. G., and Mitra, S. K., 2011, "Focused Ion Beam-Scanning Electron Microscopy on Solid-Oxide Fuel-Cell Electrode: Image Analysis and Computing Effective Transport Properties," *J. Power Sources*, **196**(7), pp. 3592–3603.

[90] Gostovic, D., Vito, N. J., O'Hara, K. A., Jones, K. S., and Wachsman, E. D., 2011,

"Microstructure and Connectivity Quantification of Complex Composite Solid Oxide Fuel Cell Electrode Three-Dimensional Networks," *J. Am. Ceram. Soc.*, **94**(2), pp. 620–627.

[91] Shikazono, N., Sakamoto, Y., Yamaguchi, Y., and Kasagi, N., 2009, "Microstructure and Polarization Characteristics of Anode Supported Tubular Solid Oxide Fuel Cell with Co-Precipitated and Mechanically Mixed Ni-YSZ Anodes," *J. Power Sources*, **193**(2), pp. 530–540.

[92] Iwai, H., Shikazono, N., Matsui, T., Teshima, H., Kishimoto, M., Kishida, R., Hayashi, D., Matsuzaki, K., Kanno, D., Saito, M., Muroyama, H., Eguchi, K., Kasagi, N., and Yoshida, H., 2010, "Quantification of SOFC Anode Microstructure Based on Dual Beam FIB-SEM Technique," *J. Power Sources*, **195**(4), pp. 955–961.

[93] Matsui, T., Mikami, Y., Muroyama, H., and Eguchi, K., 2010, "Quantitative Analysis of Microstructural Change at the Interface Between (La,Sr)MnO_3 Cathode and YSZ Electrolyte upon Discharge Operation," *J. Electrochem. Soc.*, **157**(12), p. B1790.

[94] Wilson, J. R., Duong, A. T., Gameiro, M., Chen, H. Y., Thornton, K., Mumm, D. R., and Barnett, S. A., 2009, "Quantitative Three-Dimensional Microstructure of a Solid Oxide Fuel Cell Cathode," *Electrochem. commun.*, **11**(5), pp. 1052–1056.

[95] Joos, J., Carraro, T., Weber, A., and Ivers-Tiffée, E., 2011, "Reconstruction of Porous Electrodes by FIB/SEM for Detailed Microstructure Modeling," *J. Power Sources*, **196**(17), pp. 7302–7307.

[96] Yang, J., Muroyama, H., Matsui, T., and Eguchi, K., 2012, "The Influence of Discharge Operation on the Microstructure of Strontium-Doped Lanthanum Manganite Cathode for Solid Oxide Fuel Cells," *J. Power Sources*, **204**, pp. 25–33.

[97] Gostovic, D., Smith, J. R., Kundinger, D. P., Jones, K. S., and Wachsman, E. D., 2007, "Three-Dimensional Reconstruction of Porous LSCF Cathodes," *Electrochem. Solid-State Lett.*, **10**(12), pp. B214–B217.

[98] Zhang, Y., Xia, C., and Chen, F., 2014, "Tortuosity Factor of Three-Dimensional Infiltrate Network," *J. Power Sources*, **269**, pp. 189–193.

[99] Matsuzaki, K., Shikazono, N., and Kasagi, N., 2011, "Three-Dimensional Numerical Analysis of Mixed Ionic and Electronic Conducting Cathode Reconstructed by Focused Ion Beam Scanning Electron Microscope," *J. Power Sources*, **196**(6), pp. 3073–3082.

[100] Shikazono, N., Kanno, D., Matsuzaki, K., Teshima, H., Sumino, S., and Kasagi, N., 2010, "Numerical Assessment of SOFC Anode Polarization Based on Three-Dimensional Model Microstructure Reconstructed from FIB-SEM Images," *J. Electrochem. Soc.*, **157**(5), p. B665.

[101] Carraro, T., Joos, J., Rüger, B., Weber, A., and Ivers-Tiffée, E., 2012, "3D Finite Element Model for Reconstructed Mixed-Conducting Cathodes: I. Performance Quantification," *Electrochim. Acta*, **77**, pp. 315–323.

[102] Lorensen, W. E., and Cline, H. E., 1987, "Marching Cubes: A High Resolution 3D Surface Construction Algorithm," *Proc. 14th Annu. Conf. Comput. Graph. Interact. Tech.* -

SIGGRAPH '87, **21**(4), pp. 163–169.

[103] Krishna, R., and Wesselingh, J. A., 1997, "The Maxwell-Stefan Approach to Mass Transfer," *Chem. Eng. Sci.*, **52**(6), pp. 861–911.

[104] 蒔田董, 1975, "粘度と熱伝導率," 培風館, Tokyo.

[105] Novak, V., Stepanek, F., Koci, P., Marek, M., and Kubicek, M., 2010, "Evaluation of Local Pore Sizes and Transport Properties in Porous Catalysts," *Chem. Eng. Sci.*, **65**(7), pp. 2352–2360.

[106] Kuhn, M., Fukuda, Y., Hashimoto, S., Sato, K., Yashiro, K., and Mizusaki, J., 2013, "Oxygen Nonstoichiometry and Thermo-Chemical Stability of Perovskite-Type $La_{0.6}Sr_{0.4}Co_{1-y}Fe_yO_{3-\delta}$ (Y = 0, 0.2, 0.4, 0.5, 0.6, 0.8, 1) Materials," *J. Electrochem. Soc.*, **160**(1), pp. 34–42.

[107] Yashiro, K., Onuma, S., Kaimai, A., Nigara, Y., Kawada, T., Mizusaki, J., Kawamura, K., Horita, T., and Yokokawa, H., 2002, "Mass Transport Properties of $Ce_{0.9}Gd_{0.1}O_{2-\delta}$at the Surface and in the Bulk," *Solid State Ionics*, **152**–**153**, pp. 469–476.

[108] Kudo, H., Yashiro, K., Hashimoto, S., Amezawa, K., Kawada, T., and Mizusaki, J., 2013, "Oxygen Transport in Perovskite Type Oxide $La_{0.6}Sr_{0.4}Co_{0.2}Fe_{0.8}O_{3-\delta}$," *ECS Trans.*, **50**(44), pp. 37–42.

[109] Søgaard, M., Vang, P., Mogensen, M., Willy, F., and Skou, E., 2006, "Oxygen Nonstoichiometry and Transport Properties of Strontium Substituted Lanthanum Cobaltite," *Soloid State Ionics*, **177**, pp. 3285–3296.

[110] Yashiro, K., Nakano, I., Kuhn, M., Hashimoto, S., Sato, K., and Mizusaki, J., 2011, "Electrical Conductivity and Oxygen Diffusivity of Perovskite-Type Solid Solution $La_{0.6}Sr_{0.4}Co_{0.2}Fe_{0.8}O_{3-\delta}$ (y=0.2, 0.4, 0.5, 0.6, 0.8)," *ECS Trans.*, **35**(1), pp. 1899–1907.

[111] Steele, B., 2000, "Appraisal of $Ce_{1-y}Gd_yO_{2-y/2}$ Electrolytes for IT-SOFC Operation at 500°C," *Solid State Ionics*, **129**(1–4), pp. 95–110.

[112] Fleig, J., 2005, "On the Current-Voltage Characteristics of Charge Transfer Reactions at Mixed Conducting Electrodes on Solid Electrolytes," *Phys. Chem. Chem. Phys.*, **7**(9), p. 2027.

[113] Mizusaki, J., Singhal, S. C., Electrochemical Society. High Temperature Materials Division., J., Electrochemical Society. Battery Division., and Electrochemical Society. Energy Technology Division., 2005, "Solid Oxide Fuel Cells IX : (SOFC-IX) : Proceedings of the International Symposium," Electrochemical Society.

[114] Suwanwarangkul, R., Croiset, E., Entchev, E., Charojrochkul, S., Pritzker, M. D., Fowler, M. W., Douglas, P. L., Chewathanakup, S., and Mahaudom, H., 2006, "Experimental and Modeling Study of Solid Oxide Fuel Cell Operating with Syngas Fuel," *J. Power Sources*, **161**(1), pp. 308–322.

[115] Nagata, S., Momma, A., Kato, T., and Kasuga, Y., 2001, "Numerical Analysis of Output Characteristics of Tubular SOFC with Internal Reformer," *J. Power Sources*, **101**(1), pp. 60–71.

[116] Esquirol, A., Brandon, N. P., Kilner, J. A., and Mogensen, M., 2004, "Electrochemical

Characterization of $La_{0.6}Sr_{0.4}Co_{0.2}Fe_{0.8}O_{3-\delta}$ Cathodes for Intermediate-Temperature SOFCs," *J. Electrochem. Soc.*, **151**(11), pp. A1847–A1855.

[117] Sukop, M. C., and Thorne, D. T., 2016, "Lattice Boltzmann Modeling: An Introduction for Geoscientists and Engineers," Springer US.

[118] Chen, S., and Doolen, G. D., 1998, "Lattice Boltzmann Method for Fluid Flows," *Annu. Rev. Fluid Mech.*, **30**(Kadanoff 1986), pp. 329–364.

[119] Wolf-Gladrow, D. A., 2004, "Lattice-Gas Cellular Automata and Lattice Boltzmann Models," Springer US.

[120] Leonide, A., 2010, "SOFC Modelling and Parameter Identificatgion by Means of Impedance Spectroscopy," Karlsruher Institut für Technologie (KIT).

[121] Ried, P., Holtappels, P., Wichser, A., Ulrich, A., and Graule, T., 2008, "Synthesis and Characterization of $La_{0.6}Sr_{0.4}Co_{0.2}Fe_{0.8}O_{3-\delta}$ and $Ba_{0.5}Sr_{0.5}Co_{0.8}Fe_{0.2}O_{3-\delta}$," *J. Electrochem. Soc.*, **155**(10), p. B1029.

[122] Oishi, J., Otomo, J., Oshima, Y., and Koyama, M., 2015, "The Effects of Minor Elements in $La_{0.6}Sr_{0.4}Co_{0.2}Fe_{0.8}O_{3-\delta}$ Cathodes on Oxygen Reduction Reaction," *J. Power Sources*, **277**, pp. 44–51.

[123] Kudo, H., Yashiro, K., Hashimoto, S. I., Amezawa, K., and Kawada, T., 2014, "Simulation of Oxygen Diffusion Process on Electrical Conductivity Relaxation," *Solid State Ionics*, **262**, pp. 696–700.

謝辞

本研究は，本著者が 2012 年 4 月に東京大学大学院工学系研究科機械工学専攻外国人研究生として生産技術研究所 2 部鹿園研究室に配属された時点から，同年の 10 月に同研究室への 2 年間の修士課程，2014 年 10 月から 3 年間の博士課程までの研究のまとめである．本研究をまとめるまでには，様々な人々にお世話になった．従って，謝辞を記録する．

一先ず，指導教員でいらっしゃる鹿園直毅教授には，研究全般的なことを指導していただいた．ただ研究内容だけではなく，自分の研究の進行方向や，着目すべき点に対してもいろいろお世話になり，研究者の役割や持つべき心得に対して詳しく指導していただいた．そして，研究全般的なこと以外にも，研究室生活を含めて日本内での生活にも様々なことを助けていただいた．卒業し，人生の第 2 幕を始めることで，先生の指導のおかげさまで研究者としての人生をきちんと生きて行くことが可能だと考えられ，とても感謝している．

助教である焦震鈞さんには，最初に研究室に配属してから，装置の使い方や実験の安定化に対していろいろお世話になった．詳しい研究テーマは違ったけれども，初めに燃料電池の研究をすることにとって，すごくお世話になったことを感謝している．

志村敬彬さんは同じ年でもあるし，研究以外にも個人的なことに対していろいろ話をした．一緒にヨーロッパの様々な研究室の見学もし，お互いに多めの思い出ができていると思う．現在は鹿園研究室で特任研究員であるが，自分の夢を広げ，将来に偉い研究者の中で一人になることを期待する．

何岸には，研究以外にも研究室生活が活力になれるようにしてもらった．同じ構造を用いて燃料電池空気極の様々なモデリングをして，現在鹿園研究室の雄一な博士課程学生であるし，将来に無事に博士を取ることを期待している．

千葉工業大学で准教授としていらっしゃる原祥太郎教授には，本研究で用いられた計算コードを頂き，そして日本での生活に対する相談や本研究でメインとして扱っている SOFC 空気極に対していろいろ話をした．現在東京大学浅野キャンパスである日本電子社製 FIB-SEM のマニュアルを作り，将来の鹿園研究室の FIB-SEM 利用でもお世話になると考えられる．

大西純也さんには，計算に必要であるサーバーの管理をしてもらい，サーバーに何か問題がある場合助けてもらった．

ドイツ KIT グループには，鹿園研究室と交流が多く，特に電気化学インピーダンス測定法に対していろいろ相談をした．特に Dino Klotz さんは DRT 手法のため投入した対象セル専用装置の設計に関していろいろ助言をもらった．まだ対象セル専用装置は安定になっていないが，将来にまた助けてもらえると期待している．

それ以外も現在，あるいは過去の研究室メンバーにもいろいろお世話になった．とても感謝しているし，全ての人々の将来に明るい光が待っていることを望む．

以上

1 - 213　ページ　完

博士論文

平成 29 年　8 月 24 日

147235　金　容兌